UNIVERSITY OF SOUTHAMPTON

FACULTY OF ENGINEERING, SCIENCE AND MATHEMATICS

INSTITUTE OF SOUND AND VIBRATION RESEARCH

ON THE APPLICATION OF FINITE ELEMENT ANALYSIS TO WAVE MOTION IN ONE-DIMENSIONAL WAVEGUIDES

by

Yoshiyuki Waki

Thesis for the degree of Doctor of Philosophy

December 2007

UNIVERSITY OF SOUTHAMPTON

ABSTRACT

FACULTY OF ENGINEERING, SCIENCE AND MATHEMATICS
INSTITUTE OF SOUND AND VIBRATION RESEARCH

Doctor of Philosophy

ON THE APPLICATION OF FINITE ELEMENT ANALYSIS TO WAVE MOTION IN ONE-DIMENSIONAL WAVEGUIDES

by Yoshiyuki Waki

This thesis considers issues concerning the application of the wave finite element (WFE) method to the free and forced vibrations of one-dimensional waveguides. A short section of the waveguide is modelled using conventional finite element (FE) methods. A periodicity condition is applied and the resulting mass and stiffness matrices are post-processed to yield the dispersion relations and so on.

First, numerical issues are discussed and methods to reduce the errors are proposed. FE discretisation errors and errors due to round-off of inertia terms are described. A method using concatenated elements is proposed to reduce those round-off errors. Conditioning of the eigenvalue problem is discussed. An application of singular value decomposition is proposed to reduce errors in numerically determining eigenvectors together with Zhong's formulation of the eigenvalue problem. Effects of the modelling of the cross-section on conditioning are shown. Three methods for numerically determining the group velocity are compared and the power and energy relationship is seen to be reliable.

The WFE method is then applied to complicated structures and its accuracy evaluated. Dispersion curves are shown including purely real, purely imaginary and complex wavenumbers. Free wave propagation in a plate strip with free edges, a ring and a cylindrical strip is predicted and the results compared with analytical or numerical solutions to the analytical dispersion equations. In particular, dispersion curves for freely propagating flexural waves, including attenuating waves, are presented. Complicated phenomena such as curve veering, non-zero cut-on phenomena and bifurcations are observed as results of wave coupling in the wave domain. A method of decomposition of the power is proposed to reduce the size of the system matrices and to investigate the wave characteristics of each wave mode.

The wave approach is then used to predict the forced response. A well-conditioned formulation for determining the amplitudes of directly excited waves is proposed. The forced response is determined by considering wave propagation and subsequent reflection at boundaries. Numerical examples of a beam, a plate and a cylinder are shown. Inclusion of rapidly decaying waves is discussed.

As a practical application, free and forced vibrations of a tyre are analysed. The complicated cross-section of a tyre is modelled using a commercial FE package. Frequency dependent material properties of rubber are included. Free wave propagation is shown including attenuating waves and predicted responses are compared with experiment. Effects of the size of the excited region are discussed.

Declaration

I, Yoshiyuki Waki, declare that the thesis entitled ON THE APPLICATION OF FINITE ELEMENT ANALYSIS TO WAVE MOTION IN ONE-DIMENSIONAL WAVEGUIDES and work presented in it are my own. I confirm that: the work has done wholly or mainly whilst in candidature at this university; where I have consulted the published work of others, this has been clearly attributed and I have acknowledged all main sources of help.

SIGNED: …….

DATE: …….

Acknowledgements

I would like to thank my supervisors Brian Mace and Michael Brennan for their kind-hearted, rigorous and patient supervisions. Their comments are always helpful and encourage me and, I am left to say, it was my great pleasure to work with them.

I would like to thank the members of my internal review panel, David Thompson and Jen Muggleton. I found their additional input from different points of view very helpful.

Also, I want to thank all those at ISVR who I have met along the way. They have provided a wealth of friendship and distraction as needed.

I would like to show my gratitude to Bridgestone Corporation for financial support.

Finally, I wish to acknowledge and thank my family who has supported me throughout my studies. I am very grateful.

Table of Contents

Abbreviations

DOF	Degree of freedom.
FE	Finite element.
FEA	Finite element analysis.
FEM	Finite element method.
SVD	Singular value decomposition.
WAC	Wave assurance criterion.
WFE	Wave finite element.

Symbols

c_g	Group velocity.
c_{L1}	Phase velocity of a quasi-longitudinal wave, $c_{L1} = \sqrt{E/\rho}$.
c_L	Phase velocity of a longitudinal wave, $c_L = \sqrt{E/\rho\left(1-\nu^2\right)}$.
c_R	Phase velocity of the Rayleigh wave.
c_s	Phase velocity associated with a shear wave, $c_s = \sqrt{G/\rho}$.
e	Amplitudes of directly excited waves.
f	Frequency $\left(\omega/2\pi\right)$.
f	Nodal forces.
h	Thickness.
j	$\sqrt{-1}$.
k	Wavenumber.
k_B	Bending wavenumber, $k_B = \sqrt[4]{\rho A\omega^2/EI}$.
k_{L1}	Quasi-longitudinal wavenumber, $k_{L1} = \sqrt{\rho\omega^2/E}$.
m	Moment.
q	Nodal displacements.
A	Cross-sectional area.
C	Damping matrix.
D	Bending rigidity, $D = Eh^3/12\left(1-\nu^2\right)$.
D	Dynamic stiffness matrix.
E	Young's modulus
E_k	Kinetic energy density per unit length.
E_p	Potential energy density per unit length.
G	Shear modulus.
I	Second moment of the cross-sectional area.
I	Identity matrix.
K	Stiffness matrix.

L	Length of a waveguide.
L_y	Width of a plate strip, $L_y = 2b$.
$\mathbf{M}$	Mass matrix.
P	Power.
$\mathbf{r}$	Reflection coefficients matrix.
R	Radius.
$\mathbf{R}$	Matrix for dynamic condensation of internal DOFs.
$\mathbf{T}$	Transfer matrix.
$\mathbf{Z}$	Matrix formed in the eigenvalue problem using Zhong's method.
δ	Kronecker delta.
ϕ	Angle.
$\boldsymbol{\varphi}$	Right eigenvector.
γ	Aspect ratio of an element, $\gamma = \Delta_x / \Delta_y$.
γ	Radius of gyration of the cross-section, $\gamma = \sqrt{I/A}$.
η	Proportional damping coefficient.
κ	Condition number.
κ	Curvature, $\kappa = 1/R$.
λ	Eigenvalue.
ν	Poisson's ratio.
θ	Rotational displacement.
ρ	Mass density.
τ	Shear force.
$\boldsymbol{\tau}$	Wave propagation matrix.
ω	Angular frequency.
ξ	Non-dimensional wavenumber.
$\boldsymbol{\psi}$	Left eigenvector.
Δ	Length of an element.
$\boldsymbol{\Phi}$	Right eigenvector matrix.
$\boldsymbol{\Theta}$	Transformation (rotation) matrix.
Ω	Non-dimensional frequency.

$\boldsymbol{\Psi}$	Left eigenvector matrix.

Superscripts

$+$	Positive-going waves.
$-$	Negative-going waves.
$\tilde{\cdot}$	Matrices formed by an FE model with internal nodes.

Subscripts

c	Cut-off frequency.
E	Nodes on edges of a section.
ext	External force.
f	Forces.
I	Internal nodes of a section.
L	Left hand side of a section.
N	Nearfield waves.
P	Propagating waves.
q	Displacements.
r	Ring frequency.
R	Right hand side of section.

Operator

H	Hermitian, complex conjugate transpose.
T	Transpose.

Vector and matrix quantities are denoted in bold font.

List of Figures and Tables

Chapter 1
INTRODUCTION

1.1 Introduction

Analysis of wave propagation in a medium is of great concern for acoustical, electrical, electromagnetical and structural engineers. Examples include sound propagation in air, the transmission of radio waves, the transmission of seismic tremors in the earth and structure-borne sound. In particular, analysis of waves in structural waveguides is of concern in this thesis. Many structures are uniform in one-direction and can hence be regarded as one-dimensional waveguides along which mechanical disturbances propagate. Examples of such waveguides include a rod, a beam, a plate, a cylinder, a railway track and a tyre. Throughout this thesis, waveguides are assumed to be uniform such that the material properties and the cross-section geometry are invariant along the axis of the waveguide.

Analytical solutions for wave propagation can in general be found only for simple waveguides. Consider for example a beam in bending. If the beam is uniform and thin enough compared to the wavelength, Euler-Bernoulli theory can be used: the plane of the cross-section is assumed to remain plane and perpendicular to the neutral axis during bending, e.g. [1,2]. The equation of motion is given by a relatively simple partial differential equation for the Euler-Bernoulli beam and the analytical solution can be obtained for time- and space-harmonic motion. However the assumption breaks down at high frequencies where the wavelength becomes comparable to the thickness. The dynamics of the beam might then be described by Rayleigh theory [1] which includes rotary inertia, or Timoshenko theory [1] which includes both rotary inertia and shear deformation. Alternatively, the beam might be composed of various layers such as a sandwich beam. For a sandwich beam, the equation of motion and associated analytical solution may be approximately found by modelling the sandwich beam as an equivalent Timoshenko beam. The distributions of the displacements and stresses across the cross-section may be more accurately expressed using the first order shear deformation theory or higher order theories [3,4]. However, the equations of motion and analytical solutions become far more complicated. It should be

noted that analytical solutions involve assumptions and the model might become complicated in various circumstances, especially when the construction of the structure becomes complicated or at high frequencies.

For two-dimensional waveguides analytical solutions are available only for specific cases such as an isotropic thin plate with simply-supported boundary conditions in which the displacement can be decomposed into harmonic components, e.g. [1]. Analytical dispersion equations may be transcendental for general waveguides such as a plate strip with free edges. Solutions to the transcendental analytical equation need to be found numerically and the exact solutions cannot be obtained. The similar discussion holds for other analytical methods such as the dynamic stiffness method [5] or the transfer matrix method [6].

In summary, therefore, the analytical solutions may involve approximations of unknown validity and they may be difficult or impossible to obtain for general waveguides with arbitrary complicated cross-sections and boundary conditions. Examples include a railway track and a tyre for both of which the geometry is complicated. To investigate the dynamics of general waveguides numerical methods have been proposed, such as the spectral finite element method [7] and the wave finite element (WFE) method [8,9].

The present work concerns the WFE method. A small section of the waveguide is modelled using finite element analysis (FEA). This yields the mass, damping and stiffness matrices, which are subsequently post-processed in conjunction with a periodicity condition to form the eigenvalue problem. The eigenvalues and eigenvectors represent the free wave propagation characteristics. Since the existing element libraries and commercial finite element (FE) packages can be utilised to model complicated structures, the WFE method is a powerful tool to investigate the dynamics of such structures.

The objectives of the present work are to extend the WFE method for the prediction of vibrational behaviour of structures in terms of wave motion. In particular it concerns the applications to one-dimensional waveguide structures with arbitrary complexities in the cross-section or complicated dispersion characteristics. The particular contributions concern numerical issues, the forced response and various applications including the forced response of an automotive tyre.

First, there are numerical issues concerning the predicted results due to FE approximations, ill-conditioning and so on, e.g. [8-10]. Numerical issues are therefore discussed in detail and methods are proposed to reduce the errors occurring in the WFE results. Formulations to calculate both free wave propagation and forced response are then described so that the WFE

method can be applied to any one-dimensional waveguides with arbitrary complexities in their cross-sections. Applications to a plate strip and an automotive tyre are presented. In the latter, frequency dependent material properties are involved and predictions are compared with experiment.

In the remainder of this chapter existing methods are reviewed and the WFE method is described in detail. The contents and original contributions of this thesis are then described.

1.2 Review of Analysis Methods for Dynamics of Waveguides

In this section analysis methods for the dynamics of waveguides are reviewed. In subsection 1.2.1 the classical analytical approach is first described. The analytical solutions are found from the analytical equation of motion. The general wave approach is also reviewed to give wave motion in general waveguides. Other analytical methods such as the dynamic stiffness method and the transfer matrix method are reviewed in subsection 1.2.2. However, such analytical approaches are in general applicable only to simple waveguides. Numerical methods such as the spectral finite element method and the WFE method are then needed to investigate waves in general waveguides. These numerical methods are described in subsection 1.2.3.

1.2.1 Analytical Method (Wave Approach)

In this subsection the classical analytical method for determining wave motion in structural waveguides is reviewed. Analytical determinations for free wave propagation, reflection and transmission, and forced response are described. The general wave approach is reviewed in which wave propagation, reflection and transmission are considered.

Free Wave Propagation

Simple waveguides, e.g. a rod and a beam, are amenable to exact analysis. For such waveguides the analytical solutions are available for the wavenumber, the group velocity, etc., e.g. [1]. As an example, for a thin beam where the Euler-Bernoulli theory holds, the governing equation for free vibration is given in form, e.g. [1],

$$\frac{\partial^4 w}{\partial x^4} + C\frac{\partial^2 w}{\partial t^2} = 0 \tag{1.1}$$

where w is the translational displacement, x is the direction along the axis of the beam, t is time and C is the constant given from its material properties and geometry of the cross-section. Assuming time- and space-harmonic motion, the displacement is written as

$$w = ae^{-jkx}e^{j\omega t} \tag{1.2}$$

where k is the wavenumber, ω is the angular frequency, a is a wave amplitude and $j = \sqrt{-1}$. Substituting the displacement (1.2) into the governing equation gives the analytical dispersion equation of the beam as

$$k^4 = C\omega^2 . \tag{1.3}$$

The beam holds four freely propagating waves with their wavenumbers being $k = \pm\sqrt[4]{C\omega^2}$, $\pm j\sqrt[4]{C\omega^2}$. The first two wavenumbers describe propagating waves and the latter two are nearfield waves. The positive real and negative imaginary wavenumbers are associated with the positive-going waves so that the waves propagate in the positive direction of the beam and the other wavenumbers are associated with the negative-going waves. Once the dispersion equation, e.g. equation (1.3), is obtained, the phase velocity ω/k and the group velocity $\partial\omega/\partial k$ can be calculated. The same approach can be used to waveguides where the analytical equations of motion are available.

Reflection and Transmission

When waves propagate along a waveguide, the waves might impinge on such as a boundary, a discontinuity and so on. The incident waves will reflect at boundaries and may reflect and transmit at discontinuities, e.g. [1,2,11].

Consider a case when a propagating wave in the beam impinges on a boundary. The displacement at the boundary can be expressed as

$$w = \left(a_i e^{-jkx} + a_{rP} e^{jkx} + a_{rN} e^{kx} \right) e^{j\omega t} \tag{1.4}$$

where a_i, a_{rP}, a_{rN} are the amplitudes of the incident, reflected propagating and reflected nearfield waves, respectively. Depending on the boundary condition, a combination of displacements and forces is given at the boundary such that the reflection coefficients, a_{rP}/a_i and a_{rN}/a_i, can be calculated. For a free boundary condition for the beam, for example, the reflection coefficients are given by $a_{rP}/a_i = -j$ and $a_{rN}/a_i = 1-j$ [1]. The complex values of the coefficient indicate that phase shifts occur in the reflected waves relative to the incident wave. In this case both propagating and nearfield waves are generated for one incident propagating wave such that wave mode conversion occurs. Knowledge of the phase change at boundaries enables one to determine the natural frequencies of a finite waveguide. When the total phase change of the propagating wave along the waveguide satisfies certain condition, system motion intensifies. Such an approach is termed as the phase closure principle [3] or phase coincidence [12].

When a wave impinges on a discontinuity such as a point mass, both reflected and transmitted waves may be generated. The continuity of displacement at the discontinuity and force equilibrium at the discontinuity give the reflection coefficients and transmission coefficients [1,2,11]. For the beam the propagating and nearfield waves may be generated for both the reflected and transmitted waves such that four waves in total can be generated. The reflection and transmission coefficients are frequency dependent in general.

Forced Response

When an excitation is applied to a waveguide, waves are generated and start propagating. The amplitudes of directly excited waves can be determined for an infinite waveguide by considering continuity of displacement and force equilibrium in conjunction with the applied excitation. Some examples of the amplitudes of directly excited waves in infinite and semi-infinite one-dimensional waveguides are tabulated in [13] for point force and moment excitation. Forced response can then be calculated using the general wave approach considering the free wave propagation and subsequent reflection and transmission, e.g. [14].

General Wave Approach

The approach described above can be applied to other cases where the equation of motion can be analytically expressed. The examples include the Timoshenko beam, a beam subjected to in-plane tension and on an elastic foundation, a general rod, a ring and plates, e.g. [1]. For waveguides in which there are many wave modes, wave motion is conveniently expressed in matrix form. Formulation for the dynamic behaviour of waveguides using the wave approach is well-conditioned. This is important for general waveguides for which numerical issues are likely to occur.

Several works about the general wave approach are reviewed here. Mace [14] studied the vibrational behaviour of a beam based on propagation, reflection and transmission of waves including the flexural nearfield waves. Inclusion of nearfield waves is particularly important when the local behaviour around a discontinuity or an excitation is of concern and when two nearfield waves propagate in opposite directions, since they can carry power [15,16]. The amplitudes of the waves and the excitation are expressed in vector forms and wave propagation, reflection and transmission are described in matrix forms. Consequences of reciprocity were shown for the reflection coefficient matrix [17] and the transmission coefficient matrix [18] including nearfield waves.

Many applications of the wave approach can be found in the literature. Miller and Von Flotow [15] used the wave approach to investigate the power in an assemblage of one-dimensional members. The coupling power between two end-coupled beams was presented by Mace [19] and that between two plates was shown by Wester and Mace [20]. Lee et al [21] analysed the power reflection and transmission for two beams connected with a U-shape beam. Yong and Lin [22] used the wave approach to calculate the forced response of a periodically supported beam. Harland et al [23] demonstrated the systematic implementation of the wave approach for arbitrary waveguides and considered in detail the cases of a sandwich beam, jointed beams and a beam with a local discontinuity.

In this thesis, the wave approach is used to give the forced response of general complicated waveguides. The approach used in this thesis is in particular close to the work done by Harland et al [23].

1.2.2 Other Analytical Methods

To investigate the dynamics of waveguides some other methods have been proposed, e.g. [24]. In this subsection some of these other analytical methods are reviewed. They include the dynamic stiffness method, the transfer matrix method, the receptance method and the spectral element method.

Dynamic Stiffness Method:

The dynamic stiffness method [5] is sometimes termed the dynamic stiffness matrix method [25] or the dynamic element method [26]. A section of a structure is modelled by the analytical relationships between displacements and forces applied at the ends or edges of the section. The equation of motion for time-harmonic behaviour is expressed as

$$\begin{bmatrix} \mathbf{D}_{LL} & \mathbf{D}_{LR} \\ \mathbf{D}_{RL} & \mathbf{D}_{RR} \end{bmatrix} \begin{bmatrix} \mathbf{q}_L \\ \mathbf{q}_R \end{bmatrix} = \begin{bmatrix} \mathbf{f}_L \\ \mathbf{f}_R \end{bmatrix} \tag{1.5}$$

where $\mathbf{D}$ is the dynamic stiffness matrix, the subscripts L and R represent the left and right hands of the section, $\mathbf{q}$ and $\mathbf{f}$ are the displacement and force vectors respectively. The matrix $\mathbf{D}$ is given in the frequency domain and its elements are frequency dependent.

Some applications can be seen in literature. Langley [27] analysed power in a beam and a truss structure. Lee and Thompson [28] applied the method to helical springs. A series of works by Banerjee present the dynamic stiffness matrix for various one-dimensional waveguides, e.g. [29,30]. Langley [31,32] applied the method to investigate free and forced vibrations of the two-dimensional structures but only for simply-supported edges where the displacement along one-dimension can be decomposed into harmonic components.

The dynamic stiffness matrix can be expanded into a power series in terms of ω [26] such that

$$\mathbf{D}(\omega) = \sum_{i=0}^{\infty} \mathbf{D}_i \left(\omega^{2i}\right). \tag{1.6}$$

The resulting matrices $\mathbf{D}_i\left(\omega^{2i}\right)$ can be regarded as the consistent stiffness matrix (i=0), the consistent mass matrix (i=1) and higher order correction terms $\left(i \geq 2\right)$.

Transfer Matrix Method:

The transfer matrix method [6], or Holzer's method [33], describes the change of wave modes, or the state vector, at two different locations (cross-sections) along the waveguide. The equation of motion of the waveguide are in general expressed as

$$\begin{bmatrix} \mathbf{T}_{11} & \mathbf{T}_{12} \\ \mathbf{T}_{21} & \mathbf{T}_{22} \end{bmatrix} \begin{bmatrix} \mathbf{q}_L \\ \mathbf{f}_L \end{bmatrix} = \begin{bmatrix} \mathbf{q}_R \\ \mathbf{f}_R \end{bmatrix}. \tag{1.7}$$

The analytical derivation of the transfer matrix $\mathbf{T}$ is summarised in [6]. Extensive examples for series of spring/mass and one-dimensional waveguides can be found in [6].

Applications to one-dimensional periodic structures and continuous waveguides joined together were studied by Lin and Donaldson [34]. The response to a point force is also considered in [34]. Lin and Yang considered free vibration of a disordered periodic beam [35]. It should be noted that the transfer matrix method can suffer from numerical ill-conditioning when solutions are to be found numerically [24,34].

Receptance Method:

Mead et al developed the receptance method mainly to analyse waves in periodic structures, e.g. [3,36]. The method starts from the equation of motion using the receptance matrix, i.e. reciprocal of the dynamic stiffness matrix, formed in the same manner as equation (1.5). A periodicity condition [37]

$$\begin{aligned} \mathbf{q}_R &= \lambda \mathbf{q}_L, \\ \mathbf{f}_R &= \lambda \mathbf{f}_L \end{aligned} \tag{1.8}$$

is then applied to the equation motion to give the polynomial eigenvalue problem in the form, e.g. [3],

$$\left[\lambda^2 \boldsymbol{\alpha}_{LR}\left(\omega\right) - \lambda\left(\boldsymbol{\alpha}_{LL}\left(\omega\right) + \boldsymbol{\alpha}_{RR}\left(\omega\right)\right) + \boldsymbol{\alpha}_{RL}\left(\omega\right)\right]\mathbf{f}_L = \mathbf{0} \tag{1.9}$$

where $\boldsymbol{\alpha}$ is the receptance matrix. The values of λ may be calculated for each given ω and indicate how waves propagate or decay at a particular frequency.

An application to a beam with periodic supports can be seen in [36] and also [38] where effects of the damping are considered. Waves in periodic structures are considered for mono-coupled systems in [39] and for multi-coupled systems in [40] where the complex conjugate wavenumbers are described. Effects of a point discontinuity on waves in periodic structures were considered in [41] and the response to convected loadings was reported in [42]. Coupling of the in-plane and flexural waves in a layered beam is described in [43]. The receptance matrix may be formed using FEA [44,45] but details are omitted here.

Spectral Element Method:

The spectral element method starts from writing the displacement along the uniform (x-) direction in the form of equation (1.2). Substituting the displacements (1.2) into the analytical governing equations gives the relationships between displacements and forces at a location. The spectral element for a segment of the waveguide between two nodes then follows. The spectral element can also be defined for a section of a waveguide extending to infinity. Such a semi-infinite spectral element is termed as a single-noded or throw-off element in [11]. Doyle [11] summarised the method and showed applications to simple waveguides.

1.2.3 Numerical Methods

Various analytical methods have been reviewed in subsections 1.2.1 and 1.2.2. The methods, however, require that the equation of motion of the waveguide is known and can be solved analytically. General complicated waveguides are not amenable to analytical solutions such that numerical methods have been then proposed, e.g. the spectral finite element method and the WFE method. These numerical methods are reviewed in this subsection.

Finite Element Method (FEM):

Although the finite element method (FEM), e.g. [46,47], does not directly provide wave properties of a waveguide, the method is briefly reviewed here. The FEM may be most commonly used to model the dynamic behaviour of structures, especially for geometrically complicated structures. Systems are discretised using finite elements (FEs). The shape

functions are defined to describe the motion of the system. These are in general low-order polynomials, e.g. [46,47]. Higher order shape functions such as *p*-elements, e.g. [47], may be defined. The system motion is then described in the time domain in terms of a discrete number of nodal degrees of freedom (DOFs) such that

$$\mathbf{K}\mathbf{q}+\mathbf{C}\dot{\mathbf{q}}+\mathbf{M}\ddot{\mathbf{q}}=\mathbf{f}(t) \tag{1.10}$$

where $\mathbf{K}$, $\mathbf{C}$, $\mathbf{M}$ are the stiffness, damping and mass matrices and $\dot{\mathbf{q}}$ is the derivative of $\mathbf{q}$ with respect to time. Since the size of elements should be small enough, e.g. [46], the size of the FE model, and hence the calculation cost, is larger at higher frequencies.

Spectral Finite Element method:

To analyse wave motion in general waveguides, the most common approach is perhaps the spectral finite element method, e.g. [11,48], or sometimes termed the waveguide finite element method [7]. Displacements are separately expressed in the direction of wave propagation, x, and over the cross-section, (y, z) such that [7,11,48]

$$w(x,y,z,t)=a\vartheta(y,z)e^{-jkx}e^{j\omega t} \tag{1.11}$$

where $\vartheta(y,z)$ is in general defined using polynomial shape functions. The displacement (1.11) is substituted into the equation of motion such that so-called spectral (finite) elements or waveguide elements [7] are formed. The equation of motion is then projected into the wave domain [7,11,48]

$$\left[\sum_i (-jk)^i \bar{\mathbf{K}}_i-\omega^2\bar{\mathbf{M}}\right]\mathbf{q}=\mathbf{f} \tag{1.12}$$

where $\bar{\mathbf{K}}$ and $\bar{\mathbf{M}}$ are the spectral matrices and i is an integer. The solutions may be found for given k to give real ω for the standard eigenvalue problem. Alternatively, solutions of k might be found for given real ω solving the polynomial eigenvalue problem.

Many applications can be found in the literature. Gavric [49] analysed waves in a thin structure and showed an implementation to improve ill-conditioning occurring around cut-

off frequencies. Finnveden [48] also applied the method to analyse wave motion in a thin wall structure and the results were used as input parameters to a statistical energy analysis model [50]. The spectral finite element method was also applied to laminated composite plates by Datta et al [51] and viscoelastic laminates by Shorter [52]. Extensive works were reported by Nilsson [7] where the spectral finite element method is applied to a thin wall structures, a fluid-filled pipe and a tyre.

However, a drawback of the spectral finite element method is the fact that the method needs appropriate spectral elements to be derived on demand for general waveguides, which is not an insignificant task.

Wave Finite Element (WFE) Method:

The WFE method is an alternative to investigate wave motion in general complicated waveguides. The method starts from modelling a short section of a waveguide using conventional FEs such that the equation of motion is given in terms of a discrete finite number of DOFs, as in equation (1.10). For time-harmonic motion equation (1.10) gives the same form as the dynamic stiffness method, i.e. equation (1.5). The transfer matrix (1.7) can be formed using elements of the dynamic stiffness matrix and applying a periodicity condition (1.8) to the equation (1.7) gives the eigenvalue problem.

The eigenvalues and eigenvectors represent the free wave propagation characteristics such as the wavenumbers and wave modes. This thesis concerns the WFE method and the method is specifically reviewed in detail in the next section.

1.3 Wave Finite Element Method

In this section, the WFE method, e.g. [8,9], is reviewed in detail. The method starts from an FE model of only a short section of the waveguide. The method involves forming the dynamic stiffness matrix using the conventional mass and stiffness matrices of the short section of the waveguide, post-processing the dynamic stiffness matrix to formulate the transfer matrix, and hence the eigenvalue problem, in conjunction with a periodicity condition. Since FEA can be used for the modelling of a cross-section, existing element libraries and commercial FE packages can be fully utilised. Since the method needs only a short section of the waveguide to be modelled, computational cost is cheap. Computational

efficiency is described in [53] where the method is termed the scale independent element method.

1.3.1 Analysis of Waves using Finite Elements for Periodic Structures

The WFE method grew out of research concerning FEA of periodic structures done by Orris and Petyt [44,45]. They used the finite elements to model periodic structures and applied the receptance method proposed by Mead, e.g. [3,36]. Extensive work has been done by Abdel-Rahmen [54]. Free wave propagation in one-, two- and three-dimensions was analysed for periodic structures using an FE model of a single periodic section. A periodicity condition was applied to the equation of motion formed from the FE model and the eigenvalue problem was formulated. Free wave propagation characteristics were determined from solutions to the eigenvalue problem. Forced responses to convected random pressure field excitation were considered.

The similar approach was applied to predict free wave propagation in truss beam structures by Signorelli and Von Flotow [55] where the complex wave modes are described. Accorsi and Bennett [56] analysed free wave propagation in a stiffened cylinder and Bennett and Accorsi investigated effects of the curvature along the axis of the cylinder [57].

1.3.2 Free Wave Propagation

Perhaps the first application to continuous structures was the work of Thompson [58] concerning railway tracks. For simple waveguides, Mace et al [8] showed free wave propagation in a rod, a beam and a plate strip with simply-supported edges using the WFE method. They also presented the free wave propagation in a layered sandwich beam.

Applications of the WFE method to more complicated waveguides are reviewed. Houillon et al [59] analysed free wave propagation in thin-walled structures in which an approach of evaluating the same wave modes at two different discretised frequencies is proposed. The approach is implicitly used throughout this thesis. Thompson [58] analysed the free wave propagation in a railway track. Thompson formulated the eigenvalue problem exploiting the symmetric nature of the waveguide. Gry [60] also analysed the dynamic behaviour of a railway track using a similar methodology to the WFE method. Mencik and Ichchou [61] investigated free wave propagation in a fluid-filled pipe considering acoustical-structural coupling. They also predicted the coupling power between two different waveguides using

the WFE method [62]. Free wave propagation in a fluid-filled pipe was also presented by Maess et al [63]. They formulated an eigenvalue problem using elements of the transfer matrix and numerical solutions were found with initial estimates. The WFE method was extended to analyse free wave propagation in two-dimensional waveguides by Manconi and Mace [64,65].

1.3.3 Forced Response

Forced response is of interest when an excitation is applied to a waveguide. Only a few papers describe the forced response using the WFE method. Duhamel et al [9] presented the formulation for calculating the forced response using a recurrence relationship. Thompson [58] calculated the forced response based on the receptance approach for the railway track. A similar, but different approach was used to analyse the forced response of a railway track by Gry [60]. However, all the approaches have ill-conditioning problems for general waveguides in which there are many wave modes.

1.3.4 Numerical Issues

In predictions using the WFE method various numerical issues occur. However, only a few papers describe such numerical issues. Several papers describe the ill-conditioning of the eigenvalue problem using the transfer matrix and reformulate the eigenvalue problem in a different form. A novel formulation for improving the conditioning of the eigenvalue problem was proposed using the symplectic relationship of the transfer matrix by Zhong and Williams [66]. Several papers used the method, called Zhong's method in this thesis, to improve the conditioning [8,60,62,67,68].

Since the WFE method starts from the FE model of a section of a waveguide, FE discretisation errors occur. Duhamel et al [67] and Mace et al [8] demonstrated FE discretisation errors occurring in the WFE method. The aliasing effect due to the discretisation and the spatial periodicity was reported by Ichchou et al [10].

However, such numerical issues have not been reported in detail. In this thesis, numerical issues are discussed in detail and methods are proposed to reduce numerical errors.

1.4 Outline of the Thesis

The thesis is outlined in this section. This thesis concerns formulation of the WFE method and its application to free wave propagation and the forced response of waveguides of arbitrary complexity in their cross-sections. Causes of numerical errors in the predicted results using the WFE method are investigated and methods for reducing errors are proposed. Applications of the WFE method to complicated structures are then presented. The forced response is calculated using the wave approach with well-conditioned formulations and numerical examples are shown. Free and forced vibrations of a tyre are then predicted and the predicted forced response is compared with experiment. Throughout this thesis, ANSYS 7.1 [69] is used to model sections of waveguides. All the subsequent calculations were performed using MATLAB^{TM} 7.0.4.

In chapter 1 the introduction is given and relevant literature is reviewed. The thesis is outlined and contributions of this thesis are then described.

In chapter 2, formulations of the WFE method are introduced. Numerical errors occurring in the WFE results are discussed. FE discretisation error and error due to round-off of inertia terms are described with particular reference to the example of an Euler-Bernoulli beam. A method of concatenating elements is proposed to reduce the round-off of inertia terms. Approximate expressions for the dynamic condensation of DOFs associated with internal nodes are derived to reduce calculation cost. Errors occurring in numerically solving the eigenvalue problem are also described. Zhong's method is used for improving the conditioning of the eigenvalue problem. An application of singular value decomposition (SVD) is proposed to reduce errors in numerically determining eigenvectors. An illustrative example of free wave propagation in a plate strip with simply-supported edges is shown considering numerical issues. Effects of how the cross-section is modelled are investigated. Methods of predicting the group velocity are described and use of the power and energy relationship is shown to be reliable.

In chapter 3, applications of the WFE method to more complicated waveguides are shown. Dispersion curves are shown including purely real, purely imaginary and complex wavenumbers. Freely propagating in-plane and flexural waves in a plate strip with free edges are presented. Analytical dispersion equations are numerically solved using the WFE results as initial estimates. Decomposition of power is proposed to reduce the size of matrices by retaining only important DOFs. Free wave propagation in a ring and a cylindrical strip are also shown where waves, e.g. longitudinal and flexural waves, couple due to the curvature.

Complicated wave behaviour is seen. Curve veering between two different purely real or two different imaginary wavenumbers is observed. Non-zero cut-on phenomena are observed where complex conjugate wavenumbers become purely real non-zero wavenumbers. Waves for which the directions of the phase and group velocities are of opposite signs are seen. Bifurcations from complex conjugate to two different purely imaginary wavenumbers or two imaginary to complex conjugate wavenumbers are observed. Decomposition of power is used to investigate characteristics of each wave mode in a cylindrical strip.

In chapter 4, formulations of forced response calculation are described. A well-conditioned formulation for numerically determining the amplitudes of directly excited waves is proposed using the orthogonality relationship between the left and right eigenvectors. Wave amplitudes are calculated considering wave propagation and subsequent reflection at boundaries. The response is then determined by superimposing the wave amplitudes at the response point. The formulations to determine responses are explicitly described. Forced responses of a beam, a plate and a cylinder are shown. Inclusion of rapidly decaying nearfield waves is discussed.

In chapter 5, the WFE method is used to predict free and forced vibrations of a tyre as an example of a practical application. Frequency dependent material properties of rubber are included. Free wave propagation is shown including attenuating waves for the tyre with and without internal pressure. Results of the forced response are compared with experiment. Effects of the size of the region of excitation are described. This strongly affects the power injected into wave modes, especially at high frequencies, and contribution of the finite shear stiffness to the response.

In chapter 6, some conclusions are drawn. Possible further work is suggested.

1.5 Contributions of this Thesis

The original contributions of this thesis are as follows.

- Causes of numerical errors are critically discussed. For simple waveguides, there are mainly two causes: FE discretisation error and error due to round-off of inertia terms. A method using concatenating elements is proposed to reduce the round-off of inertia

terms. Approximate expressions for dynamic condensation of DOFs associated with internal nodes are derived [70].

- Numerical issues remain even when Zhong's method is used to reformulate the eigenvalue problem. An application of SVD is proposed to reduce errors in numerically determining eigenvectors [70,71].

- Three methods for predicting the group velocity are described and relative errors in the group velocity compared. Use of the power and energy relationship is then shown to be reliable [70,71].

- Freely propagating flexural waves are predicted including attenuating waves and results are compared with numerical solutions to the analytical dispersion equation. Bifurcations from the complex conjugate to purely imaginary wavenumbers and from purely imaginary to complex conjugate wavenumbers are observed [72].

- Decomposition of the power is proposed. The approach can be used for determining the DOFs to be condensed or to be removed. Such manipulation can improve the conditioning due to the smaller size of matrices. The approach is also applied to investigate wave characteristics of each wave mode.

- The wave approach is applied to calculate forced response. A well-conditioned formulation for determining the amplitudes of directly excited waves is proposed using the orthogonality relationship between the left and right eigenvectors [73,74].

- The WFE method is applied to predict free and forced vibrations of a tyre as a practical application [73,74]. Frequency dependent material properties of rubber are included. Predictions are compared with experiment.

Chapter 2
FREE WAVE PROPAGATION

2.1 Introduction

Many waveguides are uniform in one-direction while their cross-sections may have a complicated construction. The dynamic properties of such waveguides can be expressed in terms of wave properties such as the wavenumbers and wave modes. In this chapter, the theory and formulations of the WFE method are introduced to predict their wave properties. Only a short section of a waveguide is modelled using a conventional FEA. A complicated cross-section can be straightforwardly modelled using existing FE libraries and FE commercial packages. The dynamic stiffness matrix of a short section of a waveguide is obtained and the matrix rearranged and partitioned to form the transfer matrix. The free wave propagation characteristic may be obtained from the transfer matrix by applying a periodicity condition [37].

In this chapter, various numerical issues involved in obtaining accurate results using the WFE method are discussed. Causes of numerical errors are investigated and implementations of the WFE method to reduce these errors are proposed. The discussions include a method using concatenating elements and conditioning of the eigenvalue problem to reduce numerical errors. The group velocity is numerically estimated in three ways and the accuracy is investigated. Some outcomes shown in this chapter have been presented in [70,71].

2.2 Transfer Matrix

In this section, the basis of the WFE method is described. The dynamic stiffness matrix of only a short section of a waveguide is first formed and the matrix post-processed. The transfer matrix is formed using the elements of the dynamic stiffness matrix and the eigenvalue problem is then formulated applying a periodicity condition. The eigenvalues and

eigenvectors of the eigenvalue problem represent phase or magnitude changes of waves over the section and associated wave modes respectively.

2.2.1 Dynamic Stiffness Matrix of a Section of a Waveguide

Consider a short of section of length Δ of a uniform waveguide as shown in Figure 2.1. The equation of motion of the section can be written as

$$\mathbf{Dq} = \mathbf{f} \tag{2.1}$$

where

$$\mathbf{D} = \mathbf{K} + j\omega\mathbf{C} - \omega^2\mathbf{M} \tag{2.2}$$

is the dynamic stiffness matrix, $\mathbf{q}$ is the nodal displacement vector, $\mathbf{f}$ is the vector of nodal forces, $\mathbf{K}$, $\mathbf{C}$, $\mathbf{M}$ are the stiffness, damping and mass matrices (termed the element matrices), which may be formed using a commercial FE package, $j = \sqrt{-1}$ and ω is angular frequency. Time harmonic motion $e^{j\omega t}$ is implicit throughout this thesis and suppressed for brevity. Equation (2.1) can be expressed in matrix form as

$$\begin{bmatrix} \mathbf{D}_{LL} & \mathbf{D}_{LR} \\ \mathbf{D}_{RL} & \mathbf{D}_{RR} \end{bmatrix} \begin{bmatrix} \mathbf{q}_L \\ \mathbf{q}_R \end{bmatrix} = \begin{bmatrix} \mathbf{f}_L \\ \mathbf{f}_R \end{bmatrix} \tag{2.3}$$

where the subscripts L and R represent the left and right hand side of the section. The WFE method starts from equation (2.3) and the eigenvalue problem is formulated using the elements of equation (2.3). For uniform waveguides, the following relationships hold:

$$\mathbf{D}_{LL}^{\mathrm{T}} = \mathbf{D}_{LL},\ \mathbf{D}_{RR}^{\mathrm{T}} = \mathbf{D}_{RR},\ \mathbf{D}_{LR}^{\mathrm{T}} = \mathbf{D}_{RL} \tag{2.4}$$

and

$$D_{RRij} = \pm D_{LLij}\ ,\quad D_{RLij} = \pm D_{LRij} \tag{2.5}$$

where $\cdot^{\mathrm{T}}$ indicates the transpose and the signs in equations (2.5) depend on whether the degrees of freedom (DOFs) at the element interface are symmetric or anti-symmetric for the (i, j) element [46,58].

If the section has internal nodes as shown in Figure 2.2, the associated DOFs can be condensed. When no external force is applied to the internal nodes the equation of motion may be expressed as

$$\begin{bmatrix} \tilde{\mathbf{D}}_{EE} & \tilde{\mathbf{D}}_{EI} \\ \tilde{\mathbf{D}}_{IE} & \tilde{\mathbf{D}}_{II} \end{bmatrix} \begin{bmatrix} \mathbf{q}_E \\ \mathbf{q}_I \end{bmatrix} = \begin{bmatrix} \mathbf{f}_E \\ \mathbf{0} \end{bmatrix} \tag{2.6}$$

where

$$\tilde{\mathbf{D}}_{EE} = \begin{bmatrix} \tilde{\mathbf{D}}_{LL} & \tilde{\mathbf{D}}_{LR} \\ \tilde{\mathbf{D}}_{RL} & \tilde{\mathbf{D}}_{RR} \end{bmatrix}, \tilde{\mathbf{D}}_{EI} = \begin{bmatrix} \tilde{\mathbf{D}}_{LI} \\ \tilde{\mathbf{D}}_{RI} \end{bmatrix}, \tilde{\mathbf{D}}_{IE} = \begin{bmatrix} \tilde{\mathbf{D}}_{IL} & \tilde{\mathbf{D}}_{IR} \end{bmatrix}, \mathbf{q}_E = \begin{bmatrix} \mathbf{q}_L \\ \mathbf{q}_R \end{bmatrix}, \mathbf{f}_E = \begin{bmatrix} \mathbf{f}_L \\ \mathbf{f}_R \end{bmatrix} \tag{2.7}$$

and the superscript $\tilde{\cdot}$ denotes that the section has internal nodes and is not condensed. The subscript *E* or *I* represents that DOFs are associated with edge nodes or internal nodes of the section. The DOFs associated with the internal nodes can be condensed as [75]

$$\tilde{\mathbf{R}}^{\mathrm{T}} \tilde{\mathbf{D}} \tilde{\mathbf{R}} \mathbf{q}_E = \mathbf{f}_E \tag{2.8}$$

where

$$\tilde{\mathbf{R}} = \begin{bmatrix} \mathbf{I} \\ -\tilde{\mathbf{D}}_{II}^{-1} \tilde{\mathbf{D}}_{IE} \end{bmatrix} \tag{2.9}$$

and $\mathbf{I}$ is the identity matrix. The matrix $\tilde{\mathbf{R}}$ transforms the original basis into the condensed basis. Expanding equation (2.8) gives

$$\left[\tilde{\mathbf{D}}_{EE} - \tilde{\mathbf{D}}_{EI} \tilde{\mathbf{D}}_{II}^{-1} \tilde{\mathbf{D}}_{IE} \right] \mathbf{q}_E = \mathbf{f}_E \,. \tag{2.10}$$

Equation (2.8) can similarly be used to condense the element matrices by expanding $\tilde{\mathbf{D}} = \tilde{\mathbf{K}} - \omega^2 \tilde{\mathbf{M}}$ [75]. It should be noted that the dynamically condensed element matrices become frequency dependent.

When the section has internal nodes, the DOFs associated with the internal nodes are always condensed and the resulting equation has the form of equation (2.3).

2.2.2 Transfer Matrix

Consider a series of sections of the waveguide as shown in Figure 2.3. The continuity of displacement and force equilibrium of adjacent sections read

$$\begin{bmatrix} \mathbf{q}_L^{(n+1)} \\ \mathbf{f}_L^{(n+1)} \end{bmatrix} = \begin{bmatrix} \mathbf{q}_R^{(n)} \\ -\mathbf{f}_R^{(n)} \end{bmatrix}. \tag{2.11}$$

For each section the transfer matrix can be defined as [37]

$$\mathbf{T}\begin{bmatrix} \mathbf{q}_L^{(n)} \\ \mathbf{f}_L^{(n)} \end{bmatrix} = \begin{bmatrix} \mathbf{q}_L^{(n+1)} \\ \mathbf{f}_L^{(n+1)} \end{bmatrix}. \tag{2.12}$$

A periodicity condition [37] represents a relationship of displacements and forces over the section such that

$$\begin{bmatrix} \mathbf{q}^{(n+1)} \\ \mathbf{f}^{(n+1)} \end{bmatrix} = \lambda \begin{bmatrix} \mathbf{q}^{(n)} \\ \mathbf{f}^{(n)} \end{bmatrix} \tag{2.13}$$

and λ describes the amplitude and phase change over a section. Free wave motion over any section of length Δ is therefore described in the form of an eigenvalue problem such that

$$\mathbf{T}\begin{bmatrix} \mathbf{q} \\ \mathbf{f} \end{bmatrix} = \lambda \begin{bmatrix} \mathbf{q} \\ \mathbf{f} \end{bmatrix}. \tag{2.14}$$

The transfer matrix $\mathbf{T}$ is formed using the elements of the dynamic stiffness matrix (2.3). The first row of equation (2.3) can be written as

$$\mathbf{q}_R = -\mathbf{D}_{LR}^{-1}\mathbf{D}_{LL}\mathbf{q}_L + \mathbf{D}_{LR}^{-1}\mathbf{f}_L \tag{2.15}$$

and the second row of equation (2.3) gives

$$\mathbf{f}_R = \left(\mathbf{D}_{RL} - \mathbf{D}_{RR}\mathbf{D}_{LR}^{-1}\mathbf{D}_{LL}\right)\mathbf{q}_L + \mathbf{D}_{RR}\mathbf{D}_{LR}^{-1}\mathbf{f}_L . \tag{2.16}$$

From equations (2.15) and (2.16) the transfer matrix $\mathbf{T}$ can be expressed as

$$\mathbf{T} = \begin{bmatrix} -\mathbf{D}_{LR}^{-1}\mathbf{D}_{LL} & \mathbf{D}_{LR}^{-1} \\ -\mathbf{D}_{RL} + \mathbf{D}_{RR}\mathbf{D}_{LR}^{-1}\mathbf{D}_{LL} & -\mathbf{D}_{RR}\mathbf{D}_{LR}^{-1} \end{bmatrix}. \tag{2.17}$$

2.2.3 Eigenvalues and Eigenvectors

If the number of DOFs associated with one side of the section is *n*, the size of the transfer matrix $\mathbf{T}$ is then $2n \times 2n$ and $2n$ sets of the eigenvalues and eigenvectors are obtained from equation (2.14). The eigenvalue λ_i in equation (2.14) relates to wave propagation over the distance Δ such that [37]

$$\lambda_i = e^{-jk_i\Delta} \tag{2.18}$$

where k_i represents the wavenumber for the *i*th wave. The wavenumber can be purely real, purely imaginary or complex, associated with a propagating, a nearfield (evanescent) or an oscillating decaying wave respectively. The right eigenvector corresponding to the *i*th eigenvalue can be written as

$$\boldsymbol{\varphi}_i = \begin{bmatrix} \mathbf{q}_i \\ \mathbf{f}_i \end{bmatrix}. \tag{2.19}$$

The eigenvector represents a wave mode and contains information about both the nodal displacements $\mathbf{q}_i$ and associated internal forces $\mathbf{f}_i$ under the propagation of the *i*th wave.

The transfer matrix is symplectic and the eigenvalues come in pairs and are of the form $\lambda_i^{\pm} = e^{\pm jk_i\Delta}$ which represent positive- and negative-going wave pairs. The eigenvalues and associated eigenvectors are then expressed as $\left(\lambda_i, \boldsymbol{\varphi}_i^{+}\right)$ and $\left(1/\lambda_i, \boldsymbol{\varphi}_i^{-}\right)$. More characteristics of the symplectic matrix are described in Appendix 1.1. Positive-going waves are those for which the magnitude of the eigenvalues is less than 1, i.e. $|\lambda_i| < 1$ or if $|\lambda_i| = 1$, the power

(energy flow) is positive, i.e. $\mathrm{Re}\left\{\mathbf{f}_i^{\mathrm{H}}\dot{\mathbf{q}}_i\right\} > 0$ [8,67] where $(\cdot)^{\mathrm{H}}$ represents the complex conjugate transpose, or Hermitian, and $\dot{\mathbf{q}}_i$ represents the partial derivative of the displacement vector $\mathbf{q}_i$ with respect to time.

2.2.4 Orthogonality Relationships between the Left and Right Eigenvectors

The right eigenvalues and eigenvectors of the transfer matrix are defined as

$$\mathbf{T}\boldsymbol{\varphi}_i = \lambda_i \boldsymbol{\varphi}_i \tag{2.20}$$

for the *i*th eigenvalue and associated eigenvector. Similarly, the left eigenvalues and eigenvectors can be expressed as

$$\boldsymbol{\psi}_i \mathbf{T} = \lambda_i \boldsymbol{\psi}_i \tag{2.21}$$

and $\boldsymbol{\psi}_i$ is a row vector of the left eigenvector and given by [9]

$$\boldsymbol{\psi}_i = \left[\mathbf{q}\left(1/\lambda_i\right)^{\mathrm{T}}\left(\mathbf{D}_{RR} + \lambda_i \mathbf{D}_{LR}\right) \quad \mathbf{q}\left(1/\lambda_i\right)^{\mathrm{T}}\right] \tag{2.22}$$

which is in the form of $\boldsymbol{\psi}_i = \left[\mathbf{f}_i^{\mathrm{T}} \quad \mathbf{q}_i^{\mathrm{T}}\right]$. From equations (2.20) and (2.21) the relationships

$$\boldsymbol{\psi}_i \mathbf{T} \boldsymbol{\varphi}_j = \lambda_j \boldsymbol{\psi}_i \boldsymbol{\varphi}_j = \lambda_i \boldsymbol{\psi}_i \boldsymbol{\varphi}_j \tag{2.23}$$

follow. This leads to

$$\left(\lambda_i - \lambda_j\right)\boldsymbol{\psi}_i \boldsymbol{\varphi}_j = 0 \tag{2.24}$$

such that if $\lambda_i \neq \lambda_j$, $\boldsymbol{\psi}_i \boldsymbol{\varphi}_j = 0$. Thus the orthogonality relationship between the left and right eigenvectors can in general be expressed as

$$\boldsymbol{\psi}_i \boldsymbol{\varphi}_j = d_i \delta_{ij} \tag{2.25}$$

where δ_{ij} is the Kronecker delta and d_i is arbitrary. The orthogonality relationships will be utilised in chapter 4 to reduce ill-conditioning in calculating the forced response.

2.3 Example of an Euler-Bernoulli Beam

In this section free wave propagation in an Euler-Bernoulli beam, e.g. [1], is investigated as an illustrative example. The analytical solution is first described. The wavenumbers and wave modes are then predicted from a single FE of the beam. No damping is assumed.

2.3.1 Analytical Solution

Consider an Euler-Bernoulli beam as shown in Figure 2.4. In the figure, w is the translational displacement, θ is the rotational displacement, m is the moment and τ is the shear force. The beam holds four freely propagating waves and the wavenumbers are, e.g. [1],

$$k = \pm k_B, \pm jk_B \tag{2.26}$$

where

$$k_B = \sqrt[4]{\frac{\rho A \omega^2}{EI}} \tag{2.27}$$

is the bending wavenumber of the beam. Here ρ is the mass density, A is the cross-sectional area, E is the Young's modulus and I is the second moment of the cross-sectional area. Each wave propagates as e^{-jkx}. The wavenumbers $k = k_B, -jk_B$ represent the positive-going propagating and nearfield waves while $k = -k_B, jk_B$ are the negative-going propagating and nearfield waves.

Using the sign convention in Figure 2.4, the wave modes associated with $k = \pm k_B, \mp jk_B$ are, e.g. [1],

$$\boldsymbol{\varphi}_B = \begin{bmatrix} w_B \\ \theta_B \\ \tau_B \\ m_B \end{bmatrix} = \begin{bmatrix} w_B \\ \partial w_B/\partial x \\ EI\,\partial^3 w_B/\partial x^3 \\ -EI\,\partial^2 w_B/\partial x^2 \end{bmatrix} = \begin{bmatrix} 1 \\ \mp jk_B \\ \pm jEIk_B^3 \\ EIk_B^2 \end{bmatrix}, \begin{bmatrix} 1 \\ \mp k_B \\ \mp EIk_B^3 \\ -EIk_B^2 \end{bmatrix} \tag{2.28}$$

where the subscript B represents the analytical solution of the beam.

2.3.2 WFE Estimates

The WFE method starts from a conventional FEA of a single beam element. For the beam element of the length Δ, the mass and stiffness matrices, using a cubic polynomial shape function, are [46]

$$\begin{aligned} \mathbf{K} &= \frac{EI}{\Delta^3}\begin{bmatrix} 12 & 6\Delta & -12 & 6\Delta \\ & 4\Delta^2 & -6\Delta & 2\Delta^2 \\ sym. & & 12 & -6\Delta \\ & & & 4\Delta^2 \end{bmatrix}, \\ \mathbf{M} &= \frac{\rho A\Delta}{420}\begin{bmatrix} 156 & 22\Delta & 54 & -13\Delta \\ & 4\Delta^2 & 13\Delta & -3\Delta^2 \\ sym. & & 156 & -22\Delta \\ & & & 4\Delta^2 \end{bmatrix}. \end{aligned} \tag{2.29}$$

The dynamic stiffness matrix, $\mathbf{D} = \mathbf{K} - \omega^2\mathbf{M}$, becomes

$$\mathbf{D} = \frac{EI}{\Delta^3}\begin{bmatrix} \left(12 - \frac{156}{420}(k_B\Delta)^4\right) & \Delta\left(6 - \frac{22}{420}(k_B\Delta)^4\right) & \left(-12 - \frac{54}{420}(k_B\Delta)^4\right) & \Delta\left(6 + \frac{13}{420}(k_B\Delta)^4\right) \\ & \Delta^2\left(4 - \frac{4}{420}(k_B\Delta)^4\right) & \Delta\left(-6 - \frac{13}{420}(k_B\Delta)^4\right) & \Delta^2\left(2 + \frac{3}{420}(k_B\Delta)^4\right) \\ sym. & & \left(12 - \frac{156}{420}(k_B\Delta)^4\right) & \Delta\left(-6 + \frac{22}{420}(k_B\Delta)^4\right) \\ & & & \Delta^2\left(4 - \frac{4}{420}(k_B\Delta)^4\right) \end{bmatrix}. \tag{2.30}$$

The analytical dynamic stiffness matrix can be found in [76]. It involves various trigonometric and hyperbolic functions of $k_B\Delta$. If the analytical dynamic stiffness matrix is expressed as a power series in $k_B\Delta$, it is found that equation (2.30) is exact up to $O\left\{\left(k_B\Delta\right)^4\right\}$.

The transfer matrix for the section can be found from equation (2.30) as [67,70]

$$\mathbf{T}=\frac{1}{302400+720\left(k_B\Delta\right)^4+\left(k_B\Delta\right)^8}\times \begin{bmatrix} 302400+13320\left(k_B\Delta\right)^4+26\left(k_B\Delta\right)^8 & \Delta\left(302400+3240\left(k_B\Delta\right)^4+2\left(k_B\Delta\right)^8\right) \\ \dfrac{50400\left(k_B\Delta\right)^4+120\left(k_B\Delta\right)^8}{\Delta} & 302400+13320\left(k_B\Delta\right)^4+10\left(k_B\Delta\right)^8 \\ \dfrac{EI\left(302400\left(k_B\Delta\right)^4+2820\left(k_B\Delta\right)^8+\frac{7}{2}\left(k_B\Delta\right)^{12}\right)}{\Delta^3} & \dfrac{EI\left(151200\left(k_B\Delta\right)^4+570\left(k_B\Delta\right)^8+\frac{1}{4}\left(k_B\Delta\right)^{12}\right)}{\Delta^2} \\ \dfrac{EI\left(-151200\left(k_B\Delta\right)^4-570\left(k_B\Delta\right)^8-\frac{1}{4}\left(k_B\Delta\right)^{12}\right)}{\Delta^2} & \dfrac{EI\left(-50400\left(k_B\Delta\right)^4-78\left(k_B\Delta\right)^8-\frac{1}{60}\left(k_B\Delta\right)^{12}\right)}{\Delta} \end{bmatrix}$$

$$\begin{bmatrix} \dfrac{\Delta^3\left(50400+180\left(k_B\Delta\right)^4\right)}{EI} & \dfrac{\Delta^2\left(-151200-780\left(k_B\Delta\right)^4\right)}{EI} \\ \dfrac{\Delta^2\left(151200+780\left(k_B\Delta\right)^4\right)}{EI} & \dfrac{\Delta\left(-302400-3240\left(k_B\Delta\right)^4\right)}{EI} \\ 302400+13320\left(k_B\Delta\right)^4+26\left(k_B\Delta\right)^8 & \dfrac{-50400\left(k_B\Delta\right)^4-120\left(k_B\Delta\right)^8}{\Delta} \\ \Delta\left(-302400-3240\left(k_B\Delta\right)^4-2\left(k_B\Delta\right)^8\right) & 302400+13320\left(k_B\Delta\right)^4+10\left(k_B\Delta\right)^8 \end{bmatrix}. \tag{2.31}$$

The characteristic equation can be derived from the transfer matrix (2.31) and the eigenvalues are given by

$$\begin{aligned} \lambda_{1,2} &= 1\mp j\left(k_B\Delta\right)-\frac{1}{2}\left(k_B\Delta\right)^2\pm\frac{j}{6}\left(k_B\Delta\right)^3+\frac{1}{24}\left(k_B\Delta\right)^4\mp\frac{23j}{2880}\left(k_B\Delta\right)^5-\frac{1}{960}\left(k_B\Delta\right)^6\pm\cdots, \\ \lambda_{3,4} &= 1\mp\left(k_B\Delta\right)+\frac{1}{2}\left(k_B\Delta\right)^2\mp\frac{1}{6}\left(k_B\Delta\right)^3+\frac{1}{24}\left(k_B\Delta\right)^4\mp\frac{23}{2880}\left(k_B\Delta\right)^5+\frac{1}{960}\left(k_B\Delta\right)^6\mp\cdots. \end{aligned} \tag{2.32}$$

The eigenvalues $\lambda_{1,2}$ of the transfer matrix are related to the propagating waves while $\lambda_{3,4}$ are related to the nearfield waves. These solutions are exact to $O\left\{\left(k_B\Delta\right)^4\right\}$ with relative errors being $O\left\{\left(k_B\Delta\right)^5\right\}$. The predicted wavenumbers, $k_i = \log\left(\lambda_i\right)/\left(-j\Delta\right)$, are therefore

$$\begin{aligned} k_{1,2} &= k_B\left\{\pm 1 \mp \left(k_B\Delta\right)^4/2880 - j\times\left(k_B\Delta\right)^5/2880\cdots\right\}, \\ k_{3,4} &= -jk_B\left\{\pm 1 \mp \left(k_B\Delta\right)^4/2880 + \cdots\right\} \end{aligned} \tag{2.33}$$

such that the relative error in the wavenumbers are $O\left\{\left(k_B\Delta\right)^4\right\}$. The eigenvectors associated with $\lambda_{1,2}$ are

$$\begin{bmatrix} w \\ \theta \\ \tau \\ m \end{bmatrix} = \begin{bmatrix} 1 \\ \mp jk_B\left\{1 \mp \left(k_B\Delta\right)^4/2880 \pm \left(k_B\Delta\right)^6/10800 \mp \cdots\right\} \\ \pm jEIk_B^3\left\{1 \mp \left(k_B\Delta\right)^4/960 \mp 13\left(k_B\Delta\right)^6/302400 \pm \cdots\right\} \\ EIk_B^2\left\{1 - \left(k_B\Delta\right)^4/1440 - \left(k_B\Delta\right)^6/18900 - \cdots\right\} \end{bmatrix}. \tag{2.34}$$

The relative errors in the elements of the eigenvectors (2.34) predicted by the WFE method are $O\left\{\left(k_B\Delta\right)^4\right\}$, compared to the analytical solution (2.28). Similar expression holds for $\lambda_{3,4}$ with the relative error in the elements of the eigenvectors being $O\left\{\left(k_B\Delta\right)^4\right\}$.

2.3.3 Numerical Example

In this subsection numerical examples of the beam are presented. The dynamic stiffness matrix and the transfer matrix were formed at each frequency and the WFE results obtained. MATLAB was used to give the results and the double precision calculation was chosen such that 16 digit numbers are effective. The numerically predicted wavenumbers for the positive-going waves are shown in Figure 2.5. The abscissa shows the non-dimensional frequency $\left(k_B\Delta\right)^2$ which is proportional to frequency. Figure 2.5(a) shows the predicted propagating wavenumber and the analytical solution. Good agreement can be seen for small $k_B\Delta$ but

discrepancy becomes large above $\left(k_B\Delta\right)^2 > 10 \approx \pi^2$ and the predicted result completely breaks down around $\left(k_B\Delta\right)^2 > 40 \approx \left(2\pi\right)^2$.

For the nearfield wavenumber in Figure 2.5(b) similar trends can be seen and the errors become large above $\left(k_B\Delta\right)^2 > 10$. The similar discussion for rod vibration can be found in [67,70].

2.4 Numerical Errors Occurring in the WFE Method

In section 2.3 the predicted wavenumbers for the Euler-Bernoulli beam were shown. In this section, causes of numerical errors occurring in the WFE results, i.e. FE discretization error and error due to round-off of inertia terms, are first discussed. The relative errors in the wavenumber and the wave mode of the beam are then illustrated.

2.4.1 FE Discretization Error

When the phase change over the length of an element Δ becomes large, the FE discretization error becomes large. Since the FE modelling is an approximation to represent a system, there are always numerical errors. In usual application of FEA, 6 or more FEs are generally needed for each wavelength to represent a system motion accurately, e.g. [46]. In the WFE method the criterion can be expressed as $k\Delta \le 2\pi/6 \approx 1.05$. Hence the phase change over an element is recommended to be

$$\left|k\Delta\right| \le 1 \tag{2.35}$$

where $\left|\cdot\right|$ is the magnitude. In general, the wavenumbers may be purely real, purely imaginary or complex. For complex wavenumbers, either equation (2.35) or

$$\left|\mathrm{Re}\left(k\Delta\right)\right| \le 1, \quad \left|\mathrm{Im}\left(k\Delta\right)\right| \le 1 \tag{2.36}$$

could be recommended. The criterion should be satisfied in both the directions of wave propagation and across the cross-section of a waveguide for small FE discretisation errors.

Even if large numerical errors are permitted, at least 3 FEs are needed to express one wavelength [46]. In the WFE method, this criterion can be expressed as

$$\mathrm{Re}\left(k\Delta\right) \le 2\pi/3 . \tag{2.37}$$

When the phase change over a section exceeds $2\pi/3$ or so, the result can break down [10,67,70] and examples are shown in the next section for the beam case.

It should be mentioned that the FE discretisation errors depend on the shape function of an element, e.g. [46,47]. Even if the values of $\left|k\Delta\right|$ are same, errors in the WFE results using a cubic polynomial shape function is smaller than those using a linear shape function, for example. Equations (2.35) and (2.36) are thus an estimate or a guideline for 'small' numerical errors in predicted results.

Propagating waves carry power and it is important to predict propagating waves accurately. The length of the section Δ should therefore be determined to satisfy the criterion, e.g. equation (2.35), at a maximum frequency of interest where a propagating wavenumber often takes the maximum value. In this and later chapters where accurate prediction are shown using the WFE method, the length of the section Δ is chosen to satisfy this criterion such that all propagating wavenumbers can predicted accurately enough.

2.4.2 Error due to Round-off of Inertia Terms

The upper bound to the length Δ of the element can be decided from the FE discretization error, e.g. equation (2.35), considering the maximum wavenumber of interest in the frequency range analysed.

On the other hand, the lower bound of Δ may be defined considering round-off of inertia terms. For finite precision of arithmetic operations, some effective digit numbers are lost in addition, subtraction and so on. In the WFE method, the round-off error can be significant specifically when $\mathbf{D} = \mathbf{K} - \omega^2\mathbf{M}$ is numerically calculated. For very small Δ, and in particular at low frequencies, some effective digits of the inertia terms will be rounded-off since K_{ij} might be very large compared to $\omega^2 M_{ij}$, e.g. equations (2.29).

The number of the effective digits lost in the subtraction which yields $D_{ij} = K_{ij} - \omega^2 M_{ij}$ can be estimated from $\alpha_{ij} = \log_{10}\left(\left|K_{ij}\right| / \left|\omega^2 M_{ij}\right|\right)$ for non-zero ω and M_{ij}, where α_{ij} is the

number of the effective digits lost. For double precision calculations an inertia term is completely rounded off if $\alpha_{ij} > 16$. The diagonals of the element matrices could be particularly important considering, e.g., the lumped mass matrix formulation [46,77]. The criteria for the smallest permissible value of Δ could be therefore determined to satisfy

$$\log_{10}\left(K_{ii}/\omega^2 M_{ii}\right) < \alpha_{ii} \tag{2.38}$$

and $\alpha_{ii} < 16$ at the minimum frequency of interest using the double precision calculations for accurate results. For frequency independent K_{ij} and M_{ij}, $K_{ij}/\omega^2 M_{ij}$ is proportional to ω^{-2}.

2.4.3 Relative Errors in the Predicted Results of the Euler-Bernoulli Beam

The relative error in the predicted propagating wavenumber (i.e. Figure 2.5), $\left|\left(k - k_B\right)/k_B\right|$, is shown in Figure 2.6. The relative error is minimum at around $k_B\Delta = 0.04$. Above $k_B\Delta = 0.04$ the relative error increases due to the FE discretisation error at a rate proportional to $\left(k_B\Delta\right)^4$, see equation (2.33). Below $k_B\Delta = 0.04$, the relative error increases as $k_B\Delta$ decreases due to the round-off of the inertia terms. For the element matrices of the beam, i.e. equation (2.29), the asymptote of the relative error for small $k_B\Delta$ is proportional to ω^{-2} and hence to $\left(k_B\Delta\right)^{-4}$. For the beam case, $\max\left\{K_{ii}/\omega^2 M_{ii}\right\} = 420/\left(k_B\Delta\right)^4$ for $i = 2, 4$ and the inertia terms are completely rounded-off if $k_B\Delta < 4\cdot 10^{-4}$ or so.

The relative error in the wave mode shows similar trends. The relative error in the rotational DOF per unit displacement, θ_B in equation (2.28), is shown for the positive-going propagating wave in Figure 2.7. The relative error in θ_B is also minimum at about $k_B\Delta = 0.04$ and changes above and below $k_B\Delta = 0.04$ in proportional to $\left(k_B\Delta\right)^{\pm 4}$, which is the same as the relative error in the wavenumber, as described in equation (2.34). A similar discussion holds for a rod vibration but the asymptote of the relative error is $\left(k\Delta\right)^{\pm 2}$ [70].

2.5 FE Modelling using Concatenating Elements

In section 2.4, two causes of numerical errors were described. There is a trade-off between the FE discretisation errors and the errors due to round-off of inertia terms such that the frequency range analysed is limited. To reduce the low frequency limit imposed by the element length Δ, a method in which a number of elements are concatenated is proposed in this section.

2.5.1 Condensations of the Dynamic Stiffness Matrix

In this subsection, a method of concatenating identical elements is described to reduce the round-off errors of inertia terms. Numerical errors due to the round-off of inertia terms occur when $K_{ij} >> \omega^2 M_{ij}$, i.e. the stiffness of the section is much greater than the inertia. This can be improved using a section with larger length Δ but FE discretisation errors become larger. An alternative way is a method using concatenating elements as shown in Figure 2.8. This method does not need re-modelling of a section since the global stiffness and mass matrices can be formed from those of an original section, e.g. [46].

The internal DOFs may be dynamically condensed using e.g. equation (2.10). However calculation cost increases because $\tilde{\mathbf{D}}_{II}^{-1}$ must be evaluated at each frequency. Alternative condensation methods are described here.

2.5.2 Approximate Expressions

In this subsection, approximate expressions for the condensation are found in order to reduce the calculation cost. The inverse of the dynamic stiffness matrix associated with internal DOFs can be expressed as

$$\tilde{\mathbf{D}}_{II}^{-1} = \left(\tilde{\mathbf{K}}_{II} - \omega^2 \tilde{\mathbf{M}}_{II}\right)^{-1} = \left(\mathbf{I} - \omega^2 \tilde{\mathbf{K}}_{II}^{-1} \tilde{\mathbf{M}}_{II}\right)^{-1} \tilde{\mathbf{K}}_{II}^{-1}. \tag{2.39}$$

For small $\tilde{\mathbf{K}}_{II}^{-1}\tilde{\mathbf{M}}_{II}$, equation (2.39) may be approximated as

$$\tilde{\mathbf{D}}_{II}^{-1} = \tilde{\mathbf{K}}_{II}^{-1} + O\left(\omega^2 \tilde{\mathbf{K}}_{II}^{-1} \tilde{\mathbf{M}}_{II} \tilde{\mathbf{K}}_{II}^{-1}\right) \tag{2.40}$$

which is same as static condensation [75]. For the static condensation of $\tilde{\mathbf{D}}_{II}$, the condensed dynamic matrix is evaluated as

$$\begin{aligned}\mathbf{D} = \tilde{\mathbf{D}}_{EE} - \tilde{\mathbf{D}}_{EI}\tilde{\mathbf{D}}_{II}^{-1}\tilde{\mathbf{D}}_{IE} \approx \tilde{\mathbf{K}}_{EE} - \tilde{\mathbf{K}}_{EI}\tilde{\mathbf{K}}_{II}^{-1}\tilde{\mathbf{K}}_{IE} \\ - \omega^2\left(\tilde{\mathbf{M}}_{EE} - \tilde{\mathbf{K}}_{EI}\tilde{\mathbf{K}}_{II}^{-1}\tilde{\mathbf{M}}_{IE} - \tilde{\mathbf{M}}_{EI}\tilde{\mathbf{K}}_{II}^{-1}\tilde{\mathbf{K}}_{IE}\right).\end{aligned} \tag{2.41}$$

To calculate equation (2.41) $\tilde{\mathbf{K}}_{II}^{-1}$ and the matrix products need to be evaluated only once so that the calculation cost is small. In addition, the large terms associated with the stiffness and the small terms associated with the inertia are appropriately grouped such that round-off errors in the arithmetic operations are reduced.

For the condensed element, the equivalent stiffness and mass matrices can be similarly calculated from equation (2.8), i.e. $\tilde{\mathbf{R}}^{\mathrm{T}}\tilde{\mathbf{D}}\tilde{\mathbf{R}}\mathbf{q}_E = \mathbf{f}_E$, by expanding $\tilde{\mathbf{D}} = \tilde{\mathbf{K}} - \omega^2\tilde{\mathbf{M}}$. This may be important to derive the potential and kinetic energy densities and the group velocity described later in this chapter. For small ω, the associated condensed stiffness and mass matrices are, from equation,

$$\begin{aligned}\mathbf{K} &= \tilde{\mathbf{R}}^{\mathrm{T}}\tilde{\mathbf{K}}\tilde{\mathbf{R}} \approx \tilde{\mathbf{K}}_{EE} - \tilde{\mathbf{K}}_{EI}\tilde{\mathbf{K}}_{II}^{-1}\tilde{\mathbf{K}}_{IE}, \\ \mathbf{M} &= \tilde{\mathbf{R}}^{\mathrm{T}}\tilde{\mathbf{M}}\tilde{\mathbf{R}} \approx \tilde{\mathbf{M}}_{EE} - \tilde{\mathbf{K}}_{EI}\tilde{\mathbf{K}}_{II}^{-1}\tilde{\mathbf{M}}_{IE} - \tilde{\mathbf{M}}_{EI}\tilde{\mathbf{K}}_{II}^{-1}\tilde{\mathbf{K}}_{IE}.\end{aligned} \tag{2.42}$$

Equations (2.40)-(2.42) describe the static condensation. However static condensation is accurate only at very low frequencies [70] since the inertia associated with $\tilde{\mathbf{D}}_{II}$ is excluded.

Alternatively, the second order approximation of the condensation of $\tilde{\mathbf{D}}_{II}$ is here proposed. Equation (2.39) can be expanded to the second order as

$$\tilde{\mathbf{D}}_{II}^{-1} = \left(\mathbf{I} + \omega^2\tilde{\mathbf{K}}_{II}^{-1}\tilde{\mathbf{M}}_{II}\right)\tilde{\mathbf{K}}_{II}^{-1} + O\left(\omega^4\tilde{\mathbf{K}}_{II}^{-1}\tilde{\mathbf{M}}_{II}\tilde{\mathbf{K}}_{II}^{-1}\tilde{\mathbf{M}}_{II}\tilde{\mathbf{K}}_{II}^{-1}\right) \tag{2.43}$$

and $\mathbf{D}$ can be evaluated after some calculations as

$$\begin{aligned}\mathbf{D} \approx & \tilde{\mathbf{K}}_{EE} - \tilde{\mathbf{K}}_{EI}\tilde{\mathbf{K}}_{II}^{-1}\tilde{\mathbf{K}}_{IE} \\ & - \omega^2\left(\tilde{\mathbf{M}}_{EE} - \tilde{\mathbf{K}}_{EI}\tilde{\mathbf{K}}_{II}^{-1}\tilde{\mathbf{M}}_{IE} - \tilde{\mathbf{M}}_{EI}\tilde{\mathbf{K}}_{II}^{-1}\tilde{\mathbf{K}}_{IE} + \tilde{\mathbf{K}}_{EI}\tilde{\mathbf{K}}_{II}^{-1}\tilde{\mathbf{M}}_{II}\tilde{\mathbf{K}}_{II}^{-1}\tilde{\mathbf{K}}_{IE}\right) \\ & - \omega^4\left(\tilde{\mathbf{M}}_{EI}\tilde{\mathbf{K}}_{II}^{-1}\tilde{\mathbf{M}}_{IE} - \tilde{\mathbf{K}}_{EI}\tilde{\mathbf{K}}_{II}^{-1}\tilde{\mathbf{M}}_{II}\tilde{\mathbf{K}}_{II}^{-1}\tilde{\mathbf{M}}_{IE} - \tilde{\mathbf{M}}_{EI}\tilde{\mathbf{K}}_{II}^{-1}\tilde{\mathbf{M}}_{II}\tilde{\mathbf{K}}_{II}^{-1}\tilde{\mathbf{K}}_{IE}\right).\end{aligned} \tag{2.44}$$

By using the second order approximation (2.43), the condensed stiffness and mass matrices can be calculated from equation (2.8) in the same manner as equations (2.42). After some calculations the resulting condensed element matrices are such that

$$\begin{aligned}\mathbf{K} \approx & \tilde{\mathbf{K}}_{EE} - \tilde{\mathbf{K}}_{EI}\tilde{\mathbf{K}}_{II}^{-1}\tilde{\mathbf{K}}_{IE} \\ & + \omega^4\left(\tilde{\mathbf{M}}_{EI}\tilde{\mathbf{K}}_{II}^{-1}\tilde{\mathbf{M}}_{IE} - \tilde{\mathbf{K}}_{EI}\tilde{\mathbf{K}}_{II}^{-1}\tilde{\mathbf{M}}_{II}\tilde{\mathbf{K}}_{II}^{-1}\tilde{\mathbf{M}}_{IE} - \tilde{\mathbf{M}}_{EI}\tilde{\mathbf{K}}_{II}^{-1}\tilde{\mathbf{M}}_{II}\tilde{\mathbf{K}}_{II}^{-1}\tilde{\mathbf{K}}_{IE}\right), \\ \mathbf{M} \approx & \tilde{\mathbf{M}}_{EE} - \tilde{\mathbf{K}}_{EI}\tilde{\mathbf{K}}_{II}^{-1}\tilde{\mathbf{M}}_{IE} - \tilde{\mathbf{M}}_{EI}\tilde{\mathbf{K}}_{II}^{-1}\tilde{\mathbf{K}}_{IE} + \tilde{\mathbf{K}}_{EI}\tilde{\mathbf{K}}_{II}^{-1}\tilde{\mathbf{M}}_{II}\tilde{\mathbf{K}}_{II}^{-1}\tilde{\mathbf{K}}_{IE} \\ & + 2\omega^2\left(\tilde{\mathbf{M}}_{EI}\tilde{\mathbf{K}}_{II}^{-1}\tilde{\mathbf{M}}_{IE} - \tilde{\mathbf{K}}_{EI}\tilde{\mathbf{K}}_{II}^{-1}\tilde{\mathbf{M}}_{II}\tilde{\mathbf{K}}_{II}^{-1}\tilde{\mathbf{M}}_{IE} - \tilde{\mathbf{M}}_{EI}\tilde{\mathbf{K}}_{II}^{-1}\tilde{\mathbf{M}}_{II}\tilde{\mathbf{K}}_{II}^{-1}\tilde{\mathbf{K}}_{IE}\right).\end{aligned} \tag{2.45}$$

Using the second order approximation, numerical results are much more accurate than the static condensation for wide range of frequency [70].

2.5.3 FE Discretisation Error Associated with Concatenated Elements

For a series of N concatenated elements of length Δ, the eigenvalues associated with N concatenated elements become $\lambda = e^{-jk(N\Delta)}$.

For a single element, the FE discretisation criterion may be expressed as $|k\Delta| \le 1$ as in equation (2.35). For N concatenated elements, the criterion therefore becomes

$$|kN\Delta| \le N. \tag{2.46}$$

2.5.4 Illustrative Example of the Beam

In this subsection, an illustrative example for a method using concatenating elements is shown for the beam. The global stiffness and mass matrices using two concatenated elements can be formed from the element matrices (2.29) and are

$$\tilde{\mathbf{K}} = \frac{EI}{\Delta^3}\begin{bmatrix} 12 & 6\Delta & -12 & 6\Delta & 0 & 0 \\ & 4\Delta^2 & -6\Delta & 2\Delta^2 & 0 & 0 \\ & & 24 & 0 & -12 & 6\Delta \\ & & & 8\Delta^2 & -6\Delta & 2\Delta^2 \\ & sym. & & & 12 & -6\Delta \\ & & & & & 4\Delta^2 \end{bmatrix},$$
$$\tilde{\mathbf{M}} = \frac{\rho A\Delta}{420}\begin{bmatrix} 156 & 22\Delta & 54 & -13\Delta & 0 & 0 \\ & 4\Delta^2 & 13\Delta & -3\Delta^2 & 0 & 0 \\ & & 312 & 0 & 54 & -13\Delta \\ & & & 8\Delta^2 & 13\Delta & -3\Delta^2 \\ & sym. & & & 156 & -22\Delta \\ & & & & & 4\Delta^2 \end{bmatrix}. \tag{2.47}$$

The condensed stiffness and mass matrices are better-conditioned in terms of $\max\left\{K_{ii}/\omega^2 M_{ii}\right\}$. The stiffness and mass matrices of equations (2.47) are, after static condensation (2.42),

$$\mathbf{K} = \frac{EI}{\Delta^3}\begin{bmatrix} 1.5 & 1.5\Delta & -1.5 & 1.5\Delta \\ & 2\Delta^2 & -1.5\Delta & \Delta^2 \\ & sym. & 1.5 & -1.5\Delta \\ & & & 2\Delta^2 \end{bmatrix},$$
$$\mathbf{M} = \frac{\rho A\Delta}{420}\begin{bmatrix} 229.5 & 47.5\Delta & 34.5 & -14.5\Delta \\ & 12\Delta^2 & 14.5\Delta & -5\Delta^2 \\ & sym. & 229.5 & -47.5\Delta \\ & & & 12\Delta^2 \end{bmatrix}. \tag{2.48}$$

For the original single element, $\max\left\{K_{ii}/\omega^2 M_{ii}\right\} = 420/\left(k_B\Delta\right)^4$ while the value for equation (2.48) is $\max\left\{K_{ii}/\omega^2 M_{ii}\right\} = 70/\left(k_B\Delta\right)^4$ such that the conditioning is improved.

The relative error in the bending wavenumber, k_B, using two concatenated elements is compared with that using one element in Figure 2.9. The result was obtained using the dynamic condensation. The relative error below $k_B\Delta = 0.04$ is marginally improved. The relative error for $k_B\Delta > 0.04$ is more-or-less identical except for $2k_B\Delta \approx \pi$ where the eigenvalue problem using the transfer matrix, e.g. equation (2.31), is ill-conditioned.

The improvements are greater, if more than 2 elements are concatenated as long as $\mathbf{D}_{II}^{-1}$ is accurately evaluated. The improvements are also greater for structures for which there are more DOFs per node. For general waveguides a number of elements are used to model a section of the waveguides. The round-off errors can therefore occur for each element and such errors could be accumulated and magnified through matrix operations such as matrix inverse. A numerical example of a plate strip is shown later.

2.6 Conditioning of the Eigenvalue Problem

The eigenvalue problem using the transfer matrix (2.14) may be used to predict free wave propagation in simple waveguides. However, results may be inaccurate for general waveguides because of the ill-conditioning of the eigenvalue problem. In this section, numerical errors occurring in the ill-conditioned eigenvalue problem are discussed. Methods for improving the conditioning of the eigenvalue problem are then described. In particular, Zhong's method [66] is introduced as the conditioned eigenvalue problem, which will be used throughout this thesis for general waveguides.

2.6.1 Numerical Issues in Accuracy of the Eigenvalue Problem

Apart from the FE discretization error and error due to the round-off of inertia terms described in section 2.4, numerical errors occur when the eigenvalue problem is numerically formed and solved. When the eigenvalue problem (2.14) is formed, numerical errors arise mainly because of the inversion of $\mathbf{D}_{LR}$. Numerical errors also occur when the ill-conditioned eigenvalue problem is to be solved.

A matrix inverse is needed to formulate the eigenvalue problem, i.e. $\mathbf{D}_{LR}^{-1}$ in equation (2.14) and $\tilde{\mathbf{D}}_{II}^{-1}$ in equation (2.10). When a general matrix $\mathbf{A}$ is numerically inverted, the maximum resulting errors in the matrix inverse $\mathbf{A}^{-1}$ are the order of $\varepsilon \cdot \kappa(\mathbf{A})$ where ε is the machine precision,

$$\kappa(\mathbf{A}) = \sigma_{\max} / \sigma_{\min} \tag{2.49}$$

is the condition number and $\sigma_{\max}$ and $\sigma_{\min}$ are the largest and smallest singular values [78]. The condition number is likely to increase as the size of the matrix increases and/or there are off-diagonal elements with comparatively large magnitudes, e.g.[78,79]. For a matrix for which κ is large, use of the matrix pseudo inverse (e.g. [78]) can be evaluated to reduce numerical errors.

Even if the eigenvalue problem is accurately formulated, numerical errors can still occur when the eigenvalue problem is to be solved. Since the matrix of the eigenvalue problem in the WFE method is square, non-symmetric and the elements could be complex, Schur factorisation is in general used [78]. This is the case in commonly-used software packages such as MATLAB^{TM} and Mathematica^{TM}.

When the eigenvalue problem $\mathbf{A}\boldsymbol{\varphi} = \lambda\boldsymbol{\varphi}$ is solved using Schur factorisation, the matrix $\mathbf{A}$ is factorised into the form $\mathbf{Q}^{\mathrm{H}}\mathbf{A}\mathbf{Q} = \mathbf{S} + \mathbf{N}$ where $\mathbf{Q}$ is unitary, $\mathbf{S}$ is diagonal and $\mathbf{N}$ is strictly upper-triangular [78,79]. The resulting errors for the eigenvalue problem are estimated from $\|\mathbf{N}\|$ or $\kappa(\mathbf{Q})$ [79] where $\|\cdot\|$ is the 2-norm.

Large $\|\mathbf{N}\|$ indicates that the matrix of the eigenvalue problem is far from normal since $\|\mathbf{N}\| = 0$ for the normal matrix $\mathbf{A}$. The columns of the unitary matrix $\mathbf{Q}$ are called the Schur vectors which have certain relationships with the eigenvectors [79]. Large $\kappa(\mathbf{Q})$ then means that the matrix composed of the Schur vectors is almost singular. This may imply that when each (right) eigenvector is far from orthogonal to each other, numerical errors can be large.

The eigenvalue problem using the transfer matrix (2.14) is in general far from normal and each (right) eigenvector is also far from orthogonal to each other. The reason is mainly because the eigenvectors contain both displacement and force components which often have very different magnitudes.

The above discussion provides some mathematical considerations. However it is less easy to evaluate the values of $\|\mathbf{N}\|$ and $\kappa(\mathbf{Q})$. In practice, the condition number of the matrix of the eigenvalue problem may be used instead to assess the conditioning.

2.6.2 Polynomial Eigenvalue Problem

In this and following subsections, the eigenvalue problem using the transfer matrix (2.14) is reformulated. The first row of equation (2.14) gives the relationship between the displacement and the force elements of the eigenvectors such that

$$\mathbf{f} = \left(\mathbf{D}_{LL} + \lambda \mathbf{D}_{LR}\right)\mathbf{q}\,. \tag{2.50}$$

Substituting equation (2.50) into the second row of equation (2.14) gives, after some manipulation [67],

$$\left[\lambda^2 \mathbf{D}_{LR} + \lambda\left(\mathbf{D}_{LL} + \mathbf{D}_{RR}\right) + \mathbf{D}_{RL}\right]\mathbf{q} = \mathbf{0}\,. \tag{2.51}$$

Equation (2.51) can be written as

$$\left[\lambda^2 \mathbf{K}_{LR} + \lambda\left(\mathbf{K}_{LL} + \mathbf{K}_{RR}\right) + \mathbf{K}_{RL}\right]\mathbf{q} = \omega^2\left[\lambda^2 \mathbf{M}_{LR} + \lambda\left(\mathbf{M}_{LL} + \mathbf{M}_{RR}\right) + \mathbf{M}_{RL}\right]\mathbf{q}\,. \tag{2.52}$$

The eigenvalue problem (2.52) can be solved for a given value of $\lambda = e^{-jk\Delta}$ such that the associated real values of ω are determined. For wavenumbers k which are purely real or purely imaginary, the solutions can be easily found. To calculate equations (2.52) there is no round-off of inertia terms described previously. However, the wavenumbers could be complex to give real values of ω for damped or undamped waveguides. For such cases, it is generally very difficult to find the complex wavenumbers which give real-valued solutions for ω from equation (2.52). In general, then, it is preferable to specify a real value of ω and calculate the (complex) solutions λ to the eigenvalue problem of equation (2.51).

A polynomial eigenvalue problem (2.51) therefore needs to be solved to find all the wavenumbers for a given real ω. The eigenvalue problem of equation (2.51) can be converted into the standard linear eigenvalue problem [80] such that

$$\begin{bmatrix} \mathbf{0} & \mathbf{I} \\ -\mathbf{D}_{LR}^{-1}\mathbf{D}_{RL} & -\mathbf{D}_{LR}^{-1}\left(\mathbf{D}_{LL} + \mathbf{D}_{RR}\right) \end{bmatrix}\begin{bmatrix} \mathbf{q} \\ \lambda\mathbf{q} \end{bmatrix} = \lambda\begin{bmatrix} \mathbf{q} \\ \lambda\mathbf{q} \end{bmatrix}. \tag{2.53}$$

Equation (2.53) is better-conditioned than equation (2.14) as the eigenvectors are associated with only the displacement components such that $\kappa(\mathbf{Q})$ discussed in subsection 2.6.1 can be particularly smaller. The associated force eigenvector can be determined from the displacement eigenvector from equation (2.50).

2.6.3 Zhong's Method

Several previous works [8,60,62,67,68] used Zhong's method [66] to formulate the eigenvalue problem. Also in this thesis the method is applied to solve free wave propagation for general waveguides. In this subsection, the method is first briefly described. An application of singular value decomposition (SVD) is proposed to determine the eigenvectors more accurately.

The details of Zhong's method can be found in [66,81,82]. The method starts from a reformulation of equation (2.12) into the relationships for the displacement vectors alone:

$$\begin{aligned}\begin{bmatrix}\mathbf{q}_L\\ \mathbf{f}_L\end{bmatrix}&=\begin{bmatrix}\mathbf{I} & \mathbf{0}\\ \mathbf{D}_{LL} & \mathbf{D}_{LR}\end{bmatrix}\begin{bmatrix}\mathbf{q}_L\\ \mathbf{q}_R\end{bmatrix},\\ \begin{bmatrix}\mathbf{q}_R\\ -\mathbf{f}_R\end{bmatrix}&=\begin{bmatrix}\mathbf{0} & \mathbf{I}\\ -\mathbf{D}_{RL} & -\mathbf{D}_{RR}\end{bmatrix}\begin{bmatrix}\mathbf{q}_L\\ \mathbf{q}_R\end{bmatrix}.\end{aligned} \tag{2.54}$$

After some matrix operations using the periodicity condition and the symplectic relationship [66], the general eigenvalue problem

$$\mu\mathbf{Z}_1\begin{bmatrix}\mathbf{q}\\ \lambda\mathbf{q}\end{bmatrix}=\mathbf{Z}_2\begin{bmatrix}\mathbf{q}\\ \lambda\mathbf{q}\end{bmatrix} \tag{2.55}$$

is formed with

$$\begin{aligned}\mathbf{Z}_1&=\begin{bmatrix}\mathbf{0} & \mathbf{D}_{LR}\\ -\mathbf{D}_{RL} & \mathbf{0}\end{bmatrix},\\ \mathbf{Z}_2&=\begin{bmatrix}(\mathbf{D}_{LR}-\mathbf{D}_{RL}) & -(\mathbf{D}_{LL}+\mathbf{D}_{RR})\\ (\mathbf{D}_{LL}+\mathbf{D}_{RR}) & (\mathbf{D}_{LR}-\mathbf{D}_{RL})\end{bmatrix}\end{aligned} \tag{2.56}$$

and

$$\mu=\lambda+\frac{1}{\lambda}. \tag{2.57}$$

More details of the formulation are given in Appendix 1.2. Equation (2.55) may be expressed in the form of the standard eigenvalue problem as

$$\mathbf{Z}\begin{bmatrix}\mathbf{q}\\ \lambda\mathbf{q}\end{bmatrix} = \mu'\begin{bmatrix}\mathbf{q}\\ \lambda\mathbf{q}\end{bmatrix} \tag{2.58}$$

where $\mathbf{Z} = \mathbf{Z}_1^{-1}\mathbf{Z}_2$ or $\mathbf{Z} = \mathbf{Z}_2^{-1}\mathbf{Z}_1$ and the matrix with the smaller condition number is inverted and $\mu' = \mu$ or $1/\mu$ respectively.

The eigenvalue problem (2.58) is better-conditioned than the other eigenvalue problems. The eigenvectors are related to only the displacement components (smaller $\kappa(\mathbf{Q})$ discussed in subsection 2.6.1) and the matrix $\mathbf{Z}$ is relatively close to normal (smaller $\|\mathbf{N}\|$ discussed in subsection 2.6.1). In addition, since $\mu = \lambda + 1/\lambda$, the eigenvalues are such that the range of the magnitude of the eigenvalues becomes roughly $e^{k\Delta}$ if rapidly decaying nearfield waves exist while that for the original eigenvalue problems is $e^{2k\Delta}$. Furthermore, the smallest eigenvalues of μ are those of most interest. For these reasons, Zhong's method is numerically better-conditioned and is used throughout this thesis.

Equation (2.55) has repeated eigenvalues of μ since both λ_i and $1/\lambda_i$ are solutions of equation of equation (2.14). The original eigenvalues $\lambda_i, 1/\lambda_i$ can be determined from the eigenvalue $\mu_i = \lambda_i + 1/\lambda_i$ by solving a quadratic equation or by noting that $\mu_i = e^{-jk_i\Delta} + e^{jk_i\Delta} = 2\cos(k_i\Delta)$. In practice one might be interested in those wave modes for which the magnitudes of the wavenumbers are smallest.

Corresponding to the repeated eigenvalues μ, there are two independent eigenvectors $\boldsymbol{\varphi}_1$ and $\boldsymbol{\varphi}_2$. These are given by

$$\boldsymbol{\varphi}_{1,2} = \begin{bmatrix}\mathbf{q}_{1,2}\\ \lambda\mathbf{q}_{1,2}\end{bmatrix} \tag{2.59}$$

where $\begin{bmatrix}\mathbf{q}_{1,2}^{\mathrm{T}} & \lambda\mathbf{q}_{1,2}^{\mathrm{T}}\end{bmatrix}$ are the eigenvectors associated with the repeated eigenvalues. The eigenvectors associated with the original eigenvalues λ_i and $1/\lambda_i$ can be found from a linear combination of $\boldsymbol{\varphi}_1$ and $\boldsymbol{\varphi}_2$ [8,66,67], i.e.,

$$\begin{bmatrix}\mathbf{q}\\ \lambda\mathbf{q}\end{bmatrix} = \alpha_1\boldsymbol{\varphi}_1 + \alpha_2\boldsymbol{\varphi}_2 \ . \tag{2.60}$$

Substituting equations (2.59) and (2.60) into the equation (A1.9) in Appendix 1.2, i.e.

$$\begin{bmatrix}-\mathbf{D}_{RL} & -\mathbf{D}_{LL}-\mathbf{D}_{RR}\\ \mathbf{0} & -\mathbf{D}_{RL}\end{bmatrix}\begin{bmatrix}\mathbf{q}\\ \lambda\mathbf{q}\end{bmatrix} = \lambda\begin{bmatrix}\mathbf{0} & \mathbf{D}_{LR}\\ -\mathbf{D}_{RL} & \mathbf{0}\end{bmatrix}\begin{bmatrix}\mathbf{q}\\ \lambda\mathbf{q}\end{bmatrix}, \tag{A1.9}$$

gives

$$\begin{bmatrix}-\mathbf{D}_{RL} & -\mathbf{D}_{LL}-\mathbf{D}_{RR}-\lambda\mathbf{D}_{LR}\\ \lambda\mathbf{D}_{RL} & -\mathbf{D}_{RL}\end{bmatrix}\left\{\alpha_1\begin{bmatrix}\mathbf{q}_1\\ \lambda\mathbf{q}_1\end{bmatrix} + \alpha_2\begin{bmatrix}\mathbf{q}_2\\ \lambda\mathbf{q}_2\end{bmatrix}\right\} = \mathbf{0}. \tag{2.61}$$

Premultiplying by $\begin{bmatrix}\mathbf{q}_1^{\mathrm{H}} & \lambda\mathbf{q}_1^{\mathrm{H}}\end{bmatrix}$ leads to a relationship between α_1 and α_2 such that [67]

$$\frac{\alpha_2}{\alpha_1} = -\frac{\begin{bmatrix}\mathbf{q}_1^{\mathrm{H}} & \lambda\mathbf{q}_1^{\mathrm{H}}\end{bmatrix}\begin{bmatrix}-\mathbf{D}_{RL} & -\mathbf{D}_{LL}-\mathbf{D}_{RR}-\lambda\mathbf{D}_{LR}\\ \lambda\mathbf{D}_{RL} & -\mathbf{D}_{RL}\end{bmatrix}\begin{bmatrix}\mathbf{q}_1\\ \lambda\mathbf{q}_1\end{bmatrix}}{\begin{bmatrix}\mathbf{q}_1^{\mathrm{H}} & \lambda\mathbf{q}_1^{\mathrm{H}}\end{bmatrix}\begin{bmatrix}-\mathbf{D}_{RL} & -\mathbf{D}_{LL}-\mathbf{D}_{RR}-\lambda\mathbf{D}_{LR}\\ \lambda\mathbf{D}_{RL} & -\mathbf{D}_{RL}\end{bmatrix}\begin{bmatrix}\mathbf{q}_2\\ \lambda\mathbf{q}_2\end{bmatrix}}. \tag{2.62}$$

Although equation (2.62) is algebraically exact, there may be difficulties when calculating it numerically as the denominator can be close to zero and round-off errors can accumulate for a large size matrix. An application of SVD is therefore proposed to avoid numerical difficulties. Equation (2.61) can be alternatively written as

$$\begin{bmatrix}-\mathbf{D}_{RL} & -\mathbf{D}_{LL}-\mathbf{D}_{RR}-\lambda\mathbf{D}_{LR}\\ \lambda\mathbf{D}_{RL} & -\mathbf{D}_{RL}\end{bmatrix}\begin{bmatrix}\mathbf{q}_1 & \mathbf{q}_2\\ \lambda\mathbf{q}_1 & \lambda\mathbf{q}_2\end{bmatrix}\begin{bmatrix}\alpha_1\\ \alpha_2\end{bmatrix} = \mathbf{0}. \tag{2.63}$$

After the multiplication of the first two matrices, equation (2.63) has the form $\mathbf{A}\begin{bmatrix}\alpha_1 & \alpha_2\end{bmatrix}^{\mathrm{T}} = \mathbf{0}$ with $\mathbf{A}$ being an $n \times 2$ rectangular matrix, where n is the length of the eigenvector. The problem is equivalent to that of solving an overdetermined set of simultaneous equations if $n \geq 3$. Performing SVD on $\mathbf{A}$ gives

$$\mathbf{A} = \mathbf{U}\mathbf{S}\mathbf{V}^{\mathrm{H}}. \tag{2.64}$$

Equation (2.64) can be then written as

$$\mathbf{A}\begin{bmatrix} v_{11} & v_{12} \\ v_{21} & v_{22} \end{bmatrix} = \mathbf{U}\begin{bmatrix} \sigma_1 & 0 & 0 & \cdots & 0 \\ 0 & \sigma_\varepsilon & 0 & \cdots & 0 \end{bmatrix}^{\mathrm{T}} \tag{2.65}$$

where $\sigma_\varepsilon \approx 0$. The matrix $\mathbf{S}$ contains two singular values on its leading diagonal and one of these is almost zero. Taking the second column of equation (2.65) and using $\mathbf{A}$ as the expression in equation (2.63) gives

$$\begin{bmatrix} -\mathbf{D}_{RL} & -\mathbf{D}_{LL} - \mathbf{D}_{RR} - \lambda\mathbf{D}_{LR} \\ \lambda\mathbf{D}_{RL} & -\mathbf{D}_{RL} \end{bmatrix}\begin{bmatrix} \mathbf{q}_1 & \mathbf{q}_2 \\ \lambda\mathbf{q}_1 & \lambda\mathbf{q}_2 \end{bmatrix}\begin{bmatrix} v_{12} \\ v_{22} \end{bmatrix} \approx \mathbf{0} \tag{2.66}$$

such that $\begin{bmatrix}\alpha_1 & \alpha_2\end{bmatrix}^{\mathrm{T}}$ are given by

$$\frac{\alpha_2}{\alpha_1} = \frac{v_{22}}{v_{21}}. \tag{2.67}$$

The orders of v_{21}, v_{22} in equation (2.67) are typically $O(1)$ while α_1 in equation (2.62) may be nearly zero. Such an application of SVD to solve an overdetermined linear equation can be found in [83]. After determining the displacement eigenvector, $\mathbf{q}$, the associated force eigenvector, $\mathbf{f}$, can be calculated from equation (2.50) to form the original eigenvector (2.19).

Another approach which is worth noting is Thompson's method [58]. Formulations are described in Appendix 1.3. Although the method can form smaller size of a matrix for an

eigenvalue problem, results may suffer numerical problems when $k \to 0$. Zhong's method was therefore used in this thesis.

2.7 Numerical Example of a Plate Strip with Simply-supported Edges

Free flexural wave propagation in a plate strip with simply-supported edges is studied to illustrate the WFE method. To improve conditioning Zhong's method described in subsection 2.6.3 is used. The effects of the number of elements across the strip and the aspect ratio of the elements on the conditioning are illustrated. Numerical errors occurring in the free wave propagation characteristics are shown and reduction of numerical errors using concatenating element is illustrated. No damping is assumed.

2.7.1 Analytical Solution

A plate strip of width L_y, shown in Figure 2.10(a), is considered. The plate is thin and isotropic with simply-supported boundary conditions, e.g. [1], along the *y*-wise plate edges. For such plate strip, the analytical wavenumber is given by [1]

$$k^2 = k_x^2 + k_y^2 = \pm\sqrt{\frac{\rho h}{D}}\omega \tag{2.68}$$

where $D = Eh^3 \big/ 12\left(1-\nu^2\right)$ is the bending rigidity, h is the thickness of the plate strip and ν is Poisson's ratio. For the simply supported boundary condition along the plate edges $y = 0, L_y$, the wave modes have displacements proportional to $\sin\left(i\pi y / L_y\right)$ where i is an integer. The wavenumbers in the *x*-direction are then given by

$$k_{xi}^2 = \pm\sqrt{\frac{\rho h}{D}}\omega - \left(\frac{i\pi}{L_y}\right)^2 \quad \left(i = 1, 2, \cdots\right). \tag{2.69}$$

Substituting $k_{xi} = 0$ into equation (2.69) gives the cut-off frequency for the ith wave mode as

$$\omega_{c,i} = \sqrt{\frac{D}{\rho h}}\left(\frac{i\pi}{L_y}\right)^2 . \tag{2.70}$$

2.7.2 WFE Results

The plate is assumed to be steel with $L_y = 0.18$, $E = 2.0\cdot 10^{11}$, $\rho = 7800$, $\nu = 0.30$ and $h = 1.8\cdot 10^{-3}$, all in SI units. The element matrices are formed using ANSYS 7.1. A four node plane strain shell element (SHELL63) was chosen. The SHELL63 element has 6 DOFs at each node. Consider a plate strip model comprising 4 elements as shown in Figure 2.10(b) with $\Delta_x = 18mm$, $\Delta_y = 45mm$. After removing the in-plane DOFs and DOFs on the boundaries which are zero because of the conditions, there are 22 resulting DOFs for the model. Since the *y*-wise wavenumber is $k_y = i\pi/L_y$ for the *i*th wave mode, only the wavenumber for the *i*=1 wave mode could be expected to be accurately evaluated since $k_y\Delta_y = \pi/4\,(<1)$.

The dispersion curves for the *i*=1 mode are shown in Figure 2.11. There are two waves associated with the *i*=1 mode; one is for a wave which propagates above its cut-off frequency and another is for a nearfield wave. Figure 2.11(a) shows the dispersion curves calculated from the eigenvalue problem using the transfer matrix (2.14) and Figure 2.11(b) shows those from the conditioned eigenvalue problem (2.55). The abscissa represents the non-dimensional frequency

$$\Omega = \frac{L_y^2}{\pi^2}\sqrt{\frac{\rho h}{D}}\omega . \tag{2.71}$$

The cut-off frequency for the *i*th mode occurs at $\Omega = i^2$. The ordinate shows the non-dimensional wavenumber, $k_x L_y/\pi$, which becomes $-ji$ for the *i*th wave mode at $\Omega = 0$.

It can be seen that the results using the transfer matrix (Figure 2.11(a)) show poor agreement around the cut-off frequency. This is a typical example of deterioration due to the ill-conditioning of the eigenvalue problem. For the plate strip, the condition number of the eigenvalue problem using the transfer matrix is $\kappa(\mathbf{T}) = O(10^{13})$ while that of Zhong's method is $\kappa(\mathbf{Z}) = O(10^{5})$. For a larger matrix (with more DOFs), results using the transfer

matrix can completely break down. On the other hand the result using Zhong's method shows reasonable agreement.

The dispersion curves using 18 elements $\left(\Delta_x = \Delta_y = 10mm\right)$ are shown in Figure 2.12. Hereafter only the results using Zhong's method are shown. In the frequency range analysed, 6 wave modes cut-on. Reasonable agreement can be seen between the analytical solutions and the WFE results on the whole. Discrepancies become larger for higher wave modes and for large wavenumbers due to the FE discretization errors. Complex conjugate wavenumbers of the form $k = \pm\alpha - j\beta$ can be seen for the n=4 $\left(\Omega \le 0.75\right)$ and the n=5 wave modes $\left(\Omega \le 2\right)$ mainly because of the FE discretisation errors. The errors can be reduced by increasing the number of elements across the plate as long as the conditioning is not a problem.

2.7.3 Wave Assurance Criterion Value

In subsection 2.7.2 the dispersion curves are shown. For general waveguides in which there are many wave modes, many eigenvalues and associated eigenvectors are calculated at each discretised frequency step. To draw dispersion curves from predicted results at each discrete frequency step, an additional procedure should be employed in order to check the correlation of the resulting dispersion branches. In this thesis, a wave assurance criterion (WAC) value is applied [59].

The idea is that if the wave characteristic is similar from one frequency to another, the eigenvectors, which represent the wave mode, should have a certain relationship such that one eigenvector is close to just a scalar multiple of the other. The value is defined as

$$WAC\left(\omega_n, \omega_{n-1}\right) = \frac{\left(\boldsymbol{\varphi}_{\omega_n}^{\mathrm{H}} \boldsymbol{\varphi}_{\omega_{n-1}}\right)^2}{\left(\boldsymbol{\varphi}_{\omega_n}^{\mathrm{H}} \boldsymbol{\varphi}_{\omega_n}\right)\left(\boldsymbol{\varphi}_{\omega_{n-1}}^{\mathrm{H}} \boldsymbol{\varphi}_{\omega_{n-1}}\right)} \tag{2.72}$$

where ω_n, ω_{n-1} is the frequency at nth and (n-1)th discrete frequency step, $\boldsymbol{\varphi}_{\omega_n}$ is the vector of the eigenvector associated with nth step. The WAC value can be calculated from two complex eigenvectors associated with two distinct eigenvalues. In practice only the nodal displacements vector, $\mathbf{q}$, can be applied instead of $\boldsymbol{\varphi}$ which contains both the displacement and force components. If the WAC value is close to unity, two eigenvectors calculated at

two consecutive steps correspond to the same wave mode. This procedure helps to allow the propagation branch as to be consistently found as well as to identify the cut-off frequencies efficiently.

2.7.4 Effect of Modelling of the Cross-section on the Conditioning

Even for the conditioned eigenvalue problem, the conditioning is still of concern. In this subsection, the effects of the matrix size and the aspect ratio of elements on the conditioning are discussed. To formulate the conditioned eigenvalue problem (2.58), either $\mathbf{Z}_1$ or $\mathbf{Z}_2$ must be inverted and large values of $\kappa(\mathbf{Z}_1)$ and $\kappa(\mathbf{Z}_2)$ can cause an inaccurate formulation. Also a large value of $\kappa(\mathbf{Z}_1)$ is in general correlated with large values of $\kappa(\mathbf{Z}_2)$ and $\kappa(\mathbf{Z})$. Here, $\kappa(\mathbf{Z}_1)$, i.e. $\kappa(\mathbf{D}_{LR})$ (see equation (2.56)), is investigated for various FE models of the plate strip.

Figure 2.13 shows the relationship between $\kappa(\mathbf{D}_{LR})$ and the size of the matrix $\mathbf{D}_{LR}$ at a particular frequency, $\Omega = 7.48$, using various different elements. The aspect ratio of an element is defined as

$$\gamma = \Delta_x / \Delta_y \,. \tag{2.73}$$

It can be seen that the condition number deteriorates as the size of the matrix increases. The relationship between the condition number and the size of the matrix, *n*, is approximately

$$\kappa \propto n^2 \tag{2.74}$$

for the same γ. Figure 2.14 shows the relationship between κ and γ for a given matrix size. The relationship is approximately such that

$$\begin{aligned} \kappa / \kappa_{\gamma=1} &\propto \gamma^{-1.6} \quad (\gamma < 1), \\ \kappa / \kappa_{\gamma=1} &\propto \gamma^{1.2} \quad (\gamma > 1). \end{aligned} \tag{2.75}$$

A square element for which $\gamma = 1$ gives the minimum value of κ for a given matrix size. If the aspect ratio significantly differs from 1, the conditioning deteriorates. This is because the magnitudes of elements in $\mathbf{D}_{LR}$ can be very different if $\gamma >> 1$ or $\gamma << 1$, e.g. [46].

Although these results are just for one example of the plate strip, a similar discussion holds for general problems. For a poorly conditioned eigenvalue problem, re-meshing of the FE model is needed. Decreasing the matrix size and using elements with $\gamma \approx 1$ to form similar magnitude of elements in $\mathbf{D}_{LR}$ are recommended to improve conditioning.

2.7.5 Relative Errors in the Eigenvalues and Eigenvectors

The relative errors in the eigenvalues and eigenvectors are discussed using various FE models. The relative errors in the propagating wavenumber associated with the i=1 wave mode are shown in Figure 2.15. The subscript WFE shows the predicted result using the WFE method. The results are shown for three FE models, which are the 18 element $\left(\Delta_x = \Delta_y = 10mm\right)$, 36 element $\left(\Delta_x = \Delta_y = 5mm\right)$ and 90 element $\left(\Delta_x = \Delta_y = 2mm\right)$ plate strip models. For the 90 element model, $k_x\Delta_x \approx 1$ around $\Omega = 900$. The peaks at the cut-off frequency $\left(\Omega = 1\right)$ occur because the denominator approaches 0 $\left(k_{x1} \to 0\right)$. The FE discretisation errors become smaller for the FE models with smaller values of Δ_x and Δ_y. However, the errors due to the round-off of inertia terms increase at low frequencies for very small Δ (i.e. the 90 element model). The relative errors in the eigenvector, the rotational displacement along the y-direction per unit displacement $\left(\theta_y / w\right)$, associated with the i=1 wave mode are shown in Figure 2.16. A trend similar to that for the eigenvalue can be seen.

The shear force is next evaluated using the SVD approach (2.67). The analytical expression for the shear force is [1]

$$\tau_{xz} / w = jDk_x\left(k_x^2 + \left(2-\nu\right)k_y^2\right) \tag{2.76}$$

where τ_{xz} is the shear force in the x-z plane. The relative errors in the calculated shear force per unit translational displacement $\left(\tau_{xz} / w\right)$ are shown in Figure 2.17. The relative errors associated with the 18 and 36 element models are similar to those for the wavenumbers and

eigenvectors. However, the error associated with the 90 element model is large because (1) $k_x\Delta_x$ is small such that $\lambda \approx 1$ in equation (2.50) which causes round-off errors in arithmetic calculations and (2) the matrix size is large such that round-off errors may accumulate. The relative error in the force components of the eigenvector is generally larger than that in the eigenvalue for a large matrix size.

The SVD approach for numerically determining the eigenvector was proposed in subsection 2.6.3. Figure 2.18 shows the relative errors in τ_{xz}/w using the original approach (2.62) and the SVD approach (2.67) for the 36 element model. It can be seen that the relative error associated with the SVD approach is generally smaller especially at low frequencies where round-off errors through the matrix operations in the original approach (2.62) are likely to occur.

2.7.6 Reducing Numerical Errors using Concatenating Elements

In Figure 2.17 the relative error associated with the 90 element model is large compared to other models at low frequencies. To reduce the error the conditioning using concatenating elements as described in section 2.5 can be used. Two strips of the FE model with 90 element $\left(\Delta_x = \Delta_y = 2mm\right)$ were concatenated in the direction of wave propagation to form a new FE model. Figure 2.19 shows the relative errors in τ_{xz}/w using the 90 element model and the concatenated model. The result using 90 rectangular elements $\left(\Delta_x = 4mm, \Delta_y = 2mm\right)$ is also shown. It can be seen that the model using the concatenating elements greatly improves the numerical error especially at low frequencies. The condition number of $\kappa\left(\tilde{\mathbf{D}}_{II}\right)$ may be of concern for the condensation and in this specific case $\kappa\left(\tilde{\mathbf{D}}_{II}\right) \approx O\left(10^{13}\right)$. Even for such large value of $\kappa\left(\tilde{\mathbf{D}}_{II}\right)$, it was observed that the relative error in τ_{xz}/w can be smaller. The relative error using the rectangular element model is large at both low and high frequencies compared to that using concatenating elements.

The approximate expression of the condensation was formulated in section 2.5.2. For the 90 element model, the maximum value of $K_{ii}/\omega^2 M_{ii}$ as a function of Ω is shown in Figure 2.20. The maximum value of $K_{ii}/\omega^2 M_{ii}$ is about 10^8 at $\Omega = 2$ such that the second order approximation (2.44) can be expected to be accurate enough for $\Omega < 2$ for the double precision calculation. Figure 2.21 compares the relative errors in τ_{xz}/w using the dynamic

condensation and the second order approximation. The result using the second order approximation is even better for small Ω . At high frequencies $\Omega > 2$, where $\max\left(K_{ii}/\omega^2 M_{ii}\right)$ become small, the relative error increases due to the second order approximation error.

2.8 Numerical Estimation of Group Velocity

The group velocity is an important wave property, for example when an application of SEA, e.g. [50], or the active control of a waveguide, e.g. [84], is of concern. In this section methods for numerically predicting the group velocity are illustrated. The accuracy of each method is evaluated for the plate strip with simply-supported edges.

2.8.1 Formulations

The group velocity is the velocity at which the energy propagates. The group velocity is defined by, e.g. [2,85],

$$c_g = \frac{\partial \omega}{\partial k}. \tag{2.77}$$

Three methods for numerically calculating the group velocity are described. Each method is shown and the accuracy is evaluated in the next subsection.

(1) Power and energy relationship

The group velocity can be calculated from the power and energy relationship [2] as

$$c_{g,i} = \frac{P_i}{E_{tot,i}} \tag{2.78}$$

where P_i is the time-averaged power transmission thorough the cross-section of a waveguide for the ith wave mode and E_{tot} is the total energy density per unit length. These values are given by [2,8]

$$P_i = \frac{1}{2}\mathrm{Re}\left\{\mathbf{f}_i^{\mathrm{H}}\dot{\mathbf{q}}_i\right\} = -\frac{\omega}{2}\mathrm{Im}\left\{\mathbf{f}_i^{\mathrm{H}}\mathbf{q}_i\right\} \tag{2.79}$$

and

$$\begin{aligned} &E_{tot,i} = E_{k,i} + E_{p,i}, \\ &E_{k,i} = \frac{1}{4\Delta}\mathrm{Re}\left\{\begin{bmatrix}\dot{\mathbf{q}}_i^{\mathrm{H}} & \lambda\dot{\mathbf{q}}_i^{\mathrm{H}}\end{bmatrix}\mathbf{M}\begin{bmatrix}\dot{\mathbf{q}}_i & \lambda\dot{\mathbf{q}}_i\end{bmatrix}\right\} = -\frac{\omega^2}{4\Delta}\mathrm{Re}\left\{\begin{bmatrix}\mathbf{q}_i^{\mathrm{H}} & \lambda\mathbf{q}_i^{\mathrm{H}}\end{bmatrix}\mathbf{M}\begin{bmatrix}\mathbf{q}_i & \lambda\mathbf{q}_i\end{bmatrix}\right\}, \\ &E_{p,i} = \frac{1}{4\Delta}\mathrm{Re}\left\{\begin{bmatrix}\mathbf{q}_i^{\mathrm{H}} & \lambda\mathbf{q}_i^{\mathrm{H}}\end{bmatrix}\mathbf{K}\begin{bmatrix}\mathbf{q}_i & \lambda\mathbf{q}_i\end{bmatrix}\right\} \end{aligned} \tag{2.80}$$

where $E_{k,i}$ and $E_{p,i}$ represent the kinetic and potential energy densities for the ith wave mode. The dissipated power follows from the imaginary part of **K** and/or the damping matrix **C**.

(2) Finite difference method

This method estimates the group velocity from a finite difference approximation such as

$$c_{g,i} = \frac{\Delta\omega}{\mathrm{Re}\left\{k_i\left(\omega + \Delta\omega/2\right)\right\} - \mathrm{Re}\left\{k_i\left(\omega - \Delta\omega/2\right)\right\}} \tag{2.81}$$

where $\Delta\omega$ is a sufficiently small increment of frequency. Equation (2.81) is formulated by the central finite difference (the second order approximation). Other definitions are possible, e.g. the first order forward or backward finite difference approximation [86].

(3) Differentiation of the eigenvalue problem

The group velocity may be determined directly by differentiating the eigenproblem [48]. The group velocity can be expressed as

$$c_g = \frac{\partial\omega}{\partial k} = \frac{1}{2\omega}\frac{\partial\omega^2}{\partial k} \tag{2.82}$$

and $\partial k/\partial\omega^2$ is found from the differentiation of the eigenvalue problem (2.14) such that

$$\frac{\partial}{\partial\left(\omega^2\right)}\left\{\left(\mathbf{T} - \lambda\mathbf{I}\right)\boldsymbol{\varphi}\right\} = \mathbf{0}. \tag{2.83}$$

Expanding equation (2.83), using equations (2.18), (2.82) and premultiplying by the left eigenvector $\boldsymbol{\psi}$ leads to

$$\boldsymbol{\psi}\left(\frac{\partial}{\partial\left(\omega^2\right)}\mathbf{T}+\frac{j\Delta}{2\omega}\lambda\frac{\partial k}{\partial\omega}\mathbf{I}\right)\boldsymbol{\varphi}=0\,. \tag{2.84}$$

Recalling equation (2.17), noting the differentiation of the matrix inverse [87] such that

$$\frac{\partial}{\partial\left(\omega^2\right)}\mathbf{D}_{LR}^{-1}=-\mathbf{D}_{LR}^{-1}\mathbf{M}_{LR}\mathbf{D}_{LR}^{-1}\,, \tag{2.85}$$

$\partial\mathbf{T}/\partial\left(\omega^2\right)$ in equation (2.84) can be evaluated as

$$\frac{\partial}{\partial\left(\omega^2\right)}\mathbf{T}=\begin{bmatrix}-\mathbf{D}_{LR}^{-1}\mathbf{M}_{LR}\mathbf{D}_{LR}^{-1}\mathbf{D}_{LL}+\mathbf{D}_{LR}^{-1}\mathbf{M}_{LL} & \mathbf{D}_{LR}^{-1}\mathbf{M}_{LR}\mathbf{D}_{LR}^{-1}\\ \mathbf{M}_{RL}-\mathbf{M}_{RR}\mathbf{D}_{LR}^{-1}\mathbf{D}_{LL}+ & \\ \mathbf{D}_{RR}\mathbf{D}_{LR}^{-1}\mathbf{M}_{LR}\mathbf{D}_{LR}^{-1}\mathbf{D}_{LL}-\mathbf{D}_{RR}\mathbf{D}_{LR}^{-1}\mathbf{M}_{LL} & \mathbf{M}_{RR}\mathbf{D}_{LR}^{-1}-\mathbf{D}_{RR}\mathbf{D}_{LR}^{-1}\mathbf{M}_{LR}\mathbf{D}_{LR}^{-1}\end{bmatrix}. \tag{2.86}$$

From the above equations the group velocity is given by

$$c_{g,i}=-\frac{j\Delta\lambda_i}{2\omega}\frac{\boldsymbol{\psi}_i\boldsymbol{\varphi}_i}{\boldsymbol{\psi}_i\dfrac{\partial}{\partial\left(\omega^2\right)}\mathbf{T}\boldsymbol{\varphi}_i}\,. \tag{2.87}$$

2.8.2 Numerical Example of the Plate Strip

The three formulations illustrated in the previous subsection are evaluated by estimating the group velocity of the plate strip considered in section 2.7. For the plate strip the wavenumbers are given by equation (2.69) and the group velocity for the *i*th wave mode is therefore analytically given as

$$c_{g,i}=\frac{\partial\omega}{\partial k_{xi}}=2\sqrt{\frac{D}{\rho h}}k_{xi}\quad,\quad\omega\geq\omega_{c,i}\,. \tag{2.88}$$

The group velocities are numerically determined using the three methods. The relative error in the group velocity associated with the i=1 wave mode is evaluated for the 18 element model and the results shown in Figure 2.22. A frequency increment of $\Delta\Omega = 7.5 \cdot 10^{-3}$ $\left(\Delta\omega = 2\pi\left[rad/s\right]\right)$ is chosen for the finite difference method.

On the whole, the power and energy relationship shows reasonable accuracy for the frequency range shown. The finite difference method also shows good accuracy but the error becomes large where the wavenumber rapidly changes. The accuracy of the finite difference method depends on the value of $\Delta\Omega$ and small $\Delta\Omega$ generally gives more accurate results. However, too small $\Delta\Omega$ can cause significant round-off errors in calculating equation (2.81) as an example can be seen in [70].

The result from differentiation of the eigenvalue problem has poor accuracy. This is because $\mathbf{D}_{LR}^{-1}$ in equation (2.86) can be poorly conditioned and numerical errors are likely to accumulate through the many matrix operations. The differentiation of the eigenvalue problem could therefore be inappropriate for general problems where the matrix can be ill-conditioned.

As a result, either use of the power and energy relationship or the finite difference method could be recommended. When both the eigenvalues and eigenvectors are accurately calculated, the power and energy relationship seems an appropriate approach. The approach is also typically reliable for damped waveguides, e.g. [88].

2.9 Conclusions

The WFE method starts from the dynamic stiffness matrix of a short section of a waveguide which can be formed using conventional FEA and commercial FE packages. The eigenvalue problem using the transfer matrix can be formed from the elements of the dynamic stiffness matrix in conjunction with the periodicity condition. An illustrative example was shown for the Euler-Bernoulli beam. Causes of numerical errors occurring in the WFE results, i.e. FE discretisation error and error due to the round-off of inertia terms, were discussed. There is a trade-off between these two causes and the method using concatenating elements followed by condensation was proposed to alleviate this compromise. Approximate expressions for the dynamic condensation were derived to reduce the calculation cost.

For general problems, conditioning of the eigenvalue problem is of concern and this was also discussed. The eigenvalue problem of the transfer matrix was reformulated using Zhong's method. An application of SVD was proposed to reduce numerical errors in determining the eigenvectors. The conditioning problem was illustrated using an example of the plate strip. The effects of the size and the aspect ratio of elements on the conditioning were also shown to give a guideline for the meshing of an FE model. It was seen that the method using concatenating elements can greatly improve numerical errors in the WFE results, in particular, for general problems.

Three methods for numerically estimating the group velocity were described, i.e. the power and energy relationship, the finite difference method and the differentiation of the eigenvalue problem. The accuracies of these methods were shown using the example of the plate strip with simply-supported edges. A method using the power and energy relationship is recommended with respect to accuracy and calculation cost.

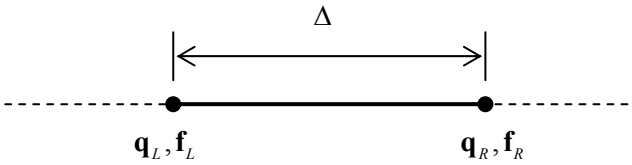

Figure 2.1: A section of a uniform waveguide.

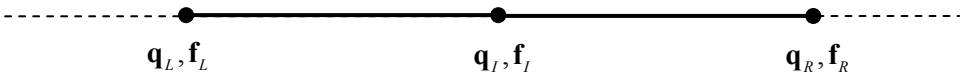

Figure 2.2: A section with an internal node.

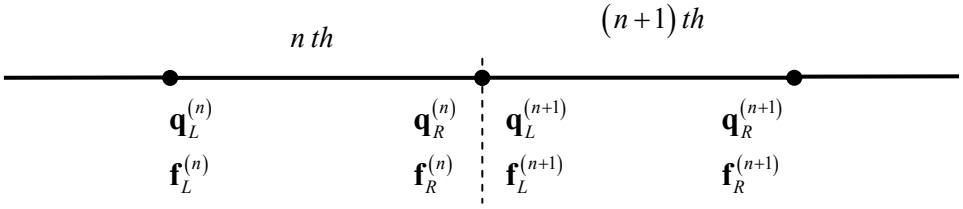

Figure 2.3: A series of sections.

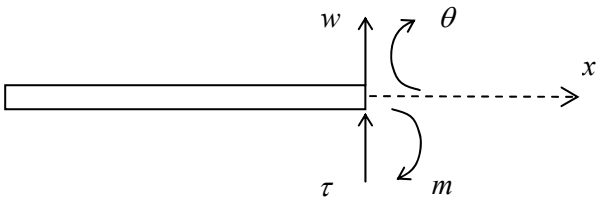

Figure 2.4: Sign convention of an Euler-Bernoulli beam.

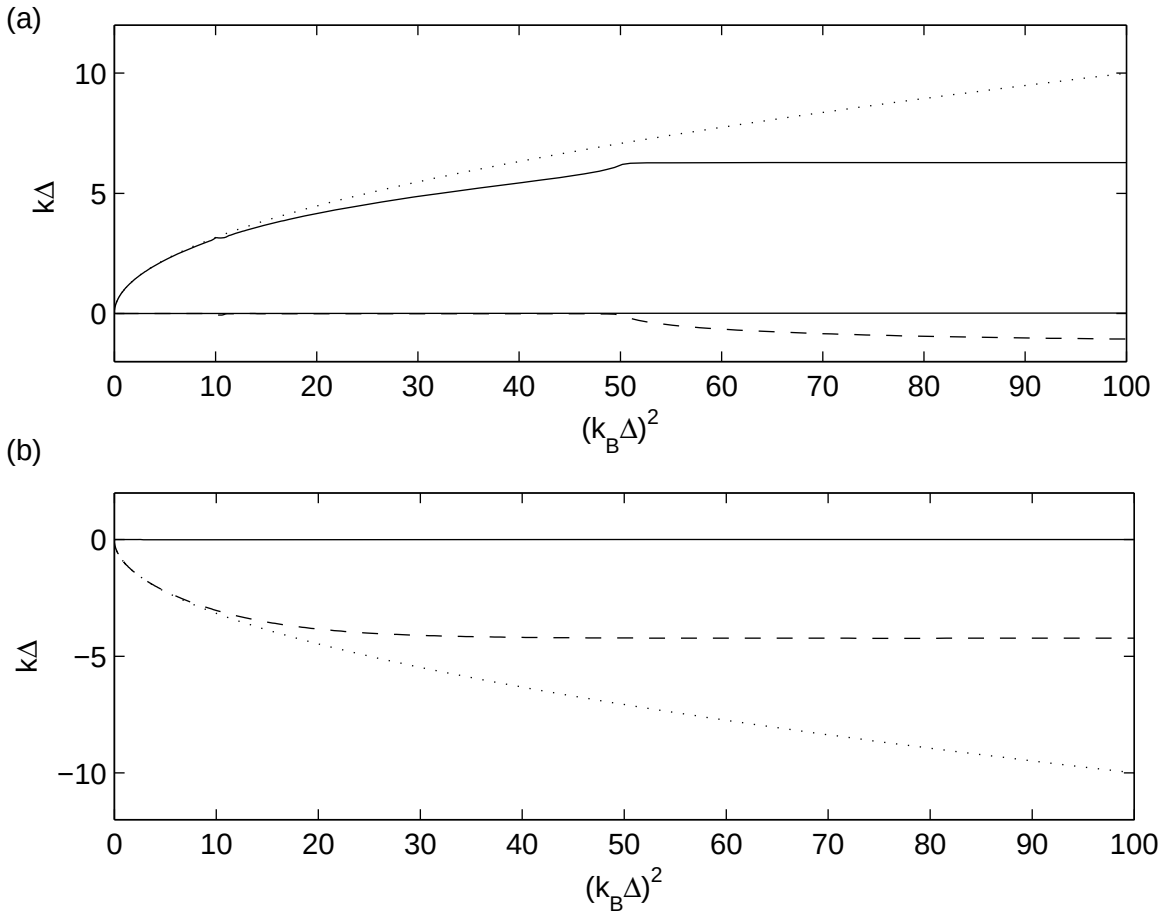

Figure 2.5: Predicted wavenumbers for the beam: (a) the propagating wave; (b) the nearfield wave; — real part, −− imaginary part, ···· analytical solution.

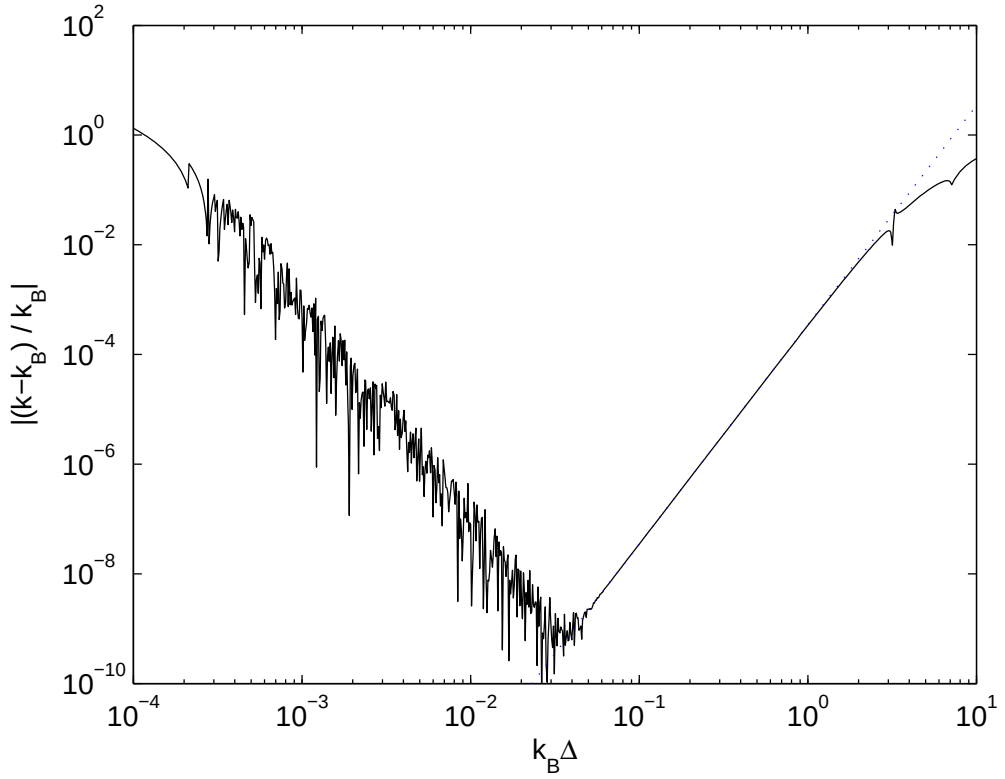

Figure 2.6: Relative error in the propagation wavenumber of the beam; ···· $(k\Delta)^4/2880$.

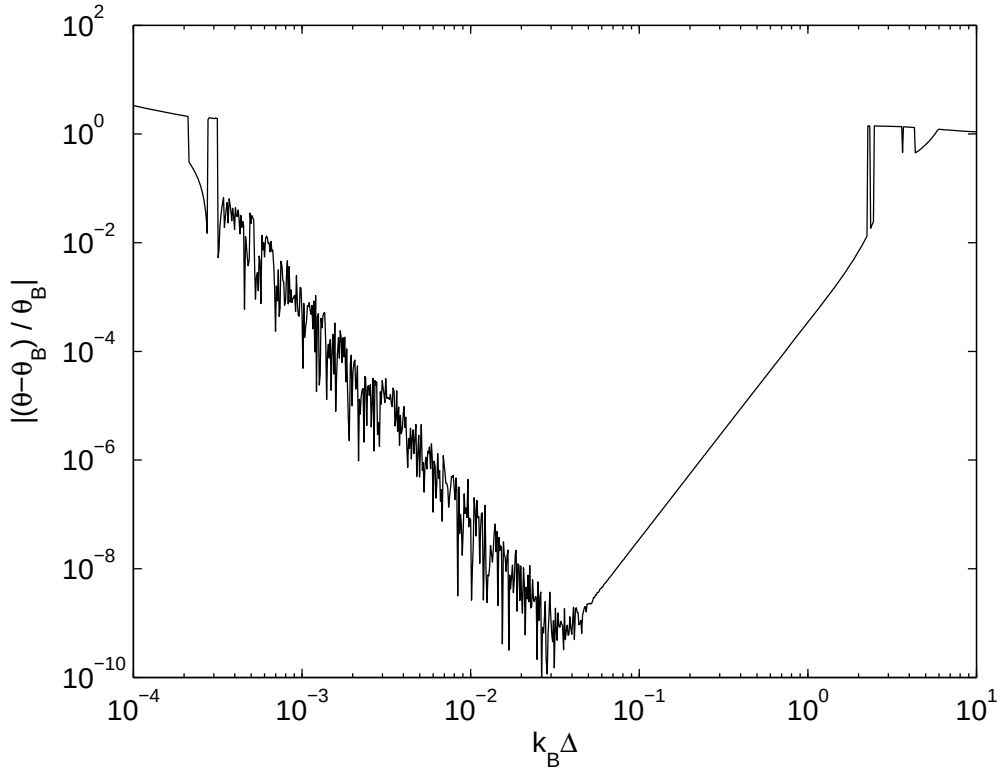

Figure 2.7: Relative error in θ_B *of the beam.*

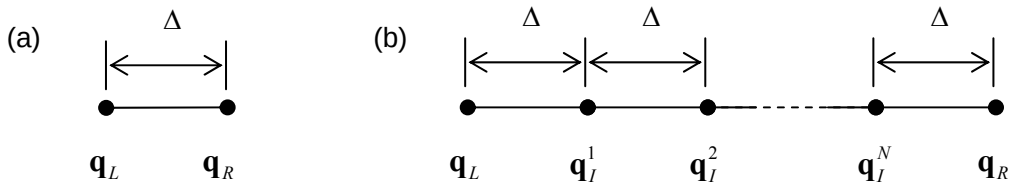

Figure 2.8: (a) Single element; (b) concatenated elements.

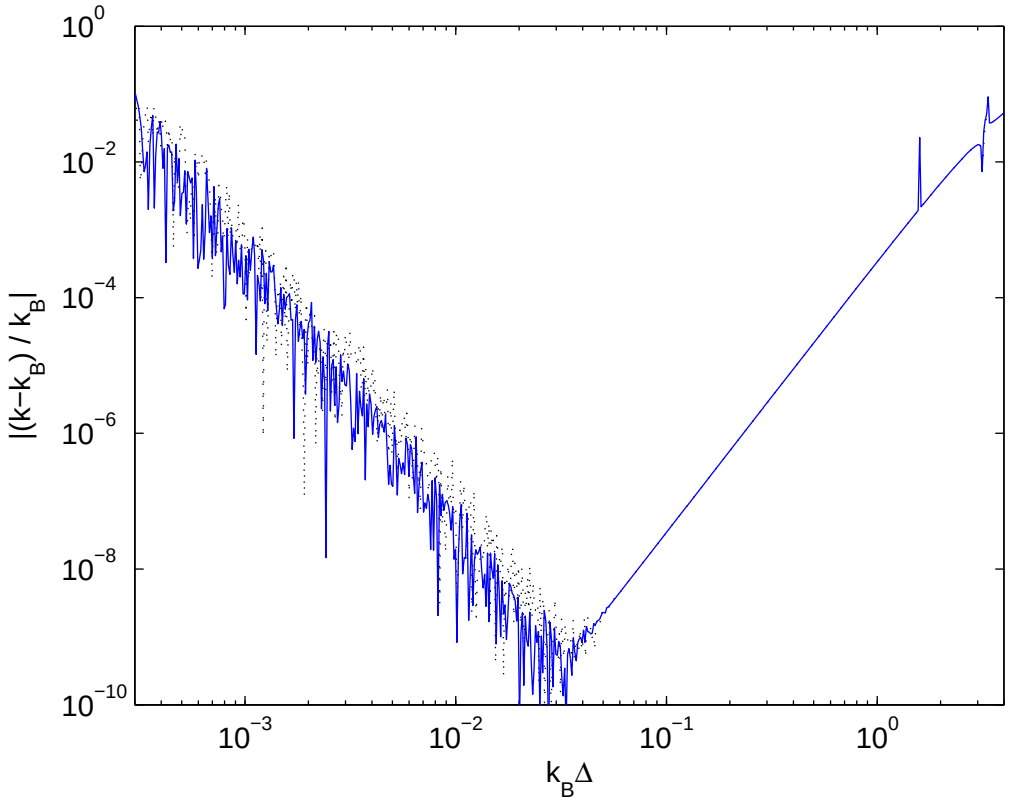

Figure 2.9: Relative error in the propagation wavenumber of the beam: — using one concatenated element; ···· using one element.

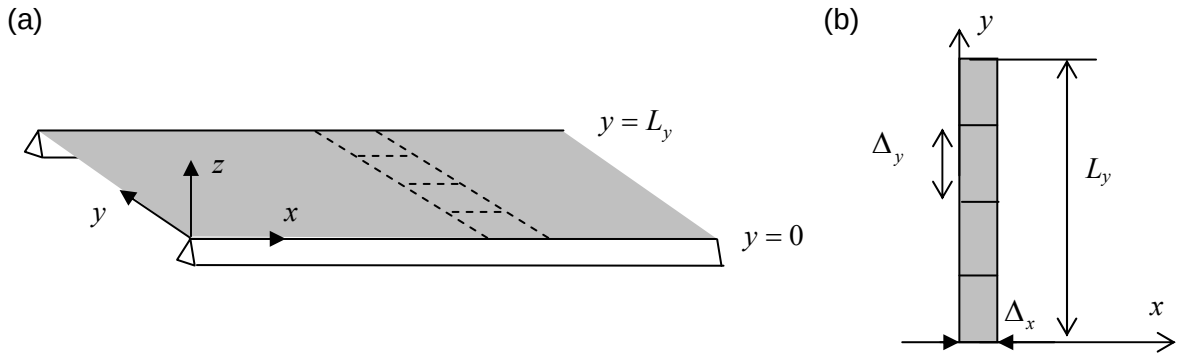

Figure 2.10: (a) Plate strip with simply-supported boundaries; (b) 4 *element model.*

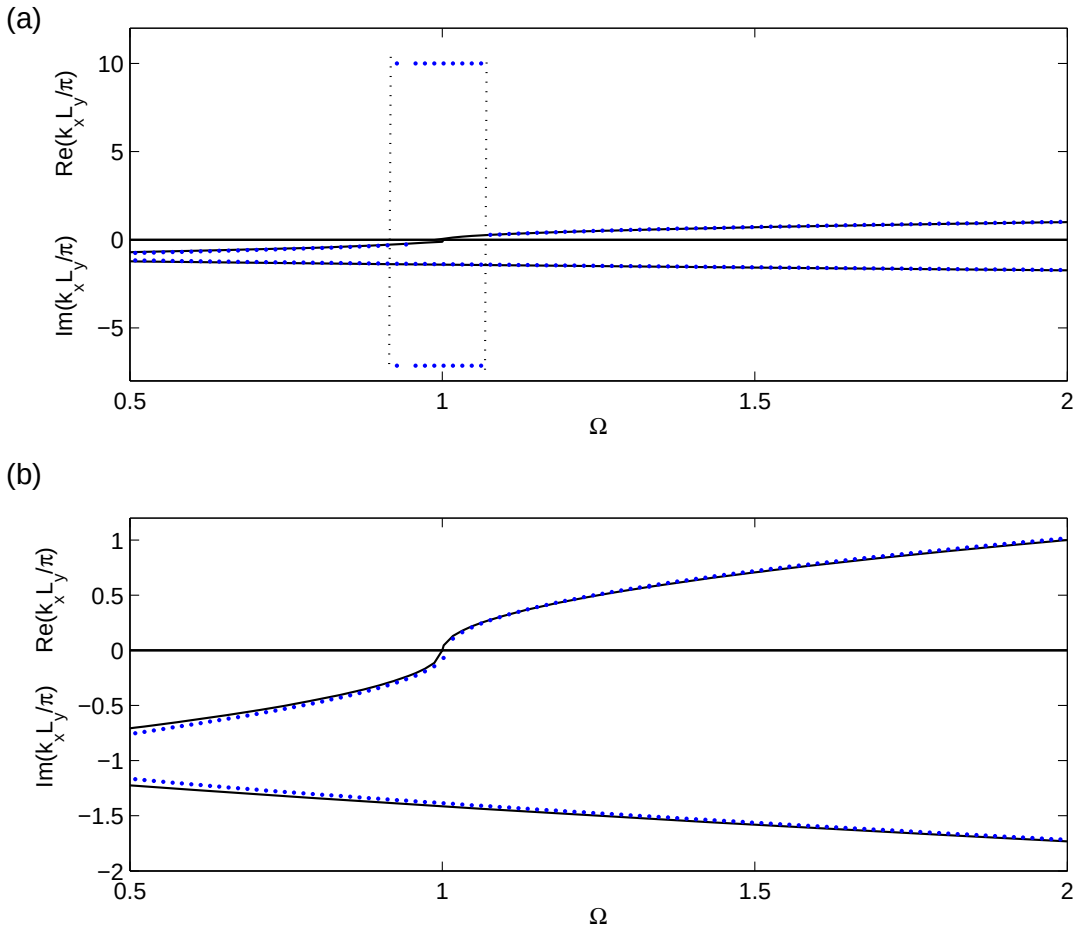

Figure 2.11: Flexural waves in a plate strip with simply-supported edges. Dispersion curves: — analytical solution; ···· the WFE result using (a) the transfer matrix approach; (b) the conditioned eigenvalue problem.

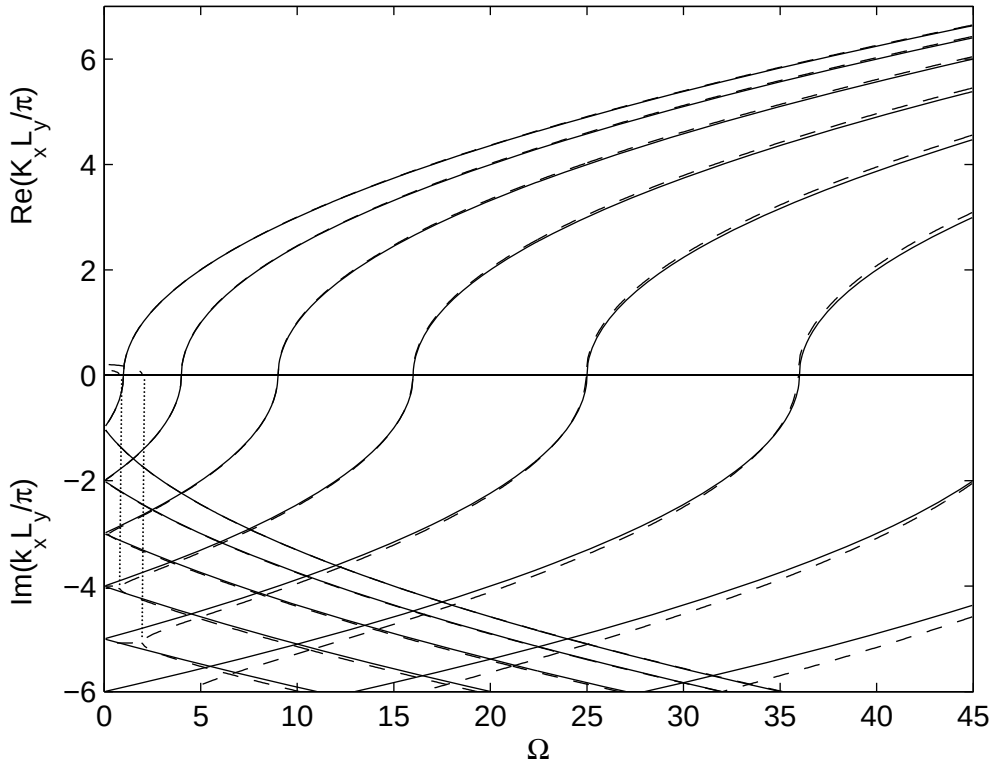

Figure 2.12: Flexural waves in a plate strip with simply-supported edges. Dispersion curves using the 18 *element plate strip* $\left(\Delta_x = \Delta_y = 10mm\right)$*: — analytical solution, – – WFE result.*

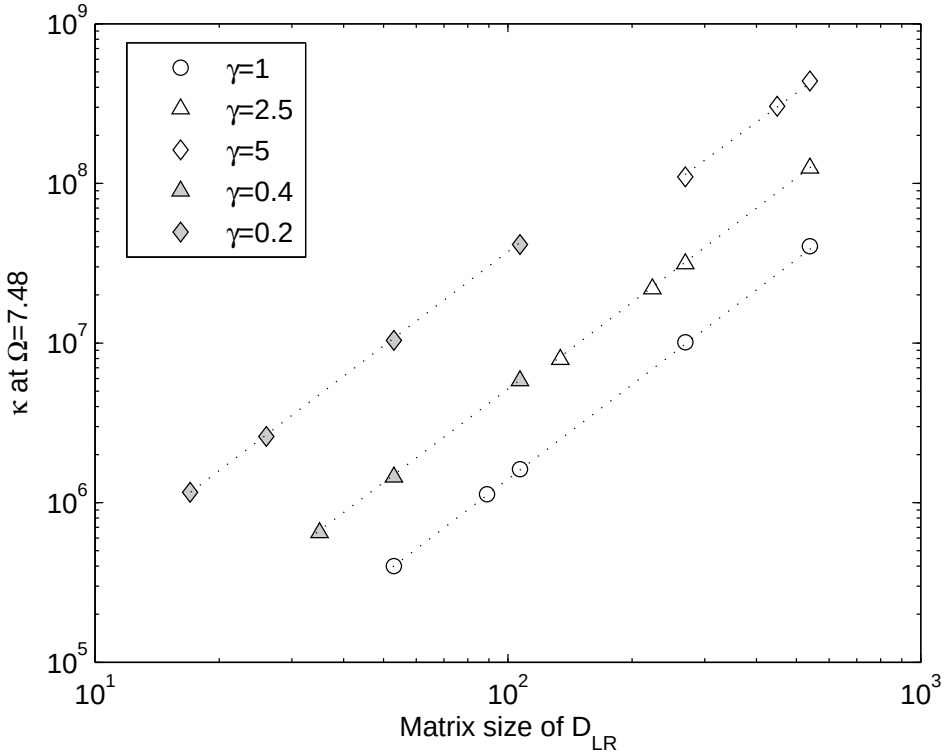

Figure 2.13: Condition numbers $\kappa\left(\mathbf{D}_{LR}\right)$ *as a function of a matrix size.*

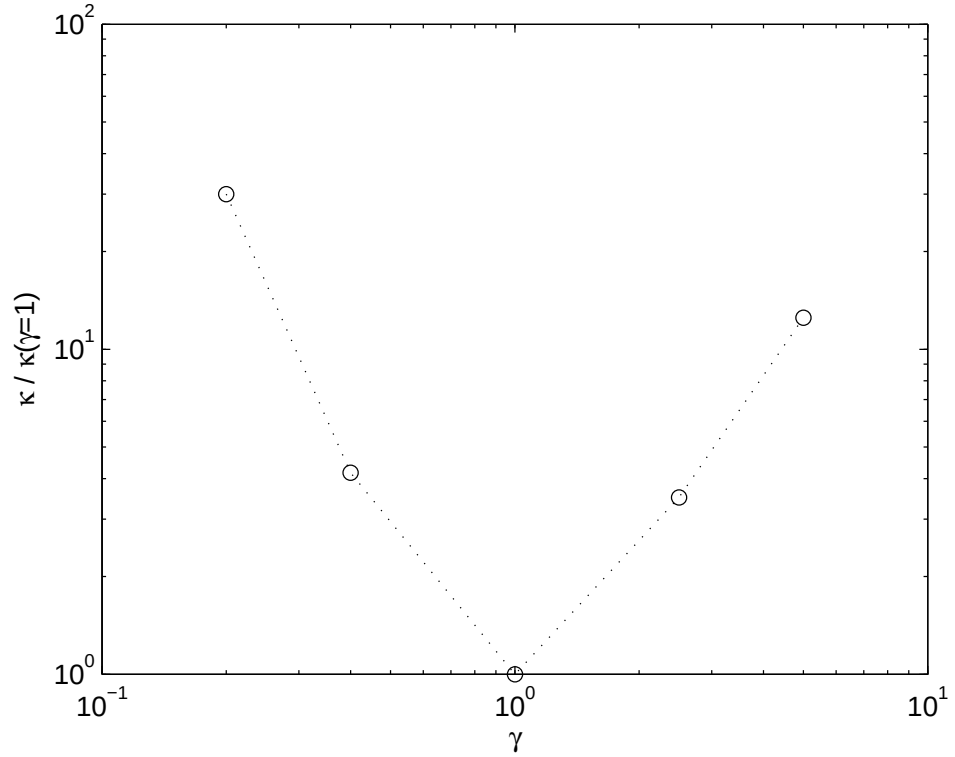

Figure 2.14: Ratio of κ for the same matrix size as a function of the aspect ratio of an element.

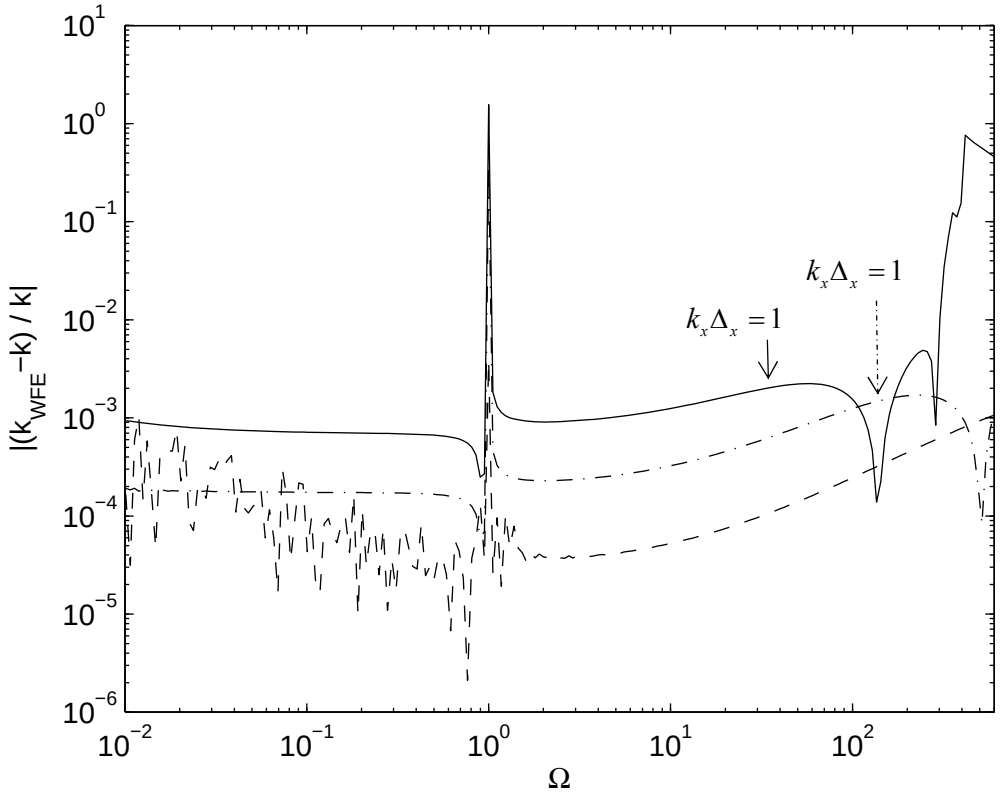

Figure 2.15: Relative errors in the wavenumber for the i=1 *wave mode: — the* 18 *element; –·– 36 element; – – 90 element plate strip model with simply-supported edges.*

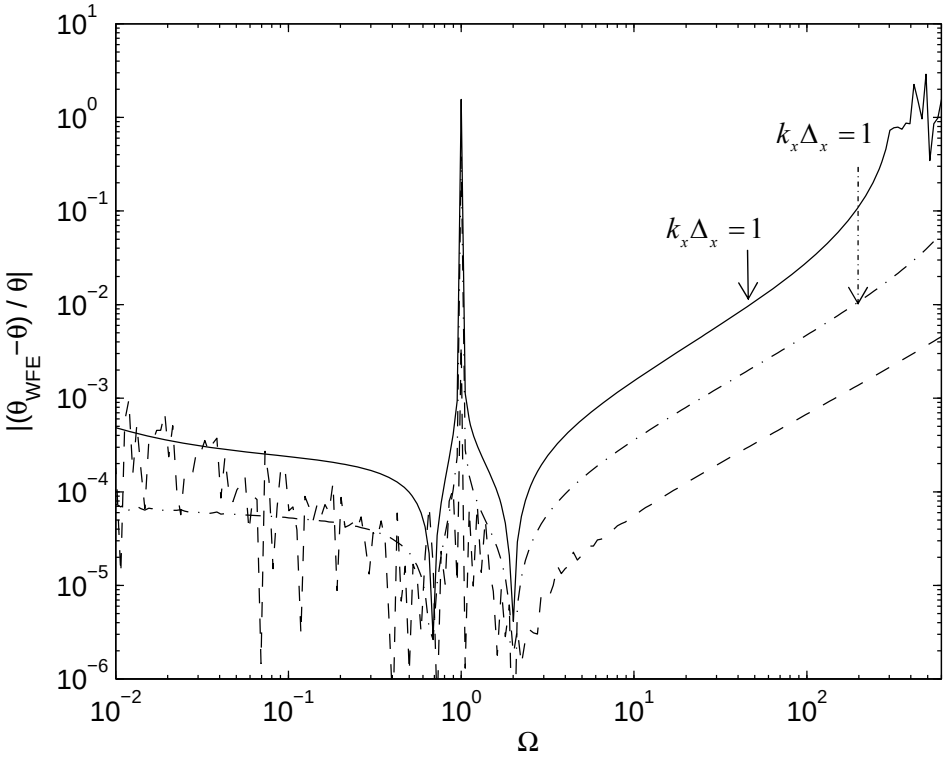

Figure 2.16: Relative errors in θ_y / w for the plate strip with simply-supported edges. Notation is same as Figure 2.15.

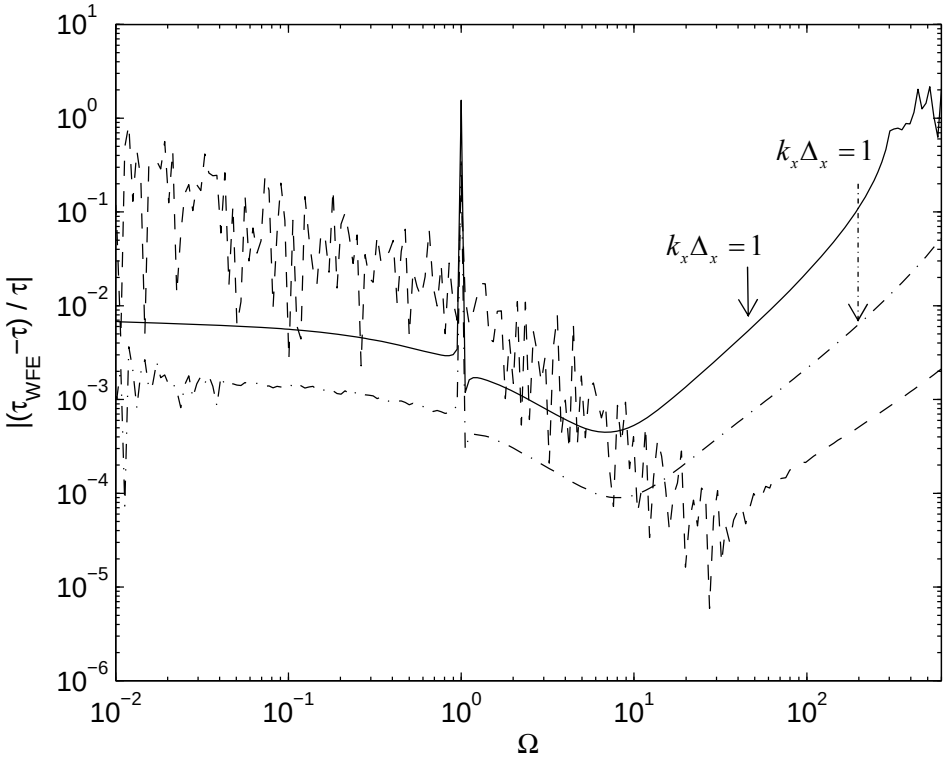

Figure 2.17: Relative errors in τ_{xz} / w for the plate strip with simply-supported edges. Notation is same as Figure 2.15.

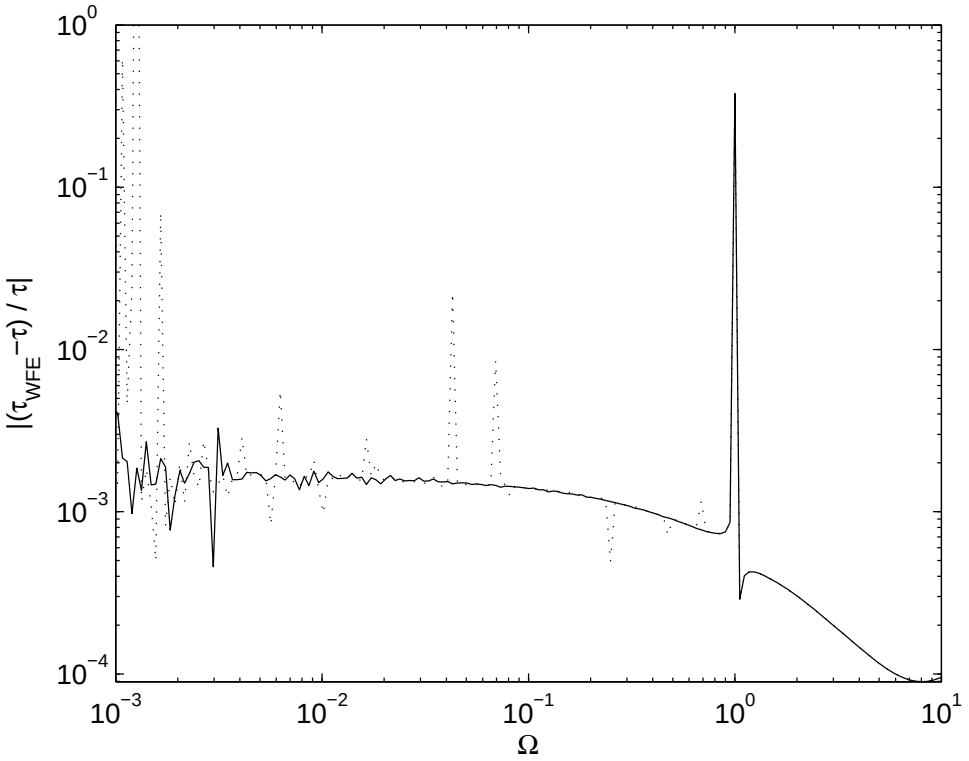

Figure 2.18: Relative errors in τ_{xz}/w for the plate strip with simply-supported edges: — the SVD approach; ····· the original approach.

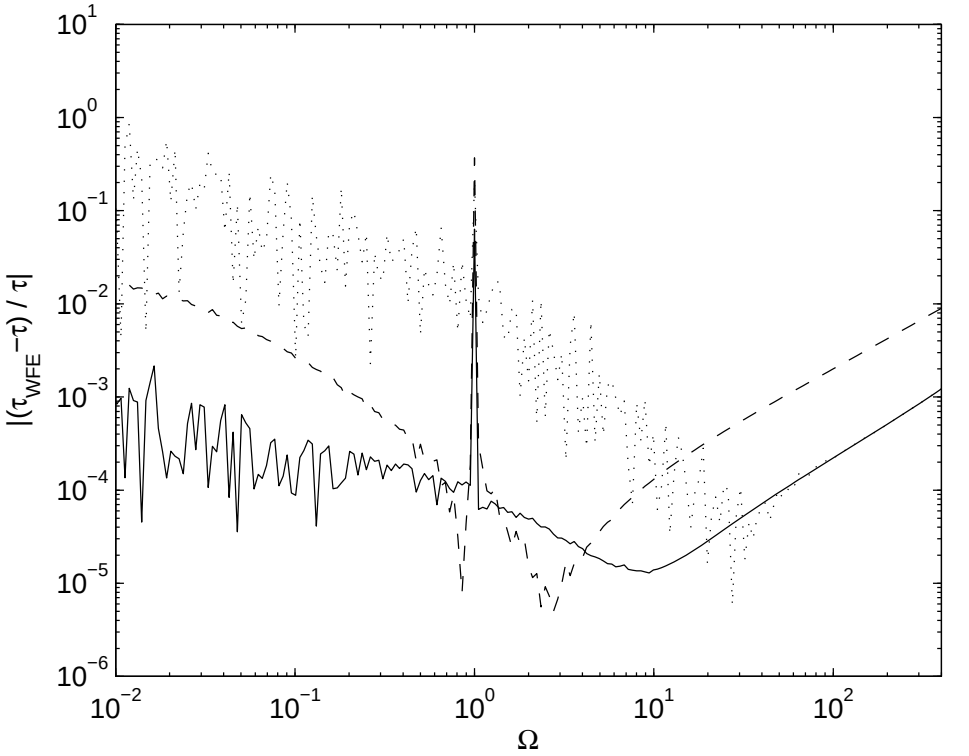

Figure 2.19: Relative errors in τ_{xz}/w for the plate strip with simply-supported edges: ····· the FE model with 90 elements; — the concatenated FE model; – – rectangular FE model.

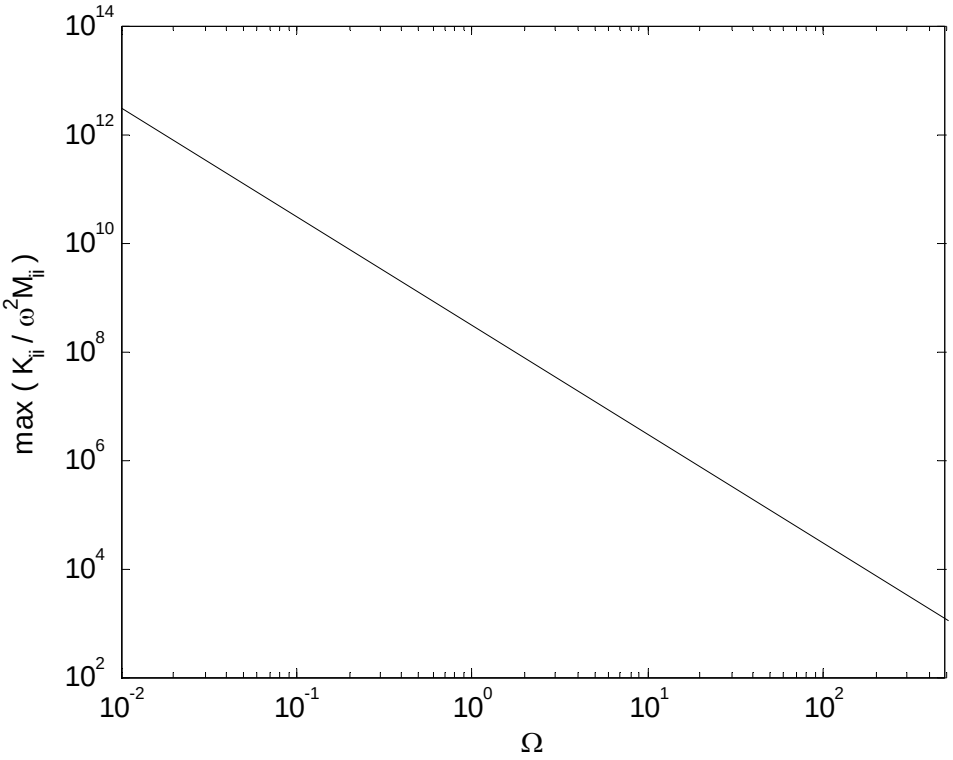

Figure 2.20: Maximum value of $K_{ii}/\omega^2 M_{ii}$ as a function of Ω for the 90 element model of the plate strip with simply-supported edges.

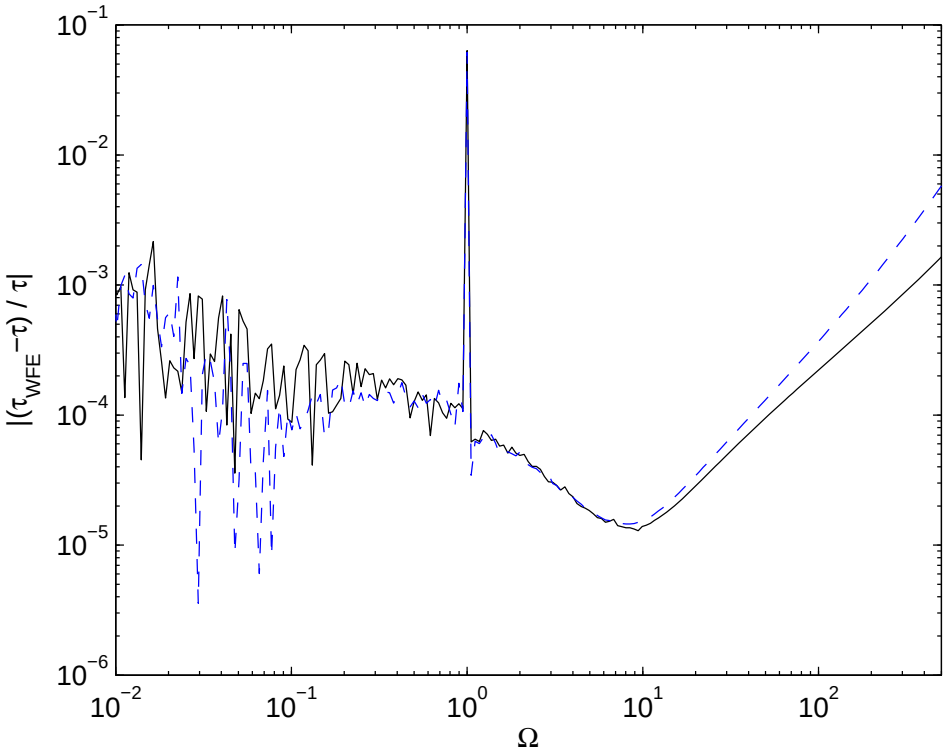

Figure 2.21: Relative errors in τ_{xz}/w for the plate strip with simply-supported edges: — dynamic condensation; – – the second order approximation.

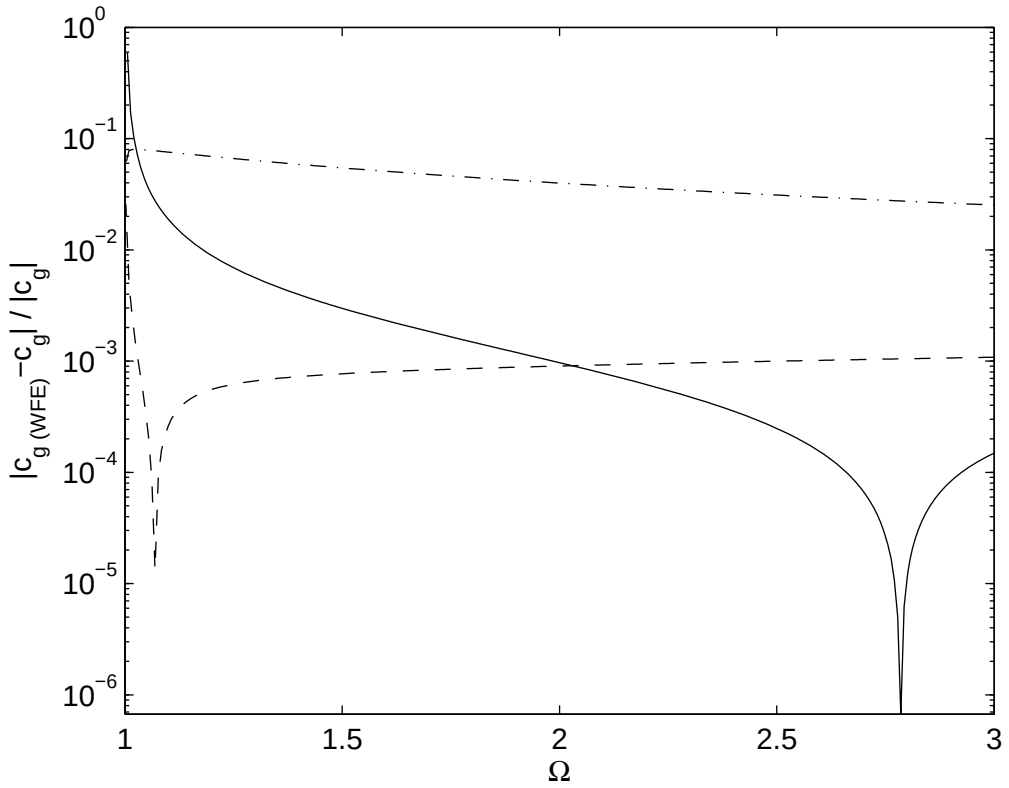

Figure 2.22: Relative errors in the estimates of the group velocity associated with the i=1 *wave mode in the plate strip with simply-supported edges: — power and energy relationship; – – finite difference; –·– differentiation of the eigenproblem.*

Chapter 3
APPLICATION TO COMPLICATED STRUCTURES

3.1 Introduction

In this chapter, the WFE method described in chapter 2 is applied to determine free wave propagation characteristics in more complex structures. Complexities of waveguides are gradually increasing. Freely propagating waves in plate strips, a ring and cylindrical strips are considered. The WFE results are compared with analytical solutions or numerical solutions to analytical dispersion equations. There are two aims for this chapter. The first is to investigate the accuracy of the WFE predictions for more complicated structures. The second is to estimate the dispersion relations for situations in which analytical dispersions are difficult or impossible to obtain.

Complicated dispersion curves with such phenomena as curve veering, non-zero cut-off phenomena and bifurcations are illustrated. In-plane waves in plate strips are first analysed. Plate strips with mixed and free boundaries are considered. A method of decomposition of the power is introduced to reduce the size of matrices. Free flexural wave propagation in a plate strip with free boundaries is shown next including purely real, purely imaginary and complex wavenumbers. Predicted results are used to give initial estimates of solutions to a transcendental analytical dispersion equation, where numerical solutions are found to compare with the WFE results.

Freely propagating waves in a ring are then considered. The WFE modelling for curved structures used in this thesis is described. Free wave propagation in cylindrical strips is also considered. For cylindrical strips, waves in both the axial and the circumferential directions are described. The decomposition of the power is used to investigate wave characteristics. No damping is assumed throughout this chapter.

3.2 Qualitative Features of Dispersion Curves

Complicated dispersion curves are illustrated in this chapter. Before presenting such dispersion curves some examples of qualitative behaviour of the wavenumbers, which will be shown in the successive sections, are described in this section. Figure 3.1 shows the behaviour of the wavenumbers associated with various phenomena in the complex *k*-plane in a particular frequency range. In the figures, the arrows represent the behaviour of the wavenumbers as frequency increases. The positive- and negative-going waves are illustrated and they exist in pairs for uniform waveguides. Although such an indication of the behaviour in the complex *k*-plane may not be common, it is helpful to understand behaviour of wavenumbers.

For the undamped beam described in chapter 2, the magnitudes of the four wavenumbers increase as shown in Figure 3.1(a). Two are real representing propagating waves, while the other two are imaginary representing evanescent waves. For the plate strip with simply-supported boundaries, the wavenumbers are imaginary at $\omega = 0$ and the magnitudes of two wavenumbers increase while the other two decrease as shown in Figure 3.1(b). Two wavenumbers become real at its cut-off frequency.

The wavenumbers may be initially complex (conjugates) as shown in Figures 3.1(c) and (d). The imaginary parts of the four complex wavenumbers may become zero with frequency as shown in Figure 3.1(c). This is the non-zero cut-on phenomena and four propagating waves cut-on at the cut-off frequency with non-zero real wavenumbers. The magnitudes of two real wavenumbers increase with frequency and those of the other two decrease. The wave for which the magnitude of real wavenumber decreases with frequency has a negative group velocity, i.e. although the phase velocity is positive the energy propagates in the negative direction.

Alternatively the real parts of complex wavenumbers may become zero instead as shown in Figure 3.1(d) and all the wavenumbers then become imaginary. The magnitudes of two imaginary wavenumbers increase while the other two decrease in the same manner as Figure 3.1(b).

3.3 In-plane Waves in a Plate Strip with Mixed Edges

In this section in-plane waves in a plate strip whose edges have mixed boundary conditions, e.g. [1], are considered. Longitudinal and shear wave modes are described.

3.3.1 Analytical Dispersion Equation

Consider a plate strip as shown in Figure 3.2. If the plane strain condition holds across the plate thickness, the governing equations for in-plane motion of a plate strip can be conveniently expressed in terms of potentials [1] such that

$$\begin{aligned}\left(\frac{\partial^2}{\partial x^2}+\frac{\partial^2}{\partial y^2}\right)H_1 &= \frac{1}{c_L^2}\frac{\partial^2}{\partial t^2}H_1,\\ \left(\frac{\partial^2}{\partial x^2}+\frac{\partial^2}{\partial y^2}\right)H_2 &= \frac{1}{c_s^2}\frac{\partial^2}{\partial t^2}H_2\end{aligned} \tag{3.1}$$

are the wave equations where H_1 and H_2 are potentials and

$$\begin{aligned}c_L &= \sqrt{E/\rho\left(1-\nu^2\right)},\\ c_S &= \sqrt{G/\rho}\end{aligned} \tag{3.2}$$

are the phase velocity associated with the longitudinal and shear waves respectively and G is the shear modulus.. The displacements are expressed by [1]

$$\begin{aligned}u &= \frac{\partial H_1}{\partial x}+\frac{\partial H_2}{\partial y},\\ v &= \frac{\partial H_1}{\partial y}-\frac{\partial H_2}{\partial x}\end{aligned} \tag{3.3}$$

where u,v are the displacements in the x- and y-directions. Trial functions are assumed for the potentials such that the displacements and stresses can be obtained [1]. The in-plane displacements in the plate strip can in general be expressed as [1]

$$\begin{aligned} u &= j\left\{k_x\left(A\sin\alpha y + B\cos\alpha y\right) + \beta\left(C\cos\beta y - D\sin\beta y\right)\right\}e^{-jk_x x}, \\ v &= \left\{\alpha\left(A\cos\alpha y - B\sin\alpha y\right) + k_x\left(C\sin\beta y + D\cos\beta y\right)\right\}e^{-jk_x x} \end{aligned} \tag{3.4}$$

where

$$\begin{aligned} \alpha^2 &= \frac{\omega^2}{c_L^2} - {k_x}^2, \\ \beta^2 &= \frac{\omega^2}{c_S^2} - {k_x}^2 \end{aligned} \tag{3.5}$$

and A, B, C and D in equation (3.4) are constant. Various boundary conditions can be applied along the edges $y = \pm b$.

Along the edges $y = \pm b$, the mixed boundary conditions [1] are given by

$$\begin{aligned} &v = 0, \\ &\tau_{xy} = G\left(\frac{\partial u}{\partial y} + \frac{\partial v}{\partial x}\right) = 0. \end{aligned} \tag{3.6}$$

After substituting the boundary conditions (3.6) into equations (3.4) and writing the equations in matrix form in terms of the constants A, B, C and D, the determinant of the matrix gives analytical solutions to the dispersion equations such that [1]

$$\begin{aligned} k_x^2 &= \frac{\omega^2}{c_L^2} - \frac{m^2\pi^2}{4b^2}, \\ k_x^2 &= \frac{\omega^2}{c_S^2} - \frac{n^2\pi^2}{4b^2}. \end{aligned} \tag{3.7}$$

The first equation of (3.7) is the analytical dispersion equation for the longitudinal wave $\left(m = 0,1,2\cdots\right)$ and the second is for the shear wave $\left(n = 1,2\cdots\right)$. The m=0 wave mode is such that the x-wise motion across the plate strip has the same amplitude and is in phase. The wave mode is a rigid body motion at $\omega = 0$. The m=1 and n=1 wave modes are associated with the half sine or cosine motion across the plate strip and higher wave modes are associated with higher order shapes across the plate strip [1]. The cut-off frequencies are given by equations (3.7) with $k_x = 0$ such that

$$\begin{aligned} \omega_{c,m} &= \frac{m\pi}{2b} c_L, \\ \omega_{c,n} &= \frac{n\pi}{2b} c_S. \end{aligned} \tag{3.8}$$

The group velocities associated with the longitudinal and shear waves are

$$\begin{aligned} c_{g,m} &= c_L \sqrt{1 - \frac{\omega_{c,m}^2}{\omega^2}} \quad \left(\omega \geq \omega_{c,m}\right), \\ c_{g,n} &= c_S \sqrt{1 - \frac{\omega_{c,n}^2}{\omega^2}} \quad \left(\omega \geq \omega_{c,n}\right). \end{aligned} \tag{3.9}$$

3.3.2 WFE Results

Freely propagating in-plane waves in the plate strip are predicted using the WFE method. The material properties and the dimensions such as the plate width, $2b = 0.18\,(\mathrm{m})$, were the same as those described in subsection 2.7.2 for the simply-supported condition. 36 elements $\left(\Delta_x = \Delta_y = 5mm\right)$ were used across the plate strip. The DOFs associated with out-of-plane motion and the DOFs which are zero because of the boundary condition were removed. For the in-plane waves in a plate strip, the DOFs associated with θ_z ('drilling stiffness DOFs') were also removed to improve conditioning.

The dispersion curves of both the analytical solutions (3.7) and the WFE results are shown in Figure 3.3. The abscissa represents non-dimensional frequency

$$\Omega = \omega / \omega_{c,n=1} \tag{3.10}$$

and the cut-off frequencies occur at $\Omega = 1, 2, \cdots$ for the shear wave modes and $\Omega = \left(c_L / c_S\right) \times 0, 1, 2, \cdots \approx 1.7 \times 0, 1, 2, \cdots$ for the longitudinal wave modes. The ordinate denotes the non-dimensional wavenumber

$$\xi = 2k_x b / \pi \tag{3.11}$$

and wavenumbers for the *m*th and *n*th wave modes become $-jm$ and $-jn$ at $\Omega = 0$. The value of $\xi = 4$ is such that $k_x\Delta_x = 0.35$ and $k_y\Delta_y = 0.43$ for the *n*=5 wave mode. In the frequency range of interest, three longitudinal and six shear wave modes cut-on. Good agreement can be seen between the analytical solutions and the WFE results especially at low frequencies and for lower $|\xi|$.

The group velocities calculated using the power and energy relationship are shown in Figure 3.4 for the first two longitudinal (*m*=0,1) and shear wave (*n*=1,2) modes. The ordinate represents the non-dimensional group velocity normalised by c_S such that the group velocities of the shear wave modes tend to 1 while those of the longitudinal wave modes tend to $c_L/c_S \approx 1.7$ as frequency increases. Good agreement can be seen.

3.3.3 Decomposition of Power

It is of interest to determine how much power in a given wave mode is associated with each variable. This enables characteristics of a wave mode to be determined. It is also useful to determine the power to assist in selecting DOFs which might be removed or condensed. For the WFE results shown in the previous subsection, the DOFs associated with θ_z were removed. The smaller size of the matrix and removing matrix elements with largely different magnitudes in general improve conditioning. However, determination of those DOFs that can be removed or condensed is in general difficult. In this subsection a method of decomposition of the power is proposed.

The power associated with each wave mode can be numerically determined by $P = \frac{1}{2}\mathrm{Re}\left\{\mathbf{f}^{\mathrm{H}}\dot{\mathbf{q}}\right\}$ as shown in section 2.8. The value of $\mathbf{f}^{\mathrm{H}}\mathbf{q}$ is a summation of the product of f^{H} and q for each DOF. If the value of $f^{\mathrm{H}}q$ is nearly zero for a propagating wave, such a DOF can be considered to be less significant. Alternatively, $\mathbf{f}^{\mathrm{H}}\mathbf{q}$ can be expressed as

$$\mathbf{f}^{\mathrm{H}}\mathbf{q} = \sum_i \mathbf{f}_{q_i}^{\mathrm{H}}\mathbf{q}_{q_i} \tag{3.12}$$

where the subscript q_i denotes a group of DOFs associated with a certain variable such as u, v and θ_z. The value of $\mathbf{f}_{q_i}^{\mathrm{H}}\mathbf{q}_{q_i}$ could represent them to what extent each variable contributes to the total power.

Figure 3.5 shows examples of the power decomposition for the *m*=0 and *n*=1 wave modes. The normalised power, $\mathbf{f}_{q_i}^{\mathrm{H}}\mathbf{q}_{q_i}\big/\mathbf{f}^{\mathrm{H}}\mathbf{q}$, is plotted for $q_i = u$, v and θ_z. For the *m*=0 wave mode, the wave motion is dominated by only the longitudinal motion, u. The other two variables give powers that are of the order of machine precision and are very small. For the *n*=1 (shear) wave mode, u and v are both significant in the frequency range shown. However, the power associated with θ_z is again very small. The values of $\mathbf{f}_{\theta_z}^{\mathrm{H}}\mathbf{q}_{\theta_z}\big/\mathbf{f}^{\mathrm{H}}\mathbf{q}$ are very small also for higher wave modes. This implies that the DOFs associated with θ_z can be removed or condensed from the original dynamic stiffness matrix since they contribute to wave motions insignificantly. The reduction can be used if off-diagonal terms of the element matrices between the DOFs to be reduced and the other DOFs are zero. In other cases the dynamic condensation is recommended. For the element matrices formed in ANSYS, the off-diagonal terms between u, v and θ_z were zero such that DOFs associated with θ_z can be removed.

3.4 In-plane Waves in a Plate Strip with Free Edges

In this section freely propagating in-plane waves in a plate strip with free edges are considered. The analytical dispersion equations are called the Rayleigh-Lamb frequency equations, e.g. [1,89,90]. The analytical dispersion equations are transcendental such that roots must be found numerically. The WFE results are used to predict the wavenumbers. These predictions are used as initial estimates for numerical solutions to the analytical dispersion equations so that the accuracy of the WFE results can be investigated. Muller's method [91] is used to find numerical solutions to the analytical equations.

3.4.1 Analytical Dispersion Equations

Consider the plate strip shown in Figure 3.2. The free boundary conditions along the plate edges, $y = \pm b$, are

$$\begin{aligned} \sigma_y &= 0, \\ \tau_{xy} &= 0 \end{aligned} \tag{3.13}$$

where σ_y is the normal stress in the *y*-direction. The analytical dispersion equations can be derived in the same manner as that for the mixed boundary condition and are [1]

$$\frac{\tan \beta b}{\tan \alpha b} = -\left\{ \frac{4\alpha\beta k_x^{\,2}}{\left(k_x^{\,2} - \beta^2\right)^2} \right\}^{\pm 1} \tag{3.14}$$

where +1 corresponds to symmetric waves and −1 corresponds to asymmetric waves and where α and β are defined by equations (3.5). These equations are transcendental and must be solved numerically. The cut-off frequencies for $k_x = 0$ are given by equations (3.8), i.e. the same as the mixed boundary condition. For the free boundary condition, however, the *n*=0 wave mode can propagate such that $m, n = 0, 1, 2 \cdots$.

3.4.2 Dispersion Curves

The plate strip was modelled in the same way as described in subsection 2.7.2 in which the material properties are also given. The number of elements was 90 $\left(\Delta_x = \Delta_y = 2mm\right)$. The DOFs associated with *u* and *v* were retained and the resulting number of DOFs was 364. Free wave propagation was predicted using the WFE method and the WFE results were also used to give initial estimates for numerical solutions to the analytical equations (3.14).

The wavenumbers can be purely real, purely imaginary or complex. To find numerical solutions to the analytical dispersion equation Muller's method [91] or the argument principle [92] may be used. These methods are described in Appendix 2. Muller's method is an interpolation method that uses quadratic interpolation. A complex root is found using a quadratic equation that passes through three points in the vicinity of an initial estimate. The method can be used to give numerical solutions with relatively cheap calculation cost when the initial estimates are close to the desired solutions. An alternative is the argument principle. This is related to the residue theorem and the number of roots in a region of the complex plane can be found by calculating the Cauchy integral along a contour enclosing the

initial estimate. In this subsection, Muller's method is used to give numerical estimates to the analytical equations (3.14). The argument principle is used in the next section.

Dispersion curves for the plate strip with free edges are shown in Figures 3.6 and 3.7. Figure 3.6 shows the purely real and purely imaginary wavenumbers. In the figure, A_i or S_i represents the asymmetric or the symmetric waves for the ith mode. Figure 3.7 shows the complex conjugate wavenumbers and A_{ij} or S_{ij} represents the asymmetric or symmetric wave mode associated with the i and jth pair of wave modes. The WFE results show very good agreement with numerical solutions to the analytical equations. Several important phenomena can be observed such as (1) curve veering, (2) non-zero cut-on and a corresponding negative phase velocity and (3) bifurcations from complex conjugate wavenumbers to two different purely imaginary wavenumbers. These are described in the next subsection.

3.4.3 Physical Interpretation of Behaviour of Wavenumbers

Curve veering occurs when two wave modes in the wave domain are not orthogonal to each other. The veering phenomena has been observed in many applications, e.g. [9397]. It can be seen that the dispersion curves for the symmetric and the asymmetric waves can cross each other but the dispersion curves for the symmetric waves never cross those for other symmetric waves due to veering. The same is true for the asymmetric waves. All the longitudinal wave modes change to shear wave modes at high enough frequencies and the phase speeds asymptote to that of the shear wave. It should be noted that the phase speeds of the first two waves, the S_0 and A_0 waves, however, approach that of the Rayleigh wave [98]. The Rayleigh wave is characterised by the displacements near free edges being large.

The displacements of the A_0 and A_1 wave modes at different frequencies are shown in Figure 3.8. It should be noted that the y-wise motion is $\pi/2$ out of phase from the x-wise motion. The wave mode in general changes with frequency especially when curve veering is observed. The A_0 wave mode can propagate over all frequencies. For the A_0 wave mode the plate strip deforms with transverse shear motion as shown in Figure 3.8(a). Displacements near the edges for the A_0 wave mode become large at high frequencies as shown in Figure 3.8(b). The deformation, mainly in the longitudinal direction, is large only near the edges so that the wave mode approaches to the Rayleigh wave. Figure 3.8(c) shows the displacement

of the A_1 wave mode at its cut-off frequency, $\Omega = 1$. The shape of the A_1 wave mode also varies with frequency as shown in Figure 3.8(d).

Non-zero cut-on phenomena can be seen at $\Omega \approx 1.59, 2.95$. The wavenumbers change with frequency in the manner depicted in Figure 3.1(c), i.e. complex conjugate wavenumbers become two real wavenumbers at the cut-off frequency. Bifurcations from complex conjugate wavenumbers to two imaginary wavenumbers are observed at $\Omega \approx 3.96, 4.76$. Such behaviour was illustrated in Figure 3.1(d). Figure 3.9 shows the loci of two wavenumbers against frequency in the complex ξ-plane. In Figure 3.9(a) complex conjugate wavenumbers (one of the wavenumbers with $\mathrm{Im}(\xi)>0$ is suppressed) become two purely real non-zero wavenumbers at $\Omega = 1.59$. One of the real wavenumbers increases while another decreases. The latter becomes purely imaginary at $\Omega = 1.70$ and the magnitude increases up to $\Omega = 1.82$. The magnitude then starts decreasing and the wavenumber becomes 0 at $\Omega = 1.99$ above which the wave propagates. Figure 3.9(b) represents the bifurcation around $\Omega = 3.96$ where two imaginary wavenumbers arise. Complex conjugate wavenumbers (one of the wavenumber with negative $\mathrm{Re}(\xi)$ is suppressed) become purely imaginary non-zero wavenumbers. The magnitude of one of the wavenumbers increases while that of another decreases. The former then cuts-on at $\Omega = 4.00$. The magnitude of the latter increases up to $\Omega = 4.23$ then starts decreasing. The wavenumber becomes 0 at $\Omega = 5.1$ and the wave starts propagating.

Figure 3.10 magnifies the dispersion curves around the non-zero cut-off of the S_1, S_2 wave modes at around $\Omega = 1.59$. The S_1 wave has a bifurcation at point A and has a negative group velocity on the curve between points A and B. It should be noted that such a wave has a positive phase velocity but a negative group velocity. The positive-going wave has a positive group velocity but may have a negative phase velocity.

The group velocities predicted using the power and energy relationship are shown in Figure 3.11 for the symmetric wave modes and in Figure 3.12 for the asymmetric wave modes. The group velocities are normalised with respect to the shear wave speed and the longitudinal wave speed is such that $c_L/c_S \approx 1.7$. The group velocities of the S_0 and A_0 wave modes asymptote to that of the Rayleigh wave [89] which is $c_R = 0.928c_S$ for $\nu = 0.3$ [2]. The group velocities of the other waves asymptote to that of the shear wave, c_S, at high enough frequencies.

3.5 Flexural Waves in a Plate Strip with Free Edges

Free flexural waves in a plate strip with simply-supported edges were described in section 2.7. Free flexural waves in a plate strip with free edges are considered in this section. In the literature, approximate solutions for the flexural vibration of a plate with free edges were determined using beam functions [99,100]. Waves propagating along the free edge, termed flexural Rayleigh edge waves, were discussed in [101105]. In particular, free wave propagation in a plate strip with free edges was described in [106] but only for propagating waves. The complete dispersion diagram including attenuating waves cannot be found in the literature to the author's knowledge. The analytical dispersion equation is transcendental [106] and the solutions can be complex. The argument principle [92] was used to give numerical solutions of the analytical dispersion equation, using the WFE results as initial estimates, to compare the WFE results with those to the analytical dispersion equation. Outcome of this section has been presented in [72].

3.5.1 Analytical Dispersion Equation

Consider the same plate strip shown in Figure 3.2. The out-of-plane displacement of the plate strip can be expressed as [106]

$$w(x,y) = e^{-jk_x x}\left\{a^{+}e^{-jk_{yP}y} + a^{-}e^{+jk_{yP}y} + a_N^{+}e^{-k_{yN}(b+y)} + a_N^{-}e^{-k_{yN}(b-y)}\right\} \tag{3.15}$$

where $a^{\pm}$, $a_N^{\pm}$ are wave amplitudes,

$$\begin{aligned} k_{yP} &= \sqrt{\gamma^2 - k_x^2}, \\ k_{yN} &= \sqrt{\gamma^2 + k_x^2} \end{aligned} \tag{3.16}$$

and

$$\gamma^2 = \sqrt{\rho h \omega^2 / D}\,. \tag{3.17}$$

The free boundary condition along the edges, $y = \pm b$, are such that both the shear force and moment are zero [1]

$$\begin{aligned}\frac{\partial^3 w}{\partial y^3}+(2-\nu)\frac{\partial^3 w}{\partial x^2\partial y}&=0,\\ \frac{\partial^2 w}{\partial y^2}+\nu\frac{\partial^2 w}{\partial x^2}&=0.\end{aligned} \tag{3.18}$$

The first term contains the information about the shear force combined with the twisting moment (i.e. the Kirchhoff shear force [1]) and the second term gives the bending moment. Substituting the boundary conditions (3.18) into equation (3.15) gives

$$\begin{bmatrix} \mu_1 e^{-jk_{yP}b} & \mu_1 e^{jk_{yP}b} & -\mu_2 e^{-2k_{yN}b} & -\mu_2 \\ \mu_1 e^{jk_{yP}b} & \mu_1 e^{-jk_{yP}b} & -\mu_2 & -\mu_2 e^{-2k_{yN}b} \\ jk_{yP}\mu_2 e^{-jk_{yP}b} & -jk_{yP}\mu_2 e^{jk_{yP}b} & -k_{yN}\mu_1 e^{-2k_{yN}b} & k_{yN}\mu_1 \\ jk_{yP}\mu_2 e^{jk_{yP}b} & -jk_{yP}\mu_2 e^{-jk_{yP}b} & -k_{yN}\mu_1 & k_{yN}\mu_1 e^{-2k_{yN}b} \end{bmatrix} \begin{bmatrix} a^+ \\ a^- \\ a_N^+ \\ a_N^- \end{bmatrix} = \begin{bmatrix} 0 \\ 0 \\ 0 \\ 0 \end{bmatrix} \tag{3.19}$$

where

$$\begin{aligned}\mu_1&=\gamma^2-(1-\nu)k_x^2,\\ \mu_2&=\gamma^2+(1-\nu)k_x^2.\end{aligned} \tag{3.20}$$

The analytical dispersion equation is derived by setting the determinant of the matrix (3.19) to zero such that, after some calculations,

$$\left(\frac{k_{yP}\mu_2^2}{k_{yN}\mu_1^2}-\frac{k_{yN}\mu_1^2}{k_{yP}\mu_2^2}\right)\sin\left(2k_{yP}b\right)\sinh\left(2k_{yN}b\right)+2\cos\left(2k_{yP}b\right)\cosh\left(2k_{yN}b\right)-2=0\,. \tag{3.21}$$

This expression, separated into symmetric and asymmetric motions, was described in [106].

3.5.2 Purely Real Wavenumbers

The same plate strip model used for predicting in-plane waves in section 3.4 was used. The number of elements across the plate strip was 90 $\left(\Delta_x=\Delta_y=2mm\right)$ and the DOFs associated with in-plane motions were removed. The resulting number of DOFs was 546. The argument principle [92] was used to find numerical solutions to equation (3.21) with the WFE results being used as initial estimates. A criterion for the convergence was set to be within 0.1%

relative accuracy for both the real and imaginary parts of the wavenumbers k_x or within 0.01 if the magnitude of either $\mathrm{Re}(k_x)$ or $\mathrm{Im}(k_x)$ is less than 0.01.

Figure 3.13 shows the dispersion curves for purely real wavenumbers. The abscissa is non-dimensional frequency

$$\Omega = \frac{4b^2}{\pi^2}\sqrt{\frac{\rho h}{D}}\omega . \tag{3.22}$$

The cut-off frequencies occur when $\Omega_{c,n} = \left\{0, 0, 1.51^2, 2.50^2, (2n+1)^2/4\cdots\right\}$ $(n = 3,4,5\cdots)$ [106]. The ordinate is the normalized wavenumber

$$\xi = 2bk_x/\pi . \tag{3.23}$$

The WFE results agree very well with numerical solutions to the analytical dispersion equation. The wave modes can be categorised into symmetric and asymmetric motions, represented by S_i and A_i $(i = 0,1,2\cdots)$ respectively. For each wave mode, there are two waves associated with the same wave mode; one is for a wave which propagates at high frequencies and another is for a nearfield wave. Two wave modes associated with rigid body motions cut-on at $\Omega = 0$. One is the symmetric mode (S_0) and the other is the asymmetric mode (A_0). They broadly represent translational (S_0) and rotational (A_0) motions of the cross-section and bending and twisting wave modes respectively. The first six wave modes at $\Omega = 37.4$ are illustrated in Figure 3.14. The wave modes change with frequency. Figure 3.15 shows the wave modes for the S_0 and A_0 modes at different frequencies. It can be seen that the displacements change with frequency especially near the plate strip edge.

The group velocities are shown in Figure 3.16. The group velocity is normalised with respect to that of the longitudinal wave, c_L. The group velocities are similar to those for the simply-supported edges except that the S_0 and A_0 wave modes. Referring to equations (2.88) and (3.2), $c_g/c_L \approx \sqrt{h\omega/c_L}$ for $\omega >> \omega_c$ and asymptotes to $\sqrt{\omega}$ at enough high frequencies.

3.5.3 Complex and Purely Imaginary Wavenumbers

The dispersion curves for purely imaginary and complex wavenumbers are shown in Figure 3.17. Only the wavenumbers with relatively small value of $\left|\mathrm{Im}\left(\xi\right)\right|$ are shown. Figure 3.17(a) shows the dispersion curves for the symmetric wave modes and 3.17(b) for the asymmetric wave modes. The frequencies where a pair of purely imaginary wavenumbers bifurcates into a complex conjugate pair or vice versa are denoted by the dotted lines. The results using the WFE method show very good agreement with numerical solutions to the analytical dispersion equation.

Complex conjugate wavenumbers occur when two different wavenumbers get close and their wave modes in the wave domain are not orthogonal. Consider two wave modes S_i, S_j $\left(i<j\right)$. When $i\geq 1, j\geq 2$ and $j=i+1$ (e.g. $S_{1,2}$ in Figure 3.17(a)), the two wave modes are associated with the complex conjugate wavenumber pairs at low frequencies (e.g. $\Omega<3.1$). As frequency increases, the complex conjugate wavenumbers become two different purely imaginary wavenumbers at the bifurcation point (e.g. $\Omega=3.1$). Above the bifurcation point the imaginary part of the S_i wave mode increases and is a rapidly decaying wave while that of the S_j wave mode decreases (e.g. $3.1<\Omega<4.3$). Eventually the propagating wave mode cuts-on at its cut-on frequency (e.g. $\Omega>12.3$). The behaviour of the wavenumbers of the positive-going waves in the complex ξ-plane is illustrated in Figure 3.18(a).

Another case occurs for the two wave modes S_i, S_j with $i\geq 0, j\geq 2$ and $j\geq i+2$ (e.g. the $S_{0,2}$ wave mode). At very low frequencies, the wavenumbers associated with both the S_i and S_j wave modes may be purely imaginary (with different wavenumbers, e.g. $3.1<\Omega<4.3$). At the bifurcation point two pure imaginary wavenumbers become a complex conjugate pair (e.g. $\Omega=4.3$). The complex conjugate wavenumbers again become purely imaginary at another bifurcation point (e.g. $\Omega=5.2$). Above the bifurcation point, the same behaviour as that described in the previous case ($j=i+1$) is observed. This phenomenon in the complex ξ-plane is illustrated in Figure 3.18(b).

The same discussion holds for the asymmetric wave modes, A_i, A_j. It should be noted that such phenomena occur only when both wave types are symmetric or asymmetric. Since the symmetric and asymmetric wave modes are orthogonal to each other in the wave domain, they are uncoupled.

The shapes of the wave modes change rapidly around the bifurcation points. The wave modes indicated by i,ii,⋯,v in Figure 3.17(a) are illustrated in Figure 3.19. The wave modes below the bifurcation point $\Omega = 4.3$ are associated with the S_0 and S_2 wave modes (Figure 3.19(a)). At transition frequencies, $4.3 < \Omega < 5.2$, the wavenumbers are complex and elements of the associated wave modes are also complex. That is, the displacements and forces are complex values, i.e. of the form $\alpha \pm j\beta$ or $\pm\alpha + j\beta$, associated with the complex conjugate wavenumber pairs. The real and imaginary parts of the displacements associated with the complex conjugate wavenumbers are therefore shown in Figure 3.19(b). The displacements were normalised such that the displacements are in the form $\alpha \pm j\beta$. Above the other bifurcation point $\Omega = 5.2$, the two wave modes are similar to their original shapes (Figure 3.19(c)).

The change of the S_2 wave mode is now described. At low frequencies where the S_2 wave mode is associated with purely imaginary ξ, antinodes are located around $y = 0, \pm 0.66b$ (Figure 3.19(a)). At the transition frequencies where the wavenumber ξ becomes complex, antinodes are observed along $y = 0, \pm b$ and also $y = \pm 0.64b$ with phase difference (Figure 3.19(b)). The wavenumber again becomes purely imaginary above the transition frequencies and antinodes are observed along $y = 0, \pm 0.6b, \pm b$ (Figure 3.19(c)). Above the cut-off frequency where the S_2 wave mode propagates with purely real wavenumber, the antinodes are along $y = 0, \pm 0.53b, \pm b$ with the maximum displacement being at the edges of the plate strip, $y = \pm b$ as shown in Figure 3.14(a).

3.6 Waves in a Ring

In this section, freely propagating waves in a thin ring are considered. FE modelling of a curved structure is discussed. The WFE results are compared with analytical solutions. Coupling between the wave modes due to curvature is described.

3.6.1 Analytical Expressions

The analytical dispersion equation for a ring as shown in Figure 3.20 is derived. In the figure R is the mean radius of the ring, r, s are the axes of the coordinates and w and u are the translational displacements in the r- and s-directions.

According to Flugge's theory [107,108], the equation of motion is

$$\begin{aligned} -EA\gamma^2\left(\frac{\partial^4 w}{\partial s^4}+\frac{2}{R^2}\frac{\partial^2 w}{\partial s^2}+\frac{w}{R^4}\right)-\frac{EA}{R}\left(\frac{w}{R}+\frac{\partial u}{\partial s}\right)&=\rho A\frac{\partial^2 w}{\partial t^2},\\ EA\left(\frac{\partial^2 u}{\partial s^2}+\frac{1}{R}\frac{\partial w}{\partial s}\right)&=\rho A\frac{\partial^2 u}{\partial t^2}\end{aligned} \tag{3.24}$$

where $\gamma=\sqrt{I/A}$ is the radius of gyration of the cross-section of the ring. Substituting the translational displacements

$$\begin{aligned} w&=C_w e^{-jks}e^{j\omega t},\\ u&=C_u e^{-jks}e^{j\omega t}\end{aligned} \tag{3.25}$$

into equation (3.24) gives

$$\begin{bmatrix} \frac{\gamma^2}{R^2}\left(k^2R^2-1\right)^2+1-k_{L1}^2R^2 & -jkR \\ jkR & k^2R^2-k_{L1}^2R^2 \end{bmatrix}\begin{bmatrix} C_w \\ C_u \end{bmatrix}=\begin{bmatrix} 0 \\ 0 \end{bmatrix} \tag{3.26}$$

where $k_{L1}^2=\rho\omega^2/E$ is the quasi-longitudinal wavenumber [1]. The analytical dispersion equation can be obtained by setting the determinant of the matrix (3.26) to zero and is [109]

$$k^6-\left(k_{L1}^2+2\kappa^2\right)k^4+\left(\kappa^4-k_B^4+2\kappa^2k_{L1}^2\right)k^2-\left(\kappa^4k_{L1}^2+\kappa^2k_B^4-k_{L1}^2k_B^4\right)=0 \tag{3.27}$$

where $\kappa=1/R$ is the curvature and $k_B^4=\rho A\omega^2/EI$ is the bending wavenumber for a straight beam. The cubic frequency equation (3.27) can be solved analytically [110]. For the limiting case $\kappa\to 0$, equation (3.27) becomes

$$\left(k^2-k_{L1}^2\right)\left(k^2-k_B^2\right)\left(k^2+k_B^2\right)=0 \tag{3.28}$$

such that the resulting wavenumbers are same as those in a straight Euler-Bernoulli beam.

The ring frequency for the curved beam, ω_{rb}, is determined from equation (3.27) for $k = 0$ such that

$$\omega_{rb} = c_{L1}\kappa\sqrt{1+\gamma^2\kappa^2} \tag{3.29}$$

where $c_{L1} = \sqrt{E/\rho}$ is the phase speed of the quasi-longitudinal wave. The waves approach those of a straight beam above the ring frequency and curvature typically affects wave behaviours for $\omega < \omega_{rb}$ [1,11,107]. As $\omega \to 0$, the wavenumbers asymptote to

$$k = 0, \quad k = \pm 1/R \tag{3.30}$$

and there are two non-zero wavenumbers. For $k = \pm 1/R$, the wavelength is $\lambda = 2\pi R$ and these describe the rigid body motion of the ring.

3.6.2 WFE Modelling of Curved Structures

There are several ways to model curved structures using conventional FE. The most common approach is to use many small flat (straight) elements to represent the curvature of structures. This approach is used in this thesis.

For general FEA curved elements may be used instead, e.g. [77]. However, curved elements may not be available for general elements such as shell or solid elements due to effects such as the locking problem [111]. The use of mid-side nodes elements is an alternative but some numerical problems are reported although the reasons are not fully understood in terms of the application of the mid-side node elements to the analysis of the wave propagation [69,112]. If the conditioning is not a matter, single element can be used by rotating its local coordinates at both ends [65].

Flat or straight elements are therefore used to model curved structures in this thesis. For the ring, two, straight, thin beam elements can be connected with their local coordinates being rotated through an angle $\Delta\phi\left(=\Delta s/R\right)$ (rad) as shown in Figure 3.21. The DOFs associated with internal nodes can be dynamically condensed in the same manner as that described in subsections 2.2.1 and 2.5.2. This WFE modelling using the internal nodes can

improve the conditioning at low frequencies as described in chapter 2 as round-off of inertia terms can be improved.

For curved structures, cylindrical coordinates may be used. The change of basis from Cartesian to cylindrical coordinates is given by

$$\begin{bmatrix} \mathbf{D}_{LL} & \mathbf{D}_{LR} \\ \mathbf{D}_{RL} & \mathbf{D}_{RR} \end{bmatrix}_{cy} = \begin{bmatrix} \mathbf{\Theta}_L & \mathbf{0} \\ \mathbf{0} & \mathbf{\Theta}_R \end{bmatrix} \begin{bmatrix} \mathbf{D}_{LL} & \mathbf{D}_{LR} \\ \mathbf{D}_{RL} & \mathbf{D}_{RR} \end{bmatrix}_{Ca} \begin{bmatrix} \mathbf{\Theta}_L & \mathbf{0} \\ \mathbf{0} & \mathbf{\Theta}_R \end{bmatrix}^{\mathrm{T}} \tag{3.31}$$

where the subscripts *cy* and *Ca* represent the cylindrical and Cartesian coordinates respectively and $\mathbf{\Theta}_{L,R}$ is the transformation (rotation) matrix whose elements contain either trigonometric functions, 0 or 1. For the WFE model shown in Figure 3.21, the transformation of $\begin{bmatrix} u & w & \theta \end{bmatrix}^{\mathrm{T}}$ at the left hand side of the section can be expressed as

$$\mathbf{\Theta}_L = \begin{bmatrix} \cos(\Delta\phi) & \sin(\Delta\phi) & 0 \\ -\sin(\Delta\phi) & \cos(\Delta\phi) & 0 \\ 0 & 0 & 1 \end{bmatrix} \tag{3.32}$$

and $\mathbf{\Theta}_R$ for the right hand side of the section is formed in the same manner by replacing $\Delta\phi$ with $-\Delta\phi$.

3.6.3 WFE results

The ring is modelled using a one-dimensional, straight, thin beam element, BEAM3, which has 3 DOFs at each node. A section subtending an angle $2\Delta s = 10(mm)$ $\left(2\Delta s/R = 1.9°\right)$ at the centre of the ring was modelled using two elements as shown in Figure 3.21. The material properties of the ring are chosen such that $E = 2.0\cdot 10^{11}$, $\rho = 7800$, $R = 0.3$, $h = 1.8\cdot 10^{-3}$ and $I = 8.748\cdot 10^{-11}$ $\left(\gamma = 5.2\cdot 10^{-4}\right)$, all in SI units.

The dispersion curves are predicted using the WFE method and the results are compared with the analytical solutions as shown in Figure 3.22. The abscissa represents the non-dimensional frequency

$$\Omega = \omega / \omega_{rb} \tag{3.33}$$

and the ordinate shows the non-dimensional wavenumber kR. Figure 3.22(a) shows the magnitude of the real part of kR and Figure 3.22(b) shows that of the imaginary part. The wave modes i=1,2,3 are associated with predominantly longitudinal, flexural propagating and flexural nearfield wave modes respectively. The WFE results using the straight elements show good agreement with the analytical solutions. At low frequencies, the i=1,3 waves couple due to the curvature and the wavenumbers become a complex conjugate pair. At the ring frequency ($\Omega = 1$), the longitudinal wave (i=1) cuts-on. Above the ring frequency two waves (i=1,2) can propagate and one wave (i=3) is a nearfield.

The relative error is shown in Figure 3.23. Figure 3.23(a) shows the relative error in the i=1 wavenumber and (b) shows that in the i=2 wavenumber. The relative errors are compared with those for a straight beam. The abscissa for the straight beam was normalised using equation (3.33) using the same ring frequency for the purpose of comparison. The relative error in the bending wavenumber was shown in subsection 2.4.3 and that in the quasi-longitudinal wavenumber can be found in [70]. It can be seen that at high frequencies where the wave coupling becomes small $(\Omega > 1)$, the relative errors for a curved beam asymptote to those for a straight beam. Three peaks in Figure 3.23(a) are associated with the two bifurcations and the cut-off frequency. At low frequencies, where the waves are strongly coupled, the relative errors for a curved beam are relatively large due to geometry approximation using straight elements but the relative errors are still at the most 1% and are very small.

3.7 Waves in Cylindrical Strips

Free wave propagation in thin, isotropic cylindrical strips is considered in this section. Waves in both the longitudinal and the circumferential directions are considered. Flugge's theory [11,108] is used to give the analytical equations. Dispersion curves are found using both the WFE method and the analytical dispersion equations. The decomposition of the power described previously is used to investigate wave characteristics.

3.7.1 Analytical Equations for Waves in the Axial Direction

Consider the cylinder shown in Figure 3.24. The Kirchhoff-Love assumption [108] is used for a thin cylinder. Based on the Flugge's theory, the equation of motion can be expressed in matrix form as [108]

$$\mathbf{L}\begin{bmatrix} u \\ v \\ w \end{bmatrix} = \mathbf{0} \tag{3.34}$$

where

$$\mathbf{L} = \begin{bmatrix} \dfrac{\partial^2}{\partial\xi^2} + \dfrac{(1-\nu)}{2}\left(1+\chi^2\right)\dfrac{\partial^2}{\partial\phi^2} - \dfrac{R^2}{c_L^2}\dfrac{\partial^2}{\partial t^2} & \dfrac{(1+\nu)}{2}\dfrac{\partial^2}{\partial\xi\partial\phi} & \nu\dfrac{\partial}{\partial\xi} + \chi^2\left(-\dfrac{\partial^3}{\partial\xi^3} + \dfrac{(1-\nu)}{2}\dfrac{\partial^3}{\partial\xi\partial\phi^2}\right) \\ \dfrac{(1+\nu)}{2}\dfrac{\partial^2}{\partial\xi\partial\phi} & \dfrac{(1-\nu)}{2}\left(1+3\chi^2\right)\dfrac{\partial^2}{\partial\xi^2} + \dfrac{\partial^2}{\partial\phi^2} - \dfrac{R^2}{c_L^2}\dfrac{\partial^2}{\partial t^2} & \dfrac{\partial}{\partial\phi} - \dfrac{(3-\nu)}{2}\chi^2\dfrac{\partial^3}{\partial\xi^2\partial\phi} \\ \nu\dfrac{\partial}{\partial\xi} + \chi^2\left(-\dfrac{\partial^3}{\partial\xi^3} + \dfrac{(1-\nu)}{2}\dfrac{\partial^3}{\partial\xi\partial\phi^2}\right) & \dfrac{\partial}{\partial\phi} - \dfrac{(3-\nu)}{2}\chi^2\dfrac{\partial^3}{\partial\xi^2\partial\phi} & \chi^2\left(\dfrac{\partial^4}{\partial\xi^4} + 2\dfrac{\partial^4}{\partial\xi^2\partial\phi^2} + \dfrac{\partial^4}{\partial\phi^4}\right) \\ & & +1+\chi^2 + 2\chi^2\dfrac{\partial^2}{\partial\phi^2} + \dfrac{R^2}{c_L^2}\dfrac{\partial^2}{\partial t^2} \end{bmatrix} \tag{3.35}$$

with

$$\begin{aligned} \xi &= \frac{x}{R}, \\ \chi^2 &= \frac{h^2}{12R^2}. \end{aligned} \tag{3.36}$$

Substituting the displacements of the cylinder [113]

$$\begin{aligned} u &= C_u \cos(n\phi)\, e^{\left(-jk^*\xi + j\pi/2\right)} e^{j\omega t}, \\ v &= C_v \sin(n\phi)\, e^{-jk^*\xi} e^{j\omega t}, \\ w &= C_w \cos(n\phi)\, e^{-jk^*\xi} e^{j\omega t} \end{aligned} \tag{3.37}$$

where $k^* = kR$ into equation (3.34) gives

$$\begin{bmatrix} -k^{*2} + \frac{(1-\nu)}{2}\left(1+\chi^2\right)n^2 + \Omega^2 & -j\frac{(1+\nu)}{2}nk^* & -j\nu k^* + \chi^2\left(-jk^{*3} + j\frac{(1-\nu)}{2}n^2k^*\right) \\ j\frac{(1+\nu)}{2}nk^* & -\frac{(1-\nu)}{2}\left(1+3\chi^2\right)k^{*2} - n^2 + \Omega^2 & -n - \frac{(3-\nu)}{2}\chi^2 nk^{*2} \\ -j\nu k^* + \chi^2\left(-jk^{*3} + j\frac{(1-\nu)}{2}n^2k^*\right) & n + \frac{(3-\nu)}{2}\chi^2 nk^{*2} & \chi^2\left(k^{*4} + 2n^2k^{*2} + n^4\right) + 1 + \chi^2 - 2\chi^2n^2 - \Omega^2 \end{bmatrix} \begin{bmatrix} C_u \\ C_v \\ C_w \end{bmatrix} = \begin{bmatrix} 0 \\ 0 \\ 0 \end{bmatrix} \tag{3.38}$$

where

$$\Omega = \omega/\omega_r \tag{3.39}$$

and

$$\omega_r = \frac{1}{R}\sqrt{\frac{E}{\rho\left(1-\nu^2\right)}} \tag{3.40}$$

is the ring frequency.

The dispersion equation can be found by setting the determinant of the matrix in equation (3.38) to zero and it becomes

$$k^{*8} + a_3k^{*6} + a_2k^{*4} + a_1k^{*2} + a_0 = 0 \tag{3.41}$$

where a_i are coefficients determined from equation (3.38). This quartic equation in k^{*2} can be solved analytically [11,110] such that the dispersion relationships can be determined for each value of n $\left(n = 0,1,2\cdots\right)$ which describes the wave mode of the cross-section or the circumferential mode order. The wave modes are separated into three groups, breathing (n=0), bending (n=1) and circumferential $\left(n \geq 2\right)$ modes [114].

There are 8 roots of the frequency equation (3.41) for each n and these are 4 positive- and negative-going wave pairs. At high enough frequencies, the waves become flexural

propagating (*i*=1), shear (*i*=2), extensional (*i*=3) and flexural nearfield (*i*=4) wave pairs [113,114].

3.7.2 WFE Results

A short section of the cylinder with an axial length Δ_x=5mm was modelled as shown in Figure 3.25. The SHELL63 element was used to model the cylindrical strip. 36 elements were used to model the cross-section and the length of elements in the ϕ-direction, Δ_ϕ=17.5mm. The properties of the cylinder are assumed to be $E = 2.0 \cdot 10^{11}$, $\nu = 0.3$, $\rho = 7800$, $h = 1.8 \cdot 10^{-3}$ and $R = 0.1$ $\left(h/R = 0.018\right)$, all in SI units.

The dispersion curves for purely real wavenumbers of the predominantly flexural propagating (*i*=1) wave modes are shown in Figure 3.26. Only the *n*=0,1,2,3,6,10,14 wave modes are plotted for clarity. Reasonable agreement for small *n* can be seen. The value of $kR = 20$ is associated with $k_x \Delta_x = 1$ such that the wave change over the section is small $\left(k_x \Delta_x < 1\right)$. The FE discretisation error across the cross-section is, however, large for higher wave modes. For the *n*=6 wave mode, the number of elements per the wavelength in the circumferential direction is 6 so that the accuracy could be expected to be reasonably good for the wave modes associated with $n \le 6$. For higher wave circumferential order modes the number of elements per wavelength decreases so that FE discretisation error increases. For example, for the *n*=10 wave mode there are only 3.6 elements in one wavelength and relatively larges error can be seen.

The behaviour of the wavenumbers changes drastically around the ring frequency, $\Omega = 1$, where the wavelength of an extensional wave equals the circumference of the cylinder. Above the ring frequency, $\Omega > 1$, the response of the cylinder is similar to that of a flat thin plate while below the ring frequency the response is far more complicated due to the increasing effect of the curvature of the cylinder [114]. The cut-off frequencies of the flexural waves are approximately [114,115]

$$\Omega_{c,n} \approx \chi n^2, \quad n \ge 2 \tag{3.42}$$

where χ is defined in equation (3.36) and in this example $\chi = 5.2 \cdot 10^{-3}$.

Figure 3.27 shows the dispersion curves for purely real wavenumbers of the shear (*i*=2) and extensional (*i*=3) wave modes. The *i*=2, *n*=0 wave mode propagates for all frequencies and the *i*=3, *n*=0 wave mode cuts-on at the ring frequency, $\Omega = 1$. Higher wave modes cut-on at higher frequencies.

Figure 3.28 shows various imaginary and complex dispersion curves for the flexural propagating (*i*=1) and shear (*i*=2) wave modes. All the *i*=1,2 type wavenumbers for $n \geq 1$ are complex below the bifurcation points (e.g. $\Omega = 0.18$ for the *n*=6 wave mode). Above the bifurcation points the complex wavenumbers become two different purely imaginary wavenumbers and the *i*=1,2 wave modes cut-on at their cut-off frequencies (e.g. $\Omega = 0.19$ for the *i*=1, *n*=6 wave mode).

Figure 3.29 shows similar dispersion curves for the predominantly extensional (*i*=3) and flexural nearfield (*i*=4) wave modes. All the *i*=3,4 types wave numbers are complex conjugate pairs below the bifurcation points. Similar bifurcations as in Figure 3.28 can be seen but only the *i*=3 wave modes cut-on as the *i*=4 modes are the flexural nearfield waves. For example, for the *i*=3,4 (*n*=0) wave mode, complex conjugate wavenumbers bifurcate to two purely imaginary wavenumbers at $\Omega = 0.96$ and the *i*=3 type wavenumber becomes purely real at $\Omega = 1.0$. The WFE results are seen to be less accurate especially at around the bifurcations. The curve which is not close to the bifurcation shows better agreement even if kR is larger than that at the bifurcation. The large errors around the bifurcations are believed to be due to both the FE discretisation and geometrical approximation errors. Although the contribution of each cause is not clear, it is believed that such approximations associated with the WFE modelling dominate the error around the bifurcation points.

3.7.3 Investigation of Wave Modes using Decomposition of Power

The group velocities using the power and energy relationship for the predominantly flexural (*i*=1) wave modes are shown in Figure 3.30. The group velocities are normalised with respect to that of the extensional wave, c_L. It can be seen that the flexural waves associated with lower order wave modes show extensional or torsional behaviour at low frequencies due to the wave coupling. This is because the wavelengths both in the axial and circumferential directions are long such that vibrational energy is associated not only with the flexural motion but also with the extensional and torsional motions. For higher wave modes and at high frequencies for lower wave modes, the flexural motion become dominant

as the wavelength becomes shorter, which can be typically seen above the ring frequency. Figure 3.31 shows the group velocities for the predominantly shear (i=2) and extensional (i=3) waves. For the purely shear waves in an isotropic plate, the group velocity $c_s/c_L = \sqrt{(1-\nu)/2} \approx 0.59$. The group velocities illustrate the change of wave characteristics with frequency and the coupling behaviour. At enough high frequencies $\Omega >> 1$ the group velocities associated with the i=2 wave modes asymptote to that of the shear wave, $c_g/c_L \approx 0.59$ and the group velocities associated with the i=3 wave modes asymptote to that of the longitudinal wave, $c_g/c_L = 1$.

Such changes of the wave characteristics may be also investigated by evaluating the power associated with various kinds of variables. The power associated with the flexural, torsional and extensional motions are analytically discussed in [113]. The total time-averaged power can be expressed as [113]

$$P = P_f + P_{ex} + P_{to} \tag{3.43}$$

where

$$\begin{aligned} P_f &= \int_0^{2\pi} \frac{1}{2} \mathrm{Re}\left(m_x^* j\omega\theta_x + \tau_{xr}^* j\omega w \right) R d\phi, \\ P_{ex} &= \int_0^{2\pi} \frac{1}{2} \mathrm{Re}\left(\sigma_x^* j\omega u \right) R d\phi, \\ P_{to} &= \int_0^{2\pi} \frac{1}{2} \mathrm{Re}\left(\tau_{x\phi}^* j\omega v \right) R d\phi \end{aligned} \tag{3.44}$$

are the powers associated with the flexural, extensional and torsional motions respectively. The superscript $\cdot^*$ is the complex conjugate and m_x is the moment along the x-axis. In reference [113] a simplified Flugge's equation [116], which neglects stress distribution over the thickness in the stress-strain relationship, is used. Instead, Flugge's equation including stress distribution over the thickness [116] is used here to give more accurate results even for higher order wave modes. Following the same procedure as that in [113], each power component can be obtained for the n=0 wave mode, after some calculations, as

$$\begin{aligned} P = {} & 2\pi\omega R\left[\hat{D}\left\{(kR)^3 C_w^2 + (kR)^2 C_u C_w\right\}\right] \\ & + \pi\omega R\left[\hat{E}\left\{(kR) C_u^2 + \nu C_u C_w\right\} + \hat{D}(kR)^2 C_u C_w\right] \end{aligned} \tag{3.45}$$

where the two terms represent flexural and extensional contributions and where

$$\begin{aligned} \hat{D} &= \frac{Eh^3}{12\left(1-\nu^2\right)R^3}, \\ \hat{E} &= \frac{Eh}{\left(1-\nu^2\right)R} \end{aligned} \tag{3.46}$$

and

$$\begin{aligned} P = {} & \pi\omega R\left[\hat{D}\left\{\begin{array}{l}(kR)^3 C_w^2 + n^2 (kR) C_w^2 + (kR)^2 C_u C_w \\ +(3+\nu) n (kR) C_v C_w/2 - (1-\nu) n^2 C_u C_w/2\end{array}\right\}\right] \\ & + \pi\omega R/2\left[\hat{E}\left\{(kR) C_u^2 + \nu n C_u C_v + \nu C_u C_w\right\} + \hat{D}(kR)^2 C_u C_w\right] \\ & + \pi\omega R(1-\nu)/4\left[\hat{E}\left\{(kR) C_v^2 + n C_u C_v\right\} + \hat{D}\left\{(kR) C_v^2 + n(kR) C_v C_w\right\}\right] \end{aligned} \tag{3.47}$$

for the $n \neq 0$ wave modes, the final term involving the torsion contribution.

Figure 3.32 shows the magnitude of power ratios associated with P_f, P_{ex}, P_{to} to the total power P of the *i*=1 (*n*=0-3) wave modes calculated using equations (3.45) and (3.47). The figures clearly show that the wave characteristics change around the ring frequency. For the *n*=0 (breathing) mode (Figure 3.32(a)), extensional motion dominates the wave motion at low frequencies while torsional (shear) motion dominates the wave for the $n \geq 1$ (bending and circumferential) modes. For all the flexural propagating waves, the flexural motion dominates above the ring frequency. It should be noted that although the total power is positive for a positive-going wave, an individual contribution to the total power may be negative. This is the reason why the power ratio sometimes exceeds unity in Figure 3.32.

To numerically investigate the changes of the wave characteristics found from WFE analysis, the decomposition of the power described in subsection 3.3.3 was used. The power ratios associated with each displacement component are shown in Figure 3.33. Each power component is normalised with respect to the total power. If the flexural motion dominates

the power, the powers associated with $q_r, q_\phi, \theta_r, \theta_\phi$ are likely to be dominant. For the extensional motion, only q_x is generally substantial. For the torsional motion, q_r, q_ϕ, θ_x are associated with the motion but only q_r, q_ϕ are often significant. "Noise" in the plots is believed to be due to numerical errors. It can be observed that the decomposition of the power can broadly describe the characteristics of each wave.

3.7.4 Analytical Equations for Waves in the Circumferential Direction

In this section, a strip along the axis of the cylinder is modelled and free wave propagation in the circumferential direction of the cylindrical strip is considered as shown in Figure 3.34. The cylinder is assumed to be finite and of length L_y. The boundary conditions along the edges of the strip $y = 0, L_y$ are taken to be [117]

$$w = m_y = u = \sigma_y = 0 . \tag{3.48}$$

For these boundary conditions, the displacements along the length of the cylinder are approximately expressed as [117]

$$\begin{aligned} u &= C_u \sin\left(k_y y\right) e^{-jkR\phi} e^{j\omega t}, \\ v &= C_v \cos\left(k_y y\right) e^{-jkR\phi} e^{j\omega t}, \\ w &= C_w \sin\left(k_y y\right) e^{-jkR\phi} e^{j\omega t} \end{aligned} \tag{3.49}$$

where

$$\phi = s/R \tag{3.50}$$

is the non-dimensional parameter for the direction of wave propagation and

$$k_y = n\pi/L_y \tag{3.51}$$

is the wavenumber in the *y*-direction for the *n*th wave mode. It should be noted that the displacements (3.49) are approximate expressions and the displacements do not exactly

satisfy the stress and displacement fields at the boundaries [117]. Substituting equation (3.49) into the governing equation (3.34) gives

$$\begin{bmatrix} \left(-k_y^2-\frac{(1-\nu)}{2}\left(1+3\chi^2\right)k^2+\frac{\Omega^2}{R^2}\right) & -j\frac{(1+\nu)}{2}kk_y & -\frac{jk_y}{R}-j\frac{(3-\nu)}{2}\chi^2Rk^2k_y \\ j\frac{(1+\nu)}{2}kk_y & \left(-\frac{(1-\nu)}{2}\left(1+\chi^2\right)k_y^2-k^2+\frac{\Omega^2}{R^2}\right) & \left(-\frac{\nu k}{R}-\chi^2Rk^3+\frac{(1-\nu)}{2}\chi^2Rkk_y^2\right) \\ -\frac{jk_y}{R}-j\frac{(3-\nu)}{2}\chi^2Rkk_y^2 & \left(\frac{\nu k}{R}+\chi^2Rk^3-\frac{(1-\nu)}{2}\chi^2Rkk_y^2\right) & \left(\chi^2R^2\left(k^4+2k^2k_y^2+k_y^4\right)+\frac{\left(1+\chi^2\right)}{R^2}-2\chi^2k_y^2-\frac{\Omega^2}{R^2}\right) \end{bmatrix} \begin{Bmatrix} C_u \\ C_v \\ C_w \end{Bmatrix} = \begin{Bmatrix} 0 \\ 0 \\ 0 \end{Bmatrix} \quad (3.52)$$

The analytical dispersion equation can be derived by setting the determinant of the matrix in equation (3.52) to zero and has the same form as equation (3.41). The dispersion equation can be solved for each value of $k_y(n)$.

3.7.5 WFE Results

The WFE model was formed as shown in Figure 3.35. The properties of the cylinder are the same as in subsection 3.7.2 with $L_y = 0.18$. A section subtending an angle $2\Delta\phi = 1.9°$ at the centre of the cylinder was modelled. The SHELL63 element was used and the number of the elements along the length of the cylinder was 36. The length of each element was such that $\Delta_\phi \approx \Delta_y = 5mm$. The series of elements was connected using a rotation of local coordinate systems to represent the curvature as described in subsection 3.6.2.

The dispersion curves for purely real wavenumbers are shown in Figure 3.36. The abscissa is the non-dimensional frequency $\Omega = \omega/\omega_r$, equation (3.39), and the ordinate is $\left|\mathrm{Re}(kR)\right|$. The value of $kR = 20$ is associated with $k\Delta_\phi = 1$. Seven flexural (n=1-7) and two shear (n=0,1) wave modes cut-on in the frequency range analysed. Good agreement between the (approximate) analytical solutions and the WFE results can be seen especially for small n. Below the ring frequency, $\Omega < 1$, complicated behaviour is observed because of wave

coupling due to the curvature. Frequency region in which the group velocity is negative can be found for all the flexural waves shown. Such behaviour was also reported by Langley [118,119].

It could be worth noting that $kR = n \quad (n = 0,1,2\cdots)$ is associated with the nth circumferential wave modes. For the n=1, i=1 wave mode the first natural frequency is associated with the fifth circumferential mode. It is of interest to investigate the characteristics of each wave mode. Figure 3.37 shows the power ratio associated with each displacement component for the i=1, n=1 flexural propagating wave mode. Figure 3.37(a) shows the power associated with each displacement component for the branch of the dispersion curve between points A and B in Figure 3.36 and (b) shows the same results for the branch between points A and C. Between points A and B, the wave is inherently flexural because the power is mainly associated with q_r and θ_y. On the other hand, shear motion dominates the behaviour of the wave between points A and C where the powers associated with q_ϕ and q_y are significant. Physically, a flexural wave couples with the in-plane motion in curved structures when the wavelength is long (small k). As the wavelength becomes shorter (large k), the coupling effect becomes smaller and the wave approaches a purely flexural wave.

Figure 3.38 shows the purely imaginary and complex conjugate wavenumbers associated with the predominantly flexural propagating (i=1) waves for n=1-3, the predominantly extensional (i=3) wave for n=1 and the predominantly flexural nearfield (i=4) wave for n=1. For the i=1,2 wave modes, the imaginary part of the complex conjugate wavenumbers becomes 0 at the cut-off frequency and two propagating waves cut-on (e.g. at $\Omega = 0.17$ for the i=1, n=1 wave mode). The real part of the wavenumber is not zero at this cut-off frequency (e.g. $kR = 4.5$). The i=3 and i=4 wave modes are also complex conjugate pairs at low frequencies (e.g. at $\Omega = 0.18$ for the i=3,4, n=1 wave mode) and bifurcate into two different purely imaginary wavenumbers.

Figure 3.39 shows the dispersion curves for purely imaginary and complex wavenumbers associated with the i=2 (n=1,3,5) and the i=3 (n=1) wave modes, which have symmetric motion across the length of the cylinder. The bifurcations of the complex conjugate and imaginary wavenumbers can be seen between wave modes associated with different values of n. The approximate analytical solutions cannot express such behaviour because they

assume that wave modes associated with different values of n are orthogonal, see equation (3.49). Only the WFE results are therefore shown.

Similarly, Figure 3.40 shows the dispersion curves associated with the asymmetric wave modes. The waves for i=2 (n=2,4,6) and i=3 (n=2) are shown. In addition to the bifurcations, curve veering between two different purely imaginary wavenumbers can be observed. Such curve veering and bifurcations can occur between two different purely imaginary wavenumbers whose wave modes are not orthogonal to each other in the wave domain.

3.8 Conclusions

In this chapter, the WFE method was used to predict free wave propagation in complicated structures. The dispersion curves were shown for purely real, purely imaginary and complex wavenumbers. The WFE results were compared with either analytical solutions or numerical solutions to analytical dispersion equations. Good agreements were observed and the accuracy of the WFE results was evaluated.

Freely propagating in-plane waves were analysed for plate strips with mixed and free edges. In particular, numerical solutions to the Rayleigh-Lamb frequency equations were calculated using Muller's method using the WFE results as initial estimates. Complicated behaviour of the wavenumbers was observed including phenomena such as non-zero cut-on and curve veering. A method of decomposition of the power was proposed to reduce the size of the matrix and to reveal the nature of energy flow associated with each wave mode.

Freely propagating flexural waves in a plate strip with free edges were also described. The analytical dispersion equation is transcendental and the argument principle was used to give numerical solutions to the analytical equation using the WFE results as accurate initial estimates. Bifurcations associated with purely imaginary and complex conjugate wavenumbers were seen. Changes of wave modes around the transition frequencies were also illustrated.

The WFE modelling of curved structures was described using straight or flat elements. Free wave propagation in a ring was considered and wave coupling due to the curvature was described. Free wave propagation in a cylinder was also analysed for strips cut from the cylinder in either the axial or circumferential direction. Decomposition of the power was used to investigate wave characteristics.

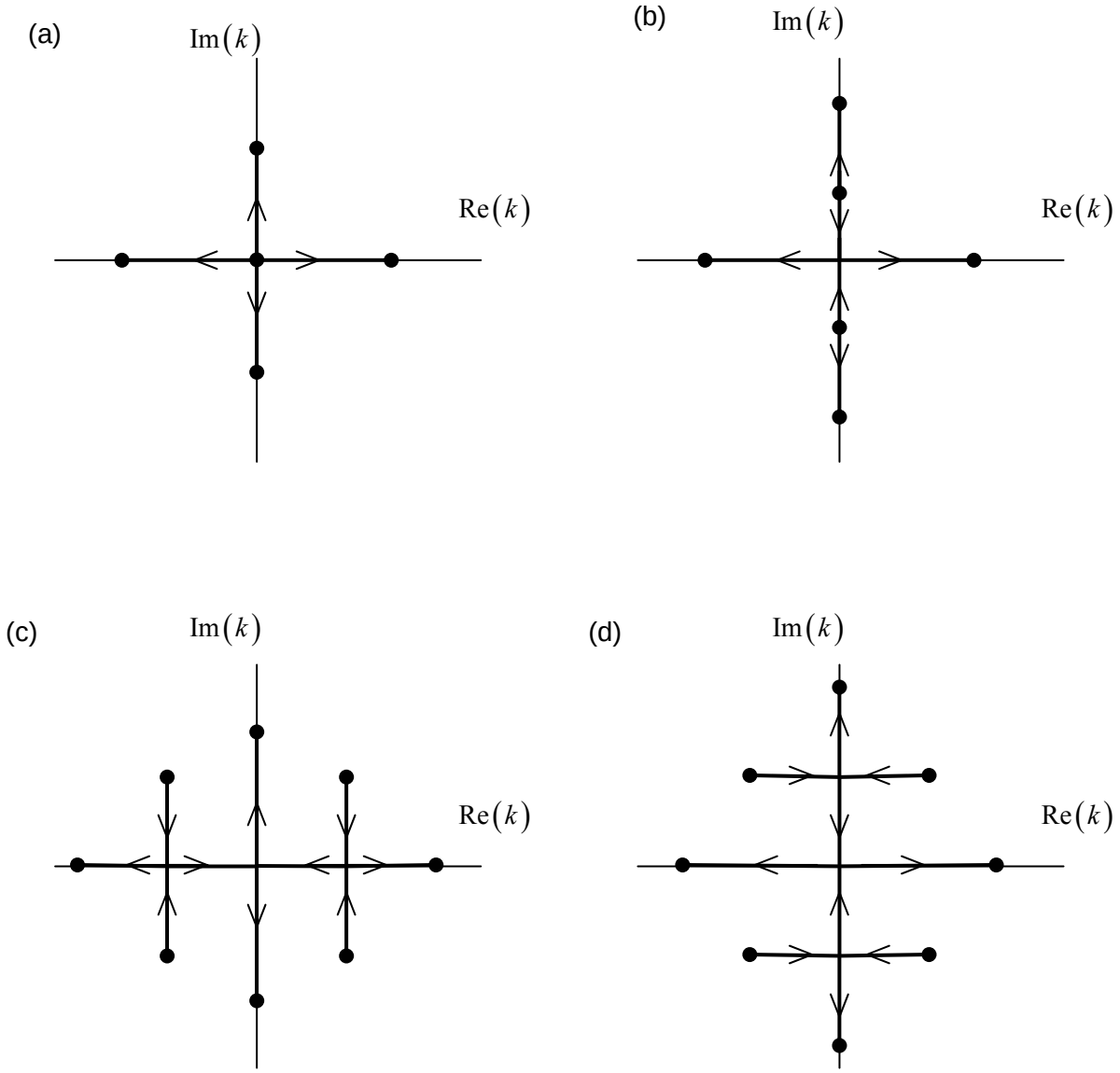

Figure 3.1: Loci of wavenumbers in the complex k-plane.

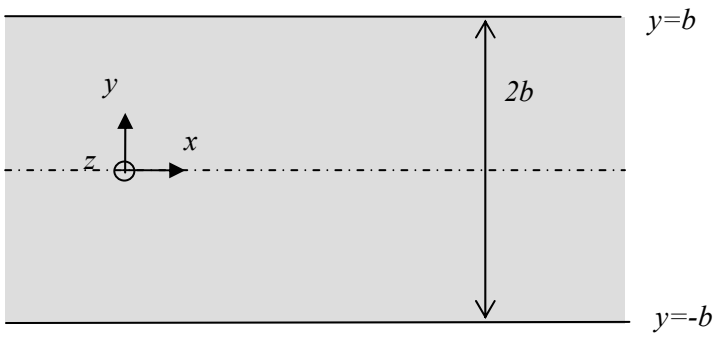

Figure 3.2: Coordinates of a plate strip.

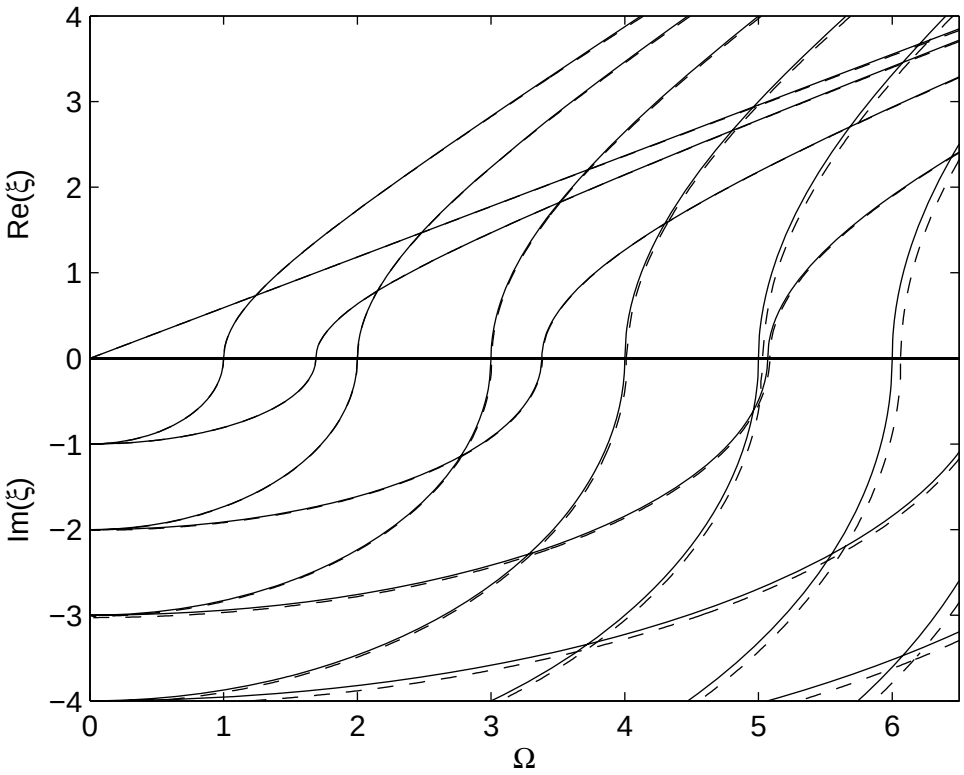

Figure 3.3: In-plane waves in a plate strip with mixed edges. Dispersion curves: — analytical solutions; – – WFE results.

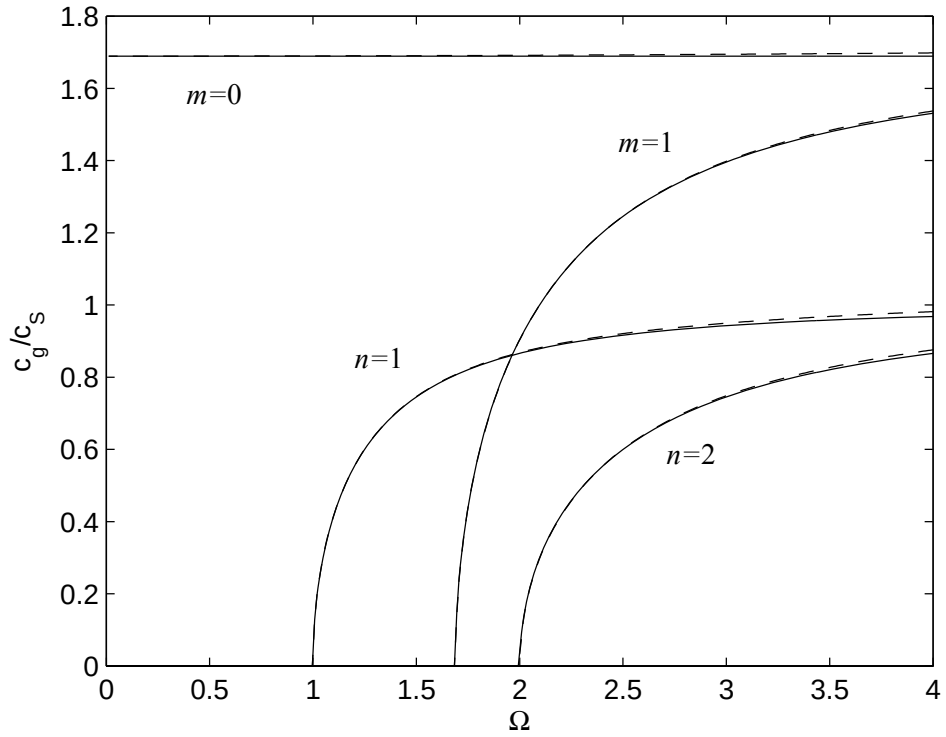

Figure 3.4: In-plane waves in a plate strip with mixed edges. Group velocities: — analytical solutions; – – WFE results.

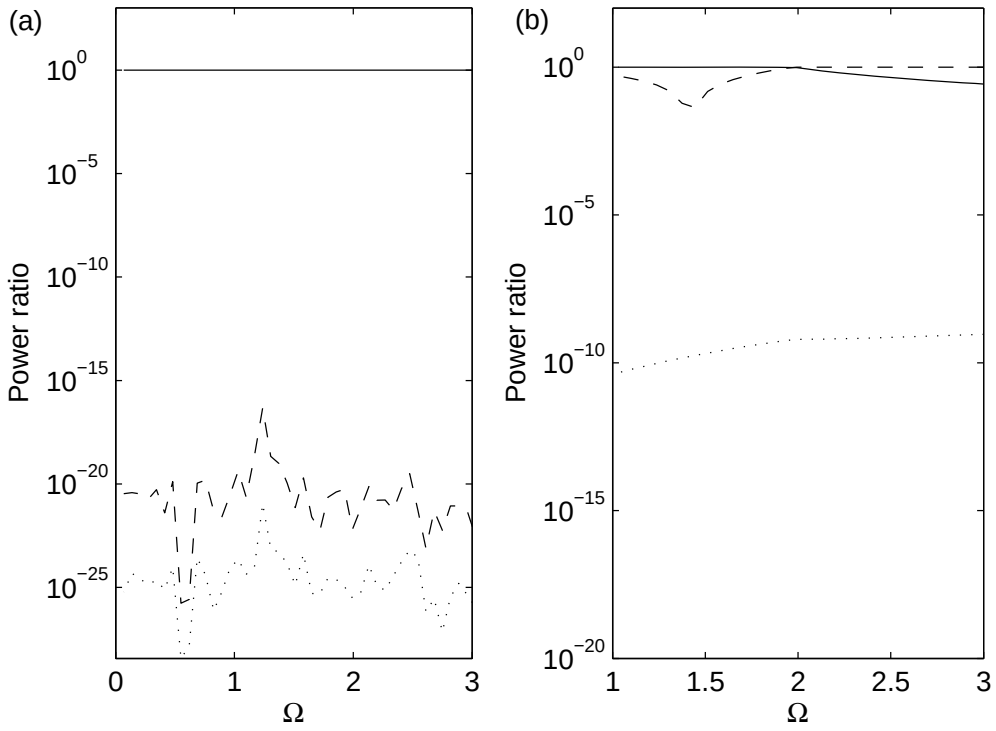

Figure 3.5: In-plane waves in a plate strip with mixed edges. Normalised power associated with —: u, – –: v, ·····: θ_z for (a) the m=0; (b) the n=1 wave mode.

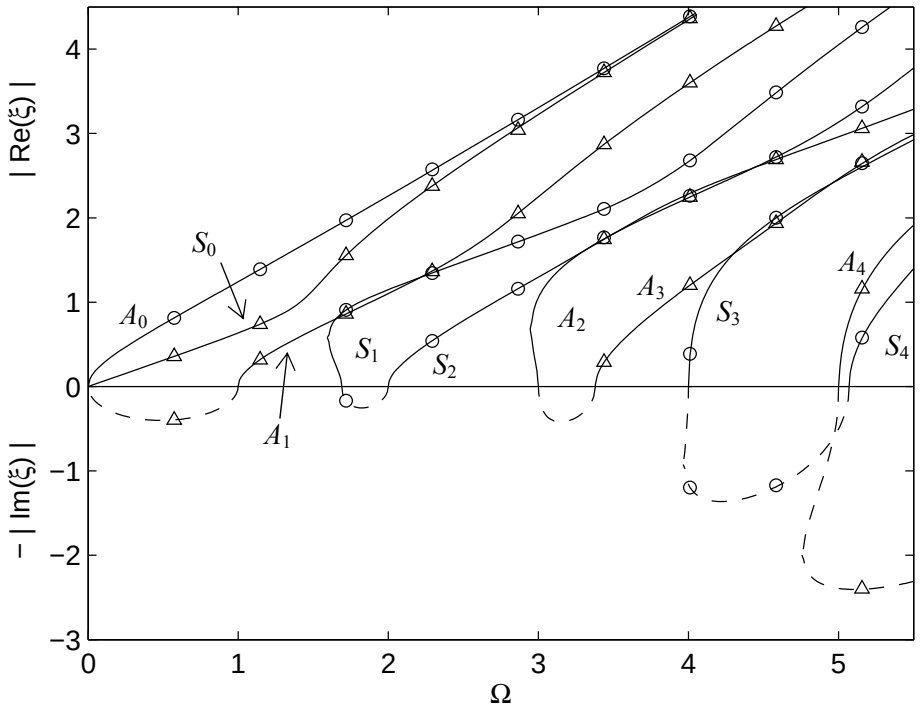

Figure 3.6: In-plane waves in a plate strip with free edges. Dispersion curves for purely real and purely imaginary wavenumbers: — WFE results; numerical solutions to the analytical equations for ○ symmetric; △ asymmetric wave modes.

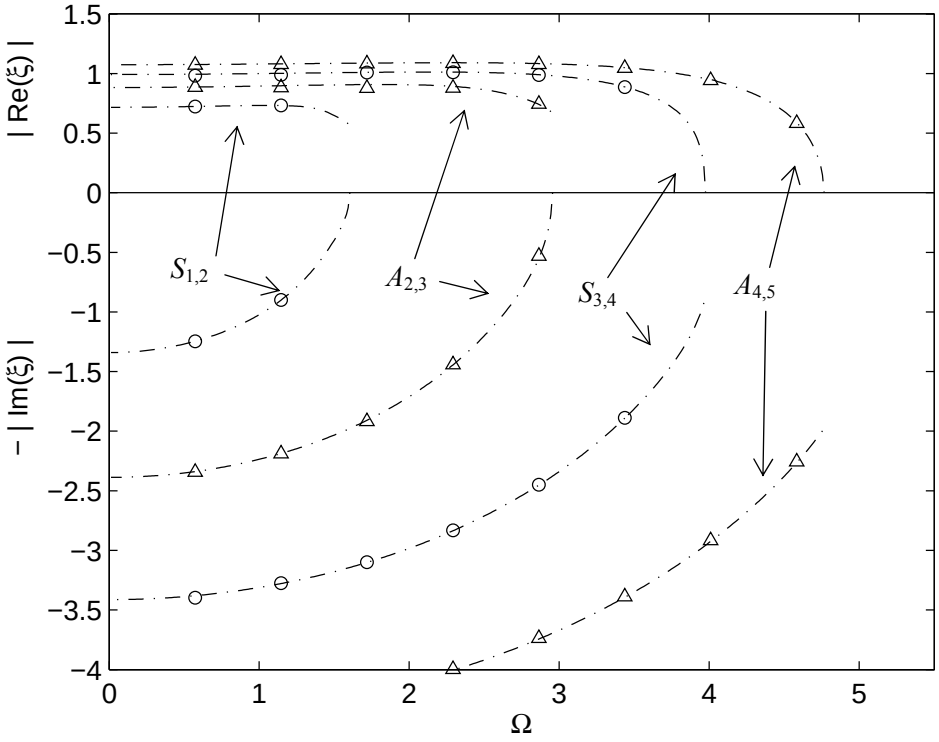

Figure 3.7: In-plane waves in a plate strip with free edges. Dispersion curves for complex wavenumbers: — WFE results; numerical solutions to the analytical equations for ○ symmetric; △ asymmetric wave modes.

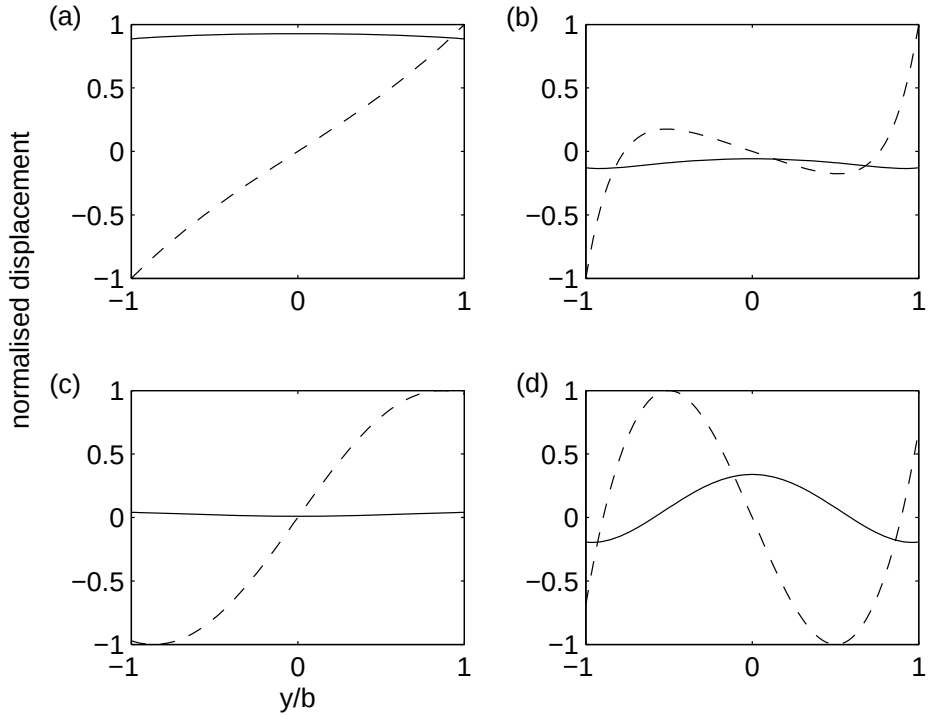

Figure 3.8: In-plane waves in a plate strip with free edges. Displacements across the plate strip for (a) A_0 $(\Omega \approx 0)$, (b) A_0 $(\Omega \approx 4)$, (c) A_1 $(\Omega \approx 1)$, (d) A_1 $(\Omega \approx 4)$ wave modes: — y-wise; – – x-wise displacement. y-wise motion is $\pi/2$ out of phase from the x-wise motion.

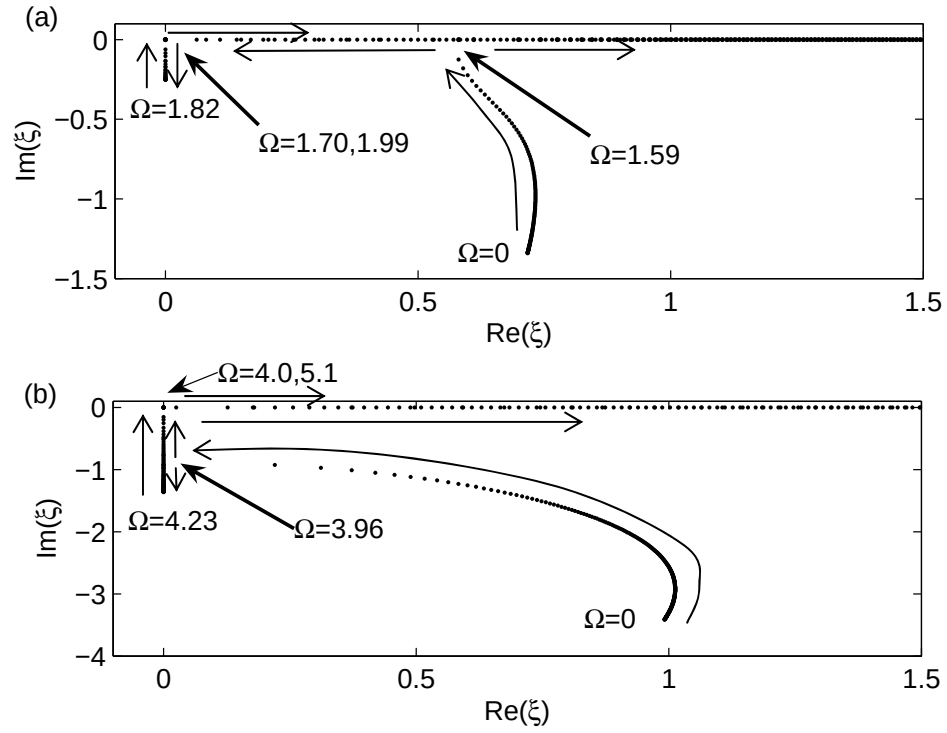

Figure 3.9: In-plane waves in a plate strip with free edges. Wavenumbers in the complex ξ-plane, (a) $S_{1,2}$ waves and non-zero wavenumber cut-on, (b) $S_{3,4}$ waves and bifurcation to two purely imaginary wavenumbers.

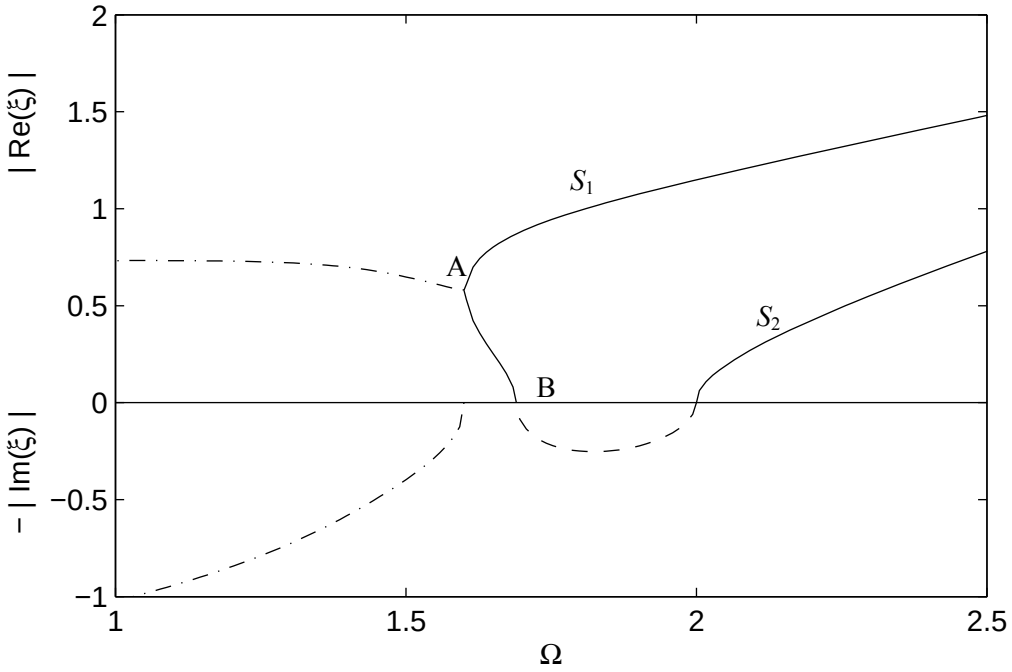

Figure 3.10: In-plane waves in a plate strip with free edges. Dispersion curves around the non-zero cut-off frequency for the S_1, S_2 wave modes: — purely real; – – purely imaginary; –·– complex wavenumbers.

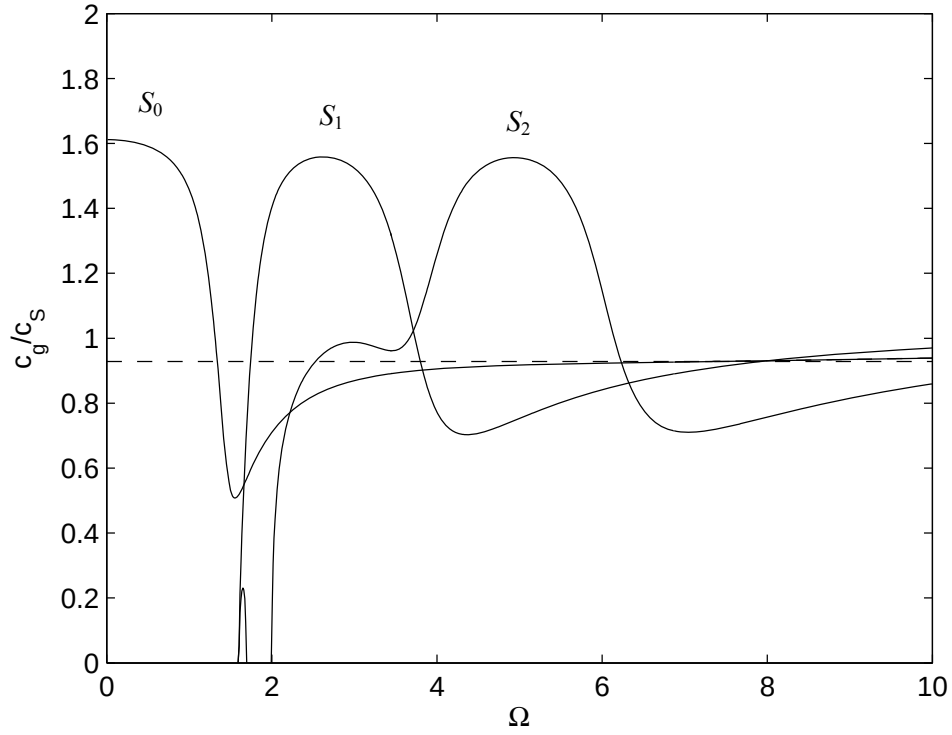

Figure 3.11: In-plane waves in a plate strip with free edges. Group velocities for the symmetric wave modes, – –: $c_R \approx 0.928 c_S \ (\nu = 0.3)$.

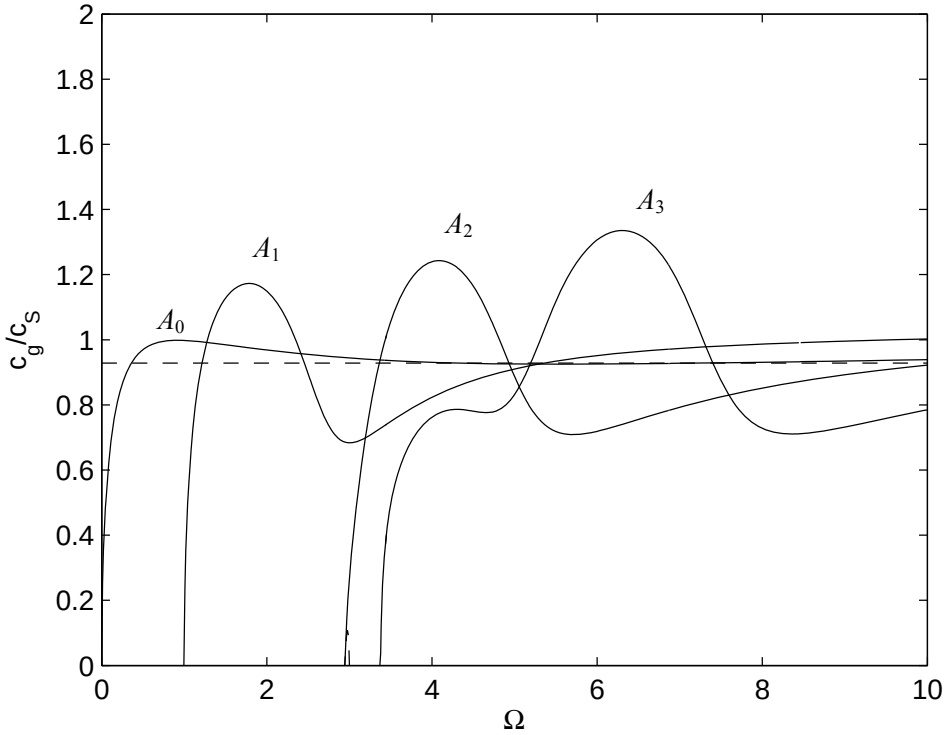

Figure 3.12: In-plane waves in a plate strip with free edges. Group velocities for the asymmetric wave modes, – –: $c_R \approx 0.928 c_S$ $(\nu = 0.3)$.

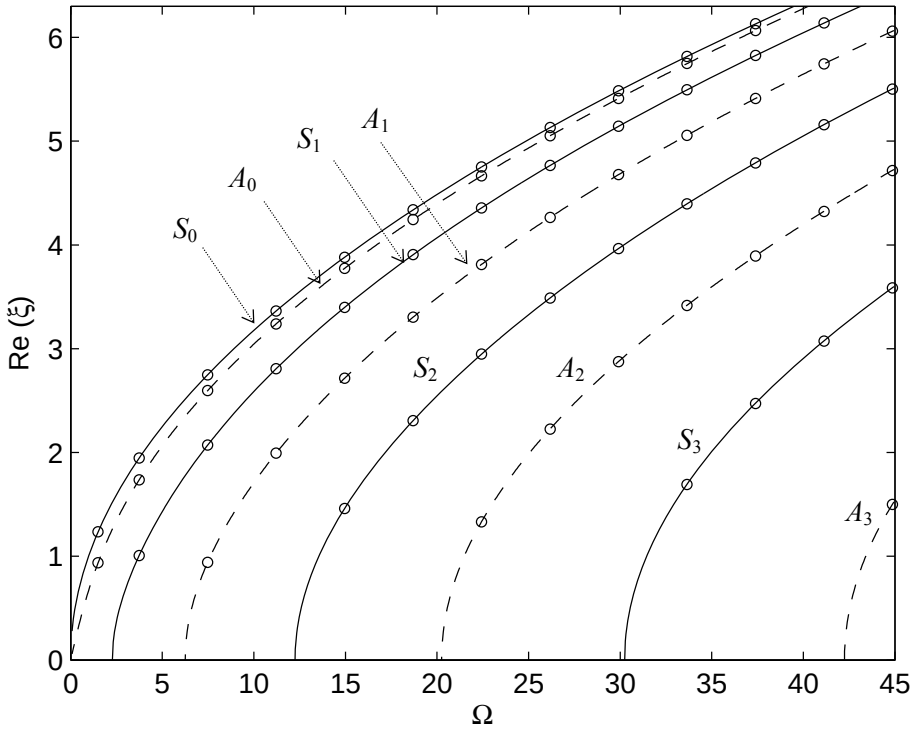

Figure 3.13: Flexural waves in a plate strip with free edges. Dispersion curves for purely real wavenumbers for — symmetric and – – asymmetric wave modes; ○ numerical solutions to the dispersion equation.

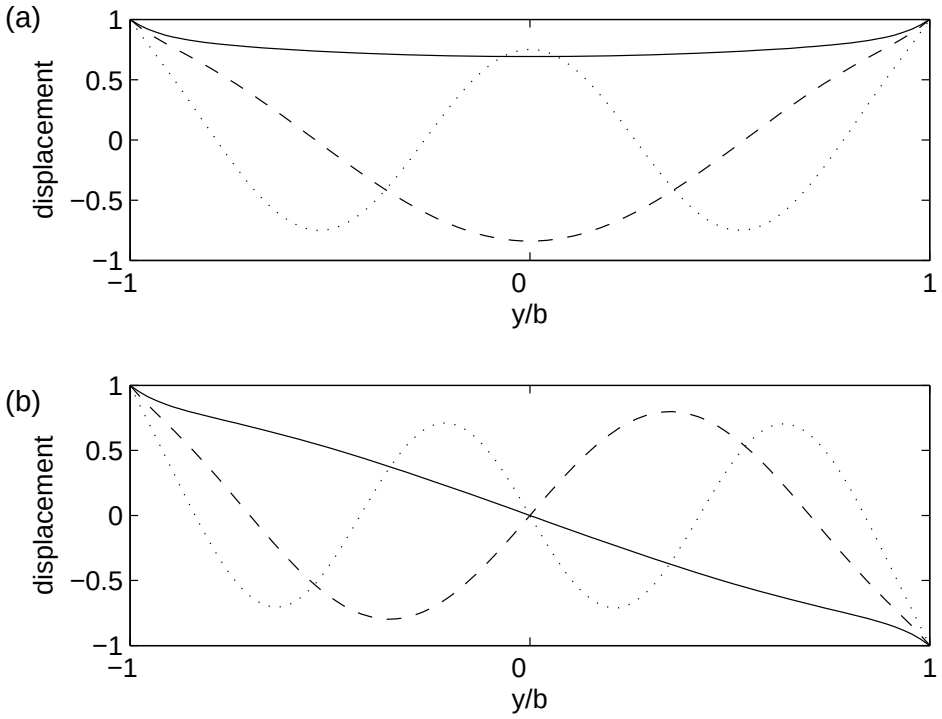

Figure 3.14: Flexural waves in a plate strip with free edges. Displacements across the plate strip at $\Omega = 37.4$ *for (a) symmetric, (b) asymmetric motions: — the* S_0, A_0; – – *the* S_1, A_1; ···· *the* S_2, A_2 *wave modes.*

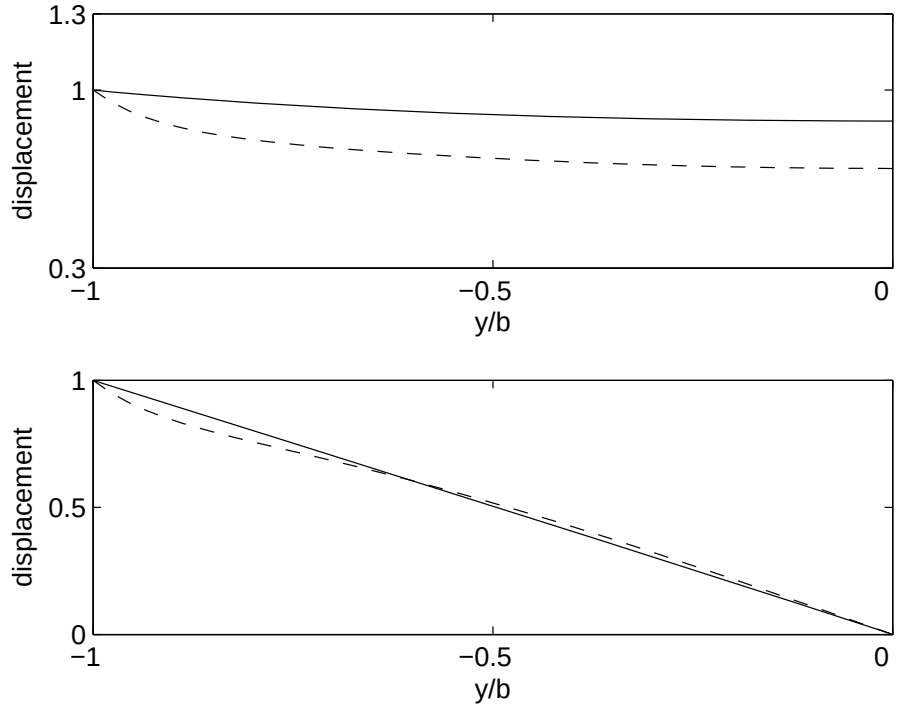

Figure 3.15: Flexural waves in a plate strip with free edges. Displacements in a half of the plate strip at — $\Omega = 0.7$ *; – –* $\Omega = 37.4$ *for: (a) the* S_0, *(b)* A_0 *wave modes.*

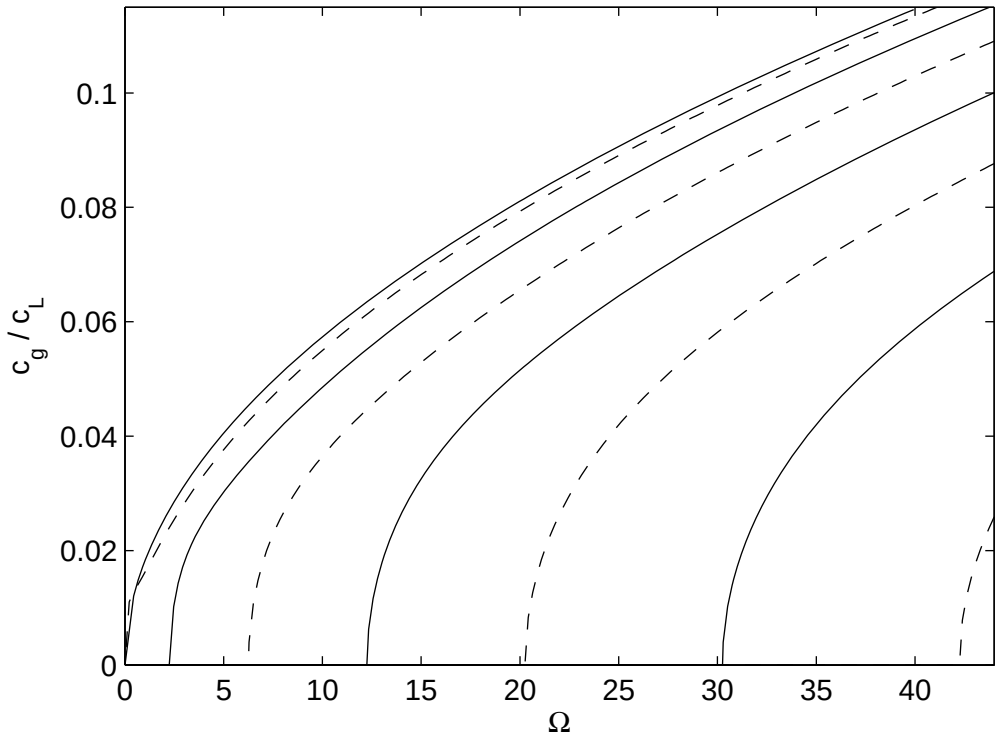

Figure 3.16: Flexural waves in a plate strip with free edges. Group velocities for — symmetric; – – asymmetric wave modes.

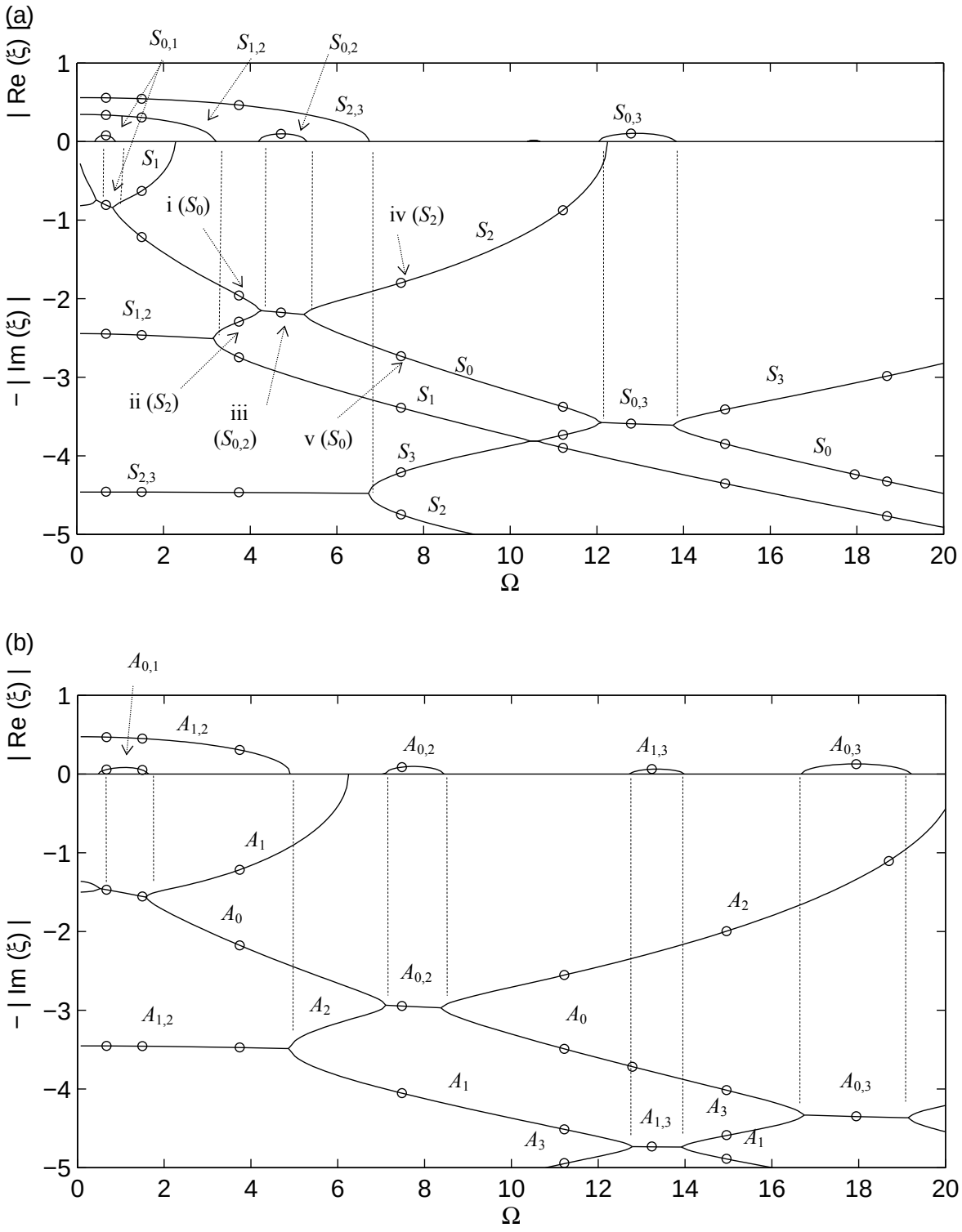

Figure 3.17: Flexural waves in a plate strip with free edges. Dispersion curves for purely imaginary and complex conjugate wavenumbers: (a) symmetric; (b) asymmetric wave modes; ○ numerical solutions to the dispersion equation.

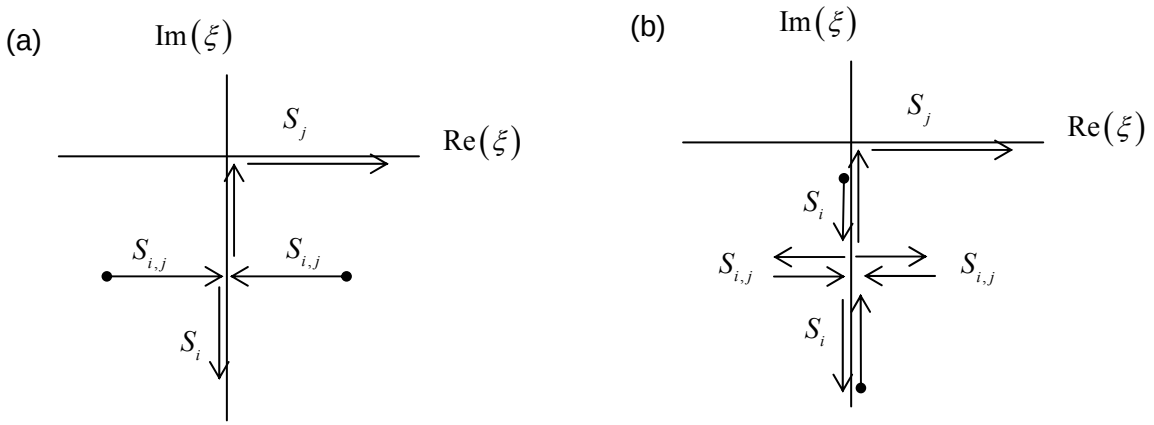

Figure 3.18: Flexural waves in a plate strip with free edges. Loci of the wavenumbers for positive going waves in the complex ξ -plane for the $S_{i,j}$ mode: (a) $i \geq 1, j \geq 2, j = i+1$; (b) $i \geq 0, j \geq 2, j \geq i+2$. Arrows indicate loci of wavenumbers as frequency increases.

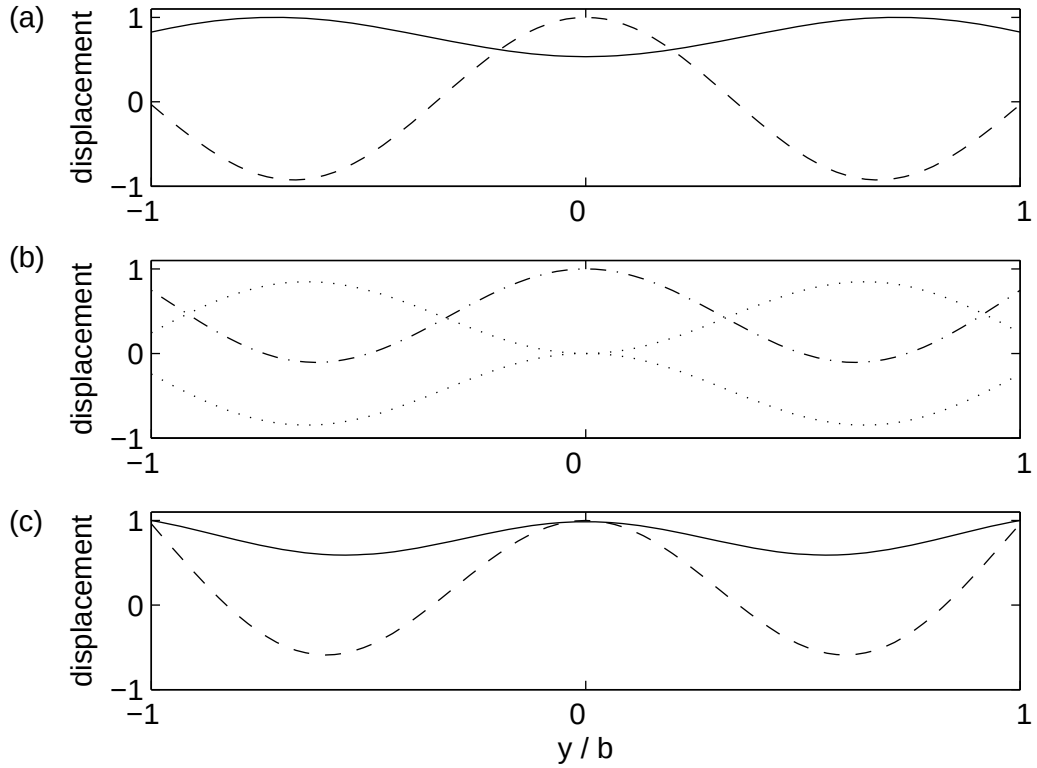

Figure 3.19: Flexural waves in a plate strip with free edges. Displacements along the plate width at various frequencies: (a) — i, – – ii at $\Omega = 3.59$; (b) –·– (real part), ···· (imaginary part) for iii at $\Omega = 4.71$; (c), – – iv, — v at $\Omega = 6.28$.

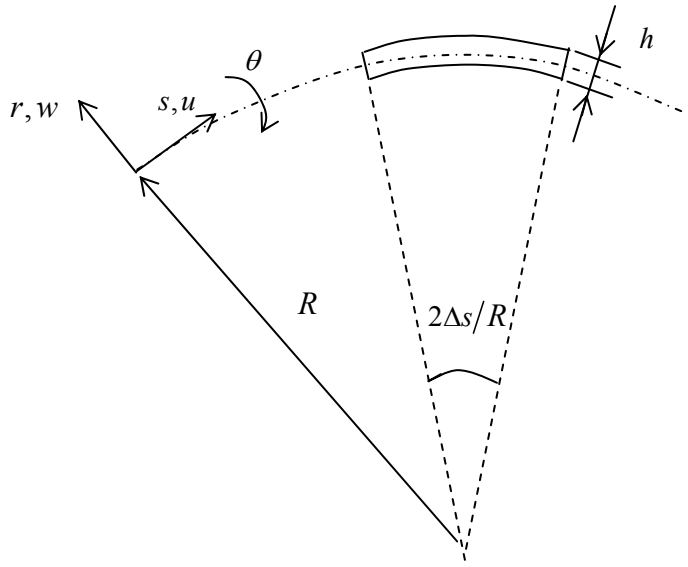

Figure 3.20: Coordinates of a ring.

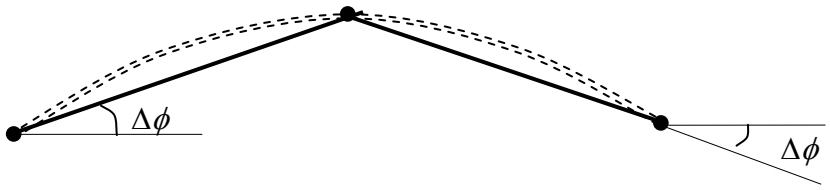

Figure 3.21: Modelling of the ring using straight elements.

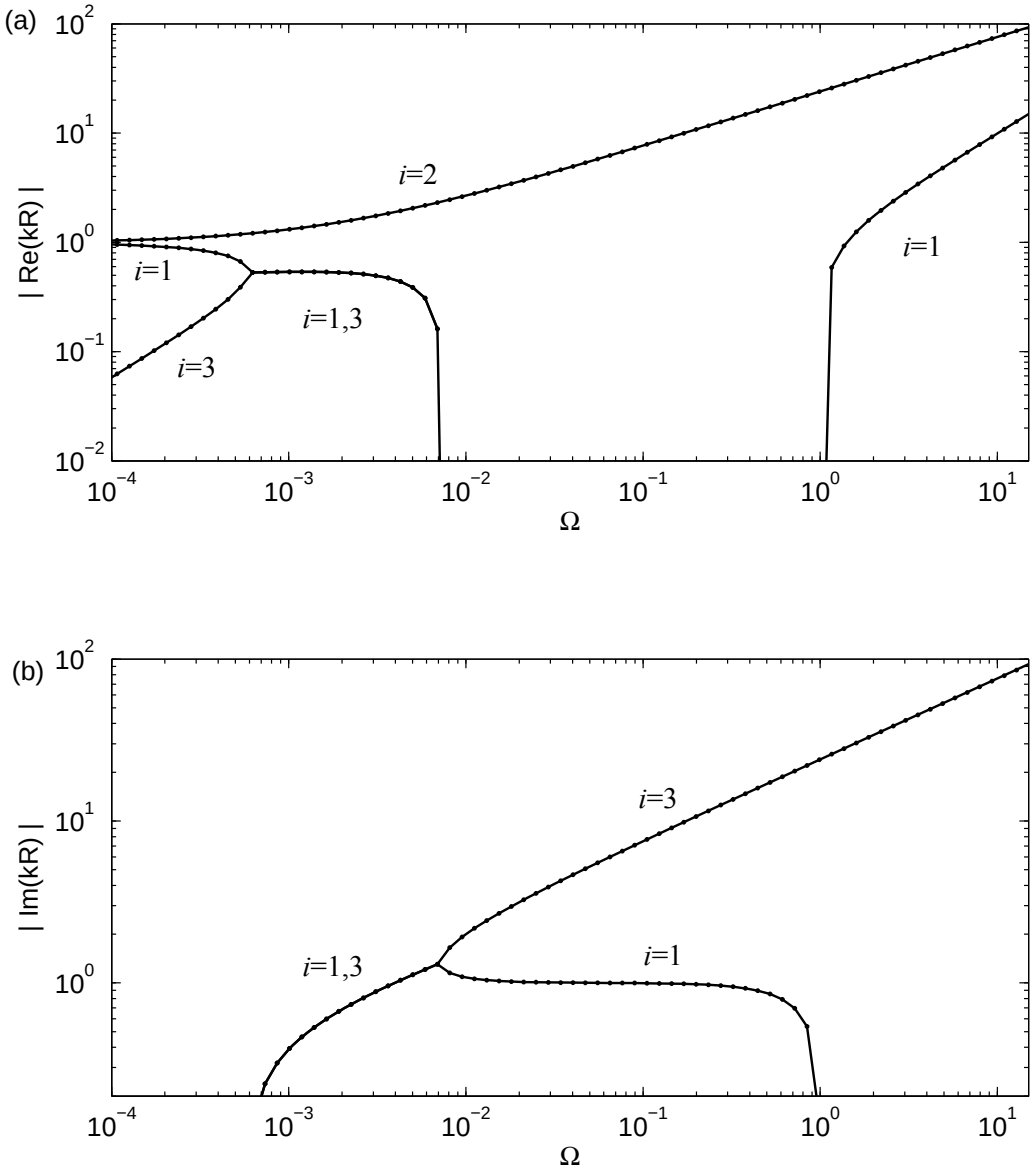

Figures 3.22: Waves in a ring. Dispersion curves for the modulus of (a) the real part, (b) the imaginary part: — analytical solutions; ···· WFE results.

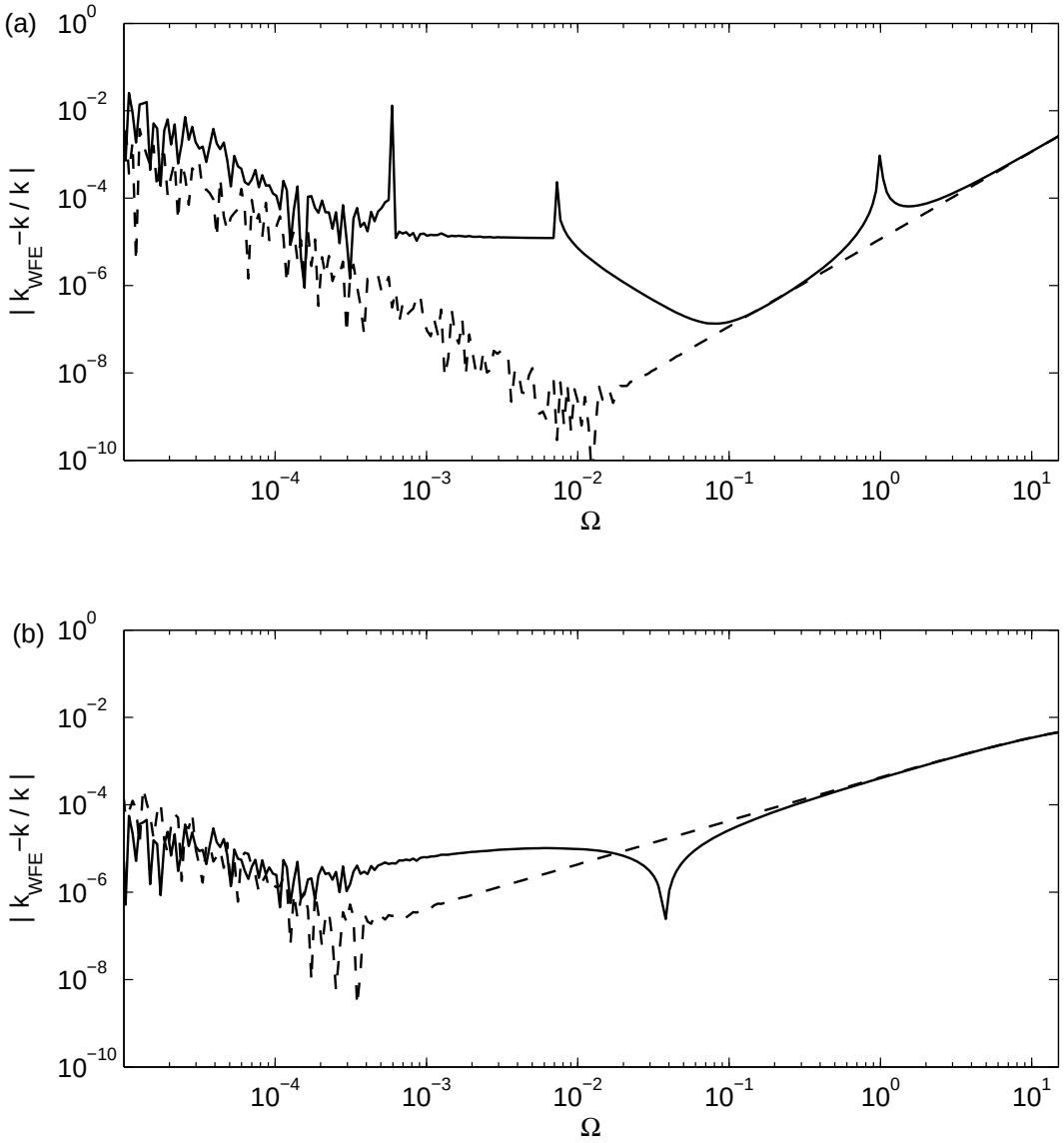

Figures 3.23: Waves in a ring. Relative errors in (a) the i=1; (b) the i=2 wavenumbers for — a curved beam; – – a straight beam.

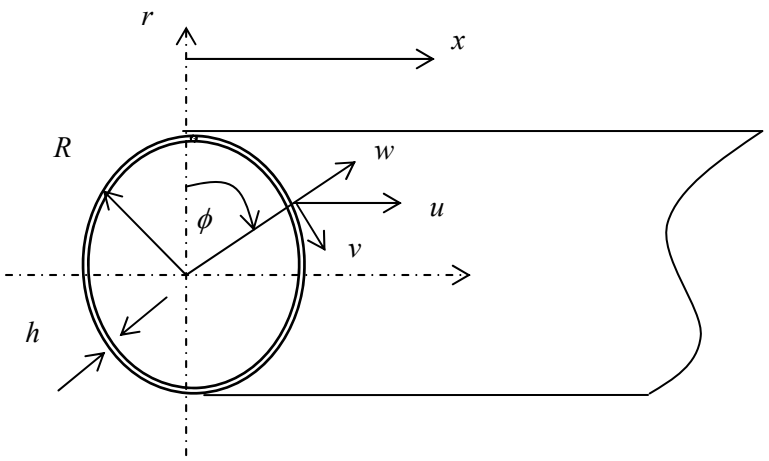

Figure 3.24: Coordinates of a cylinder.

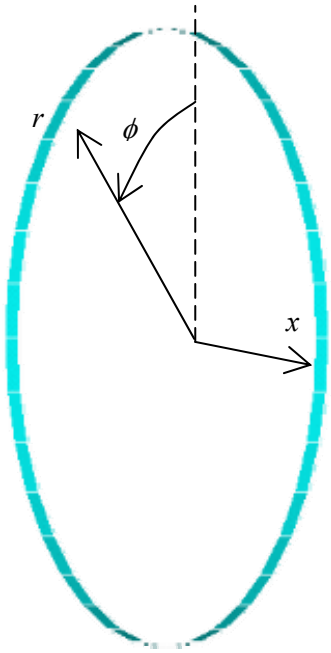

Figure 3.25: WFE model of an axial section of the cylinder.

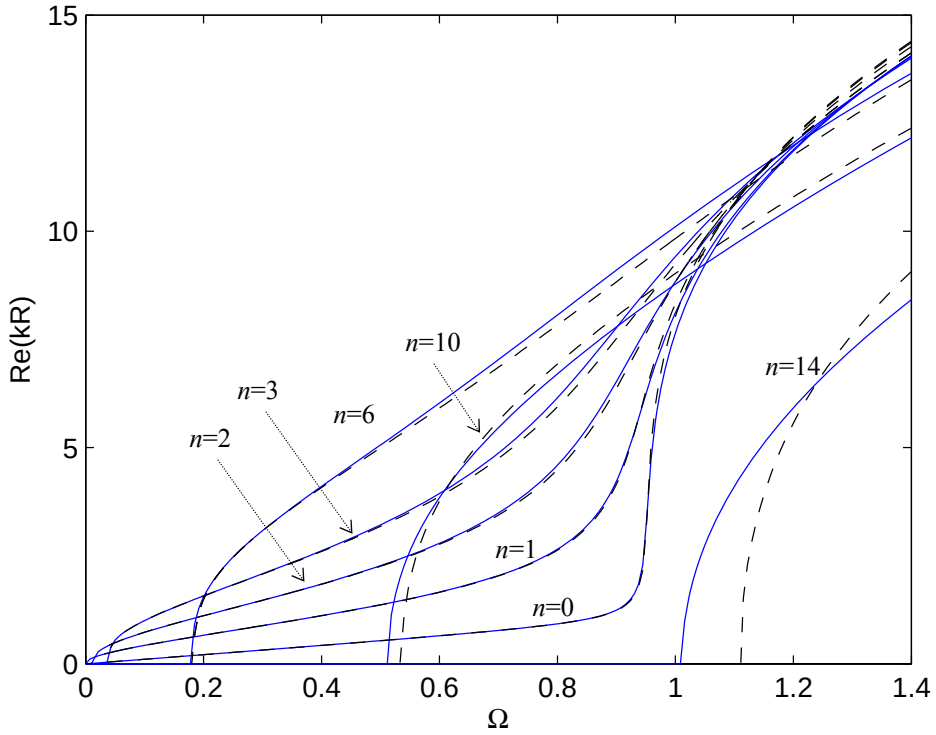

Figure 3.26: Dispersion curves for the predominantly flexural (i=1) waves in a cylinder, n=0,1,2,3,6,10,14: — analytical solutions; – – WFE results.

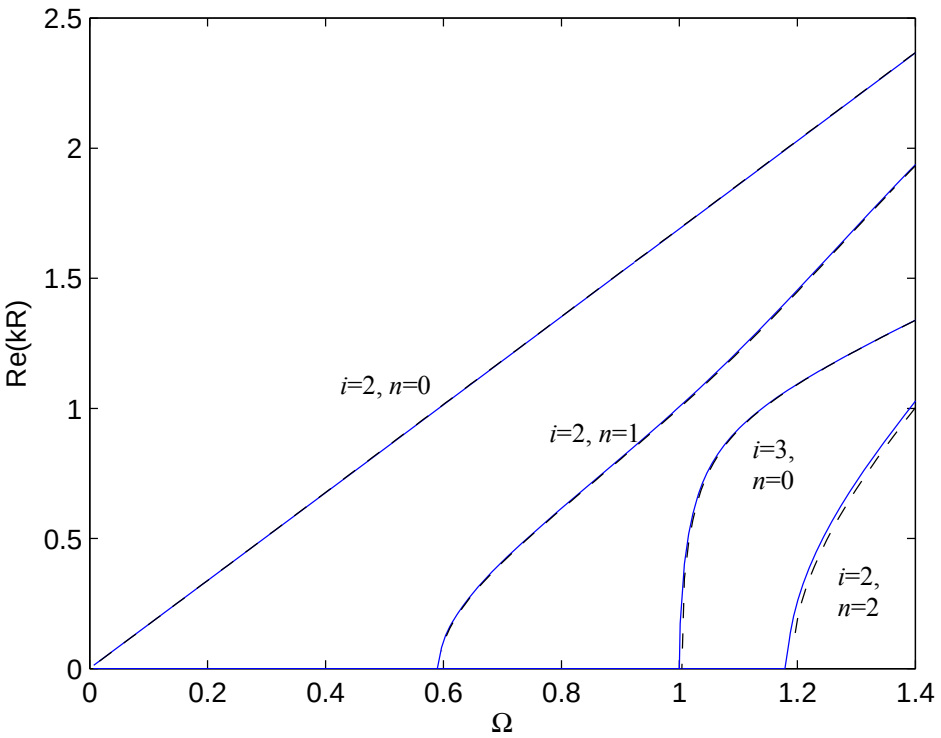

Figure 3.27: Dispersion curves for the predominantly shear (i=2) and extensional (i=3) waves in a cylinder: — analytical solutions; – – WFE results.

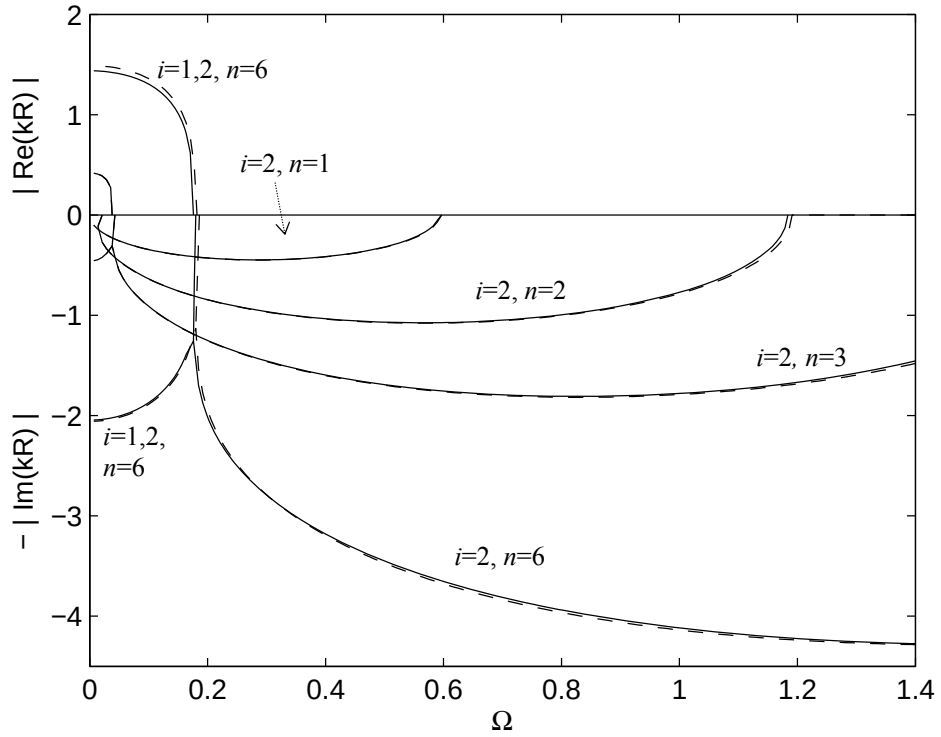

Figure 3.28: Dispersion curves for purely imaginary and complex wavenumbers of the i=1,2 (n=1,2,3,6) wave modes in a cylinder: — analytical solutions; – – WFE results.

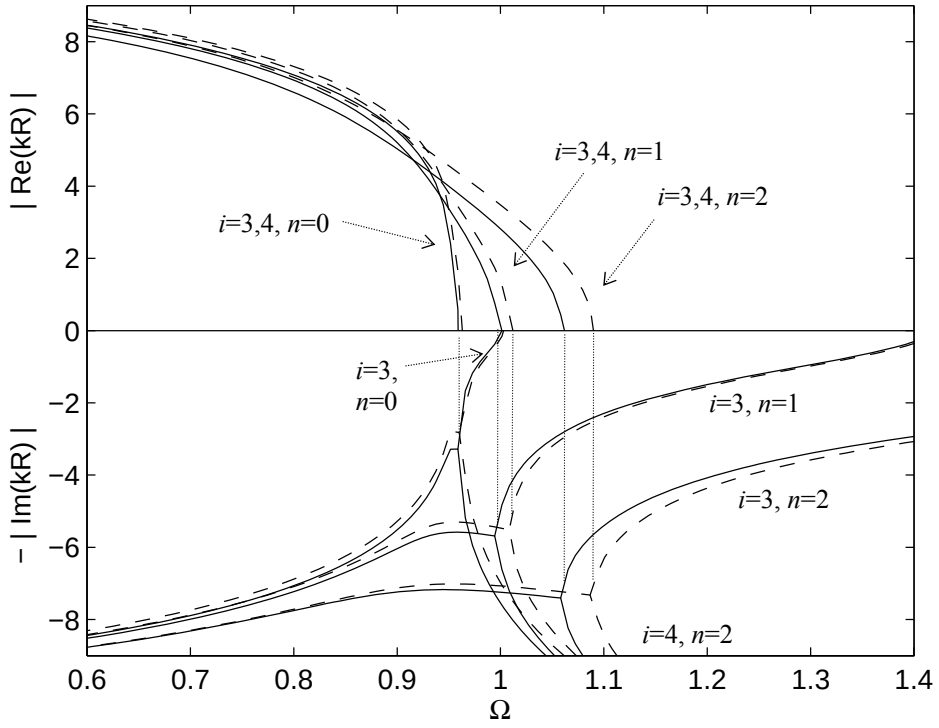

Figure 3.29: Dispersion curves for purely imaginary and complex wavenumbers of the i=3,4 (n=0,1,2) wave modes in a cylinder: — analytical solutions; – – WFE results.

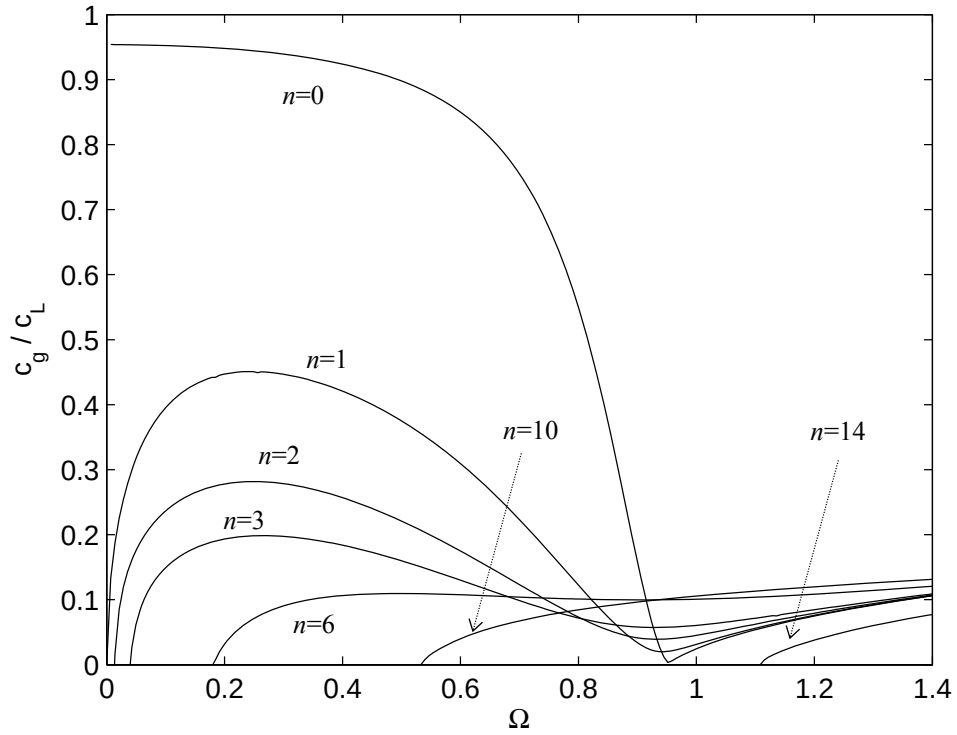

Figure 3.30: Group velocities associated with the i=1 (n=0,1,2,3,6,10,14) wave modes in a cylinder.

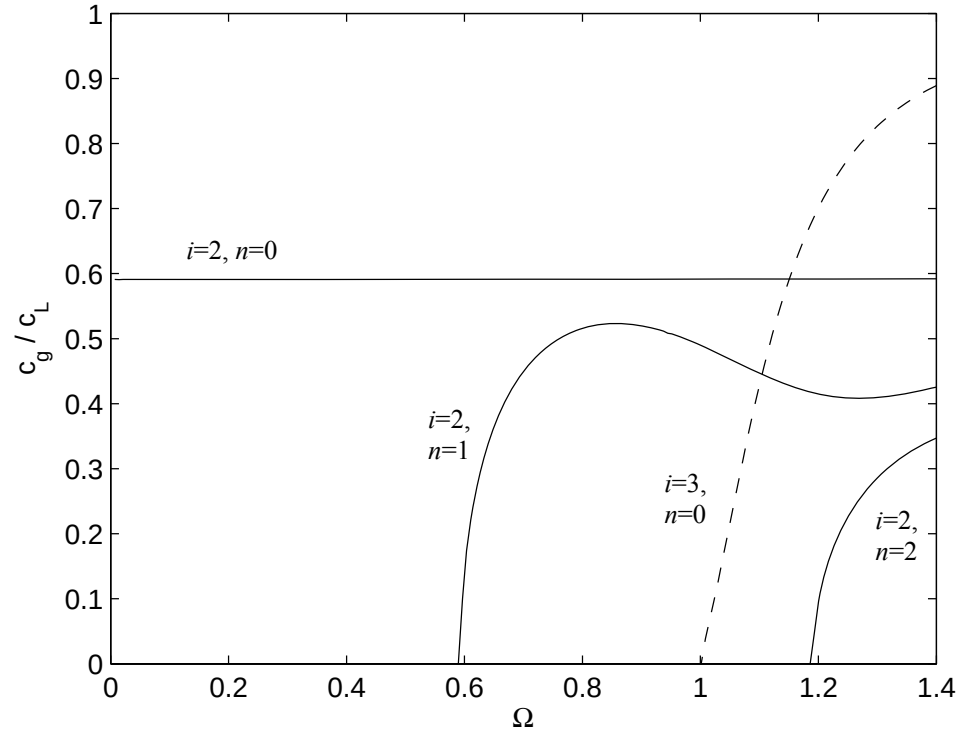

Figure 3.31: Group velocities associated with — the i=2 (n=0,1,2); – – the i=3 (n=0) wave modes in a cylinder.

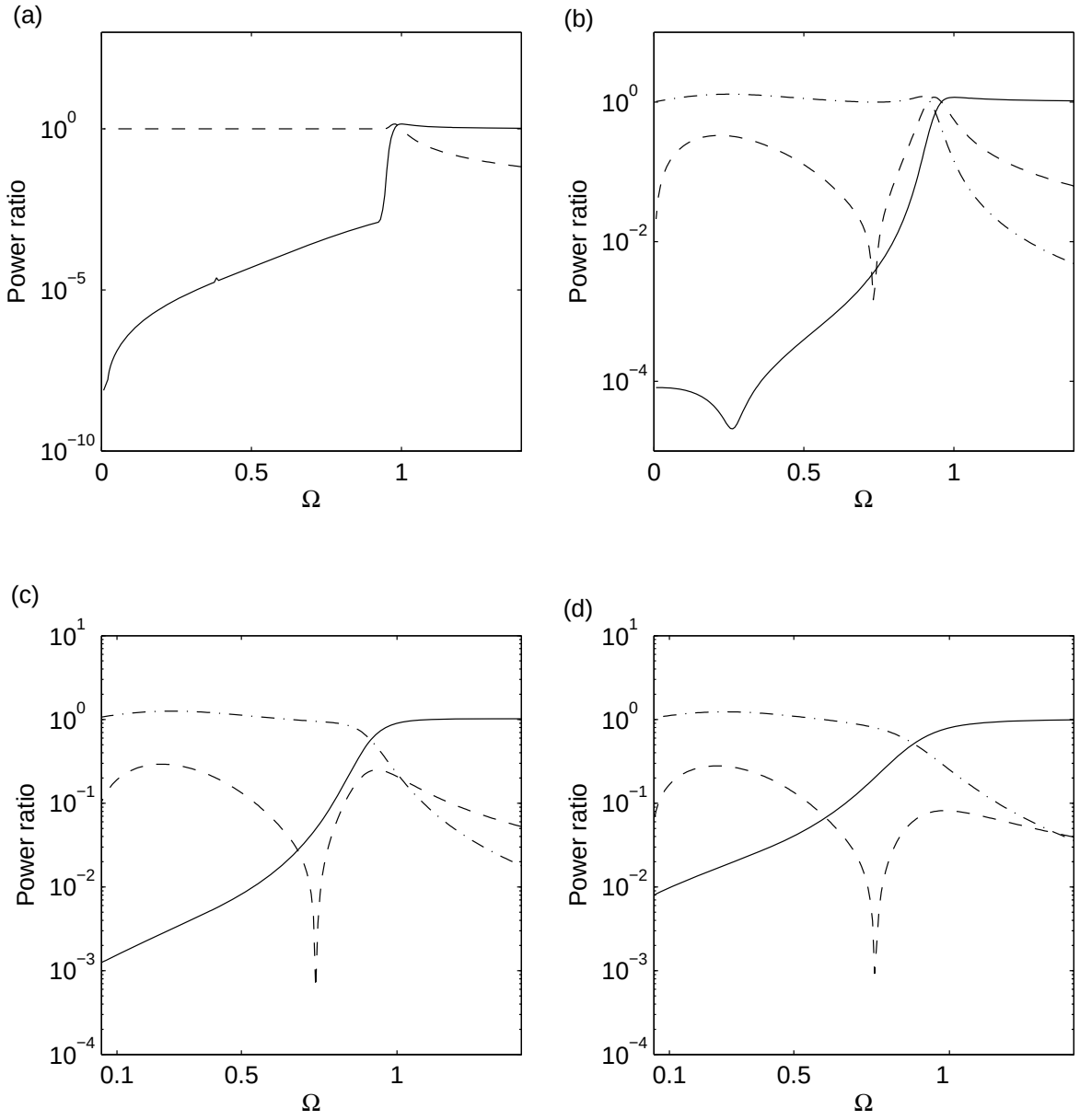

Figures 3.32: Power ratio for the i=1 wave modes in a cylinder calculated by analytical expressions: (a) n=0; (b) n=1; (c) n=2; (d) n=3. — P_f/P_s, – – P_{ex}/P_s, –·– P_{to}/P_s.

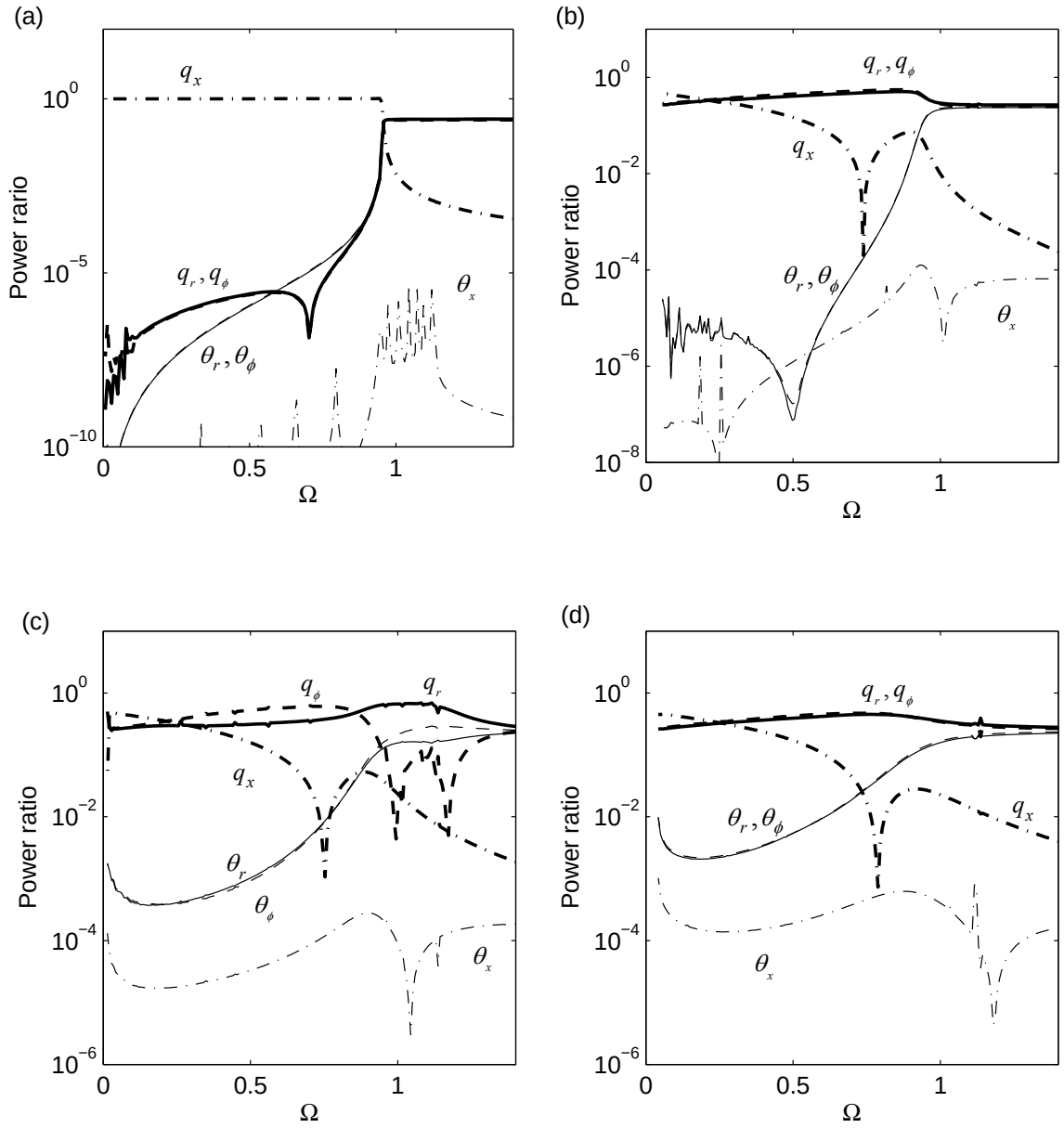

Figures 3.33: Power ratio associated with each variable for the i=1 wave modes in a cylinder using WFE results: (a) n=0; (b) n=1; (c) n=2; (d) n=3. $-\cdot-$ q_x, — q_r, – – q_ϕ, $-\cdot-$ θ_x, — θ_r, – – θ_ϕ.

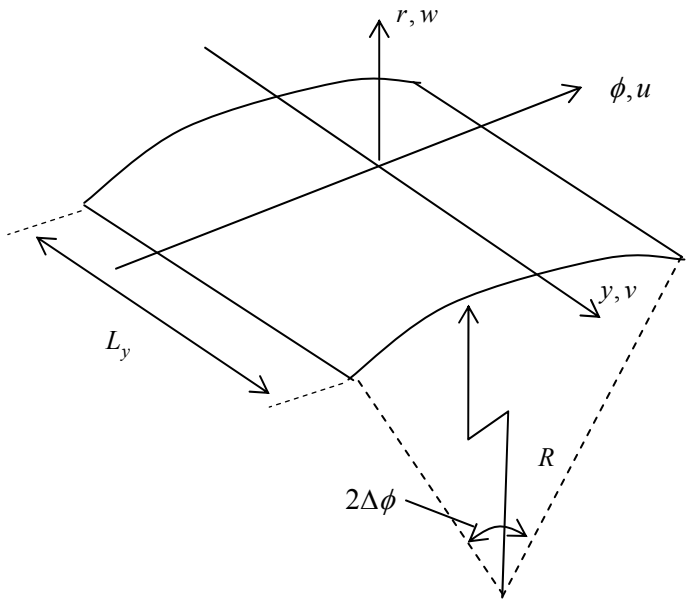

Figure 3.34: Section of a cylinder with finite length.

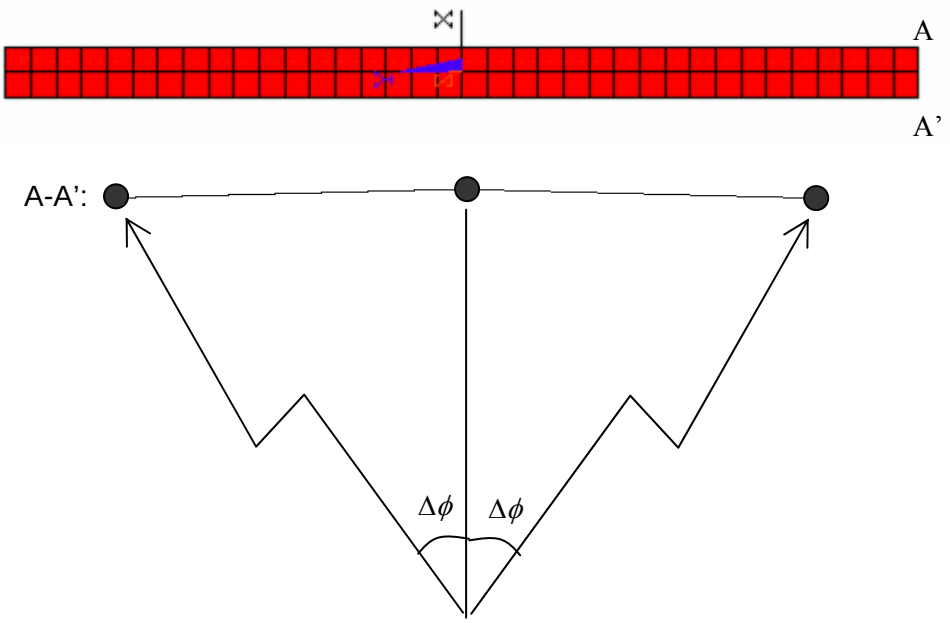

Figures 3.35: WFE model of a circumferential section of the cylinder using two series of the sections.

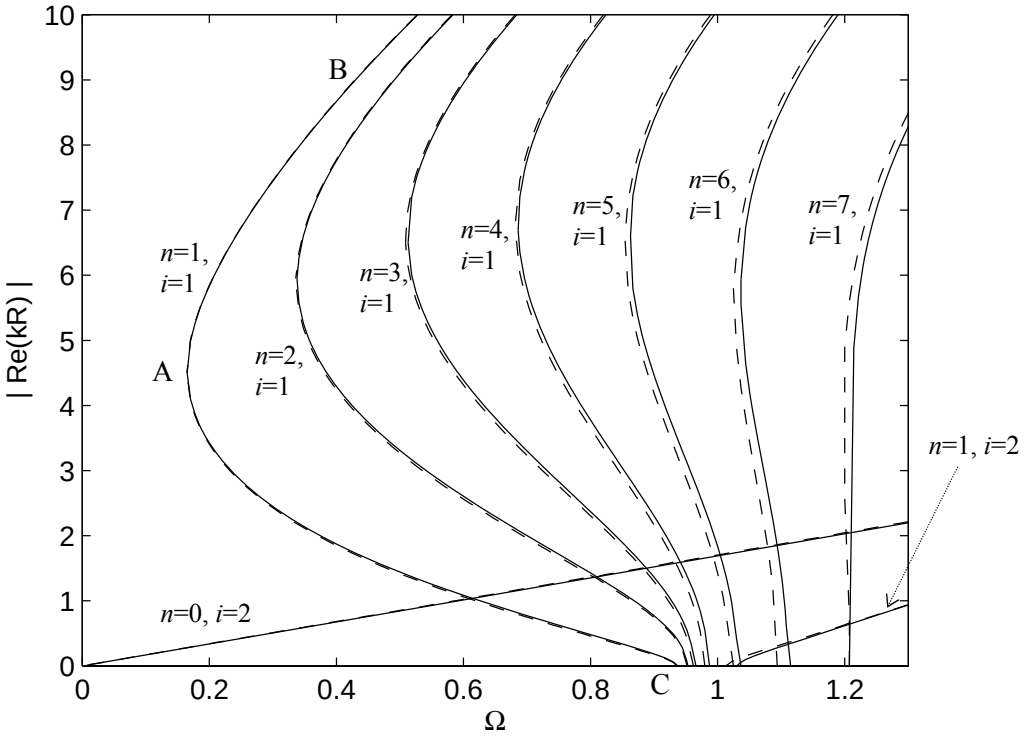

Figure 3.36: Dispersion curves for the propagating waves in a cylinder: — analytical solutions; – – WFE results.

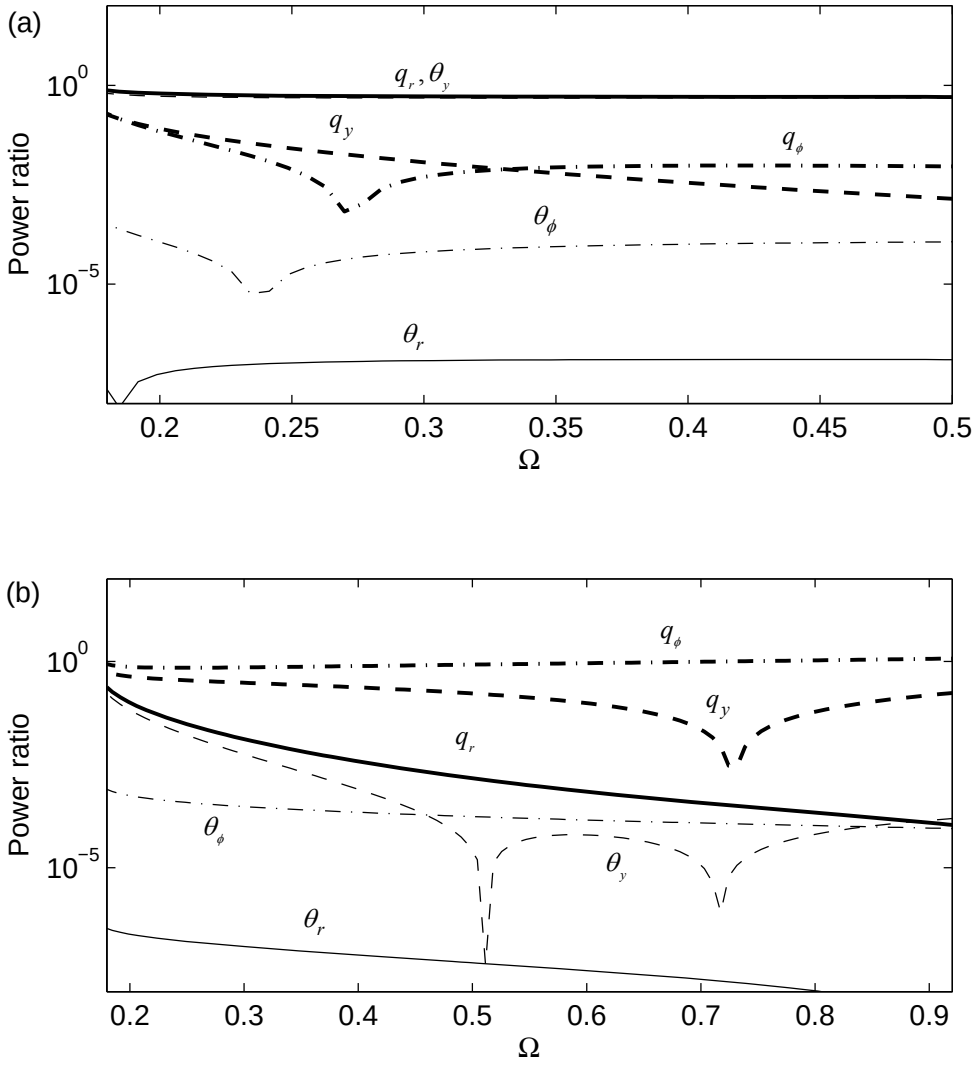

Figures 3.37: Power ratio associated with each variable for the i=1*, n*=1 *wave mode in a cylinder: (a) between points A and B; (b) between points A and C.* $-\cdot- q_\phi$, $-- q_y$, $— q_r$, $-\cdot- \theta_\phi$, $-- \theta_y$, $— \theta_r$.

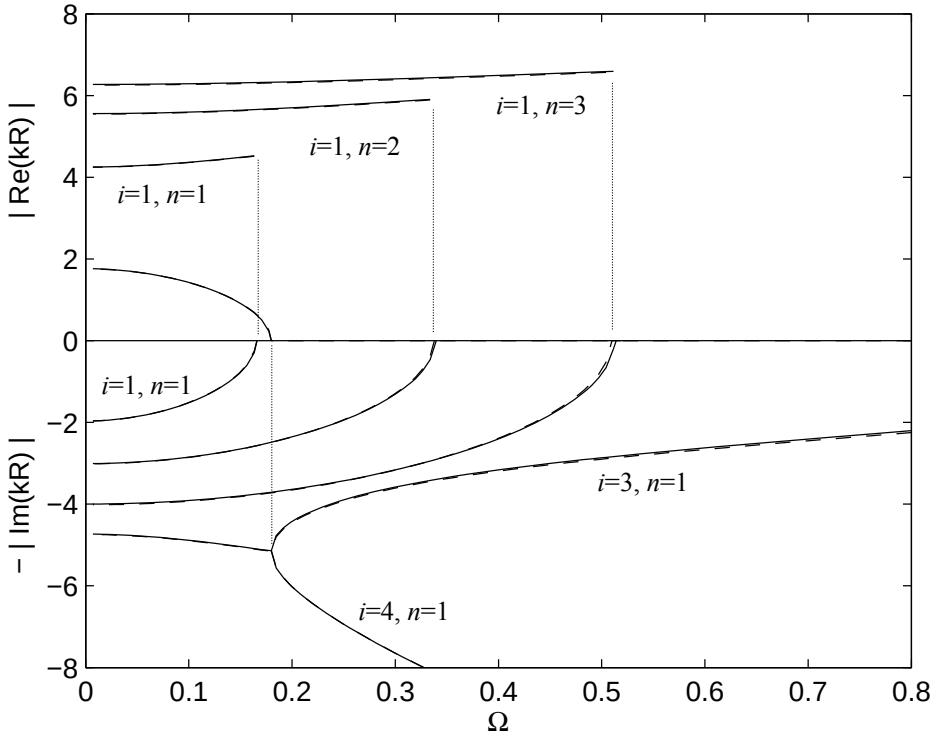

Figure 3.38: Dispersion curves for purely imaginary and complex conjugates wavenumbers for the i=1, n=1-3; i=3, n=1; i=4, n=1 wave modes in a cylinder: — analytical solutions; – – WFE results.

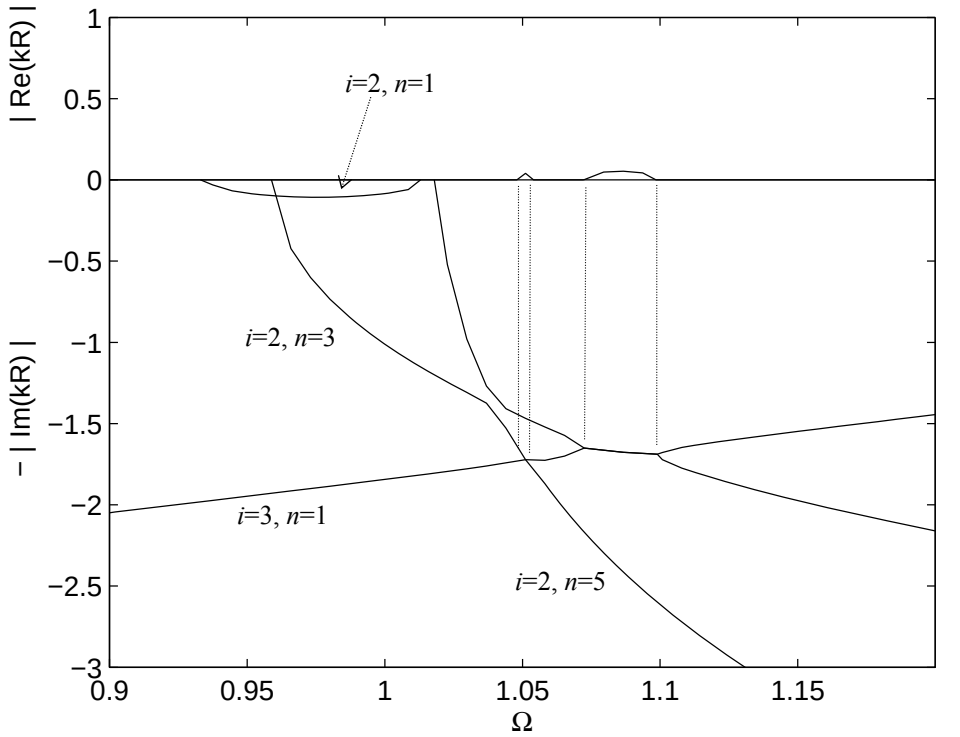

Figure 3.39: Dispersion curves for purely imaginary and complex conjugate wavenumbers for the i=2, n=1,3,5; i=3, n=1 (symmetric) wave modes in a cylinder. Only WFE results are shown.

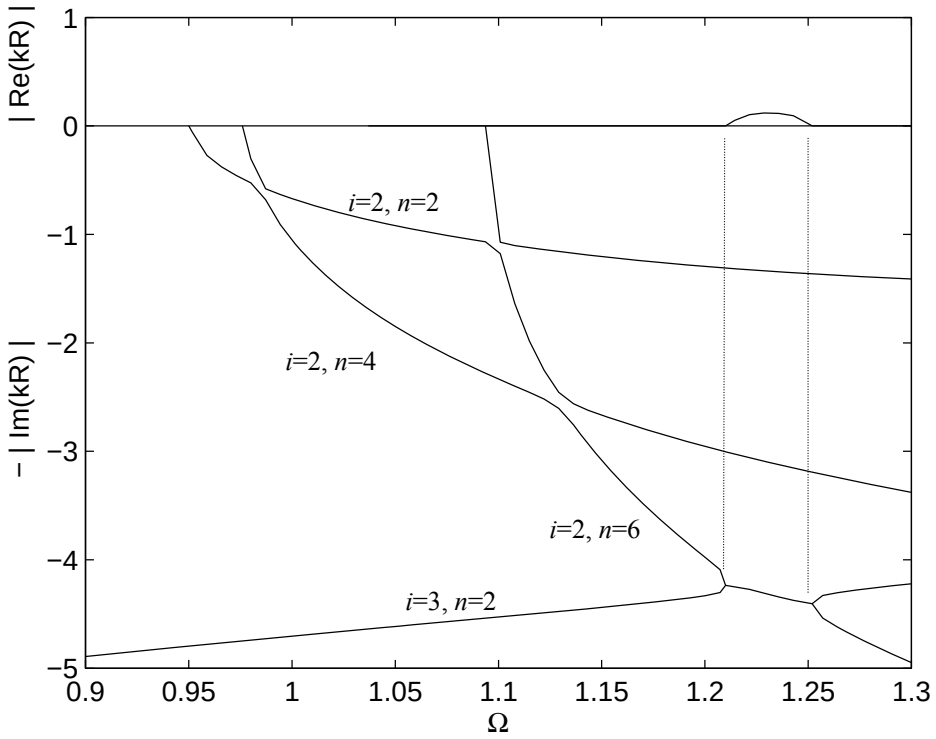

Figure 3.40: Dispersion curves for purely imaginary and complex conjugate wavenumbers for the i=2, n=2,4,6; i=3, n=2 (asymmetric) wave modes in a cylinder. Only WFE results are shown.

Chapter 4
FORCED RESPONSE CALCULATION USING THE WAVE APPROACH

4.1 Introduction

The forced response can be calculated from knowledge of the properties of freely propagating waves. In this chapter the wave approach is applied to calculate the forced response. The approach comprises three steps, i.e., (1) determining the amplitudes of directly excited waves of an infinite waveguide by excitation, (2) calculating the reflection coefficient matrix for boundaries and (3) superimposing wave amplitudes at a response point considering wave propagation and subsequent reflection. The procedure is illustrated in Figure 4.1. A numerical implementation for determining the amplitudes of the directly excited waves is proposed to reduce ill-conditioning.

Only a few papers describe the forced response of a waveguide using the wave properties, e.g. [14,22]. An approach based on the dynamic stiffness method was applied to a rod and an isotropic plate [9] and to a fluid filled pipe [61]. However, the approach might be ill-conditioned for general structures in which there are many wave modes. Another approach based on the modal decomposition method was applied to a tyre [7] but this approach is limited to specific boundary conditions for which the phase closure principle [3,12] can be explicitly drawn.

On the other hand, the wave approach illustrated in this chapter can be applied for any boundary conditions. The formulations, including a numerical implementation to reduce ill-conditioning, are first introduced. Illustrative examples of a beam, a plate and a cylinder are then presented. The case of a tyre is considered in chapter 5.

4.2 Formulations

Formulation by which the forced response is calculated using the wave approach is described in this section. The amplitudes of the directly excited waves are first determined. A numerical implementation to reduce ill-conditioning is proposed. The reflection coefficient matrix for boundaries is then derived. The total wave amplitude can then be formed by superposition. It should be noted that the wave approach is not a unique approach to the WFE method. As long as wavenumbers and associated wave modes in a waveguide are available, either analytical results or numerical results from, e.g., the spectral finite element methods can be used to find the forced response.

4.2.1 Forced Wave Amplitude: Wave Decomposition

An external force in the physical domain is first decomposed into the wave domain. When an external force is applied to an infinite waveguide shown in Figure 4.2, continuity of displacement and force equilibrium give in matrix form

$$\begin{bmatrix} \boldsymbol{\Phi}_q^+ & -\boldsymbol{\Phi}_q^- \\ \boldsymbol{\Phi}_f^+ & -\boldsymbol{\Phi}_f^- \end{bmatrix} \begin{bmatrix} \mathbf{e}^+ \\ \mathbf{e}^- \end{bmatrix} = \begin{bmatrix} \mathbf{0} \\ \mathbf{f}_{ext} \end{bmatrix} \tag{4.1}$$

where $\mathbf{e}^{\pm}$ are column vectors of directly excited wave amplitudes, $\mathbf{f}_{ext}$ is the external force vector and the matrices $\boldsymbol{\Phi}_q^{\pm}$, $\boldsymbol{\Phi}_f^{\pm}$ contain the displacement and force eigenvectors, i.e. $\boldsymbol{\Phi}_q^{\pm} = \begin{bmatrix} \mathbf{q}_1^{\pm} & \cdots & \mathbf{q}_n^{\pm} \end{bmatrix}$ and n is the number of wave modes. The excited wave amplitudes, $\mathbf{e}^{\pm}$, may be directly determined from equation (4.1) as

$$\begin{bmatrix} \mathbf{e}^+ \\ \mathbf{e}^- \end{bmatrix} = \begin{bmatrix} \boldsymbol{\Phi}_q^+ & -\boldsymbol{\Phi}_q^- \\ \boldsymbol{\Phi}_f^+ & -\boldsymbol{\Phi}_f^- \end{bmatrix}^{-1} \begin{bmatrix} \mathbf{0} \\ \mathbf{f}_{ext} \end{bmatrix}. \tag{4.2}$$

However, numerical problems are likely to occur for general structures because of ill-conditioning of the matrix to be inverted.

4.2.2 Forced Wave Amplitude: Numerical Implementation

A numerical implementation is here proposed which exploits the orthogonality of the left and right eigenvectors of the transfer matrix, i.e. equation (2.25). Premultiplying the left eigenvector matrix $\boldsymbol{\Psi}^{\pm}$ (equation (2.21)), where $\boldsymbol{\Psi}^{\pm\mathrm{T}} = \begin{bmatrix} \boldsymbol{\psi}_1^{\pm\mathrm{T}} & \cdots & \boldsymbol{\psi}_n^{\pm\mathrm{T}} \end{bmatrix}$, by equation (4.1) gives

$$\begin{bmatrix} \boldsymbol{\Psi}_f^+ & \boldsymbol{\Psi}_q^+ \\ \boldsymbol{\Psi}_f^- & \boldsymbol{\Psi}_q^- \end{bmatrix} \begin{bmatrix} \boldsymbol{\Phi}_q^+ & -\boldsymbol{\Phi}_q^- \\ \boldsymbol{\Phi}_f^+ & -\boldsymbol{\Phi}_f^- \end{bmatrix} \begin{bmatrix} \mathbf{e}^+ \\ \mathbf{e}^- \end{bmatrix} = \begin{bmatrix} \boldsymbol{\Psi}_f^+ & \boldsymbol{\Psi}_q^+ \\ \boldsymbol{\Psi}_f^- & \boldsymbol{\Psi}_q^- \end{bmatrix} \begin{bmatrix} \mathbf{0} \\ \mathbf{f}_{ext} \end{bmatrix}, \tag{4.3}$$

which gives

$$\begin{bmatrix} \boldsymbol{\Psi}^+\boldsymbol{\Phi}^+ & \mathbf{0} \\ \mathbf{0} & -\boldsymbol{\Psi}^-\boldsymbol{\Phi}^- \end{bmatrix} \begin{bmatrix} \mathbf{e}^+ \\ \mathbf{e}^- \end{bmatrix} = \begin{bmatrix} \boldsymbol{\Psi}_q^+\mathbf{f}_{ext} \\ \boldsymbol{\Psi}_q^-\mathbf{f}_{ext} \end{bmatrix}. \tag{4.4}$$

When all the eigenvalues are distinct, the orthogonality relationship (2.25) implies that

$$\boldsymbol{\Psi}^{\pm}\boldsymbol{\Phi}^{\pm} = diag\begin{pmatrix} d_1 & \cdots & d_n \end{pmatrix} \tag{4.5}$$

is the diagonal matrix. The eigenvectors can be normalised so that $d_i = 1$ and hence $\boldsymbol{\Psi}^{\pm}\boldsymbol{\Phi}^{\pm} = \mathbf{I}$. With these normalised eigenvectors, equation (4.4) becomes

$$\begin{aligned} \mathbf{e}^+ &= \boldsymbol{\Psi}_q^+\mathbf{f}_{ext}, \\ \mathbf{e}^- &= -\boldsymbol{\Psi}_q^-\mathbf{f}_{ext}. \end{aligned} \tag{4.6}$$

Equations (4.6) are always well-conditioned. Even if all the eigenvalues are not distinct, $\boldsymbol{\Psi}\boldsymbol{\Phi}$ is a block diagonal matrix and the ill-conditioning in equation (4.2) can be removed.

In practice, only the first $m\left(\leq n\right)$ waves might be retained, these being waves for which $\left|\mathrm{Im}\left(k\right)\right|$ are sufficiently small. The rapidly decaying waves often have a small contribution to the response. Numerical examples are shown in the subsequent sections.

4.2.3 Reflection Coefficient Matrix

The directly excited waves propagate along the waveguide. When the waveguide has boundaries, waves are reflected at the boundaries (see Figure 4.3). The wave change at the boundaries can be expressed by the reflection coefficient matrix $\mathbf{r}$ such that

$$\mathbf{a}^{-} = \mathbf{r}\mathbf{a}^{+} \tag{4.7}$$

where $\mathbf{a}^{\pm}$ is the wave amplitude vector. A boundary condition at a boundary can be in general written as [23]

$$\mathbf{A}\mathbf{f} + \mathbf{B}\mathbf{q} = \mathbf{0} \tag{4.8}$$

where **A** and **B** are matrices whose element may involve stiffness, damping, etc. and are in general complex and frequency dependent. The displacement and force vectors in equation (4.8) are expressed in terms of wave properties as

$$\begin{aligned} \mathbf{q} &= \mathbf{\Phi}_q^{+}\mathbf{a}^{+} + \mathbf{\Phi}_q^{-}\mathbf{a}^{-}, \\ \mathbf{f} &= \mathbf{\Phi}_f^{+}\mathbf{a}^{+} + \mathbf{\Phi}_f^{-}\mathbf{a}^{-}. \end{aligned} \tag{4.9}$$

Equations (4.7)-(4.9) lead to the reflection coefficient matrix as

$$\mathbf{r} = -\left(\mathbf{A}\mathbf{\Phi}_f^{-} + \mathbf{B}\mathbf{\Phi}_q^{-}\right)^{-1}\left(\mathbf{A}\mathbf{\Phi}_f^{+} + \mathbf{B}\mathbf{\Phi}_q^{+}\right). \tag{4.10}$$

The reflection coefficient matrix $\mathbf{r}$ gives the amplitudes of the reflected waves in terms of those of the incident waves. If $\mathbf{r}$ is a diagonal matrix, each wave mode reflects at the boundary without wave mode conversion. Finite, perhaps complex, off-diagonal terms in $\mathbf{r}$ represent wave mode conversion such that one type of incident wave will be scattered to other wave modes. In equation (4.10) pseudo matrix inverse is used to give matrix inverse if only m wave modes $(m < n)$ are retained.

4.2.4 Wave Propagation Matrix

The wave amplitudes will change as waves freely propagate in a waveguide as described by the wave propagation matrix. Using the notation in Figure 4.4, the wave propagation matrix $\boldsymbol{\tau}$ is such that

$$\begin{aligned} \mathbf{b}^{+} &= \boldsymbol{\tau}(l)\mathbf{a}^{+}, \\ \mathbf{a}^{-} &= \boldsymbol{\tau}(l)\mathbf{b}^{-} \end{aligned} \tag{4.11}$$

and

$$\boldsymbol{\tau}(l) = diag\left(e^{-jk_1 l}, e^{-jk_2 l}, \cdots, e^{-jk_n l}\right) \tag{4.12}$$

when waves propagate over a distance l in space and the waveguide has n wave components.

4.2.5 Total Wave Amplitude: Wave Superposition

The displacement of the waveguide is in general expressed as

$$\mathbf{q} = \sum_{i=1}^{n}\left(a_i^{+}\boldsymbol{\varphi}_{qi}^{+} + a_i^{-}\boldsymbol{\varphi}_{qi}^{-}\right). \tag{4.13}$$

The wave amplitudes $a_i^{\pm}$ can be determined considering the wave propagation and subsequent reflection. Consider a finite waveguide shown in Figure 4.5. The input response, $x_r = x_e$, is first determined where $x_{r,e}$ are the points where the response is calculated and the excitation is applied respectively. The wave amplitudes $\mathbf{a}^{\pm}$ are given from the sum of the directly excited waves and the travelling waves from left or right side, hence

$$\begin{aligned} \mathbf{a}^{+} &= \mathbf{e}^{+} + \mathbf{g}^{+}, \\ \mathbf{g}^{-} &= \mathbf{e}^{-} + \mathbf{a}^{-}. \end{aligned} \tag{4.14}$$

Using the wave propagation and reflection coefficient matrices, $\mathbf{a}^{+}$ in equations (4.14) can be expressed as

$$\mathbf{a}^{+} = \mathbf{e}^{+} + \boldsymbol{\tau}\left(x_e\right)\mathbf{r}_L\boldsymbol{\tau}\left(x_e\right)\mathbf{g}^{-} \tag{4.15}$$

such that

$$\mathbf{a}^{+} = \mathbf{e}^{+} + \boldsymbol{\tau}\left(x_e\right)\mathbf{r}_L\boldsymbol{\tau}\left(L\right)\mathbf{r}_R\boldsymbol{\tau}\left(L-x_e\right)\mathbf{a}^{+} + \boldsymbol{\tau}\left(x_e\right)\mathbf{r}_L\boldsymbol{\tau}\left(x_e\right)\mathbf{e}^{-}, \tag{4.16}$$

hence

$$\mathbf{a}^{+} = \left\{\mathbf{I} - \boldsymbol{\tau}\left(x_e\right)\mathbf{r}_L\boldsymbol{\tau}\left(L\right)\mathbf{r}_R\boldsymbol{\tau}\left(L-x_e\right)\right\}^{-1}\left\{\mathbf{e}^{+} + \boldsymbol{\tau}\left(x_e\right)\mathbf{r}_L\boldsymbol{\tau}\left(x_e\right)\mathbf{e}^{-}\right\} \tag{4.17}$$

where L is the total length of a waveguide. The negative going wave amplitude $\mathbf{a}^{-}$ can be obtained similarly as

$$\mathbf{a}^{-} = \left\{\mathbf{I} - \boldsymbol{\tau}\left(L-x_e\right)\mathbf{r}_R\boldsymbol{\tau}\left(L\right)\mathbf{r}_L\boldsymbol{\tau}\left(x_e\right)\right\}^{-1}\left\{\mathbf{e}^{-} + \boldsymbol{\tau}\left(L-x_e\right)\mathbf{r}_R\boldsymbol{\tau}\left(L-x_e\right)\mathbf{e}^{+}\right\} - \mathbf{e}^{-} \tag{4.18}$$

or using $\mathbf{a}^{+}$ as

$$\mathbf{a}^{-} = \boldsymbol{\tau}\left(L-x_e\right)\mathbf{r}_R\boldsymbol{\tau}\left(L-x_e\right)\mathbf{a}^{+}. \tag{4.19}$$

The total displacement at the excitation point can then be obtained by substituting equations (4.17) and (4.19) together with the wave modes $\boldsymbol{\varphi}_q^{\pm}$ into equation (4.13).

The transfer response may be obtained from $\mathbf{a}^{+}$ as

$$\mathbf{b}^{+} = \boldsymbol{\tau}\left(x_r - x_e\right)\mathbf{a}^{+} \tag{4.20}$$

and

$$\mathbf{b}^{-} = \boldsymbol{\tau}\left(L-x_r\right)\mathbf{r}_R\boldsymbol{\tau}\left(L-x_r\right)\mathbf{b}^{+}. \tag{4.21}$$

When the waveguide is closed such as a ring shown in Figure 4.6, there is no reflection coefficient matrix. The polar wavenumber (the phase change per unit radian) may be used for convenience. The polar wavenumber is defined as

$$k^{*} = kR \tag{4.22}$$

where R is the radius of the waveguide. By using the polar wavenumbers, the input response $\mathbf{a}^{\pm}$ can be expressed as

$$\begin{aligned}\mathbf{a}^{+} &= \left\{\mathbf{I}-\boldsymbol{\tau}^{*}\left(2\pi\right)\right\}^{-1}\mathbf{e}^{+},\\ \mathbf{a}^{-} &= \left\{\mathbf{I}-\boldsymbol{\tau}^{*}\left(2\pi\right)\right\}^{-1}\mathbf{e}^{-}-\mathbf{e}^{-}\end{aligned} \tag{4.23}$$

where $\boldsymbol{\tau}^{*}\left(\phi\right)=diag\left(e^{-jk_1^{*}\phi},e^{-jk_2^{*}\phi},\cdots,e^{-jk_n^{*}\phi}\right)$ is the wave propagation matrix for the polar wavenumbers instead of equation (4.12). Transfer responses are given as

$$\begin{aligned}\mathbf{b}^{+} &= \boldsymbol{\tau}^{*}\left(\phi_r\right)\mathbf{a}^{+},\\ \mathbf{b}^{-} &= \boldsymbol{\tau}^{*}\left(2\pi-\phi_r\right)\left(\mathbf{a}^{-}+\mathbf{e}^{-}\right)\end{aligned} \tag{4.24}$$

where ϕ_r is the angle between the excitation and the response point.

4.3 Numerical Examples

The forced response is calculated for simple waveguides using the wave approach described in the previous section. The response of a beam, a plate and a cylinder are considered where either an analytical solution or an explicit formulation using modal decomposition can be found. Throughout this section, proportional damping is assumed such that the Young's modulus becomes $E\left(1+j\eta\right)$. The value of $\eta=0.03$ is applied. The wavenumbers and wave modes then become complex.

4.3.1 Euler-Bernoulli Beam with Sliding Boundary Conditions

As an illustrative example, the forced response of the Euler-Bernoulli beam with sliding boundary conditions at both ends shown in Figure 4.7 is considered. The sliding boundary condition constrains the rotation and the shear force to be zero and the beam has a rigid body mode.

The procedures of the wave approach are followed to give the forced response. The method starts from determining the amplitudes of directly excited waves, i.e. equation (4.6). For the beam, $\boldsymbol{\Psi}^{+}\boldsymbol{\Phi}^{+}$ becomes, i.e. from equations (2.28) ,

$$\boldsymbol{\Psi}^{+}\boldsymbol{\Phi}^{+}=\begin{bmatrix} jEIk_B^3 & -EIk_B^2 & 1 & jk_B \\ -EIk_B^3 & EIk_B^2 & 1 & k_B \end{bmatrix}\begin{bmatrix} 1 & 1 \\ -jk_B & -k_B \\ jEIk_B^3 & -EIk_B^3 \\ EIk_B^2 & -EIk_B^2 \end{bmatrix}=\begin{bmatrix} 4jEIk_B^3 & 0 \\ 0 & -4EIk_B^3 \end{bmatrix}. \tag{4.25}$$

The first element of the vector of the wave amplitudes is associated with the propagating wave and the second with the nearfield wave. Similarly, $\boldsymbol{\Psi}^{-}\boldsymbol{\Phi}^{-}=diag\left(-4jEIk_B^3,\quad 4EIk_B^3\right)$ for the negative-going waves. For a point force excitation such that $\mathbf{f}^{\mathrm{T}}=\begin{bmatrix}1 & 0\end{bmatrix}$, equations (4.6) then give

$$\begin{aligned} \mathbf{e}^{+} &= \boldsymbol{\Psi}_q^{+}\begin{bmatrix}1\\0\end{bmatrix}=\frac{1}{4jEIk_B^3}\begin{bmatrix}1\\-j\end{bmatrix}, \\ \mathbf{e}^{-} &= -\boldsymbol{\Psi}_q^{-}\begin{bmatrix}1\\0\end{bmatrix}=\frac{1}{4jEIk_B^3}\begin{bmatrix}1\\-j\end{bmatrix} \end{aligned} \tag{4.26}$$

using the normalised eigenvectors. The positive- and negative-going waves with the same amplitudes are generated by the external force. The results (4.26) are same as those given analytically [13].

The reflection coefficient at the boundary is next calculated. For the sliding condition, both the rotation and the shear force are zero at the boundaries so that equation (4.8) becomes

$$\begin{bmatrix}0 & 0\\ 1 & 0\end{bmatrix}\begin{bmatrix}f\\m\end{bmatrix}+\begin{bmatrix}0 & 1\\ 0 & 0\end{bmatrix}\begin{bmatrix}w\\\theta\end{bmatrix}=\begin{bmatrix}0\\0\end{bmatrix}. \tag{4.27}$$

The reflection coefficient matrix in equation (4.10) then becomes

$$\begin{aligned}\mathbf{r} = &-\left(\begin{bmatrix}0 & 0\\ 1 & 0\end{bmatrix}\begin{bmatrix}-jEIk_B^3 & EIk_B^3\\ -EIk_B^2 & EIk_B^2\end{bmatrix}+\begin{bmatrix}0 & 1\\ 0 & 0\end{bmatrix}\begin{bmatrix}1 & 1\\ jk_B & k_B\end{bmatrix}\right)^{-1}\cdot\\ &\left(\begin{bmatrix}0 & 0\\ 1 & 0\end{bmatrix}\begin{bmatrix}jEIk_B^3 & -EIk_B^3\\ -EIk_B^2 & EIk_B^2\end{bmatrix}+\begin{bmatrix}0 & 1\\ 0 & 0\end{bmatrix}\begin{bmatrix}1 & 1\\ -jk_B & -k_B\end{bmatrix}\right)\\ =&\begin{bmatrix}1 & 0\\ 0 & 1\end{bmatrix}\end{aligned} \tag{4.28}$$

and both the propagating and nearfield waves reflect with the same amplitude, without phase change at the boundaries and without wave mode conversion.

For the input response $x_r = x_e$, $\mathbf{a}^+ + \mathbf{a}^-$ in equations (4.17) and (4.19) becomes, after some calculations,

$$\mathbf{a}^+ + \mathbf{a}^- = \frac{1}{4jEIk_B^3}\begin{bmatrix}\dfrac{1}{1-e^{-2jk_BL}}\left(1+e^{-2jk_Bx_e}\right)\left(1+e^{-2jk_B(L-x_e)}\right)\\ \dfrac{1}{1-e^{-2k_BL}}\left(1+e^{-2k_Bx_e}\right)\left(1+e^{-2k_B(L-x_e)}\right)\end{bmatrix}. \tag{4.29}$$

The first row is the amplitude of the propagating wave while the second row is that of the nearfield wave. The sum of the first and the second row gives the displacement at the input point. It should be noted that $k_BL = 0, \pm 2\pi, \pm 4\pi \cdots$ gives an infinite response. This is equivalent to the phase closure principle and the response becomes infinity for undamped waveguides.

These procedures are now numerically evaluated using the WFE method and the results compared with the analytical solution (4.29). The properties are set to be $EI = 1$, $\rho A = 1$ and $x_e = 0.44L$. Figures 4.8 and 4.9 show the input mobility of the beam using the different element length $\Delta = L/6$ and $\Delta = L/10^4$ respectively. The abscissa is the non-dimensional frequency $\left(k_BL\right)^2$ which is proportional to frequency and resonances occur at $\left(k_BL\right)^2 = \left(n\pi\right)^2$ for $n = 0,1,2\cdots$.

Consequences of the numerical errors discussed in section 2.4 can be seen. When the length of the FE is large ($\Delta = L/6$, Figure 4.8), the discrepancy becomes large at high frequencies due to the FE discretisation error but good agreement can be seen at low

frequencies. By using a small element length ($\Delta = L/10^4$, Figure 4.9), the response at low frequencies breaks down because of the error due to round-off of inertia terms.

4.3.2 Thin Plate with Simply-supported Boundaries

The forced response of a thin plate with all edges simply-supported shown in Figure 4.10 is considered. The locations where the point excitation is applied and the response is calculated are (x_e, y_e) and (x_r, y_r) respectively. The response using the modal decomposition method can be expressed as [120]

$$w(x_r, y_r) = \frac{4 f_{ext}}{\rho h L_x L_y} \sum_{m=1}^{\infty} \sum_{n=1}^{\infty} \frac{\phi_{mn}(x_r, y_r)\phi_{mn}(x_e, y_e)}{\left\{\omega_{mn}^2 (1 + j\eta) - \omega^2\right\}} \tag{4.30}$$

where

$$\phi_{mn}(x, y) = \sin(m\pi x / L_x)\sin(n\pi y / L_y) \tag{4.31}$$

and

$$\omega_{mn} = \pi^2 \sqrt{D/\rho h}\left\{(m/L_x)^2 + (n/L_y)^2\right\}. \tag{4.32}$$

The plate is assumed to be steel $(E = 2.0 \cdot 10^{11}, \rho = 7800, \nu = 0.3)$ with $L_x = 0.6, L_y = 0.18$ and the thickness $h = 0.0018$, all in SI units.

The plate strip model with 18 elements across the cross-section $(\Delta_x = \Delta_y = 10mm)$ is used. Since the model has 106 DOFs, 106 wave modes can be obtained at each given frequency. In practice, only some wave modes with sufficiently small $|\mathrm{Im}(k_x)|$ are retained to calculate the forced response. It should be noted that all propagating waves should be retained by carefully choosing Δ_x as stated in subsection 2.4.1. Most wave modes are strongly decaying waves at each frequency and the contribution of such wave modes to the forced response is often very small. In addition, such wave modes are likely to be numerically inaccurate because of the FE discretisation error.

Figure 4.11 shows the magnitude of the input mobility (at the point A in Figure 4.10) calculated by both the wave approach and the modal decomposition method. The abscissa is the non-dimensional frequency $\Omega = L_y^2 / \pi^2 \sqrt{\rho h / D}\ \omega$.

The waves associated with $\left|\mathrm{Re}\left(k\Delta\right)\right|<1$ and $\left|\mathrm{Im}\left(k\Delta\right)\right|<1$ are retained for the WFE result, which are all propagating waves and few nearfield waves with small $\left|\mathrm{Im}\left(k\right)\right|$. In the frequency range shown, only about 8 (positive- and negative-going wave) pairs of wave modes are retained, which are all the propagating waves and some of the nearfield waves. On the other hand for the modal solution, the number of the modes included is about 1000. Reasonable agreement can be seen for the frequency range analysed. The first wave mode cuts-on at $\Omega=1$ and successive peaks for $1<\Omega<4$ are associated with the first wave mode. At $\Omega=4$ the second wave mode cuts-on. The response asymptotes to $Y_\infty=1/8\sqrt{D\rho h}\approx 0.0032$ [2] at high enough frequencies. Figure 4.12 shows the input mobility calculated in the same manner over a wide frequency range. The 10th wave mode cuts-on at $\Omega=100$, for example, and only 3.6 elements are associated with one wavelength for the wave mode across the plate strip. Above $\Omega=30$ or so a consistent discrepancy can be therefore seen due to the FE discretisation error, however, the frequency averaged response still shows more-or-less reasonable agreement.

If all the wave modes are included to calculate the response, the result breaks down as shown in Figure 4.13. This is because rapidly decaying nearfield waves are inaccurately estimated and such waves can contaminate the whole predicted response. It is therefore crucial to retain only the wave modes which are reasonably accurately predicted.

On the other hand, Figure 4.14 shows the input mobility calculated by retaining only the waves associated with $\mathrm{Re}\left|k_x\Delta_x\right|<1$, $\mathrm{Im}\left|k_x\Delta_x\right|<0.2$ such that at most 5 pairs of wave modes are retained. Regardless of such small numbers of wave modes, the response still shows reasonable agreement. Discrepancies can be seen at anti-resonances and below the first resonance $\Omega<1$ where the stiffness dominates the system.

When the transfer response is of concern, the effect of the nearfield waves is much smaller than that for the input response. Figure 4.15 shows the transfer mobility at the response point B (Figure 4.10) using the same wave modes, i.e. $\left|\mathrm{Re}\left(k_x\Delta_x\right)\right|<1$, $\left|\mathrm{Im}\left(k_x\Delta_x\right)\right|<0.2$. Good agreement can be seen. As the amplitude of the nearfield wave decays to 0.1% in one wavelength, the transfer response is dominated by propagating waves. This result implies that only a few nearfield waves with small $\left|\mathrm{Im}\left(k\right)\right|$ are important in determining the transfer response.

The forced response of the plate at $\Omega = 21.8$ are shown for different proportional damping η. The case of $\eta = 0.01, 0.03, 0.1$ are shown in Figures 4.16-4.18. The results are calculated using wave modes for which $\left|\mathrm{Re}\left(k_x \Delta_x\right)\right| < 1$, $\left|\mathrm{Im}\left(k_x \Delta_x\right)\right| < 1$. It can be seen that when the damping is small as shown in Figure 4.16, the response is dominated by the response of the mode for which $(m,n) = (8,4)$. As the damping increases, the modal overlap becomes large and more modes contribute to the response. For $\eta = 0.03$ as shown in Figure 4.17, the response becomes significant around the excitation. For $\eta = 0.1$ as shown in Figure 4.18, the response approaches that in an infinite plate [13].

4.3.3 Finite Cylinder

The forced response of a cylinder is considered as shown in Figure 4.19. The boundary conditions along the edges are taken to be same as those defined in subsection 3.7.4 such that $w = m_y = u = \sigma_y = 0$, equation (3.48).

Under the boundary conditions, approximate analytical mode shapes can be obtained and the response in the *r*-direction for point force excitation can be calculated using modal decomposition [120] as

$$w\left(y_{res}, \varphi_{res}\right) = \frac{2 f_{ext}}{\rho h R L_y \pi} \sum_{m=1}^{\infty} \sum_{n=0}^{\infty} \frac{\sin\left(m\pi y_e / L_y\right) \sin\left(m\pi y_{res} / L_y\right) \cos n\left(\varphi_e - \varphi_{res}\right)}{\varepsilon_n \left\{\omega_{mn}^2 \left(1 + j\eta\right) - \omega^2\right\}} \tag{4.33}$$

and $\varepsilon_0 = 2, \varepsilon_n = 1 \left(n \neq 0\right)$. The subscript '*res*' is used here to represent the response point for clarity. The same material properties as the plate in the previous subsection are assumed for the cylinder with $L_y = 0.18$ and $R = 0.1$.

The cylinder is uniform in two directions, i.e. in the circumferential (φ-) and the axial (y-) directions. The WFE model can therefore be formed in either direction as shown in Figure 4.20. For a short cylinder a WFE model in the φ-direction as shown in Figure 4.20(a) might be preferable as the number of DOF can be smaller considering the FE discretisation error. The WFE model shown in subsection 3.7.5 was also used here and the number of element along the axis of the cylinder was 36. It should be noted that the modal solution is approximate since the displacement do not exactly satisfy the stress and displacement at

boundaries [117] as discussed in subsection 3.7.5. The WFE method may therefore provide more accurate results.

The input mobility calculated by the wave approach and the modal decomposition is shown in Figure 4.21. The waves associated with $\left|\mathrm{Re}\left(k^*\Delta_\varphi\right)\right|<1$ and $\left|\mathrm{Im}\left(k^*\Delta_\varphi\right)\right|<1$ are retained and the number of (positive- and negative-going) wave mode pairs is about 75. For the modal solution about 4000 modes were used for convergence. The abscissa represents the non-dimensional frequency $\Omega=\omega/\omega_r$, equation (3.39). For a cylinder, the modal density becomes high around the ring frequency, $\Omega=1$. At high enough frequencies $\Omega \gg 1$, the response asymptotes to that of a flat plate such that $Y_\infty=1/8\sqrt{D\rho h}\approx 0.0032$ [2].

It is of interest to see the input mobility using limiting number of waves. Figure 4.22 shows the input mobility using waves for which $\left|\mathrm{Re}\left(k^*\Delta_\varphi\right)\right|<1$ and $\left|\mathrm{Im}\left(k^*\Delta_\varphi\right)\right|<0.75$. Only about 60 pairs of wave modes are retained and about 15 pairs of rapidly decaying wave modes are excluded compared to the result using waves for which $\left|\mathrm{Im}\left(k^*\Delta_\varphi\right)\right|<1$. Although the number of the wave modes decreases, such implementation seems reasonable because some wave modes around $\left|\mathrm{Im}\left(k^*\Delta_\varphi\right)\right|\approx 1$ are inaccurately predicted.

The well-conditioned formulation for determining the amplitudes of the directly excited waves proposed in equation (4.6) are used to reduce numerical results. Figure 4.23 shows an example of the input mobility calculated using the original formulation (4.2). It can be seen that the results using the original formulation (4.2) are very inaccurate because of the ill-conditioning. Use of the well-conditioned formulation (4.6) is therefore necessarily for general waveguides.

4.4 Conclusions

In this chapter the formulation of calculating the forced response using the wave approach was described. In particular the well-conditioned formulation for determining the amplitudes of directly excited waves was proposed using the orthogonality relationship between the left and right eigenvectors. The wave amplitude in finite structures was explicitly shown using the wave propagation, reflection coefficient matrices.

Numerical examples of a beam, a plate and a cylinder were shown. For the beam vibration the analytical solution holds and the predicted response was compared with the analytical solution. The effects of numerical errors occurring in the WFE results have been shown. For the plate vibration, there are inherently an infinite numbers of wave modes. Since the plate strip was modelled using FEs only a finite number of wave modes are considered in which there are a few propagating and some nearfield waves. The effect of the inclusion of rapidly decaying nearfield waves with large $\left|\mathrm{Im}\left(k\right)\right|$ was discussed. In general, the rapidly decaying waves contribute to the response insignificantly, in particular for the transfer response. The inclusion of the rapidly decaying waves may even break down the whole response because the rapidly decaying waves are likely to be inaccurately predicted. Similar effects were observed for the cylinder vibration. The well-conditioned formulation for determining the amplitudes of directly excited waves was evaluated for the cylinder example.

(1) Determine the amplitudes of directly excited waves in an infinite waveguide by an external force.

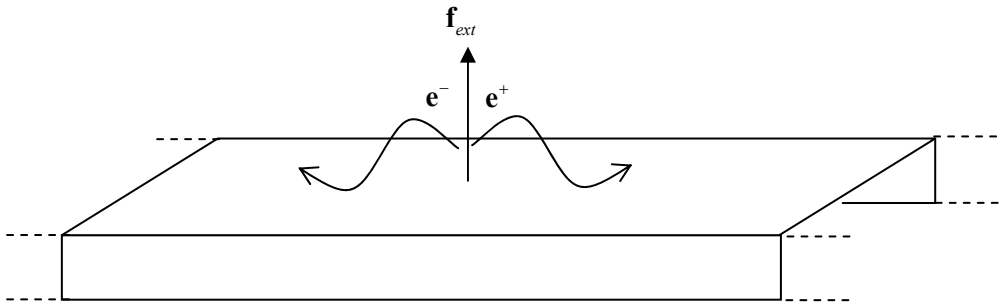

(2) Derive the reflection coefficient matrix at boundaries.

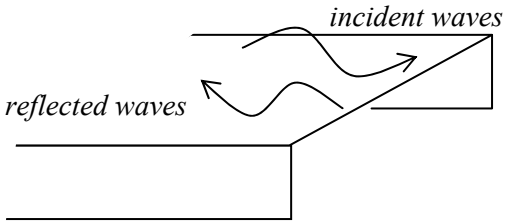

(3) Superimpose wave amplitudes at a response point

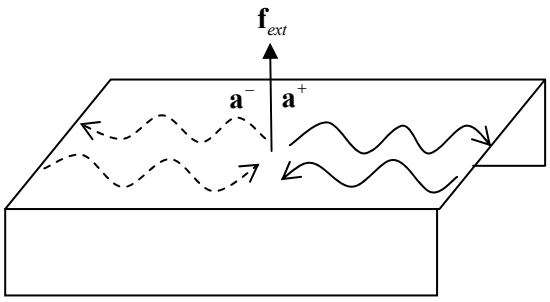

Figure 4.1: Procedure of forced response calculation using the wave approach.

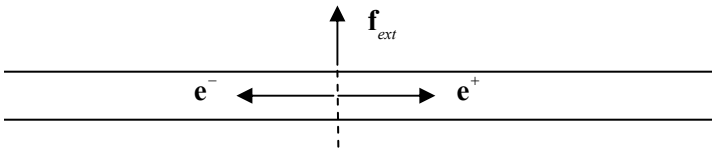

Figure 4.2: Waves directly excited by local harmonic excitation applied at a point.

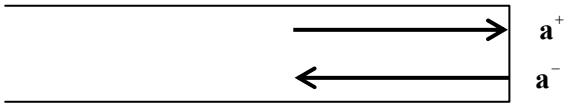

Figure 4.3: Wave reflection at a boundary.

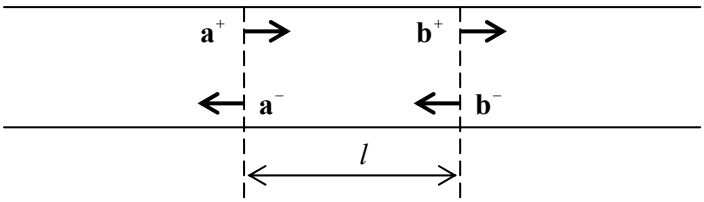

Figure 4.4: Wave propagation in a waveguide.

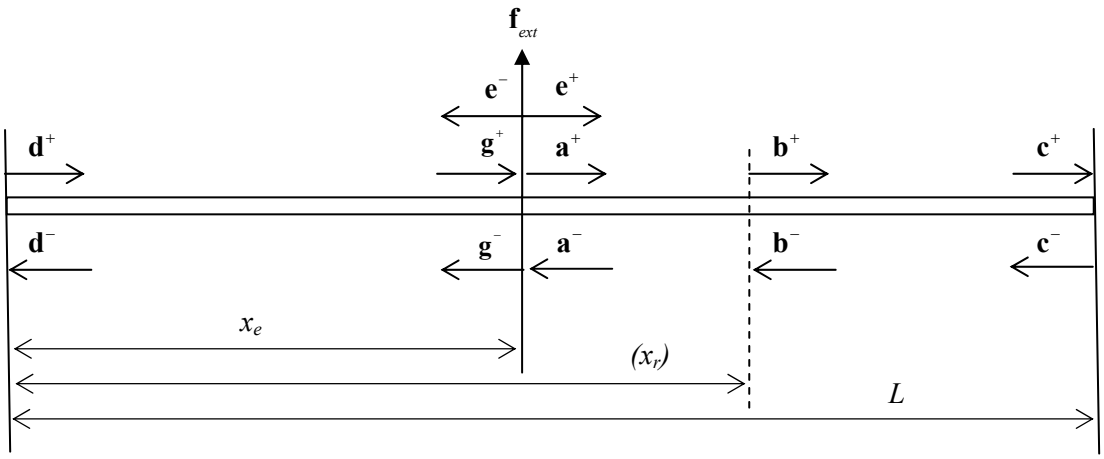

Figure 4.5: Wave amplitudes in a finite structure.

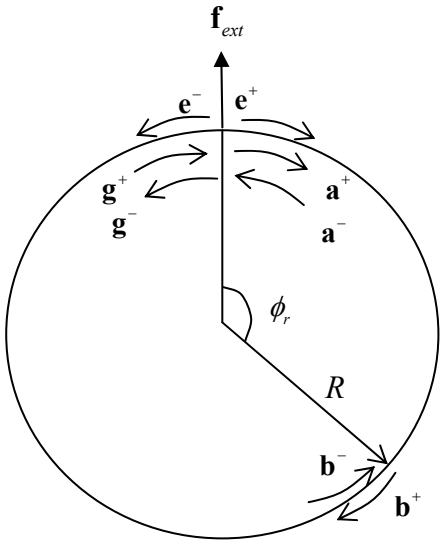

Figure 4.6: Wave amplitudes in a ring.

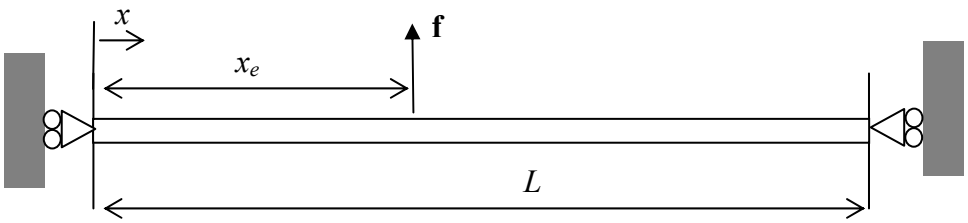

Figure 4.7: The beam with sliding boundary conditions at both ends.

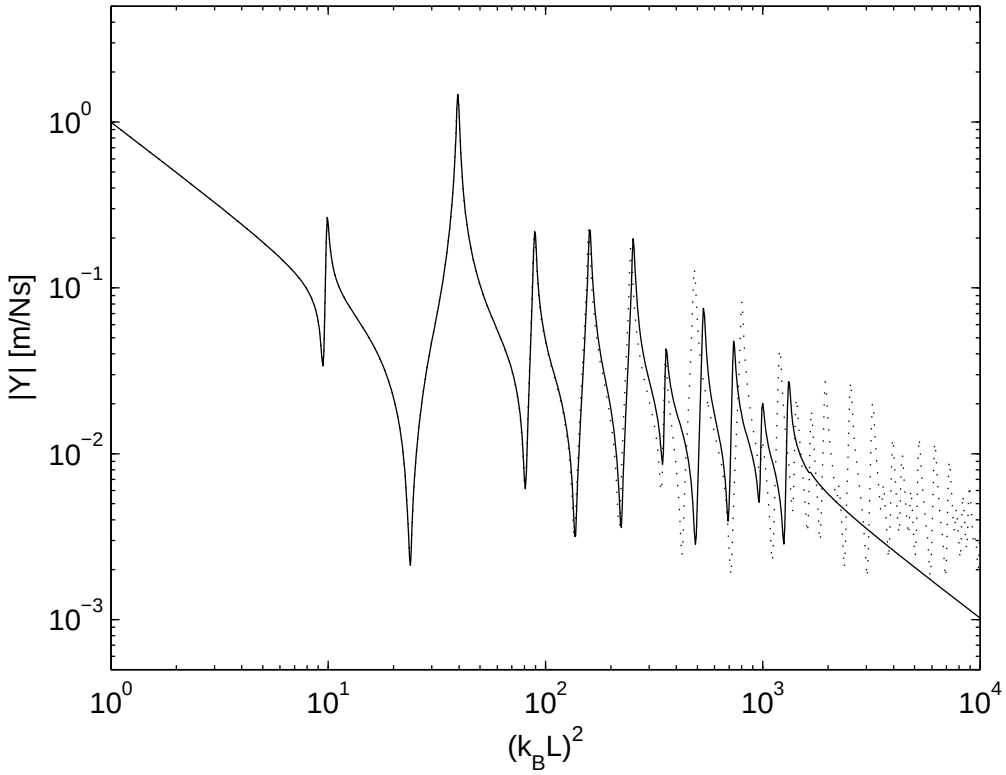

Figure 4.8: Magnitude of the input mobility of the beam: — WFE result $(\Delta = L/6)$; ···· analytical solution.

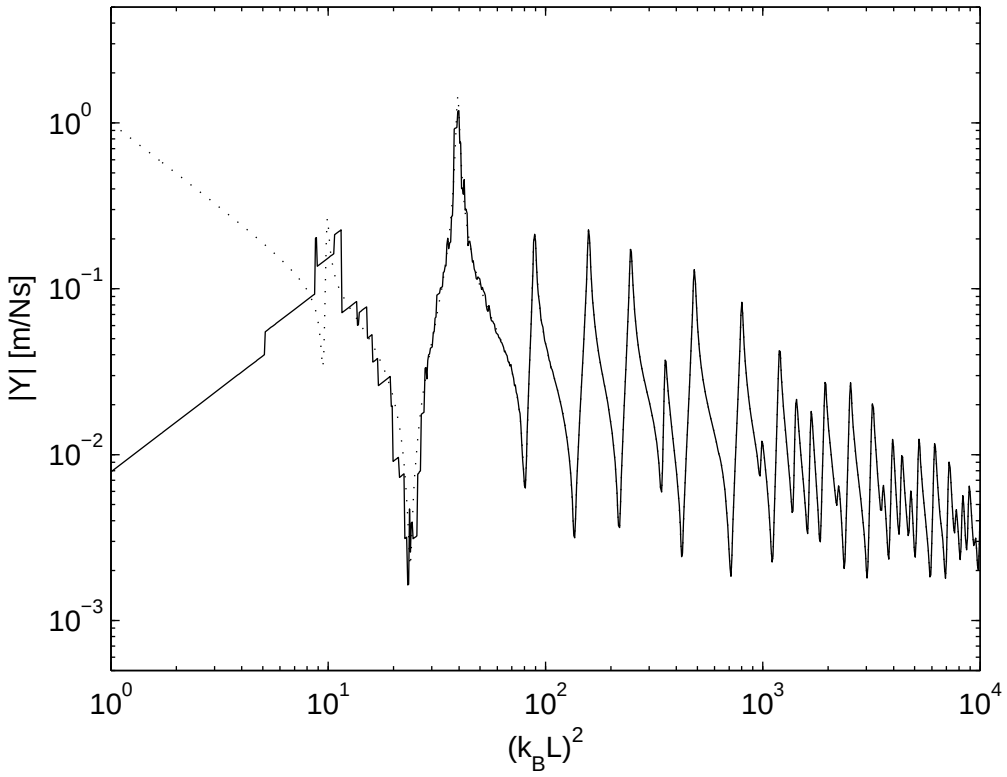

Figure 4.9: Magnitude of the input mobility of the beam over wide frequency range: — WFE result $\left(\Delta = L/10^4\right)$*; ···· analytical solution.*

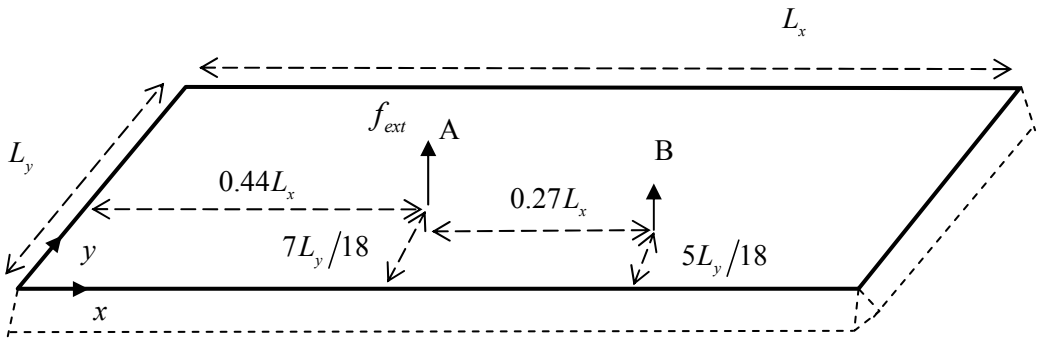

Figure 4.10: A thin plate with all edges simply-supported.

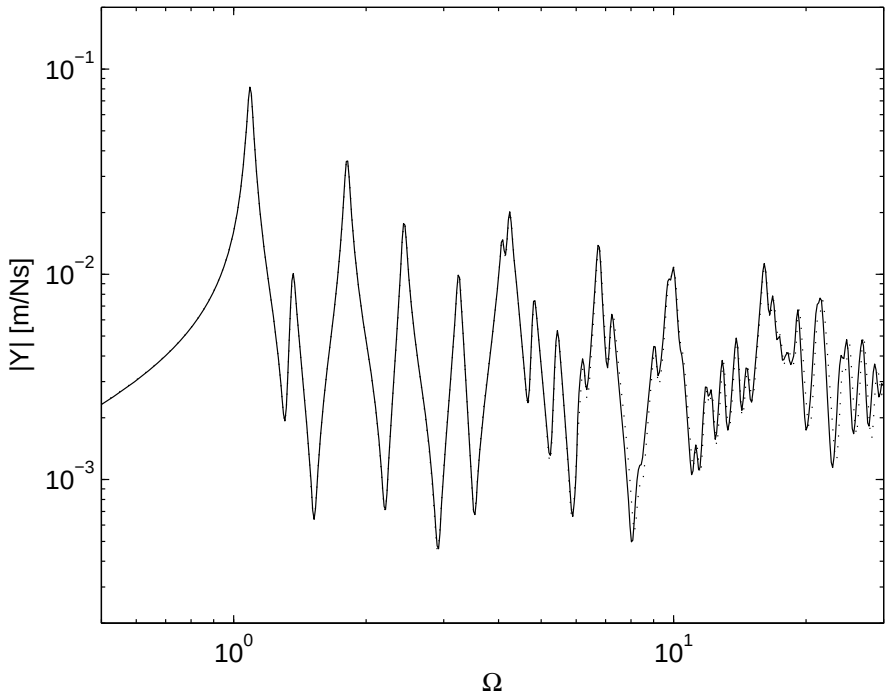

Figure 4.11: Magnitude of the input mobility of the plate: — WFE result with $\left|\mathrm{Re}\left(k_x\Delta_x\right)\right|<1$, $\left|\mathrm{Im}\left(k_x\Delta_x\right)\right|<1$; ···· *modal solution.*

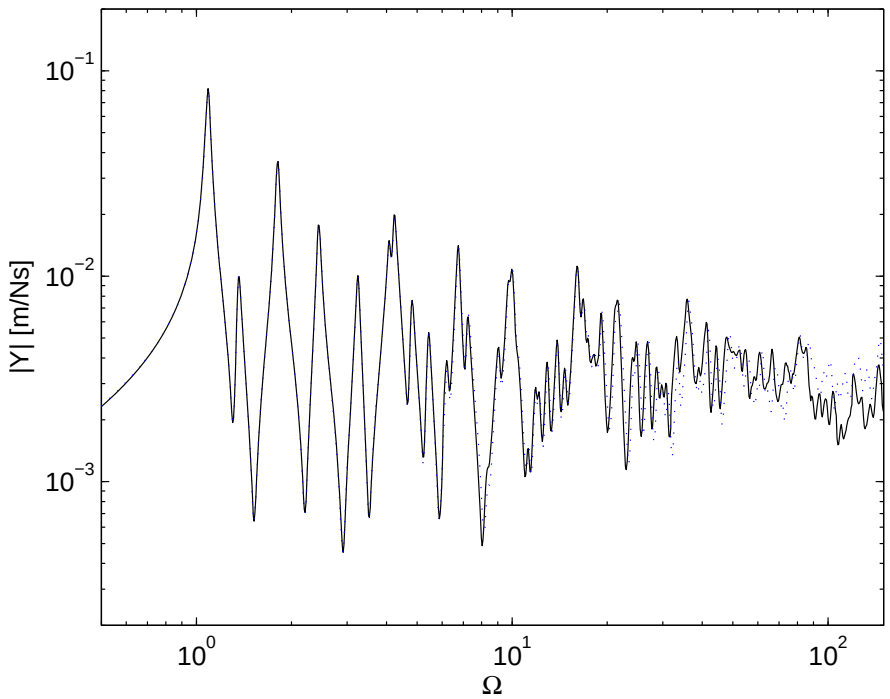

Figure 4.12: Magnitude of the input mobility of the plate over wide frequency range: — WFE result with $\left|\mathrm{Re}\left(k_x\Delta_x\right)\right|<1$, $\left|\mathrm{Im}\left(k_x\Delta_x\right)\right|<1$; ···· *modal solution.*

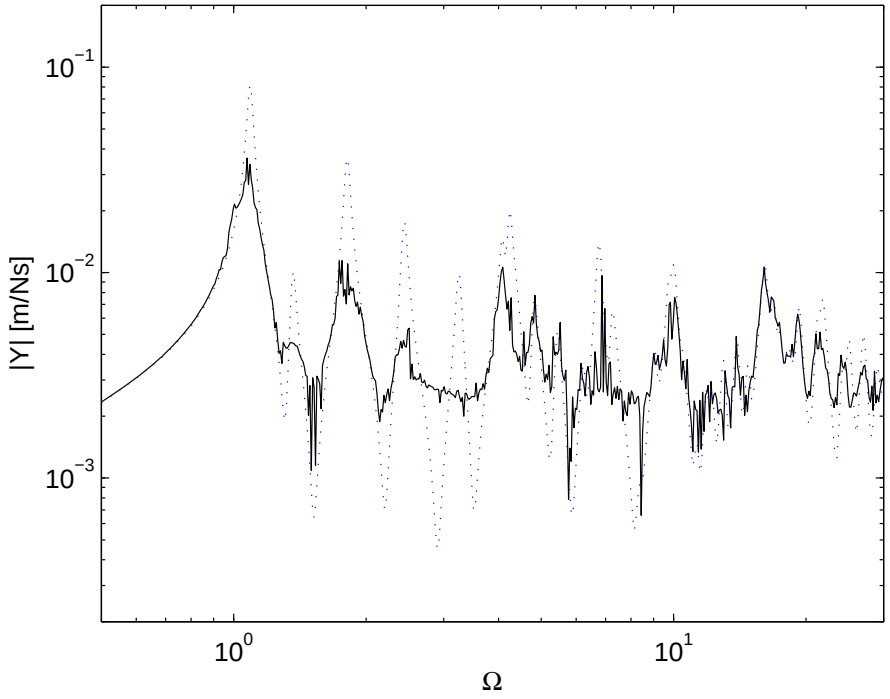

Figure 4.13: Magnitude of the input mobility of the plate: — WFE result using all waves; ···· modal solution.

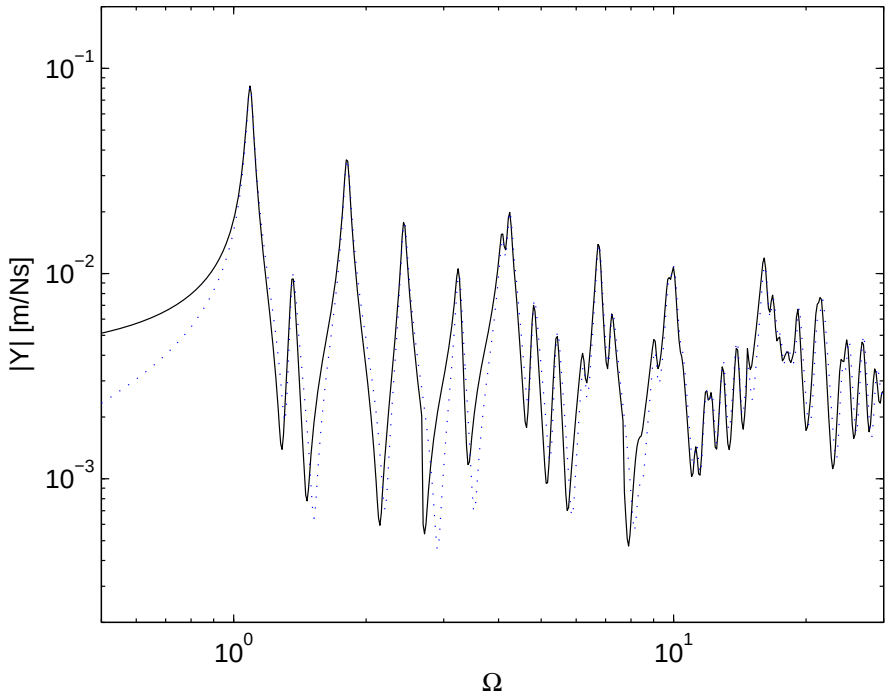

Figure 4.14: Magnitude of the input mobility of the plate: — WFE result with $\left|\mathrm{Re}\left(k_x\Delta_x\right)\right|<1$, $\left|\mathrm{Im}\left(k_x\Delta_x\right)\right|<0.2$*; ···· modal solution.*

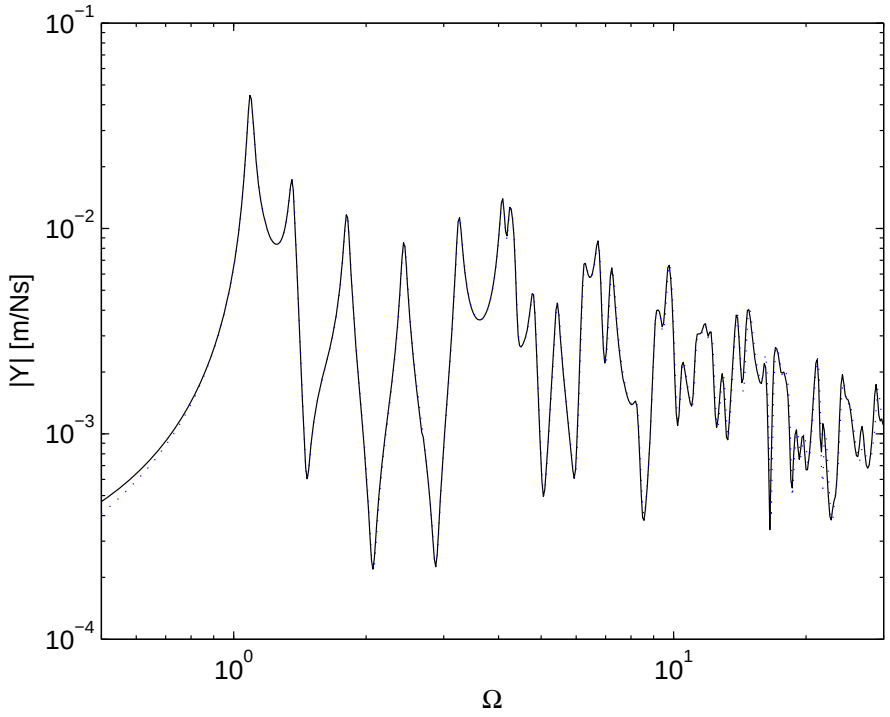

Figure 4.15: Magnitude of the transfer mobility of the plate: — WFE result with $\left|\mathrm{Re}\left(k_x\Delta_x\right)\right|<1$, $\left|\mathrm{Im}\left(k_x\Delta_x\right)\right|<0.2$ *; ···· modal solution.*

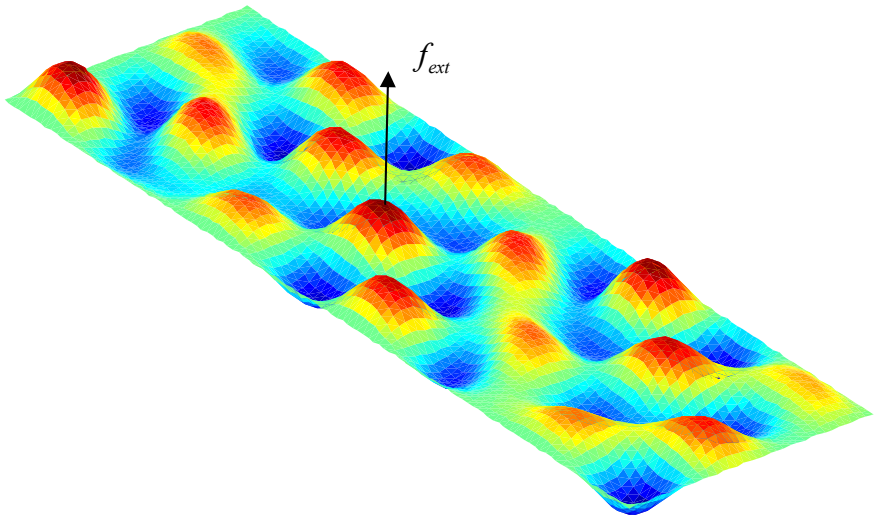

Figure 4.16: The forced response of the plate with $\eta=0.01$ *at* $\Omega=21.8$.

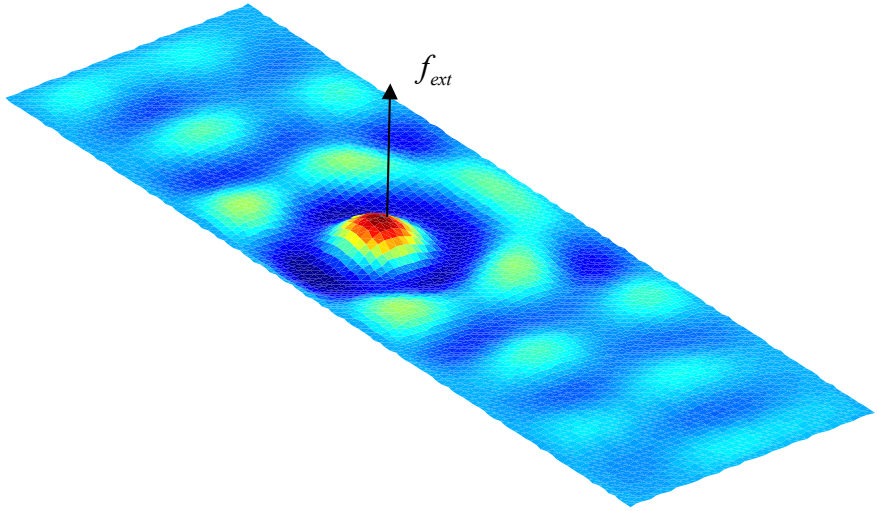

Figure 4.17: The forced response of the plate with $\eta = 0.03$ *at* $\Omega = 21.8$.

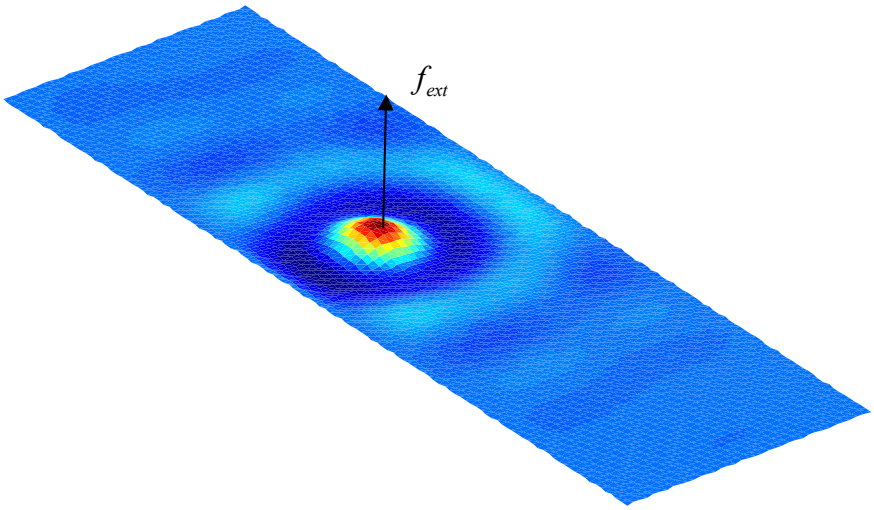

Figure 4.18: The forced response of the plate with $\eta = 0.1$ *at* $\Omega = 21.8$.

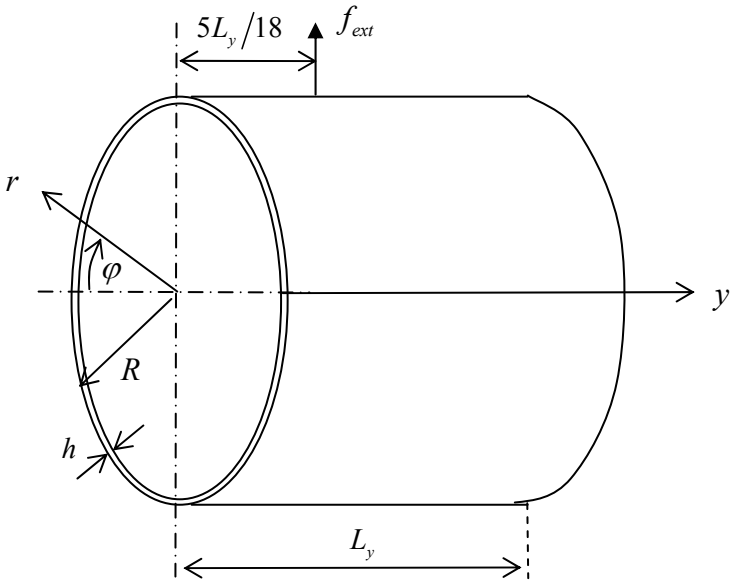

Figure 4.19: Cylinder with a finite length.

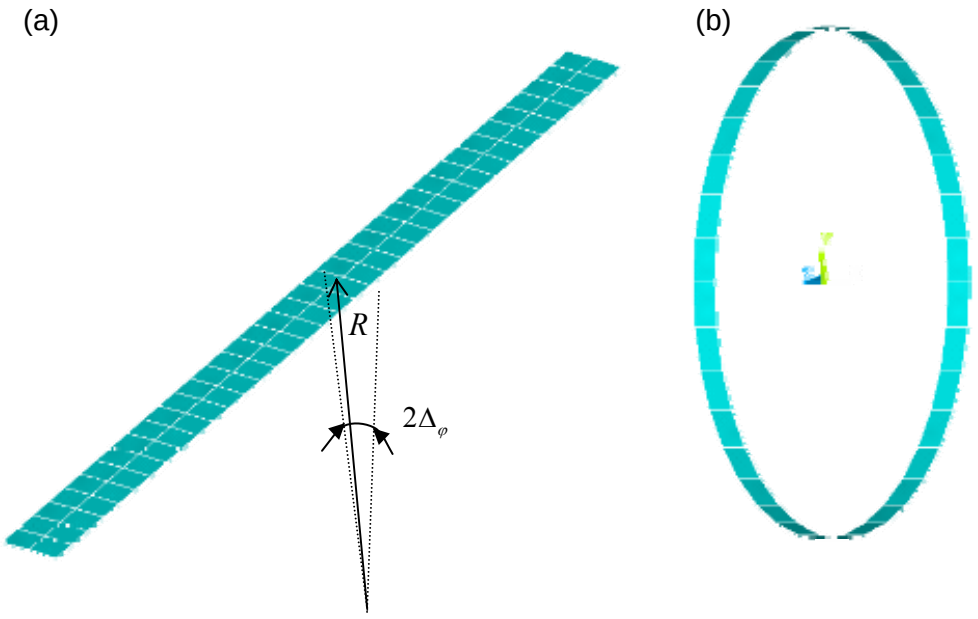

Figures 4.20: WFE models of the cylinder (a) in the φ-direction; (b) in the y-direction.

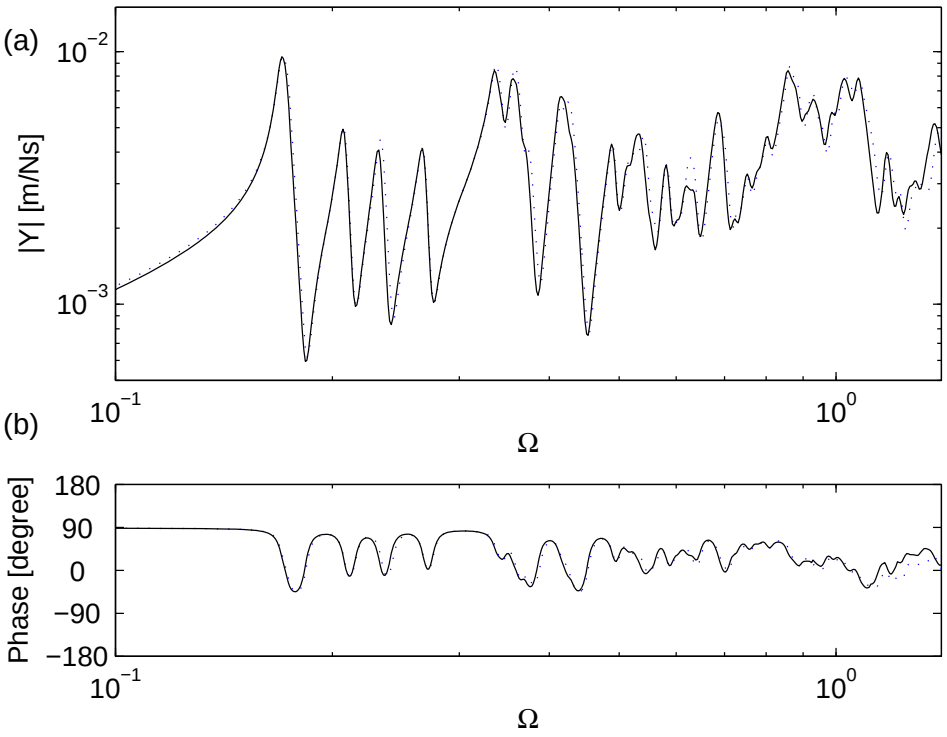

Figure 4.21: (a) Magnitude and (b) phase of the input mobility of the cylinder: — WFE result with $\left|\mathrm{Re}\left(k^{*}\Delta_{\varphi}\right)\right|<1,\left|\mathrm{Im}\left(k^{*}\Delta_{\varphi}\right)\right|<1$; ···· *modal solution.*

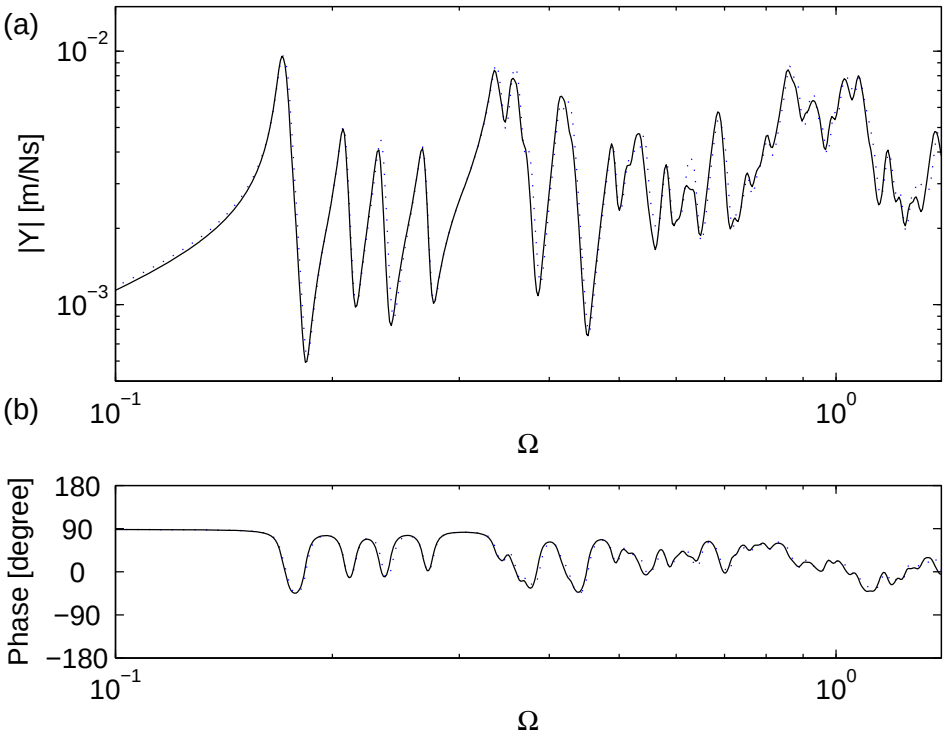

Figure 4.22: (a) Magnitude and (b) phase of the input mobility of the cylinder: — WFE result with $\left|\mathrm{Re}\left(k^{*}\Delta_{\varphi}\right)\right|<1,\left|\mathrm{Im}\left(k^{*}\Delta_{\varphi}\right)\right|<0.75$; ···· *modal solution.*

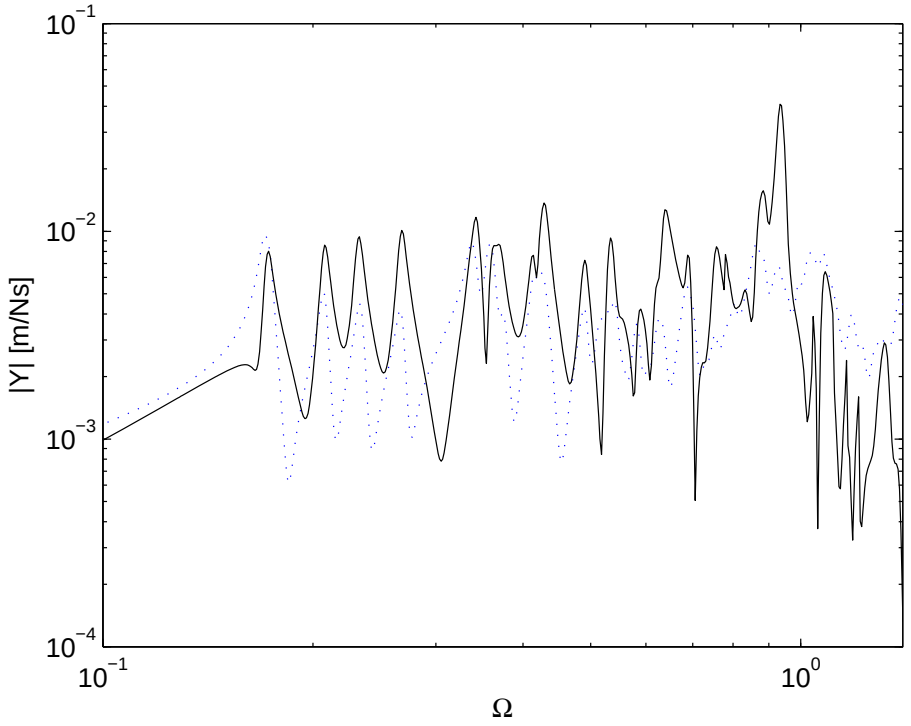

Figure 4.23: Magnitude of the input mobility of the cylinder: — the WFE result using equation (4.2) with $\left|\mathrm{Re}\left(k^{*}\Delta_{\varphi}\right)\right|<1,\left|\mathrm{Im}\left(k^{*}\Delta_{\varphi}\right)\right|<0.75$ *;* ···· *modal solution.*

Chapter 5
APPLICATION OF THE WFE METHOD TO A TYRE

5.1 Introduction

Tyre noise is becoming a significant source for traffic noise [121,122]. Understanding the vibrational behaviour of a tyre is thus becoming more important. Measured spectra of tyre noise show a broad peak around 1 kHz at which frequency the wavelengths in the tyre are short. At such high frequencies the computational cost of FEA becomes impractically large [123126] and knowledge of wave properties is of interest.

In this chapter, the WFE method is applied to analyse tyre vibrations as a practical application. No analytical solution is available. The approaches previously described are used. A segment of a tyre is modelled using ANSYS 7.1. Frequency dependent material properties of rubber are included. Free and forced vibrations are considered. Free wave propagation is illustrated for purely real, purely imaginary and complex wavenumbers. The effects of curvature and internal pressure are analysed. The forced response is predicted and compared with experimental data. The outcomes of this chapter have been presented in [73,74].

5.2 Overview of Tyre Analysis

A tyre is a complicated structure composed from steel and textile fibre reinforced rubber sheets and several different rubbers (see details in Appendix 3.1). A cross-section of a commercial tyre and terminology are illustrated in Figure 5.1.

Several analytical wave models have been proposed to investigate waves in a tyre. The classical and simple one-dimensional model using a curved beam subjected to in-plane tension and lying on an elastic foundation was proposed by Böhm [127]. Pinnington extended the one-dimensional model to include the shear stiffness and the rotary inertia of

the tread and considered both the shear and rotational waves [128]. Two-dimensional models have been proposed by several researchers. Kropp et al developed a model for a layered flat plate on an elastic foundation [129,130]. They also investigated the contact model [131] and the noise radiation from a tyre [131]. Their extensive work is summarised in [132,133]. Pinnington modelled a tyre as a curved plate on a sidewall impedance [134,135]. Muggleton et al modelled a tyre as three flat plates joined by springs [136]. However, it is difficult or impossible to include structural details in these analytical models, hence numerical solutions are desired.

Relatively few works have investigated waves in a tyre using numerical methods. Bolton et al estimated the dispersion curves from a FE model of a cylinder representing a tyre [137,138], but this approach provides only rough estimates of predicting propagating wavenumbers from natural frequencies. A notable work was that of Nilsson [7] using the spectral finite element method. He modelled a tyre using spectral elements and showed good agreements between the calculated forced response and experimental results. However, the method needs special elements to model a tyre as stated in subsection 1.2.3.

These works focus on only propagating waves. In this chapter, the WFE method is applied to a tyre. Propagating, evanescent and oscillating decaying waves are considered and results for free and forced vibrations are presented.

5.3 Tyre Model

A ‘slick’ tyre attached to an aluminium rim (see Figure 5.2) together with material data was provided by Bridgestone Corporation. Details are given in Appendix 3.1. In this section, a WFE model of the tyre is briefly described. Frequency dependent material properties of rubber are considered.

5.3.1 WFE Model

A short section of the tyre was modelled using ANSYS 7.1 as shown in Figure 5.3. The coordinates and dimensions are shown in Figure 5.4. Cylindrical coordinates were used. The eight node solid element SOLID 46, which generates equivalent anisotropic material properties for a layered structure, was used. The element has three translational DOFs at each node. A segment of the tyre subtending an angle of $2\Delta_\varphi = 1.8^\circ$ was modelled. To

represent the curvature of the tyre, adjacent segments of the tyre are connected together with their local coordinates being rotated through $\pm\Delta_\varphi\left(0.9^\circ\right)$. This models the curved tyre as being composed of piecewise-plane elements as described in subsection 3.6.2. An internal pressure of 200 kPa was simulated by the application of surface loads on the elements (see Appendix 3.2). Boundary conditions at the bottom of the section were imposed by setting the DOFs to be zero. The number of DOFs was 324 after the condensation of interior DOFs. More details are given in Appendix 3.2.

5.3.2 Inclusion of Frequency Dependent Material Properties of Rubber

Material properties of rubber depend on frequency [139]. To include the frequency dependent properties of rubber, the stiffness matrix was decomposed as

$$\mathbf{K}\left(f\right)=\mathbf{K}_{fibre}+\mathbf{K}_{rubber}\left(f\right)+\mathbf{K}_{tension} \tag{5.1}$$

where $f=\omega/2\pi$ is frequency in Hz. The stiffness matrices $\mathbf{K}_{fibre}$ and $\mathbf{K}_{tension}$ represent the frequency independent contributions of the fibres and the in-plane tension due to the internal pressure. The latter was derived from the difference between two stiffness matrices associated with FE models with and without the internal pressure. The stiffness matrix of the rubber elements is frequency dependent. If Poisson's ratio is assumed constant, the stiffness matrix is proportional to the Young's modulus E. The frequency dependent stiffness matrix $\mathbf{K}_{rubber}\left(f\right)$ at frequency f is then given by

$$\mathbf{K}_{rubber}\left(f\right)=\frac{E\left(f\right)}{E\left(f_0\right)}\mathbf{K}_{rubber}\left(f_0\right)\left\{1+j\eta\left(f\right)\right\} \tag{5.2}$$

where $\eta\left(f\right)$ is the frequency dependent loss factor and f_0 is a reference frequency at which the stiffness matrix $\mathbf{K}_{rubber}\left(f_0\right)$ is evaluated (neglecting damping).

To determine $E\left(f\right)$ and $\eta\left(f\right)$ in equation (5.2), the rubbers were assumed to behave like the American National Standards Institute (ANSI) standard polymer for which data is

available in the literature [140]. In the frequency range of interest $\left(0 < f \le 2\text{kHz}, 30°\text{C}\right)$, $E\left(f\right)$ and $\eta\left(f\right)$ may be approximated by [140]

$$\log\left(E\left(f\right)\right) = \alpha_E \cdot \log\left(f\right) + \beta_E, \tag{5.3}$$

$$\eta\left(f\right) = \alpha_\eta \cdot \log\left(f\right)^2 + \beta_\eta. \tag{5.4}$$

The coefficients were estimated from the literature [140] to be $\alpha_E = 0.1, \alpha_\eta = 0.01, \beta_\eta = 0.1$ and β_E was determined from given material data for each rubber. The data used to estimate the coefficients are given in Appendix 3.3 and the values of β_E are tabulated in Appendix 3.1. For the tyre model, the effect of the change in the stiffness of the rubber is relatively small in the frequency range analysed because the magnitudes of the elements of $\mathbf{K}_{fibre}$ (and $\mathbf{K}_{tension}$) are much larger than the changes in the elements of $\mathbf{K}_{rubber}\left(f\right)$.

5.4 Free Wave Propagation

In this section the dispersion curves are numerically determined for an undamped tyre including purely real, purely imaginary and complex wavenumbers. To investigate the effects of the tyre curvature and internal pressure, three models are analysed. These are (I) a straight section without internal pressure, (II) a curved section without internal pressure and (III) a curved section with internal pressure. Complicated dispersion curves including the bifurcations and the existence of a negative group velocity discussed in chapter 3 are seen. The curvature and the in-plane tension increase the stiffness especially at low frequencies. No damping is assumed throughout this section for the sake of clarity.

5.4.1 Straight Section without Internal Pressure

A straight section of the tyre $\left(R = \infty\right)$ is first analysed to illustrate the effect of curvature. A straight segment is modelled so that there is no rotation of the coordinate system at the end of the segment. The dispersion curves below 450 Hz are shown in Figure 5.5 for the asymmetric (A_i) modes and in Figure 5.6 for the symmetric modes (S_i). Results for purely

real, purely imaginary and complex (conjugate) wavenumbers are shown. Only wavenumbers for which $\left|\mathrm{Im}\left(k\right)\right|$ is small are shown for clarity. Wave modes in which the wave is characterised by predominantly transverse shear motion are described as T_i where the subscript i denotes the associated wave modes (A_i, S_i).

The asymmetric A_1 mode cuts-on first at about 25Hz (Figure 5.5). This mode comprises side-to-side motion of the tread as illustrated in Figure 5.5(a). The A_1 mode (Figure 5.5(a)) and the symmetric S_1 (Figure 5.6(a)) mode are bouncing modes where the tread mass is vibrating on the sidewall stiffness. The A_2 (Figure 5.5(c)), S_2 (Figure 5.6(b)) and higher modes are cross-sectional modes where the cross-sectional deformation becomes more complex, with more nodes along the cross-section.

All wavenumbers at low frequencies are purely imaginary or complex (conjugate). Complex conjugate wavenumbers bifurcate into two purely imaginary or purely real numbers. In Figure 5.6 a bifurcation into two real wavenumbers can be seen at around 200 Hz. For a general structure, the flexural and shear wave modes in general couple even if the structure is straight due to finite shear stiffness and Poisson contraction effect. Curve veering between two propagating wavenumbers represents that two wave modes are not orthogonal in the wave domain. The shape of the wave mode changes around the frequency where the veering occurs. An example is depicted in Figure 5.5(b) for the A_1 mode.

5.4.2 Curved Section without Internal Pressure

The dispersion curve of a curved segment below 450 Hz is shown in Figure 5.7. The asymmetric modes are illustrated in Figure 5.7(a) and the symmetric modes in Figure 5.7(b). The polar wavenumber (rad/rad), $k^* = kR\ \left(R = 0.3185\right)$, is used. The value of $k = 10$ for the straight section in Figures 5.5 and 5.6 is associated with $k^* = 3.185$. Natural frequencies occur at $k^* = 1, 2\cdots$ associated with circumferential mode orders and also at $k^* = 0$ for a breathing mode. The wave mode shapes are similar to those in Figures 5.5 and 5.6.

The curvature increases the stiffness due to the coupling between flexural and in-plane motions especially at low frequencies (below the ring frequency). The curvature therefore increases the cut-off frequencies and decreases $\left|\mathrm{Re}\left(k^*\right)\right|$. However, the cut-off frequency of the A_1 mode remains the same because the wave mode relates to side-to-side motion of the tread and is irrelevant to curvature. Apart from the stiffening effect, the curvature introduces

the non-zero cut-on phenomena and one wave has a negative group velocity as discussed in subsection 3.7.5. Such phenomena are clearly seen for the A_2 and S_2 modes.

5.4.3 Curved Section with Internal Pressure

A tyre is subjected to internal pressure. Internal pressure causes in-plane tension both in the circumferential direction and across the tread and sidewall. The in-plane tension increases the stiffness especially at low frequencies [1] such that the effects are similar to those of the curvature. The dispersion curves below 600 Hz is shown in Figure 5.8(a) for the asymmetric modes and (b) for the symmetric modes. The polar wavenumber $k^* = kR$ is again shown. Internal pressure increases the cut-off frequencies especially of the lower order wave modes and decreases $\left|\mathrm{Re}\left(k^*\right)\right|$.

The dispersion curves of the cut-off of the S_2 mode is shown in Figure 5.9 for a narrow frequency range around the cut-off frequency. The non-zero cut-off of the S_2 mode occurs at around 326.8 Hz above which frequency there are two propagating waves. One wavenumber increases with frequency and the other decreases and becomes complex (conjugate) around 327.0 Hz where the S_2 and T_{S1} modes couple. The complex conjugate waves again become two propagating waves at around 332.8 Hz.

All propagating wavenumbers associated with the symmetric modes in the frequencies of interest, i.e. up to 2 kHz, are shown in Figure 5.10. The value of $k^* = 60$ is associated with $k^*\Delta_\phi = 1$. In total 16 waves propagate at 2 kHz and there are 8 S_i and 8 T_i modes. Since there are only 28 elements across the cross-section, a relatively large FE discretisation error may occur. Another model using 50 elements was formed to investigate the error. The details are shown in Appendix 3.4. Although results using 28 and 50 elements differ such that the result using 28 elements is not converged, it was observed that the 28 element model gives a reasonable response. The difference between 28 and 50 element models at lower frequencies is believed that 50 element model can represent geometry of cross-section of a tyre more accurately.

The group velocity can be numerically calculated using the power and energy relationship. The group velocities associated with the S_1, S_2, T_{S1} modes are shown in Figure 5.11. The group velocities predominantly associated with the flexural motion (S_1, S_2) are about typically 80 m/s (25 rad/s) and that with the shear motion (T_{S1}) is about 240 m/s (76 rad/s).

These values are similar to results in [138]. Figures 5.12 and 5.13 focus on the frequencies where the S_2 mode cuts-on. Three waves propagate in the frequencies between 333 Hz and 341 Hz (Figure 5.12) and between 326.8 Hz and 327.0 Hz where there is one wave propagating with a negative group velocity. The power and energy relationship can be used even if the damping is included, i.e. equation (5.4). The group velocities of the damped S_1, S_2, T_{S1} modes are illustrated in Figure 5.14. The distinct peaks and troughs in Figure 5.11 disappear due to the damping. The group velocities at relatively high frequencies shown are the same as those of the undamped case but the details of the curves differ.

5.5 Forced Response

The forced response of the tyre is calculated using the wave approach described in chapter 4 and the results compared with experimental data. Excitation is applied to the centre of the tread. The effect of the size of the region over which the excitation is applied is numerically analysed. This affects the response especially at high frequencies.

5.5.1 Experimental Setup

The tyre attached to the rim was suspended using flexible rubber strings as shown in Figure 5.15. The excitation was a random signal applied by a shaker attached to the tread centre through a relatively rigid metal disc of diameter, $d = 23.5$ mm and 1 mm thickness as shown in Figure 5.16. The equipment used is summarised in Table 5.1. Measured signals were analysed using the Hanning window and averaged (at least 30 averages). The room temperature was about 30 ˚C throughout the measurement. Mass cancellation [141] was applied by post-processing the measured data to cancel the mass effect of the force transducer and the accelerometer. An example of a measured input mobility of the tyre without internal pressure is shown in Figure 5.17. The response below 30 Hz is dominated by the boundary conditions (i.e. free) and a resonance of the experimental rig occurs around 2.7 kHz. Reliable measured data is therefore expected to be roughly between 30 Hz and 2 kHz.

5.5.2 Forced Response of a Tyre with Finite Area Excitation

The forced response is calculated using the wave approach. A frequency dependent loss factor for rubber $\eta(f)$ in equation (5.4) was included. Waves for which $\left|\mathrm{Im}\left(k\Delta_{\varphi}\right)\right| \le 0.75$ were retained to calculate the response based on the discussion in chapter 4. For the tyre without internal pressure, the number of the positive- and negative going wave pairs was about 80 in the frequency range analysed while about 70 wave mode pairs were retained for the tyre with internal pressure. The region of the excitation was modelled as shown in Figure 5.18. Because of the element size of the model, the circle area over which the excitation was applied in the experiment was modelled as an oval shape such that the area of the excitation is same. The weighted average responses from 5 different excitation points corresponding to nodes in the FE model were found. The weights were chosen such that at the centre is 2 and the other points are 1 by considering the representative area of each excitation point.

The predicted and measured forced responses of the tyre without and with internal pressure are shown in Figures 5.19 and 5.20, respectively. In both figures, the maximum frequency is approximately the frequency where the S_8 mode cuts-on. Reasonable agreements between the predicted results and the measured data can be seen in both figures.

For the response of the tyre without internal pressure (Figure 5.19), there are broad peaks because of the large damping. The predicted natural frequencies are larger than those in the experiment such that the stiffness associated with the FE model is expected to be greater than that of the real tyre. Differences of the magnitude of the response below the first resonance are believed to be due to the boundary conditions, i.e. the WFE results assumed the fixed boundary condition but the real tyre was attached to a rim and has a rigid body motion. The peak occurring at frequencies around 170 Hz in the numerical result, which is associated with the shear mode T_{s1}, cannot be clearly seen in the measured result. The deformation of the whole tyre corresponds to a breathing mode at this frequency. The reason for the discrepancy is believed to be the effect of the internal cavity since the bulk modulus of the internal air can resist the breathing deformation, which is neglected in the numerical results. At high frequencies, the predicted and measured results asymptote to a similar magnitude.

For the tyre with internal pressure (Figure 5.20), the response shows several maxima and minima below 300 Hz. These correspond to individual resonances. The response of the tyre

can be categorised into three regions. Below the first resonance at around 90 Hz where the S_1 mode cuts-on, the sidewall stiffness is dominant. Above the first resonance there are several peaks associated with vibrational modes of the tyre around the circumferential deformation across the tread and sidewall in the S_1 mode. The response is similar to that of the beam on an elastic foundation. Above 350 Hz where the S_2 mode cuts-on, the response becomes more or less constant. At high frequencies the response tends to that of a plate with finite shear stiffness or that of an elastic half space with excitation applied over finite area. This is discussed further in the next subsection.

The predicted frequency of the first resonance is smaller than the measured result. But the frequency difference between successive peaks is larger. This implies that the stiffness across the tread and sidewall is smaller than that of the real tyre but that in the circumferential direction is larger. A complete set of the data for the FE model could improve such discrepancy.

5.5.3 Effect of the Size of the Excited Area

The structural response is particularly sensitive to the spatial distribution of the excitation at high frequencies where the wavelengths become small. For example, considering an excitation of uniform force f_0 per unit length, applied along a line of length 2*r*. The force injected into each wave mode can be expressed as

$$f(k) = \frac{f_0}{2\pi} \int_{-r}^{r} f_0 \exp(jkr)\, dr = \frac{f_0 r}{\pi} \frac{\sin(kr)}{kr}. \tag{5.5}$$

For $kr << 1$, equation (5.5) gives $f(k) \approx f_0 r/\pi$ and the value is independent of k. But for $kr = O(1)$ or larger, the effective force injected to the wave decreases and the wave is not excited as much.

In addition, if the thickness of the structure, *h*, is not thin enough compared to the radius of excitation, typically when $h/r \geq 5$, the response of the structure approaches that of an elastic half space so that the shear stiffness and local stiffness become more important [142].

To illustrate the effect of the spatial distribution of the excitation, the responses of the tyre with internal pressure for both the finite area excitation and point excitation are shown in

Figure 5.21. At low and moderate frequencies the responses are almost the same but their asymptotes at high frequencies differ. The shear deformation becomes more important for the point force excitation and the response becomes reactive. These numerical results show that the dynamic behaviour of a tyre at high frequencies can be strongly affected by the distribution of the excitation.

In the previous subsection the external force is assumed to be applied uniformly over a region. However, in the experiment the force distribution was not uniform and, instead, the velocity over the excitation region was more or less uniform. The nodal forces $\mathbf{f}_e$ for nodal velocities $\mathbf{v}_e$ can be calculated from the mobility of the tyre such that

$$\mathbf{f}_e = \mathbf{Y}_e^{-1}\mathbf{v}_e \tag{5.6}$$

where the subscript e represents that the vectors and the matrix are associated with the nodal DOFs within the excited region. The force vector $\mathbf{f}_e$ is determined from velocity vector $\mathbf{v}_e = \begin{bmatrix}1 & \cdots & 1\end{bmatrix}^{\mathrm{T}}$. It should be noted that the matrix $\mathbf{Y}_e$ could be ill-conditioned but that was not found to be the case here. The response for the uniformly distributed force and velocity are shown in Figure 5.22. Because the force along the edge of the excited region is likely to be greater than that inside the excited region, the response at high frequencies tends to be more mass-like. The size of the region as well as the distribution of the force over the excited region is therefore important for high frequency response.

In the experiment, there was small gap between edges of the metal disc and the tyre due to the curvature of the tyre. The response for uniform force distribution might therefore represent the experimental condition better.

5.5.4 Response in the Circumferential and Lateral Directions

In the previous subsections, the response of the tread centre in the radial direction was considered. However, the response to be calculated and the excitation to be applied can be any DOFs. As an example, the input mobility of the centre of the tyre in the circumferential direction is shown in Figure 5.23. It can be seen that the response of the circumferential direction at high frequencies rises at 10 dB/decade (proportional to f). Above 600 Hz or so the response in the circumferential direction is greater than that in the radial direction so that

the response in the circumferential direction can be also important to reduce tyre noise [130,143].

5.6 Conclusions

The WFE method was applied to tyre vibrations as a practical application. The segment of the tyre with internal pressure was modelled in ANSYS 7.1 and the resulting number of DOFs was only 324. Frequency dependent material properties of rubber were included.

Free wave propagation was calculated and the effects of the curvature and internal pressure were illustrated. Complicated dispersion curves were observed. Curve veering occurs and rapid changes of the wavenumber together with wave mode shape were observed. The non-zero cut-on phenomena was also seen for waves in which the flexural and shear waves couple. Associated with the non-zero cut-on phenomena, a wave with a negative group velocity was observed.

The forced response was calculated using the wave approach. The predicted results were compared with experiment results and reasonable agreement was seen. At high frequencies the response approaches that of a plate with finite shear stiffness or that of an elastic half space. The size of region of and spatial distribution of the excitation were discussed. The excitation force injected into a wave mode was described and the effect of finite shear stiffness was mentioned. These were seen to be particularly important at high frequencies.

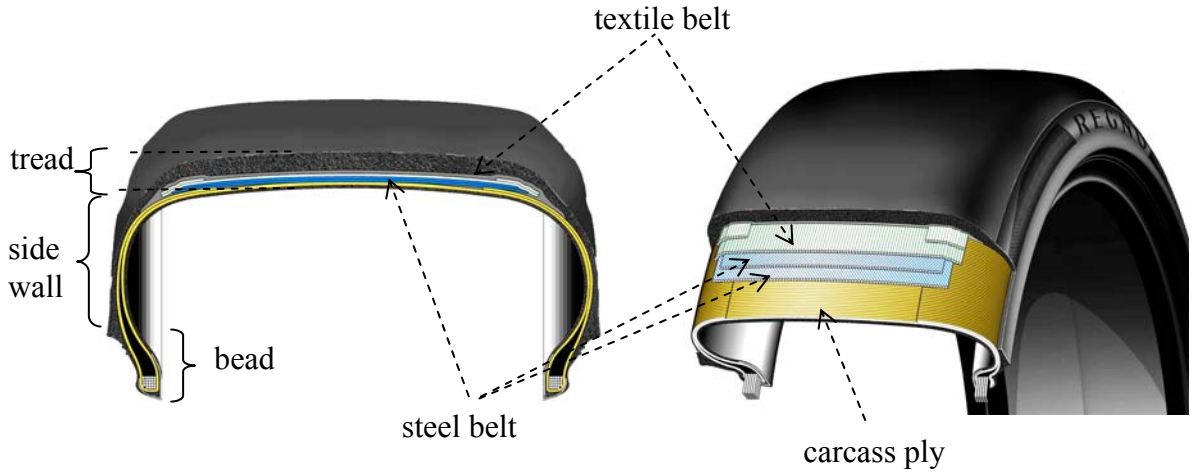

Figure 5.1: Cross-section of a tyre.

Figure 5.2: A tyre with an aluminium rim (195/65R15).

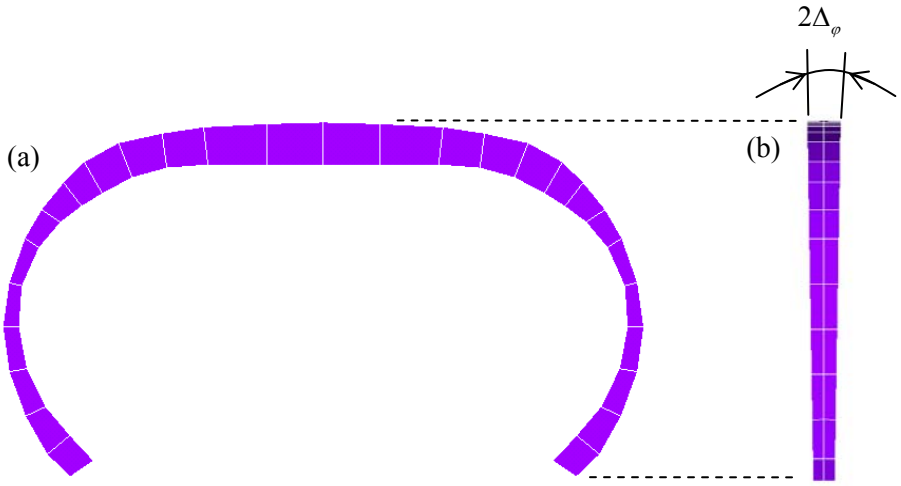

Figure 5.3: Segment of the WFE tyre model: (a) in the tyre cross-section; (b) in the circumferential direction.

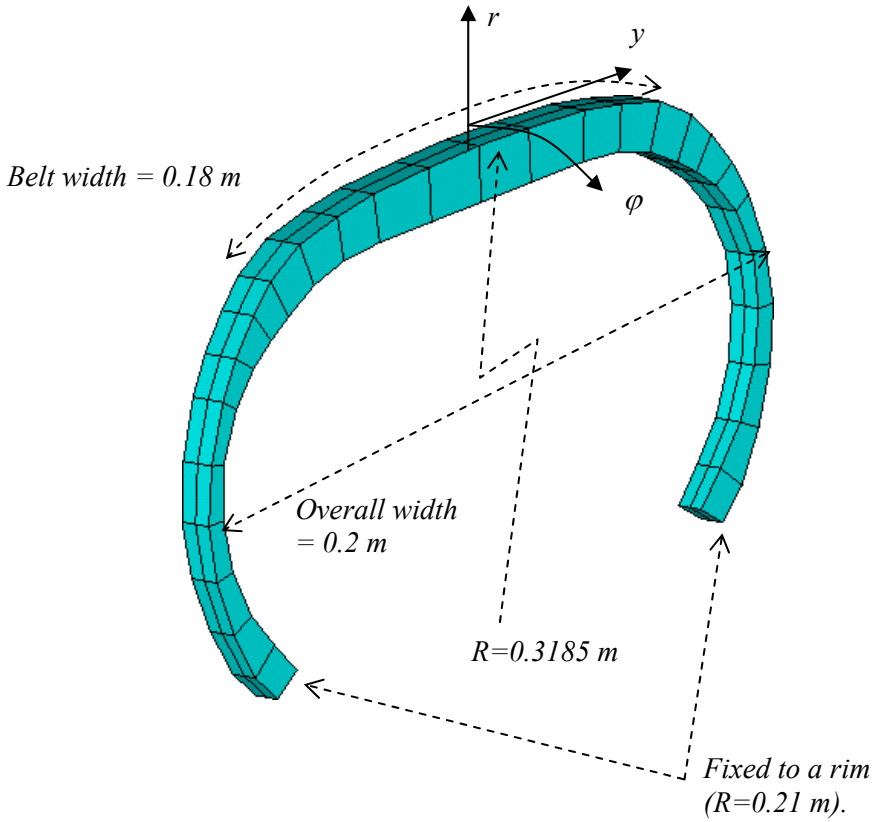

Figure 5.4: Coordinates and a WFE model of the tyre section.

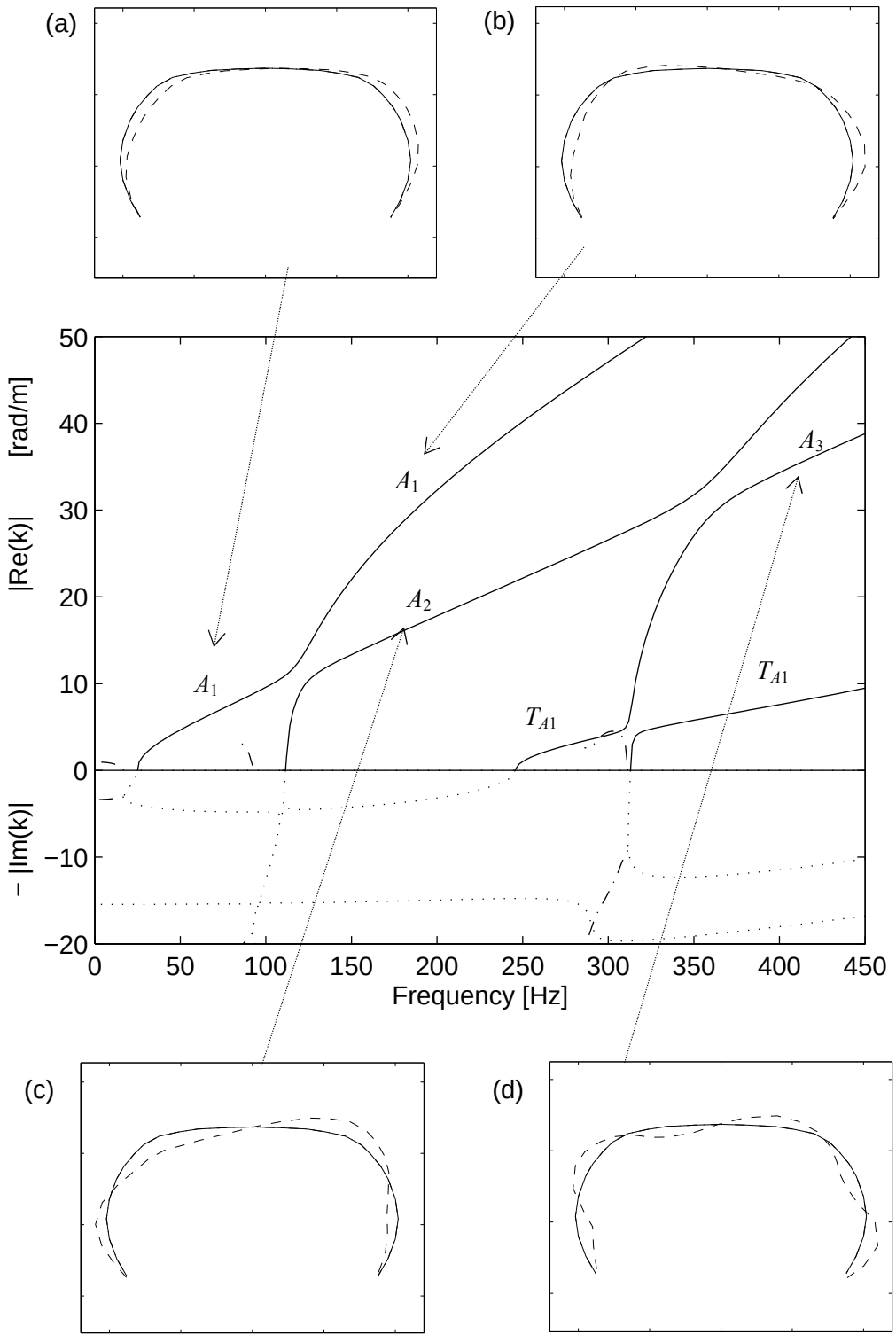

Figure 5.5: Dispersion curves of a straight segment for asymmetric modes: — purely real; ···· purely imaginary; −·− complex conjugate wavenumbers. T_i denotes the shear wave mode. Small figure (a)-(d) illustrates the deformation associated with each wave mode. The solid line is the original shape and the dashed line is the deformed shape.

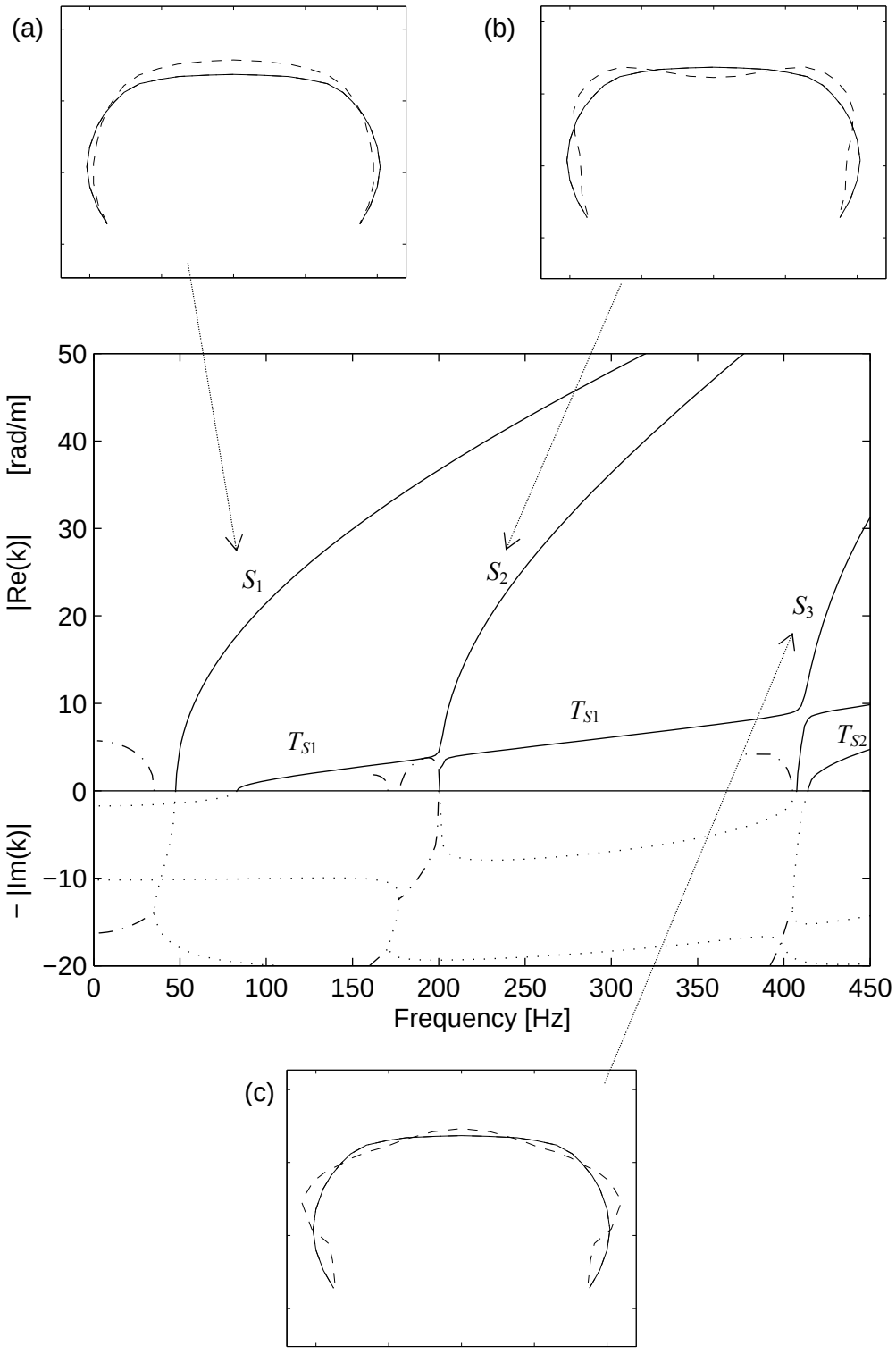

Figure 5.6: Dispersion curves of a straight segment for <u>symmetric</u> modes: — purely real; ···· purely imaginary; −·− complex conjugate wavenumbers. T_i denotes the shear wave mode. Small figure (a)-(c) illustrates the deformation associated with each wave mode. The solid line is the original shape and the dashed line is the deformed shape.

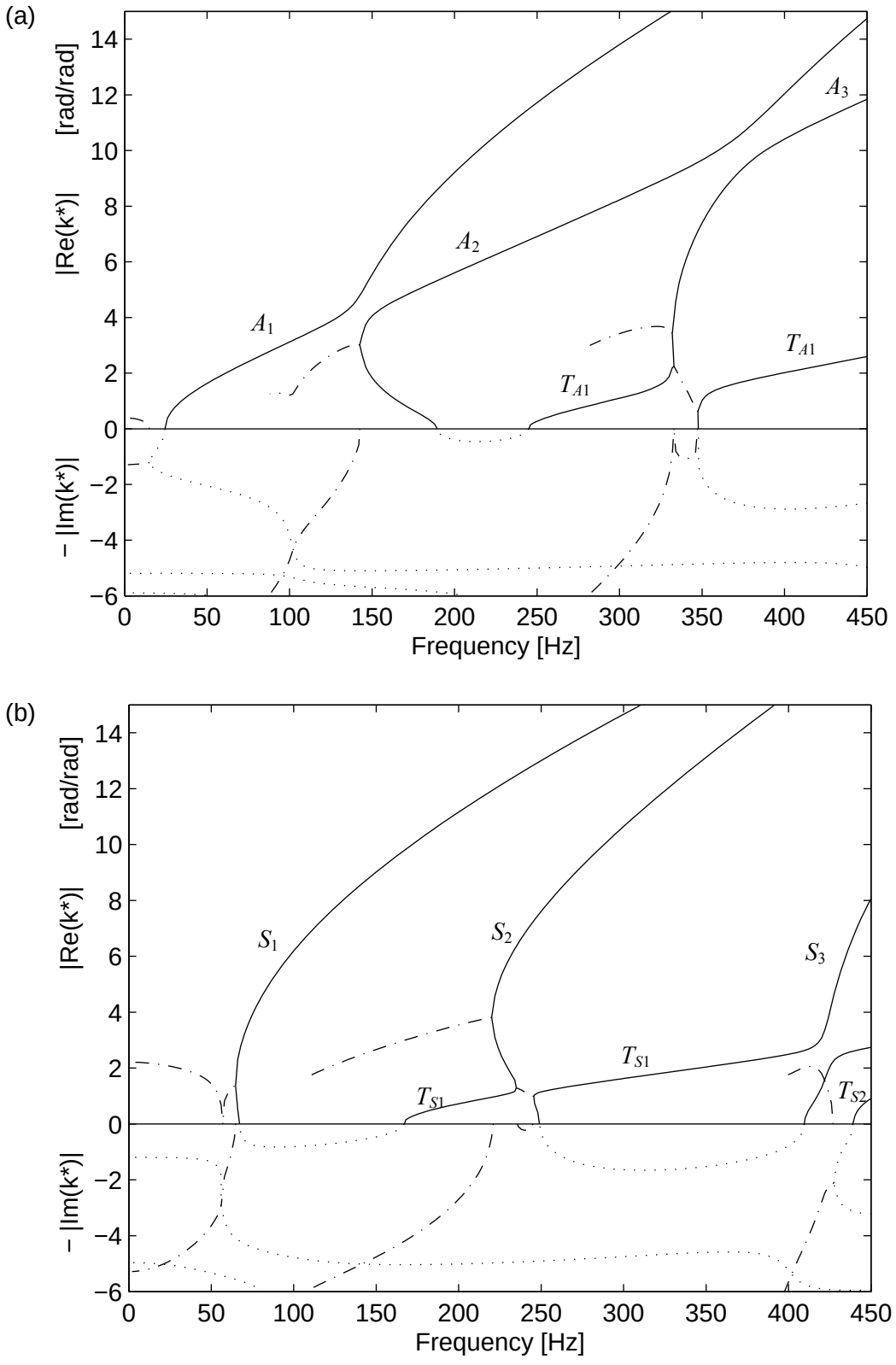

Figure 5.7: Dispersion curves of a curved segment for (a) the asymmetric, (b) symmetric modes: — purely real; ···· purely imaginary; −·− complex conjugate wavenumbers. T_i denotes the shear wave mode.

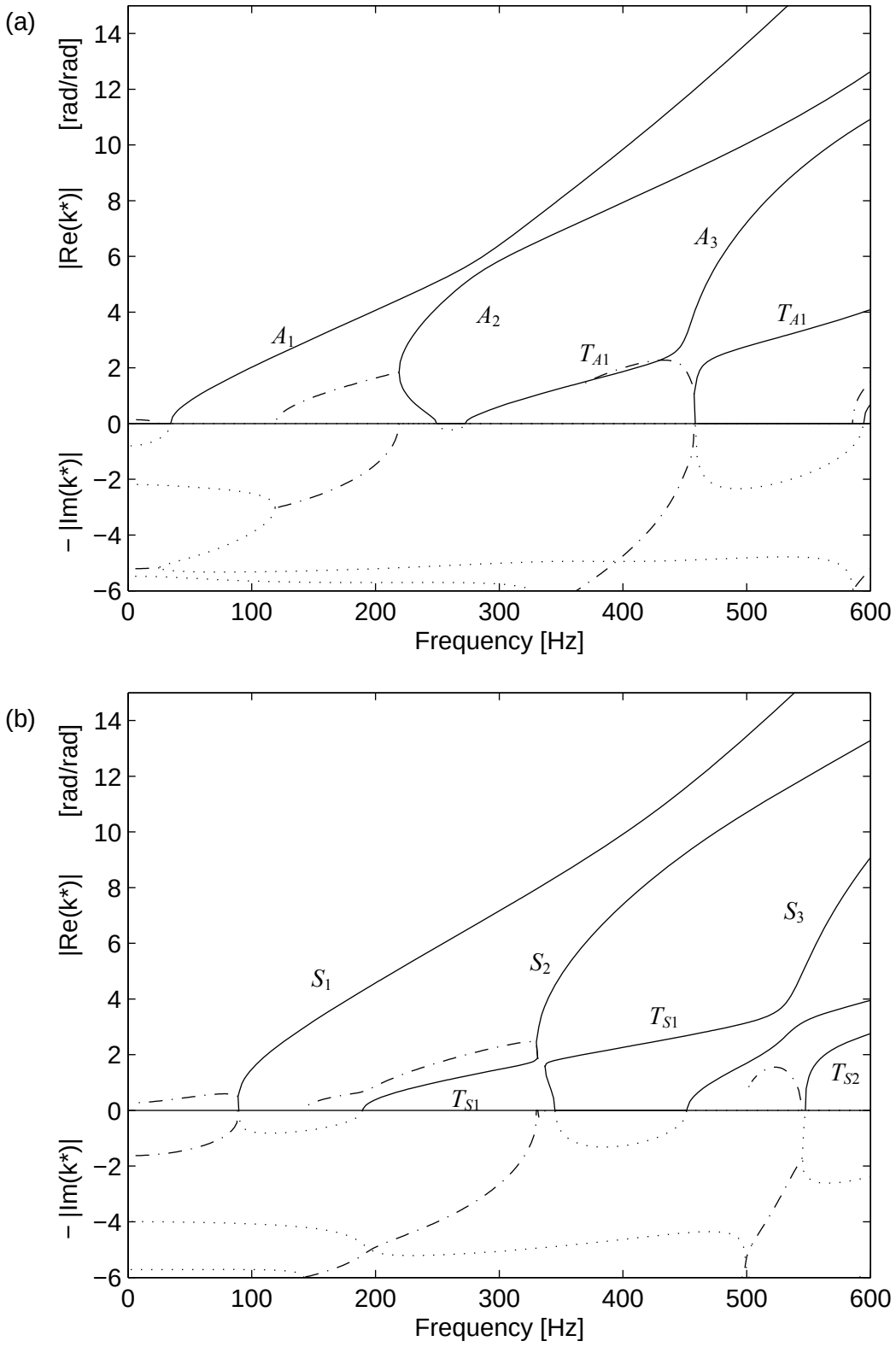

Figure 5.8: Dispersion curves of a curved segment with internal pressure for (a) the asymmetric, (b) symmetric modes: — purely real; ···· purely imaginary; –·– complex conjugate wavenumbers. T_i denotes the shear wave mode.

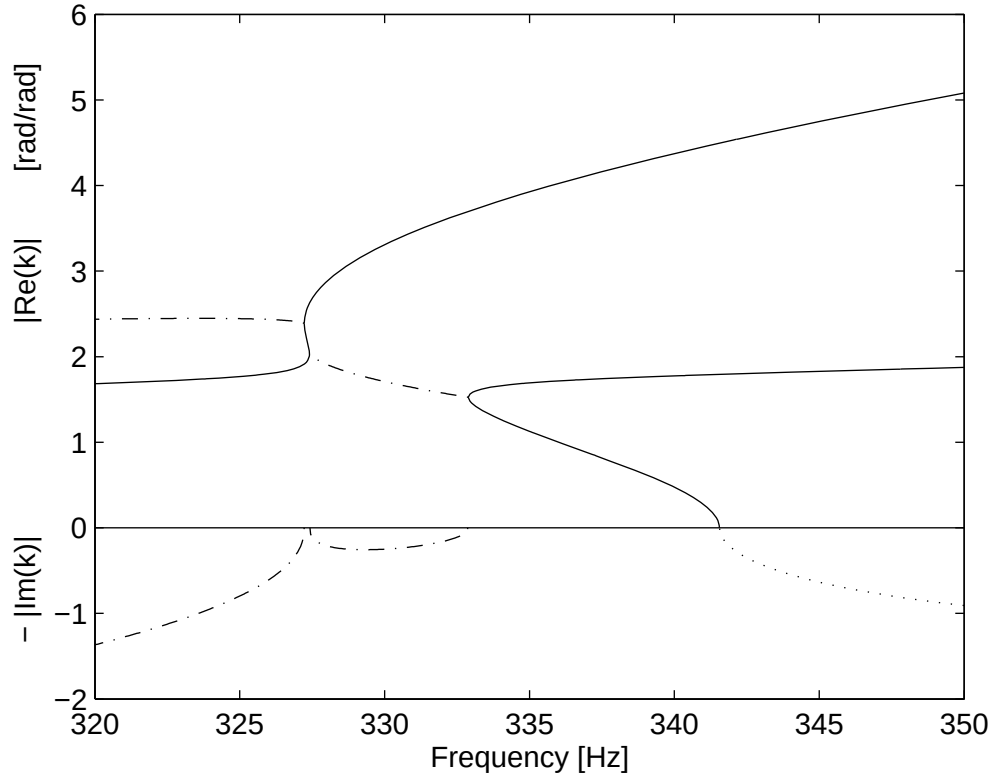

Figure 5.9: Dispersion curves around the cut-on of the S_2 mode: — purely real; ···· purely imaginary; −·− complex conjugate wavenumbers

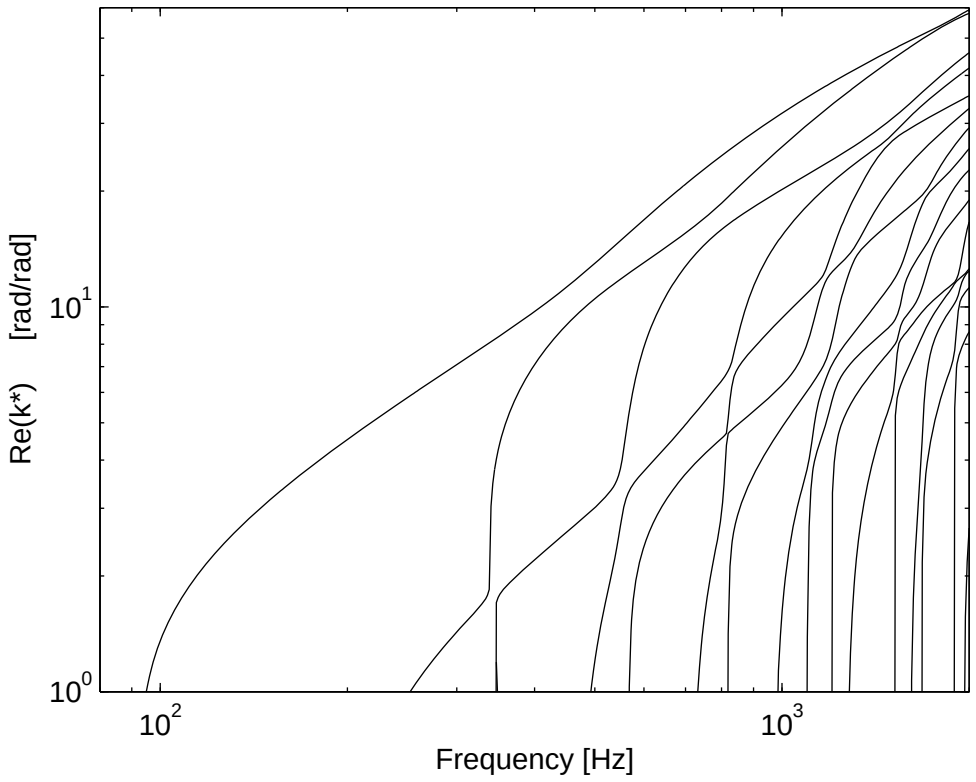

Figure 5.10: Dispersion curves for propagating waves of the symmetric modes.

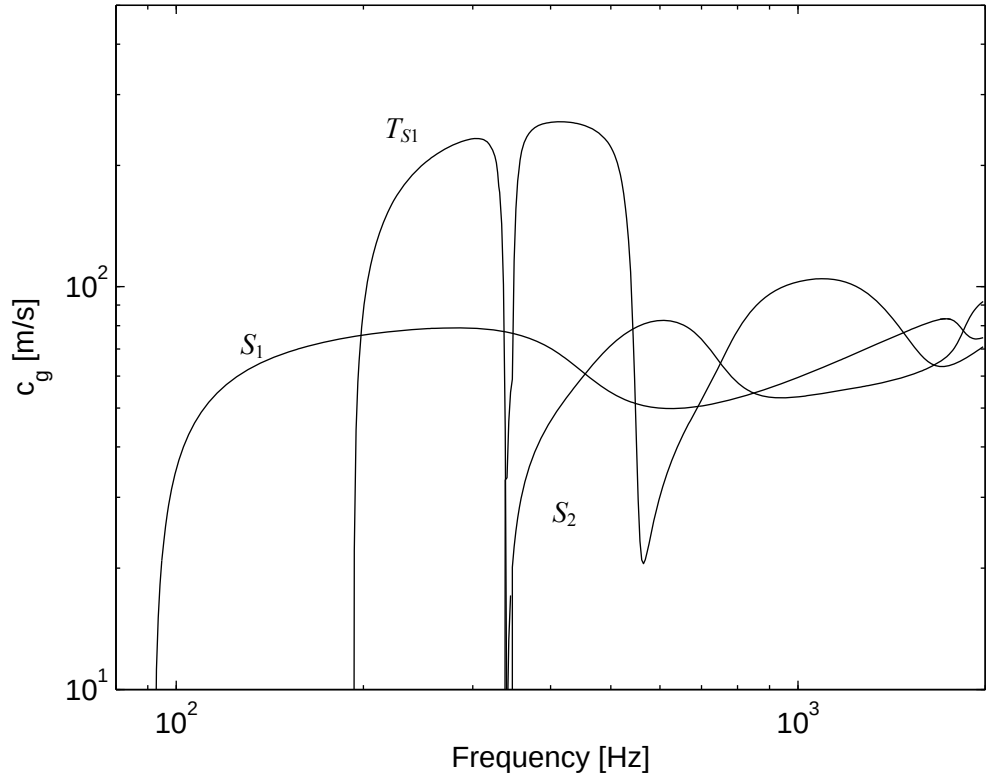

Figure 5.11: Group velocities for the S_1, S_2, T_{s1} modes.

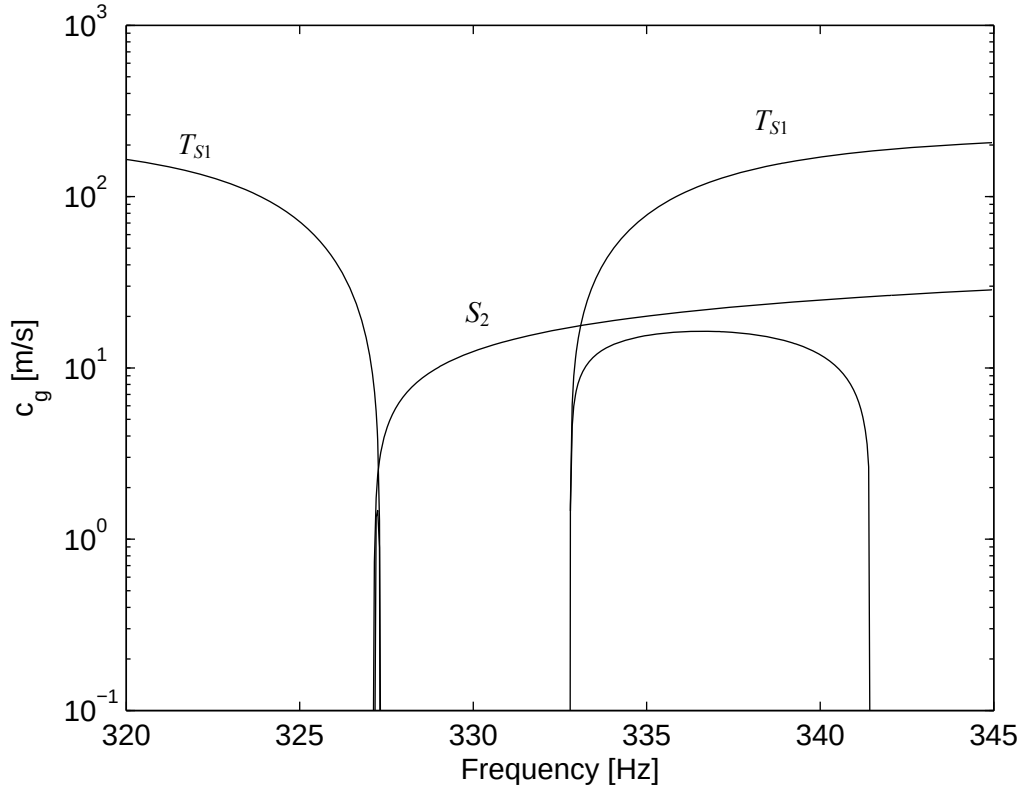

Figure 5.12: Group velocities for the S_2, T_{s1} modes.

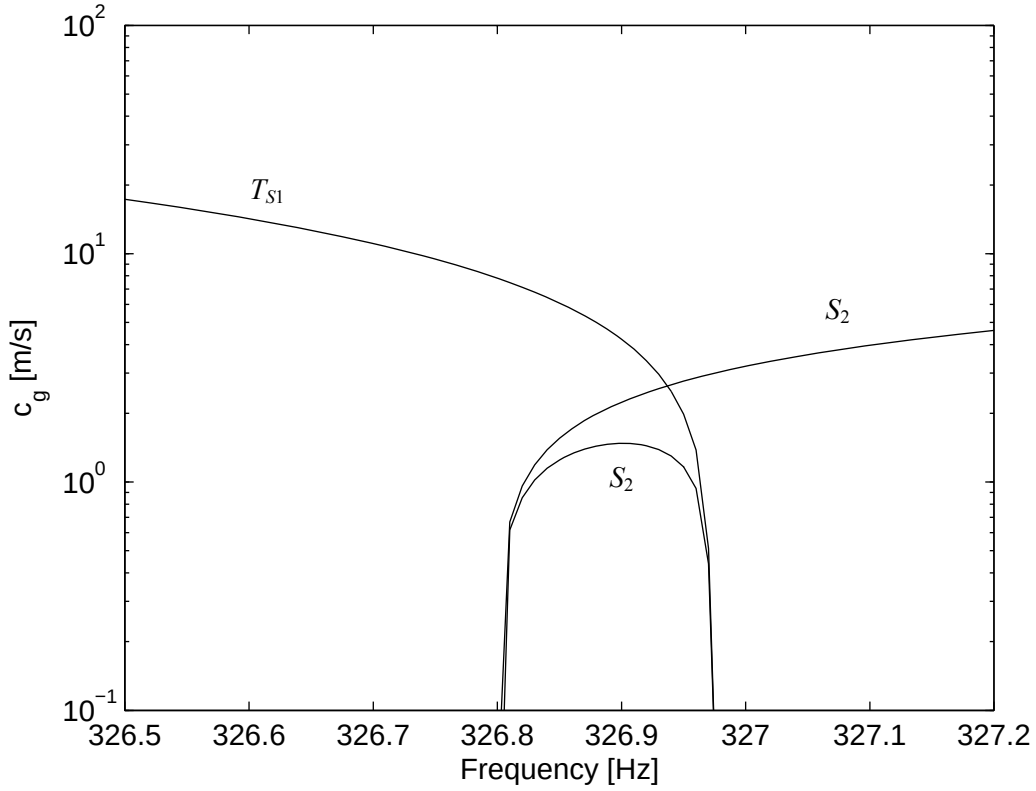

Figure 5.13: Group velocities for the S_2, T_{s1} modes around the bifurcation.

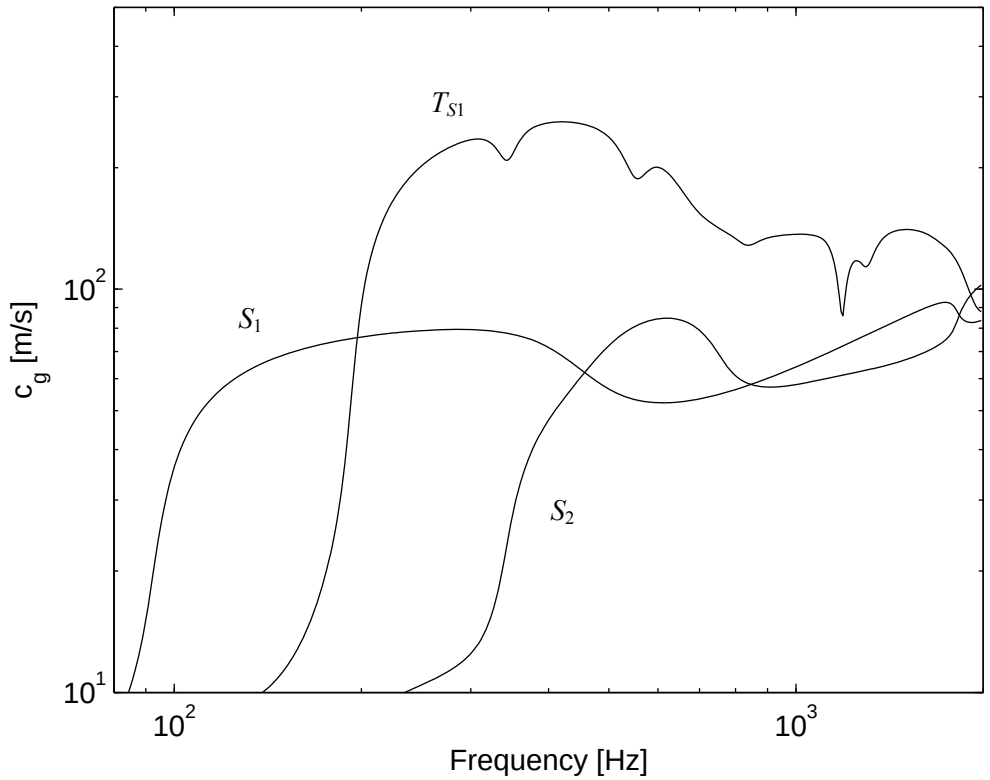

Figure 5.14: Group velocities for the damped S_1, S_2, T_{s1} modes.

Figure 5.15: Experimental setup.

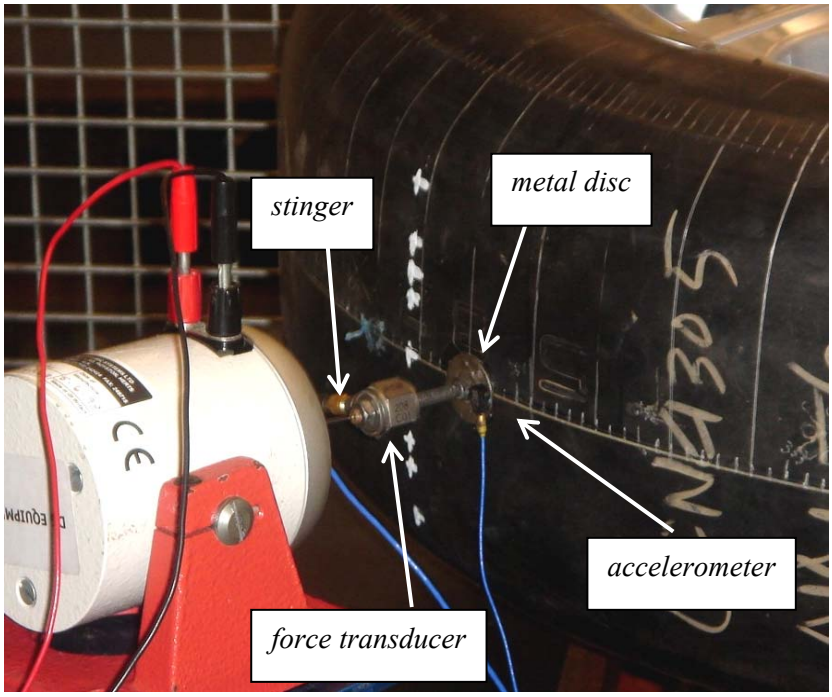

Figure 5.16: Excitation arrangement.

	Manufacturer	Model No.	Serial No.
Accelerometer	PCB Piezotronics	352C22	70096
Exciter	LDS Dynamics systems Lab.	V201	54587.43
Force transducer	PCB Piezotronics	208C01	20824
Amplifier	H/H Electronic	TPA50D	-
FFT Analyzer	Data Physics	Signal Mobilyzer 2	-

Table 5.1: Summary of equipment.

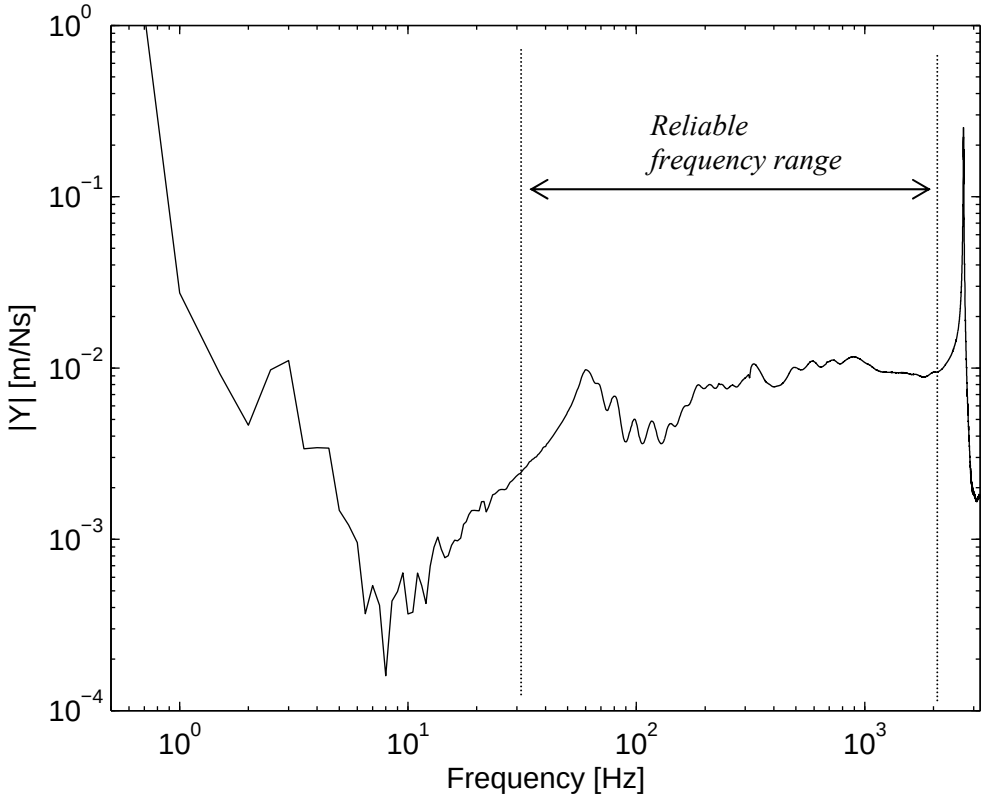

Figure 5.17: Typical measured input mobility of the tyre.

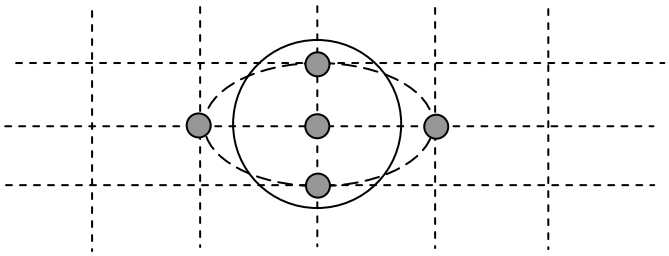

Figure 5.18: Modelling of the excitation region: — experimental; −− numerical modelling. Dots represent nodes where excitations applied. Dashed grid lines (····) represent FE.

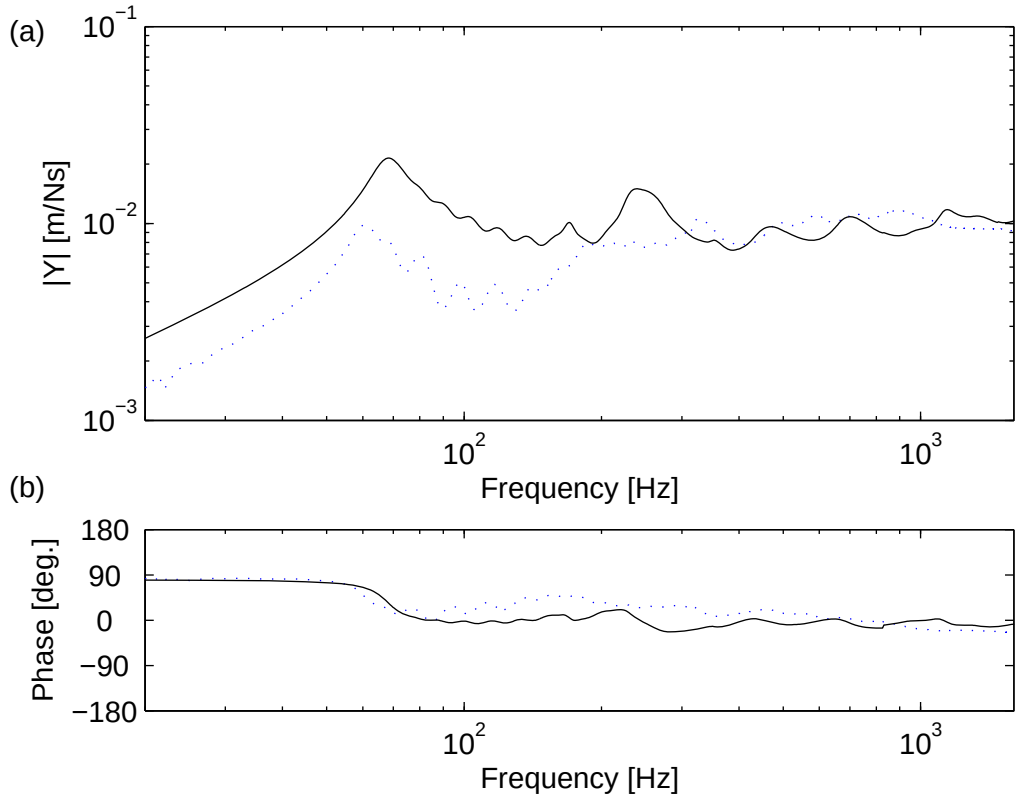

Figure 5.19: (a) Magnitude and (b) phase of the input mobility at the tread centre of the tyre without internal pressure: — the WFE result; ···· experiment.

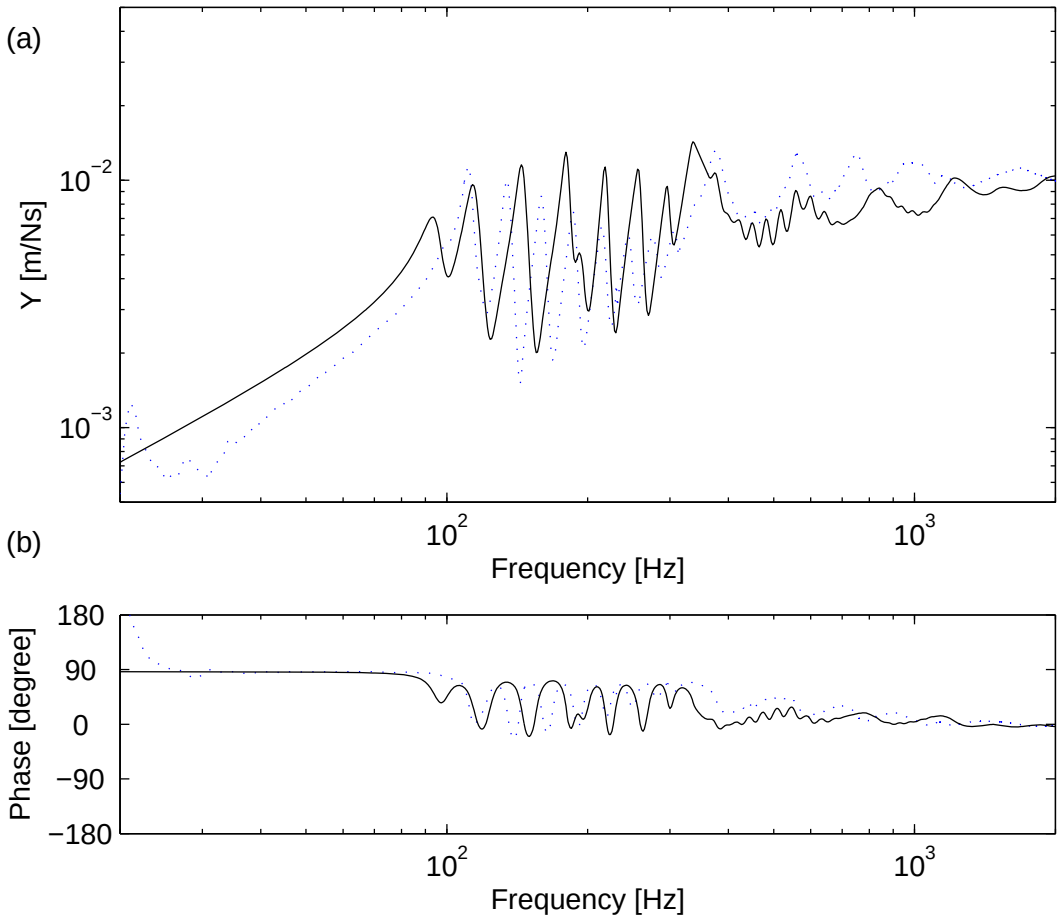

Figure 5.20: (a) Magnitude and (b) phase of the input mobility at the tread centre of the tyre with internal pressure: — the WFE result; ···· experiment.

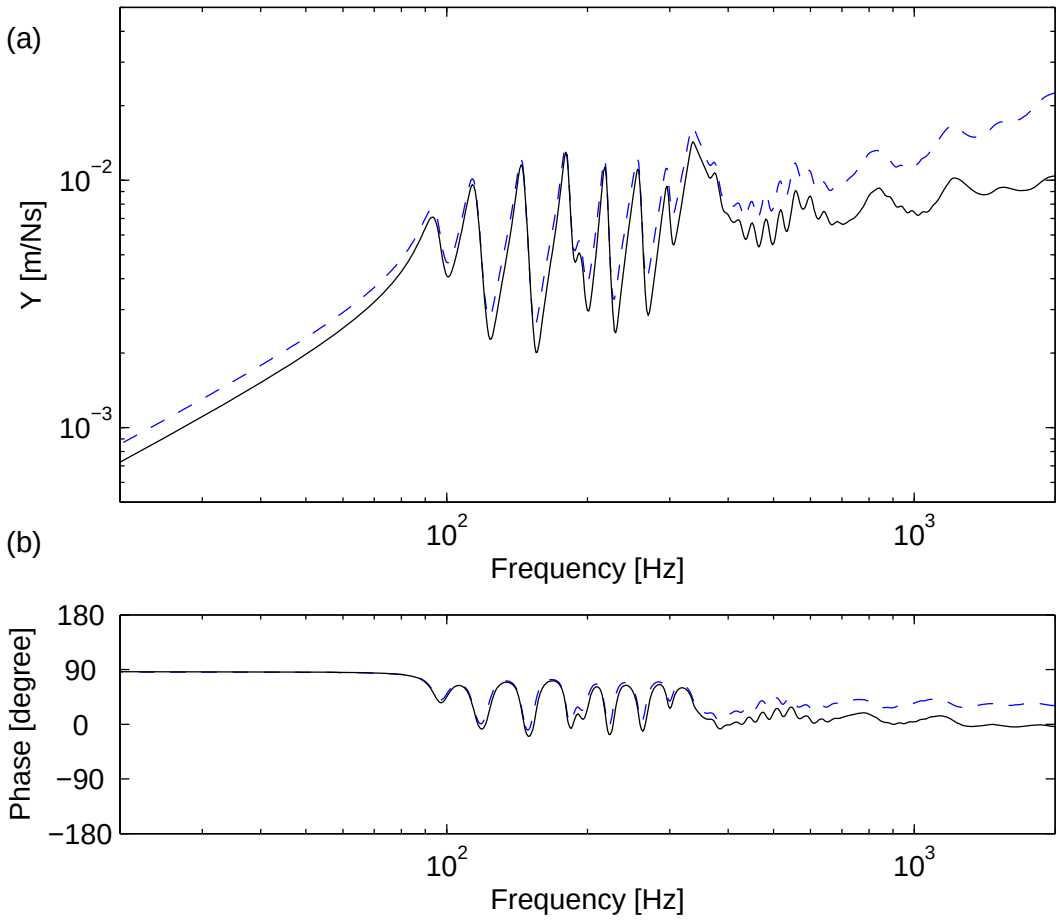

Figure 5.21: (a) Magnitude and (b) phase of the predicted input mobility of the tyre for — the finite area excitation; −− a point excitation.

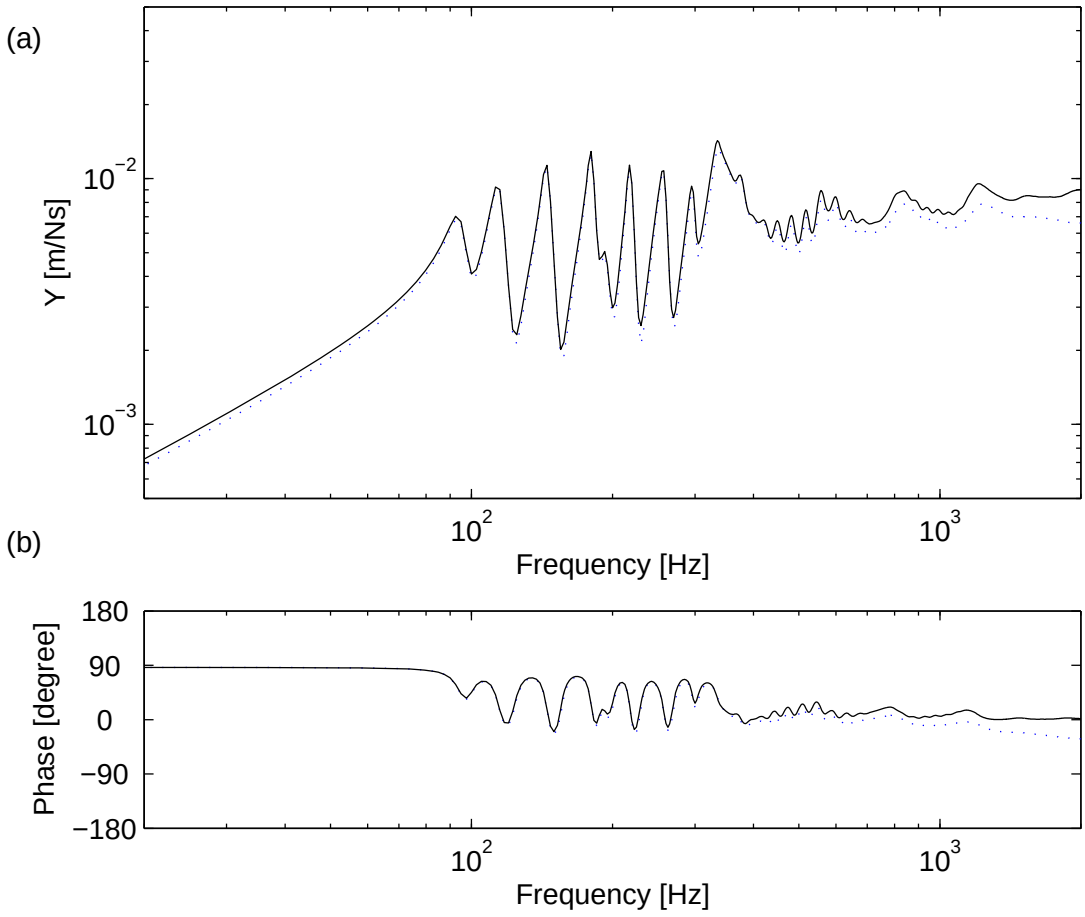

Figure 5.22: (a) Magnitude and (b) phase of the predicted input mobility of the tyre for — the uniform force excitation; ···· uniform velocity excitation.

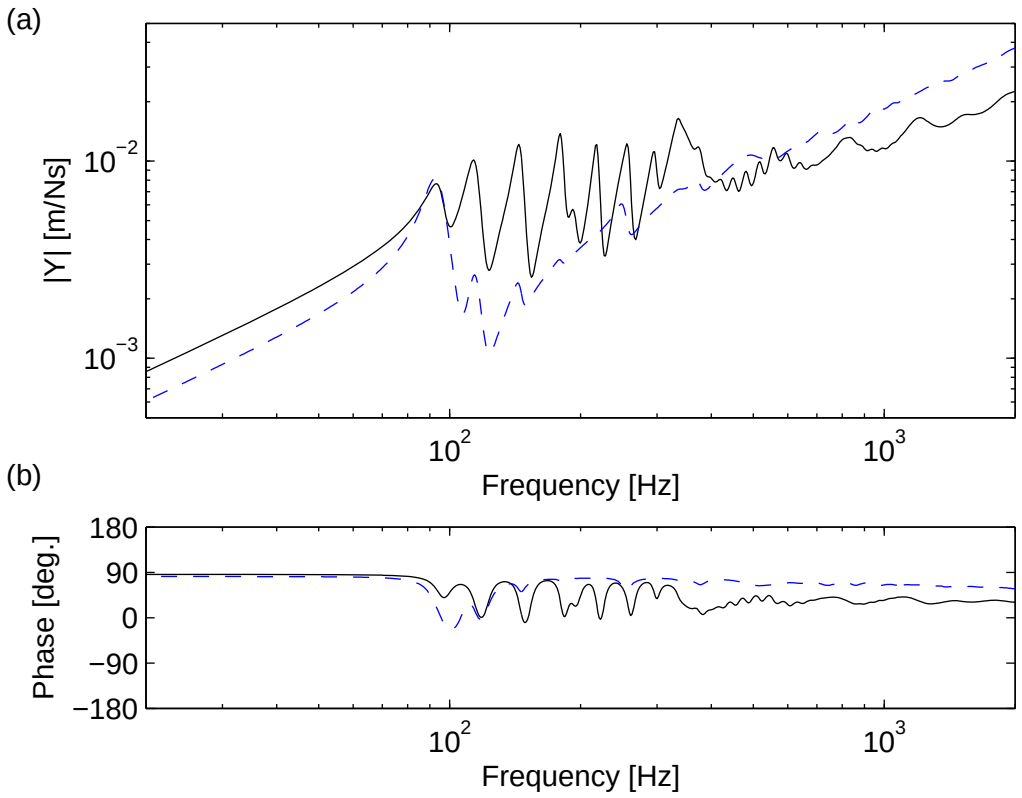

Figure 5.23: (a) Magnitude and (b) phase of the predicted input mobility of the tyre in — the radial direction; −− the circumferential direction.

Chapter 6
CONCLUDING REMARKS

6.1 Summary of Present Work

In this thesis, free wave propagation and forced response for general waveguides with arbitrary complexities in the cross-sections using the WFE method were considered.

In chapter 2 the WFE formulation was presented and numerical issues were discussed. It was seen that reformulating the eigenvalue problem using Zhong's method improves the conditioning. However, numerical issues remain. An application of SVD was proposed for reducing errors for numerically determining the eigenvectors. FE discretisation errors become large if the change in the phase or magnitude of the wave over the length of the section modelled becomes large. Use of a shorter section for modelling the waveguide reduces FE discretisation errors but there are large errors due to round-off of inertia terms because the stiffness terms of the section can become much greater than the inertia terms. A method of concatenating elements was thus proposed to reduce the round-off errors. The DOFs associated with internal nodes are dynamically condensed at each discrete frequency. Approximate expressions for the condensation were derived to reduce calculation cost. Three methods for predicting the group velocity were compared and the power and energy relationship was shown to be reliable to predict the group velocity.

The WFE method was then applied to complicated structures. Dispersion curves were shown including purely real, purely imaginary and complex wavenumbers. Freely propagating in-plane waves were considered for a plate strip with free edges and complicated phenomena such as non-zero cut-off phenomena and curve veering were described in section 3.4. A wave having a negative group velocity was observed to be associated with the non-zero cut-off phenomena. The WFE results were compared with numerical solutions to the analytical dispersion equations, i.e. the Rayleigh-Lamb frequency equations, using the WFE results as initial estimates. Freely propagating flexural waves in a plate strip with free edges were also presented including attenuating waves in section 3.5 and the results were compared with numerical solutions to the analytical dispersion equation

using the WFE results as initial estimates. Bifurcations from purely imaginary to complex wavenumbers or vice versa were described.

Free wave propagation in curved structures was then described. In curved structures, wave modes couple due to the curvature, especially below the ring frequency, and characteristics of wave modes change rapidly around the ring frequency. Dispersion curves for a ring were presented in section 3.6 and wave coupling due to the curvature was described. Free wave propagation in a cylindrical strip was considered in section 3.7 and waves in both the axial and circumferential directions were analysed.

The characteristics of the wave modes change rapidly around the frequencies where curve veering and bifurcation occur, and also around the ring frequency for the curved structures. Such wave mode change may be illustrated by their wave shapes as described in section 3.4 for in-plane wave modes, for which the longitudinal and shear wave modes couple, and in section 3.5 for flexural waves, for which two different orders of flexural wave modes couple. A method of decomposition of power was proposed which can be applied to general waveguides. The power associated with each DOF was analysed using this method for waves in a cylindrical strip to investigate the change of characteristics of wave modes with frequency in section 3.7. The method was also used to determine the DOFs which can be condensed or removed if power associated with a variable or a DOF is negligible. Such implementation was used in sections 3.3 and 3.4 for improving conditioning.

The method for determining the forced response of a finite waveguide using the wave approach was described in chapter 4. A well-conditioned formulation for determining the amplitudes of directly excited waves was proposed. Wave amplitudes were calculated considering the wave propagation and subsequent reflection at boundaries and the response was then determined by superimposing the wave amplitudes at the response point. Numerical examples for a beam, a plate and a cylinder were shown in section 4.2. The rapidly decaying nearfield waves often show insignificant contribution to the response. Inclusion of the rapidly decaying wave modes was discussed for a plate and a cylinder.

The method was also applied to a tyre in which the frequency dependent material properties of rubber were included into the WFE model. Freely propagating waves in a tyre were presented including attenuating waves. The predicted forced response was compared with experiment and reasonable agreement was seen. The size of the region of excitation was described. It was shown that the power injected into each wave mode and the effect of the

shear stiffness become important especially at high frequencies where the wavelengths become small.

In summary the WFE method provides a strong basis for the analysis of free and forced vibrations of waveguides of arbitrary complexity. Free wave propagation characteristics such as the wavenumber, the wave mode and the group velocity describe the dynamics of the waveguides. Such variables can be used as input parameters for, e.g., statistical energy analysis.

6.2 Conclusions

The following general conclusions can be drawn from this thesis.

- The WFE method is an accurate and powerful approach to the analysis of free and forced vibrations of waveguide structures.
- Commercial FE packages can be exploited.
- Computational cost is very low.

There are various issues concerning numerical errors.

- $|k\Delta| < 1$ or so (as discussed in subsection 2.4.1) is recommended to avoid FE discretisation errors.
- $\log_{10}(K_{ii}/M_{ii}) < 16$ in order that round-off errors of inertia terms are not substantial in double precision calculations.
- The method of concatenating elements described in section 2.5 can be used to reduce the round-off errors.
- The internal DOFs should be reduced at each frequency or using the approximate expression described in subsection 2.5.2.
- Zhong's formulation should be used to improve conditioning of the eigenvalue problem.
- The SVD procedure described in subsection 2.6.3 should be used when the eigenvectors are numerically determined.
- The power and energy relationship provides reliable estimates of the group velocity.

- Power associated with individual DOFs should be evaluated to indicate the characteristics of the wave motion and to indicate which DOFs can be condensed.
- The forced response of structures can be calculated using the wave approach. It is recommended that all propagating waves are included and some attenuating waves which decay least rapidly. As rule of thumb, attenuating waves for which $\mathrm{Im}\left|k\Delta\right| < 1$ should be included.
- Forced wave amplitudes should be estimated using the orthogonality relationship between the left and right eigenvectors as described in subsection 4.2.2.

The WFE method was applied to various waveguide structures. In particular the application to analysis of tyre vibrations was shown. The following were observed.

- Shapes of wave modes rapidly change around frequencies at which the bifurcation occurs.
- The area over which the excitation is applied affects the response at high frequencies.
- With regard to response of a tyre, modes are dominant at low frequencies but waves are dominant at high frequencies.

6.3 Suggestions for Further Research

Throughout this thesis, the WFE method has been shown to be reliable and a powerful tool to investigate the wave properties in and dynamics of waveguides. In this section possible further research related to the WFE method are proposed.

The cases may be listed as:

- Use of higher order FEs, mid-side nodes FEs and curved FEs are of interest especially for curved structures. Single straight FEs could be also possible to represent curved structures by rotating the coordinates at its edges.

- For rotating structures such as a tyre in the operating condition, the effects of the rotation such as Coriolis effect and centrifugal force may be included into the WFE model. The change in the phase velocity can be post-processed for positive- and negative-going waves by adding or subtracting the rotational velocity respectively.

- Inclusion of deterministic change in a cross-section along the waveguide could be considered. Examples include tread pattern of a tyre or a periodically stiffened panel. The forced response may be calculated considering the reflection and transmission at discontinuities.

- The effect of small variation along the waveguide can be another topic, for example a waveguide composed of Honeycomb structure. The WFE modelling and the limitation of the analysis in terms of wavelengths compared to the variation is of consideration.

Appendix 1
SUPPLEMENTS TO THE EIGENVALUE PROBLEMS

A1.1 Transfer Matrix Approach

This section gives supplementary explanations of the transfer matrix $\mathbf{T}$ in equation (2.14). The matrix $\mathbf{T}$ is a symplectic matrix [66,82,144] such that

$$\mathbf{T}^{\mathrm{T}}\mathbf{J}\mathbf{T}=\mathbf{J} \tag{A1.1}$$

or equivalently, $\mathbf{T}\mathbf{J}\mathbf{T}^{\mathrm{T}}=\mathbf{J}$ where

$$\begin{aligned}&\mathbf{J}=\begin{bmatrix}\mathbf{0} & \mathbf{I}\\ -\mathbf{I} & \mathbf{0}\end{bmatrix},\\ &\mathbf{J}^{\mathrm{T}}=\mathbf{J}^{-1}=-\mathbf{J}.\end{aligned} \tag{A1.2}$$

The eigenvalues of symplectic matrices occur in reciprocal pairs, i.e. if λ is an eigenvalue so is λ^{-1}. This characteristic is sometimes termed symplectic adjoint, e.g. [145]. The eigenvectors of $\mathbf{T}$, $\boldsymbol{\varphi}^{\pm}$, associated with $\lambda^{\pm}$ have the symplectic orthogonality relationship [82] such that

$$\boldsymbol{\varphi}_i^{+\mathrm{T}}\mathbf{J}\boldsymbol{\varphi}_k^{-}=0 \quad (i\neq k) \tag{A1.3}$$

and

$$\begin{aligned}&\boldsymbol{\varphi}_i^{+\mathrm{T}}\mathbf{J}\boldsymbol{\varphi}_i^{-}=1,\\ &\boldsymbol{\varphi}_i^{-\mathrm{T}}\mathbf{J}\boldsymbol{\varphi}_i^{+}=-1.\end{aligned} \tag{A1.4}$$

Discussions about the similarity between the symplectic orthogonality relationship and the Betti reciprocal theorem can be seen in [146]. More mathematical characteristics of the symplectic matrix and its decomposition are illustrated in [144].

The symplectic matrix arises in applications of such as the discrete linear-quadratic regulator problem, discrete Kalman filtering, the solution of discrete-time algebraic Ricatti equations and certain large, sparse quadratic eigenvalue problems [147]. Mathematical difficulties about solving the eigenvalue problem of the symplectic matrix can be also found in [147]. Zhong and Williams [82] showed the analogy of wave propagation in a periodic structure to optimal control. They also showed the application of symplectic mathematics to such problems [82].

It may be worth noting that the matrix inverse of the symplectic matrix can be found from equation (A1.1) to be $\mathbf{T}^{-1} = \mathbf{J}^{\mathrm{T}}\mathbf{T}^{\mathrm{T}}\mathbf{J}$, which is generally better-conditioned if the matrix needs to be inverted.

A1.2 Derivation of Zhong's Method

This section describes details of the derivation of the conditioned eigenvalue problem (2.55), i.e. Zhong's method [66]. The method starts from rearranging the equation of motion (2.3) as

$$\begin{bmatrix} \mathbf{q}_L \\ \mathbf{f}_L \end{bmatrix} = \begin{bmatrix} \mathbf{I} & \mathbf{0} \\ \mathbf{D}_{LL} & \mathbf{D}_{LR} \end{bmatrix} \begin{bmatrix} \mathbf{q}_L \\ \mathbf{q}_R \end{bmatrix}, \qquad \begin{bmatrix} \mathbf{q}_R \\ -\mathbf{f}_R \end{bmatrix} = \begin{bmatrix} \mathbf{0} & \mathbf{I} \\ -\mathbf{D}_{RL} & -\mathbf{D}_{RR} \end{bmatrix} \begin{bmatrix} \mathbf{q}_L \\ \mathbf{q}_R \end{bmatrix} \tag{2.54}$$

such that, using the periodicity condition (2.13),

$$\begin{bmatrix} \mathbf{0} & \mathbf{I} \\ -\mathbf{D}_{RL} & -\mathbf{D}_{RR} \end{bmatrix} \begin{bmatrix} \mathbf{q} \\ \lambda\mathbf{q} \end{bmatrix} = \lambda \begin{bmatrix} \mathbf{I} & \mathbf{0} \\ \mathbf{D}_{LL} & \mathbf{D}_{LR} \end{bmatrix} \begin{bmatrix} \mathbf{q} \\ \lambda\mathbf{q} \end{bmatrix}. \tag{A1.5}$$

From equation (A1.5), the transfer matrix $\mathbf{T}$ can be alternatively expressed as

$$\mathbf{T} = \mathbf{L}^{-1}\mathbf{N} \tag{A1.6}$$

where

$$\mathbf{L} = \begin{bmatrix} \mathbf{I} & \mathbf{0} \\ \mathbf{D}_{LL} & \mathbf{D}_{LR} \end{bmatrix}, \qquad \mathbf{N} = \begin{bmatrix} \mathbf{0} & \mathbf{I} \\ -\mathbf{D}_{RL} & -\mathbf{D}_{RR} \end{bmatrix}. \tag{A1.7}$$

For the matrices $\mathbf{L}, \mathbf{N}$ the relationship

$$\mathbf{L}^{\mathrm{T}}\mathbf{J}\mathbf{L} = \mathbf{N}^{\mathrm{T}}\mathbf{J}\mathbf{N} = \begin{bmatrix} \mathbf{0} & \mathbf{D}_{LR} \\ -\mathbf{D}_{RL} & \mathbf{0} \end{bmatrix} \tag{A1.8}$$

holds [66]. Premultiplying equation (A1.5) by $\mathbf{L}^{\mathrm{T}}\mathbf{J}$ and by $\mathbf{N}^{\mathrm{T}}\mathbf{J}$ in turn gives

$$\begin{bmatrix} -\mathbf{D}_{RL} & -\mathbf{D}_{LL} - \mathbf{D}_{RR} \\ \mathbf{0} & -\mathbf{D}_{RL} \end{bmatrix} \begin{bmatrix} \mathbf{q} \\ \lambda\mathbf{q} \end{bmatrix} = \lambda \begin{bmatrix} \mathbf{0} & \mathbf{D}_{LR} \\ -\mathbf{D}_{RL} & \mathbf{0} \end{bmatrix} \begin{bmatrix} \mathbf{q} \\ \lambda\mathbf{q} \end{bmatrix} \tag{A1.9}$$

and

$$\begin{bmatrix} \mathbf{D}_{LR} & \mathbf{0} \\ \mathbf{D}_{RR} + \mathbf{D}_{LL} & \mathbf{D}_{LR} \end{bmatrix} \begin{bmatrix} \mathbf{q} \\ \lambda\mathbf{q} \end{bmatrix} = \frac{1}{\lambda} \begin{bmatrix} \mathbf{0} & \mathbf{D}_{LR} \\ -\mathbf{D}_{RL} & \mathbf{0} \end{bmatrix} \begin{bmatrix} \mathbf{q} \\ \lambda\mathbf{q} \end{bmatrix}. \tag{A1.10}$$

Adding these two equations (A1.9) and (A1.10) gives the conditioned eigenvalue problem, equations (2.55)-(2.57), i.e.

$$\left(\lambda + \frac{1}{\lambda}\right) \begin{bmatrix} \mathbf{0} & \mathbf{D}_{LR} \\ -\mathbf{D}_{RL} & \mathbf{0} \end{bmatrix} \begin{bmatrix} \mathbf{q} \\ \lambda\mathbf{q} \end{bmatrix} = \begin{bmatrix} \left(\mathbf{D}_{LR} - \mathbf{D}_{RL}\right) & -\left(\mathbf{D}_{LL} + \mathbf{D}_{RR}\right) \\ \left(\mathbf{D}_{LL} + \mathbf{D}_{RR}\right) & \left(\mathbf{D}_{LR} - \mathbf{D}_{RL}\right) \end{bmatrix} \begin{bmatrix} \mathbf{q} \\ \lambda\mathbf{q} \end{bmatrix}. \tag{A1.11}$$

A1.3 Thompson's Method

Another method for improving the conditioning of the eigenvalue problem, which is worth noting, is Thompson's method [58]. The conditioning starts from the polynomial eigenvalue problem, i.e.

$$\left[\lambda^2\mathbf{D}_{LR}+\lambda\left(\mathbf{D}_{LL}+\mathbf{D}_{RR}\right)+\mathbf{D}_{RL}\right]\mathbf{q}=\mathbf{0}. \tag{2.51}$$

For uniform waveguides all the elements of the dynamic stiffness matrix have certain relationships depending on whether the DOFs at element interface are symmetric (S) or asymmetric (A) between adjoint sections, i.e. equation (2.5) [58].

After partitioning the dynamic stiffness matrix associated with the force components being symmetric at the interface and the displacement components being symmetric (S-S) vice versa, the matrix operation in equation (2.51) can be expressed for elements associated with S-S or A-A DOFs as

$$\lambda\mathbf{D}_{LR}+\left(\mathbf{D}_{LL}+\mathbf{D}_{RR}\right)+\frac{1}{\lambda}\mathbf{D}_{RL}=2\left\{\cosh\left(\mu\right)\mathbf{D}_{LR}+\mathbf{D}_{LL}\right\} \tag{A1.12}$$

for $\lambda\neq 0$ and

$$\lambda=e^{\mu}. \tag{A1.13}$$

Similarly, the matrix operation for elements associated with the S-A and the A-S DOFs can be expressed as

$$\lambda\mathbf{D}_{LR}+\left(\mathbf{D}_{LL}+\mathbf{D}_{RR}\right)+\frac{1}{\lambda}\mathbf{D}_{RL}=2\sinh\left(\mu\right)\mathbf{D}_{LR}. \tag{A1.14}$$

From equations (A1.12) and (A1.14), equation (2.51) can be reformulated as

$$\begin{bmatrix}\cosh\left(\mu\right)\mathbf{D}_{LR}^{(SS)}+\mathbf{D}_{LL}^{(SS)} & \sinh\left(\mu\right)\mathbf{D}_{LR}^{(SA)}\\ \sinh\left(\mu\right)\mathbf{D}_{LR}^{(AS)} & \cosh\left(\mu\right)\mathbf{D}_{LR}^{(AA)}+\mathbf{D}_{LL}^{(AA)}\end{bmatrix}\begin{bmatrix}\mathbf{q}^{(S)}\\ \mathbf{q}^{(A)}\end{bmatrix}=\mathbf{0} \tag{A1.15}$$

where the superscript S denotes the symmetric DOF and A is the anti-symmetric DOF. After some manipulations, equation (A1.15) becomes the general eigenvalue problem

$$\begin{bmatrix}\mathbf{D}_{LL}^{(SS)} & \mathbf{D}_{LR}^{(SA)}\\ -\mathbf{D}_{LR}^{(AS)} & \mathbf{D}_{LL}^{(AA)}\end{bmatrix}\begin{bmatrix}\left(\cosh\left(\mu\right)+1\right)\mathbf{q}^{(S)}\\ \sinh\left(\mu\right)\mathbf{q}^{(A)}\end{bmatrix}=-\cosh\left(\mu\right)\begin{bmatrix}\mathbf{D}_{LR}^{(SS)} & \mathbf{D}_{LR}^{(SA)}\\ \mathbf{D}_{LR}^{(AS)} & \mathbf{D}_{LR}^{(AA)}\end{bmatrix}\begin{bmatrix}\left(\cosh\left(\mu\right)+1\right)\mathbf{q}^{(S)}\\ \sinh\left(\mu\right)\mathbf{q}^{(A)}\end{bmatrix}. \tag{A1.16}$$

The matrix of the eigenvalue problem in equation (A1.16) is only half the size of Zhong's method and its eigenvectors are associated with only the displacement components such that the conditioning may be expected to be better than Zhong's method.

Physically asymmetric DOFs such as the moment is zero at the cut-off frequency, $\mu = 0$. However numerical difficulties arise when the eigenvalue problem (A1.16) is numerically solved and the original eigenvector is numerically determined. The coefficients of the eigenvectors, $\sinh(\mu)$ in equation (A1.16) approaches 0 and $\cosh(\mu)+1$ approaches to 2 when $\mu \to 0$. Even small errors in $\mathbf{q}^{(A)}$ can be magnified when $\mathbf{q}^{(A)}$ is numerically evaluated divided by $\sinh(\mu)$. Zhong's method was therefore applied throughout this thesis and the method worked well for the problems.

Appendix 2
NUMERICAL METHODS FOR SOLVING A TRANSCENDENTAL EQUATION

A2.1 Muller's Method

Muller's method is an interpolation method that uses quadratic interpolation [91]. A complex root, $z = x + jy$, is found using a quadratic equation that passes through three complex values in the vicinity of an initial estimate as shown in Figure A2.1. Suppose that it is desired to find the solutions to $f(z) = 0$. Approximating $f(z)$ as a quadratic in z gives $f(z) = az^2 + bz + c$. Let $h_1 = z_1 - z_0$ and $h_2 = z_2 - z_0$ thus

$$\begin{aligned} a(0^2) + b(0) + c &= f_0, \\ a(h_1^2) + b(h_1) + c &= f_1, \\ a(h_2^2) - b(h_2) + c &= f_1. \end{aligned} \tag{A2.1}$$

The coefficients are evaluated such that

$$\begin{aligned} a &= \frac{\gamma f_1 - f_0(1+\gamma) + f_2}{\gamma h_1^2 (1+\gamma)}, \\ b &= \frac{f_1 - f_0 - a h_1^2}{h_1} \end{aligned} \tag{A2.2}$$

where $\gamma = h_2 / h_1$. The trial quadratic equation is solved to give the estimate, $\hat{z}$,

$$\hat{z} = z_0 - \frac{2c}{b \pm \sqrt{b^2 - 4ac}}. \tag{A2.3}$$

The sign in the denominator is taken so as to give the larger absolute value. The calculation is repeated till the root converges. In this thesis the threshold value for convergence is set as $\left|f\left(\hat{z}\right)\right| < 10^{-3}$.

In practice, the root finding process (A2.3) may be applied to $\left|f\left(z\right)\right|$ or both $\mathrm{Re}\left\{f\left(z\right)\right\}$ and $\mathrm{Im}\left\{f\left(z\right)\right\}$. Figure A2.2 shows an example of the solution space of $\left|f\left(z\right)\right|$. An initial estimate is represented by $*$ and an arrow denotes to the direction of an approximate solution from the initial estimate. It can be seen that in this case the solution space is more sensitive to $\mathrm{Re}\left(z\right)$ than $\mathrm{Im}\left(z\right)$. In such a case, it may be difficult for the method to converge to the right answer, especially for obtaining an accurate estimate of $\mathrm{Im}\left(z\right)$. Alternatively if the cost function is chosen as both $\mathrm{Re}\left\{f\left(z\right)\right\}$ and $\mathrm{Im}\left\{f\left(z\right)\right\}$, as in Figure A2.3, such difficulties for convergence may be reduced. After the root finding process (A2.3) is repeated both for $\mathrm{Re}\left\{f\left(z\right)\right\}$ and $\mathrm{Im}\left\{f\left(z\right)\right\}$, the next initial estimate is given as a superposition of each result. Figure A2.3 illustrates the root finding procedure for each of $\mathrm{Re}\left\{f\left(z\right)\right\}$ and $\mathrm{Im}\left\{f\left(z\right)\right\}$. Adding each change, $\Delta\mathrm{Re}\left(z\right)+\Delta\mathrm{Im}\left(z\right)$, is then used to give the next estimate of $\hat{z}$.

A2.2 Argument Principle

Complex roots of the function $f\left(z\right)$ can be also estimated using the argument principle [92]. Consider $f\left(z\right)$ in some region of the complex z-plane enclosed by a contour γ. If $f\left(z\right)$ has no singularity within γ, the number of zeros of $f\left(z\right)$ within the contour γ is given by [92]

$$N = \frac{1}{2\pi j}\int_{\gamma}\frac{f'\left(z\right)}{f\left(z\right)}dz \tag{A2.4}$$

where N is the number of zeros of $f(z)$ in γ. Numerical integration, e.g. the trapezoidal rule, may be applied to give the calculation (A2.4) such that [148]

$$\int f(z)dz = S_n + R_n,$$

$$S_n = \frac{(z_1 - z_0)}{2} f(z_0) + \frac{(z_n - z_{n-1})}{2} f(z_n) + \sum_{k=1}^{n-1} \frac{(z_{k+1} - z_{k-1})}{2} f(z_k), \tag{A2.5}$$

$$|R_n| \le \frac{|z_n - z_0|^3}{12n^2} \max|f''| \approx \frac{|z_n - z_0|^3}{3n^2} \max\left|\frac{f(z_{i+1}) - 2f(z_i) + f(z_{i-1})}{z_{i+1} - z_{i-1}}\right|, i = 1, \cdots, n-1$$

where S_n is the numerical value of the integral and R_n is the residual. In this thesis the number of discrete points n is taken to be such that $R_n \le 10^{-4}$.

It should be noted that the finite difference approximation in the last equation in equations (A2.5) is derived from Taylor series expansion. The distance between two discrete numerical integration points therefore needs to be equal to satisfy Taylor series expansion.

The shape of γ is chosen as a rectangle in the complex z-plane. The region γ is chosen to be relatively large for the first integral around a contour enclosing an initial estimate of a root. Bisection of this region is then used to give a better estimate of the solution. The calculations are repeated until γ converges to be smaller than some chosen values.

In this thesis the method was used to give N=1 with the criteria of the convergence as ±0.1% of the estimation for both $\mathrm{Re}(\hat{z})$ and $\mathrm{Im}(\hat{z})$ such that $\gamma \subseteq \{\mathrm{Re}(\hat{z}) \times (1 \pm 0.001), \mathrm{Im}(\hat{z}) \times (1 \pm 0.001)\}$. If either $\mathrm{Re}(\hat{z})$ or $\mathrm{Im}(\hat{z})$ of an estimation is close to zero, ±0.01 is applied such that $\gamma \subseteq \{\mathrm{Re}(\hat{z}) \times (1 \pm 0.001), (\pm 0.01)\}$ if $|\mathrm{Im}(\hat{z})| < 0.01$. The region γ can determine the error bound of an estimated solution.

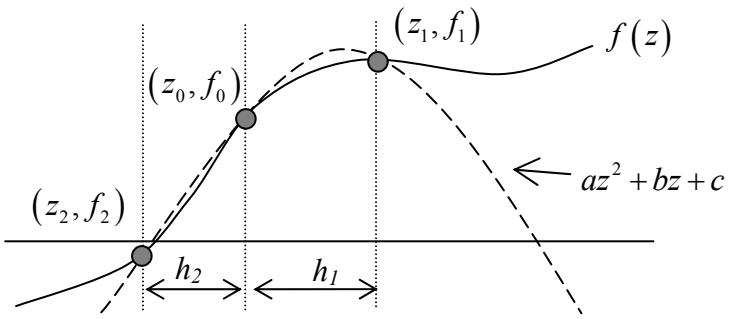

Figure A2.1: Muller's method using a quadratic function.

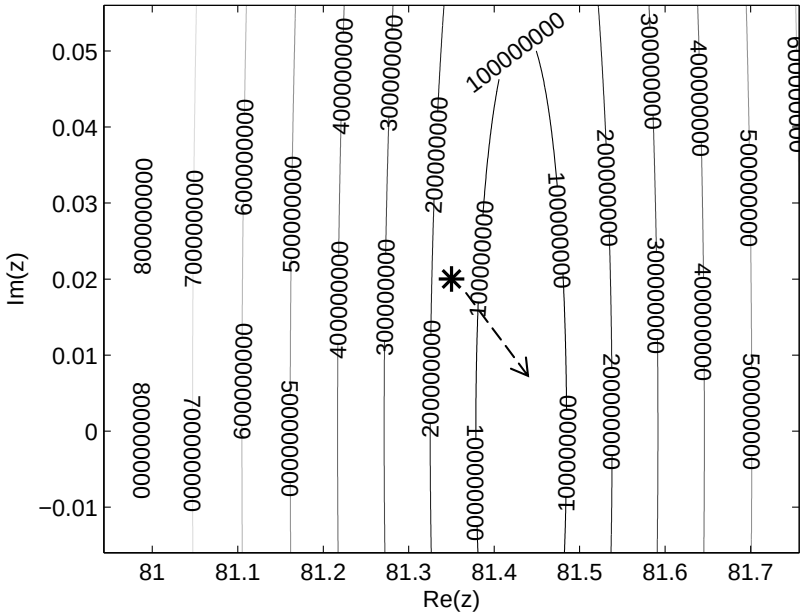

Figure A2.2: Example of a contour plot for $\left|f(z)\right|$.

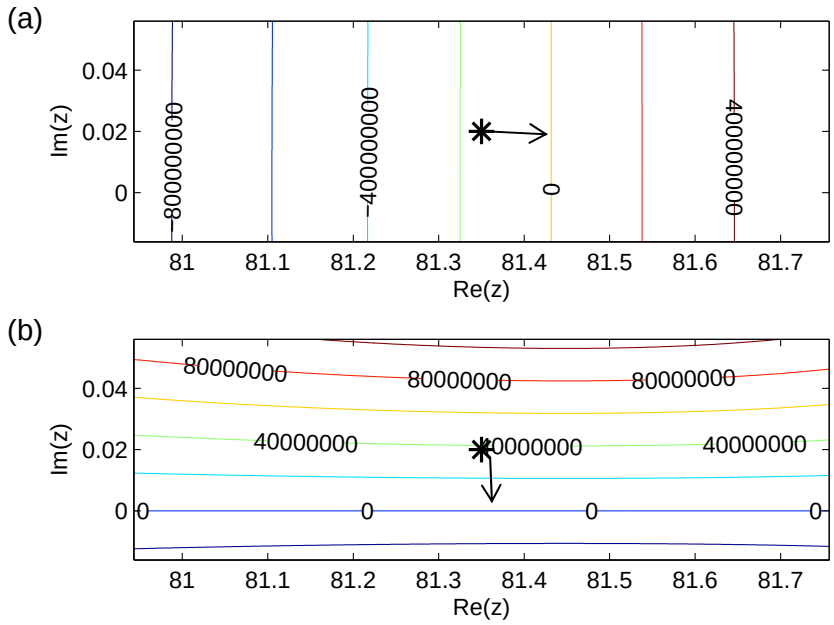

Figure A2.3: Contour plot of (a) $\mathrm{Re}\{f(z)\}$*; (b)* $\mathrm{Im}\{f(z)\}$.

Appendix 3
MODELLING AND MATERIAL PROPERTIES OF A TYRE

A3.1 Cross-section of a Tyre

This section gives supplementary details about the tyre. A 'slick' tyre without tread design (tyre size: 195/65R15) was provided by Bridgestone Corporation. An illustration of the cross-section of the tyre is shown in Figure A3.1. The structure of the cross-section of the tyre is simpler than general commercial tyres but similar. A tyre is composed of steel and textile fibre reinforced rubber (FRR) sheets and several different rubbers.

Material properties provided are given in Table A3.1 for rubber and A3.2 for the FRR sheets. In Table A3.1, β_E represent the coefficients of the frequency dependent stiffness in equation (5.3). All properties were measured at about 30°C. For rubber, material properties were measured under the condition of 1% strain, 50 Hz. Poisson's ratio ν is assumed to be 0.49 for rubber [149]. In Table A3.2, E_L and E_T are the Young's modulus in the direction of the fibre and in the transverse direction of the fibre respectively. The angle is that between the fibre extending in the tyre and the circumferential direction of the tyre. There are two steel belts and one has an angle of 22 degrees and another has that of -22 degrees.

The rubber at the lower part of the sidewall is relatively stiff and the upper part is more flexible. The FRR sheets termed 'carcass ply' extend to the inside of the tyre and turn up enclosing the bead wire locate being at the bottom of the sidewall. The bead wire fixes the tyre to a rim. This is not modelled and the fixed boundary conditions were imposed. The steel and textile FRR sheets, termed belt and cap/layer, extend only over the tread region. The belt and cap/layer will be referred as the 'belt package' in this appendix.

Because the two steel belts have different angles, they show the same characteristics as a composite layer or a laminate. A laminate shows behaviour depending on the angles of the layers due to the coupling between the in-plane and out-of-plane deformation even for a flat composite layer, e.g. [150]. Such deformation is particularly obvious only around the edge of

the composite layer. This behaviour brings asymmetry of the structure and causes complicated phenomena. Inclusion of such behaviour is beyond the scope of this thesis and the two steel belts were modelled as a single orthotropic plate. The equivalent material properties were derived using formulas described in [150]. For a laminate illustrated in Figure A3.2, the Young's modulus can be expressed as

$$E_x = \frac{E_L E_T \left(\sin^4\theta - \sin^2\theta\cos^2\theta + \cos^2\theta\right) + 3/4\, E_T^2}{E_L \sin^4\theta + E_T},$$
$$E_y = \frac{E_L E_T \left(\sin^4\theta - \sin^2\theta\cos^2\theta + \cos^2\theta\right) + 3/4\, E_T^2}{E_L \cos^4\theta + E_T} \qquad \text{(A3.1)}$$

and the shear modulus is given by

$$G_{xy} = E_L \sin^2\theta\cos^2\theta + \frac{1}{4} E_T \cos^2 2\theta \ . \qquad \text{(A3.2)}$$

Poisson's ratio ν_{xy} is assumed to be 0.3 for simplicity and the Maxwell-Betti relationship gives $\nu_{xy}/\nu_{yx} = E_x/E_y$.

A3.2 FE Modelling of the Cross-section of the Tyre

This section describes details of the FE model shown in Figures 5.3 and 5.4. The segment of the tyre was modelled using SOLID46 elements in ANSYS 7.1. The element generates equivalent material properties for a layered structure in a single element. The values given in equations (A3.1) and (A3.2) were used for the properties of the belt.

A tyre is subjected to internal pressure and this pressure stiffens the tyre due to the in-plane tension it produces. In particular, the stiffening effect is significant in the circumferential direction for the tread region and in the cross-sectional direction for the sidewall region. To represent the phenomena, surface loads were applied as shown in Figure A3.3(a). In the sidewall regions (both the left and right hand sides), uniform pressure of

$P = 200$ kPa was applied. In the tread regions (both the fore and aft sides) the value of pressure was determined by the equivalent in-plane tension associated with the belt package. From the classical membrane theory e.g. [151] the membrane force (the tensile force per unit thickness), T (N/m), is expressed as

$$T = PR \tag{A3.3}$$

where R is the representative radius of the belt package. The equivalent pressure over the element surfaces is thus given by T/h where h is the thickness of the tread including the rubber and belt package. Since the in-plane tension is mostly subjected to the belt package in the tread region, the surface loads were applied as distributed pressure across the tread thickness as Figure A3.3(b). The pressure distribution was modelled as a triangular shape such that the value of pressure was $2P/h$ along the bottom of the tread region and there is no pressure along the top of the tread region. Necessary constraints such as the circumferential deformation of the sidewall region and the lateral deformation of the tread region were imposed.

A3.3 Inclusion of Frequency Dependent Material Properties of Rubber

Frequency dependent material properties of rubber were included using equations (5.3) and (5.4). Since the details of the frequency dependent properties were not available, they were approximated using the available data in literature [140]. The literature provides the data of the ANSI standard polymer. Although the polymer may not always represent all different rubbers in the tyre, the trend is assumed to be same. Figures A3.4 and A3.5 show the frequency dependencies of the Young's modulus and the loss factor, respectively [140]. The abscissa is the reduced frequency in which the temperature effect is included at the reference temperature of 25 ºC. The shift factor with temperature, α_T, is shown in Figure A3.6. The reduced frequency f_{red} is defined as

$$f_{red} = \alpha_T f \,. \tag{A3.4}$$

This implies that the material properties of the rubber at 1 Hz, -14.5 ºC are equivalent to those at 10^5 Hz, 25 ºC. This is a reason why such wide range of the reduced frequency is illustrated in Figures A3.4 and A3.5.

Since the measured material properties provided were measured around 30 ºC, $\alpha_T = 0.1$ $\left(\log \alpha_T = -1\right)$ was read from Figure A3.6 such that the frequency range of interest is $f_{red} = 1 \sim 200$ $\left(f = 10 \sim 2000\right)$ Hz for the tyre vibration analysis. The values $\alpha_E = 0.1, \alpha_\eta = 0.01, \beta_\eta = 0.1$ in equations (5.3) and (5.4) were determined from Figures A3.4 and A3.5.

A3.4 Forced Response using Different FE Models

As an illustrative example of the WFE method, the free and forced vibrations of the tyre are described in chapter 5. At high frequencies (around 2 kHz) the highest order of the propagating wave is the S_8 mode in which there are about 8.5 wavelengths across the cross-section. The model with 28 elements used in Chapter 5 (see Figure A3.7(a)) may be not enough to represent such high wave modes. To investigate the FE discretisation error, another 'fine' FE model was formed as Figure A3.7(b). The FE model contains 50 elements in the cross-section such that there are about 6 elements per wavelength for the S_8 mode and the FE discretisation error can be expected to be smaller.

The forced response for the point excitation applied to the tread centre is shown in Figure A3.8. Each resonance peak at low frequencies differs because the 'fine' model can model more details of the distributions of the stiffness and mass of the tyre as well as the shape of the cross-section. However, the trend is the same for both FE models especially for low and middle frequencies. At high frequencies the slope of the asymptote differs but the magnitude increases with frequency and the response is rather stiffness-like (reactive). The discussion in chapter 5 therefore holds for both FE models and the simple FE model was used because the conditioning of the eigenvalue problem is better and the calculation cost is much cheaper. As an illustrative example of a practical application, it can be seen that such small FE model (computational cost) can give good estimates of the dynamic behaviours of a complicated structure using the WFE method.

A3.5 Operational Deflection Shape

The input mobilities are shown in Chapter 5. The transfer responses can be similarly calculated. The forced response of the whole tyre can therefore be calculated at each discretised frequency.

The responses, i.e. the operational deflection shape, of the tyre with internal pressure are shown. The point force excitation is applied at the centre of the tyre. Figure A3.9 shows the operational deflection shape at 93 Hz, which is associated with the first natural frequency. At the frequency the tread mass is vibrating on the sidewall stiffness such that the tyre vibrates as the single degree of freedom system. At middle frequencies where higher wave modes cut-on, the tyre deforms in a more complicated shape. The deformation at 374 Hz is shown in Figure A3.10. It can be seen that as the wavelengths in a tyre become shorter, the waves decay more quickly compared to Figure A3.9 due to the damping of rubber. Figure A3.11 shows the deformation at 1209 Hz. At such high frequencies, the deformation localized only around the excitation. One can understand that the response can be well expressed in terms of waves at such high frequencies.

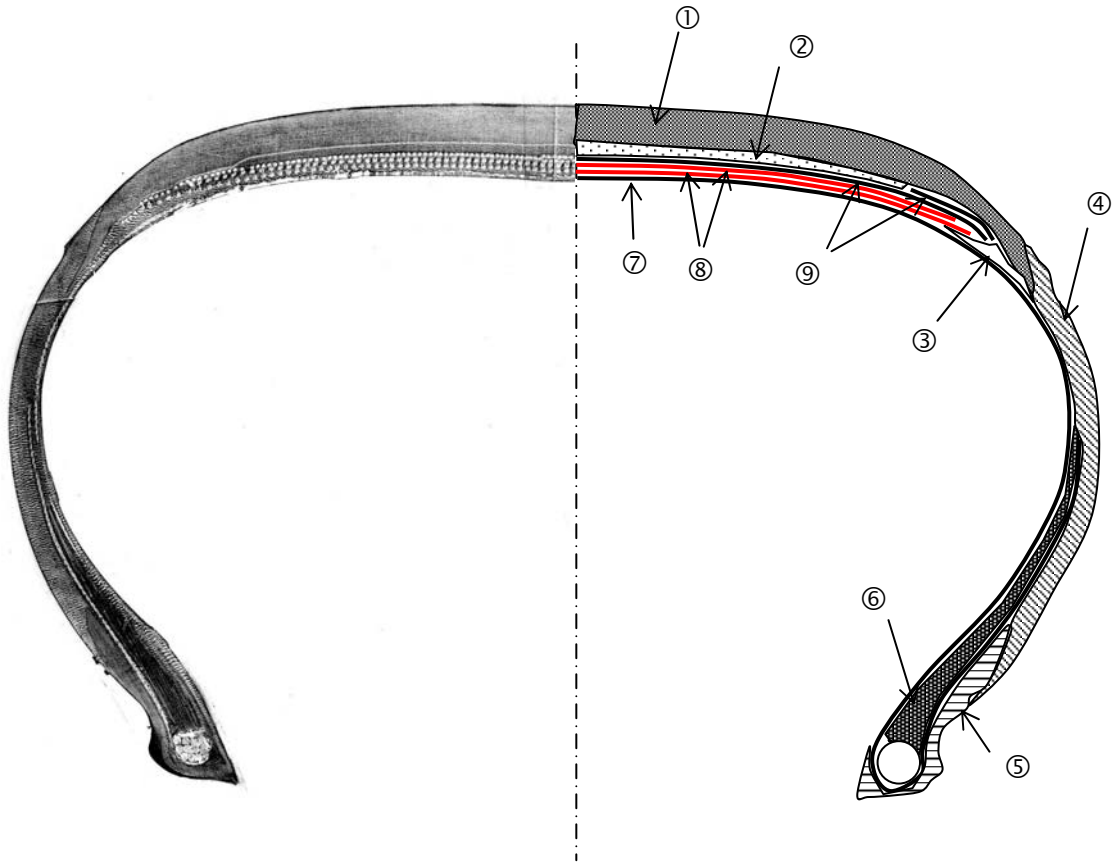

Figure A3.1: Cross-section of the tyre. Right hand side exaggerates the structure for clarity.

		E	β_E (Eq. 5.3)	ρ
①	Top	$1 \cdot 10^7$	7	1000
②	Base	$4 \cdot 10^6$	6	1100
③	Cushion	$1 \cdot 10^7$	7	1100
④	Side	$4 \cdot 10^6$	7	1100
⑤	Chafer	$2 \cdot 10^7$	7	1200
⑥	Filler	$1 \cdot 10^8$	8	1200

Table A3.1: Material properties of rubber in SI units. Numerical values are rounded to 1 significant figure because they are commercially sensitive.

		E_L	E_T	ν_{LT}	ρ	angle (degree)
⑦	Carcass ply	$2 \cdot 10^9$	$1 \cdot 10^7$	0.4	1200	90
⑧	Belt (steel)	$5 \cdot 10^{10}$	$2 \cdot 10^7$	0.4	3100	±22
⑨	Cap/Layer (textile)	$1 \cdot 10^9$	$1 \cdot 10^7$	0.4	1100	0

Table A3.2: Material properties of FRR sheets in SI units. Numerical values are rounded to 1 significant figure because they are commercially sensitive.

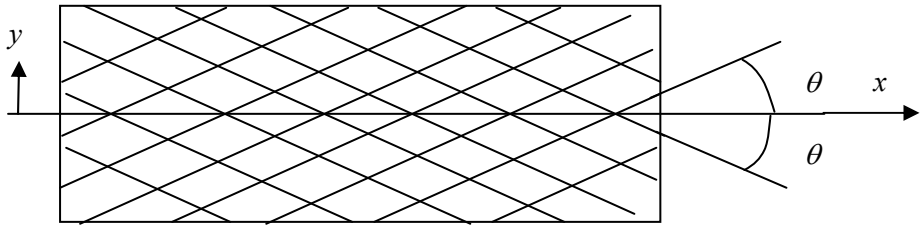

Figure A3.2: Laminate of two FRR sheets with angle of $\pm\theta$.

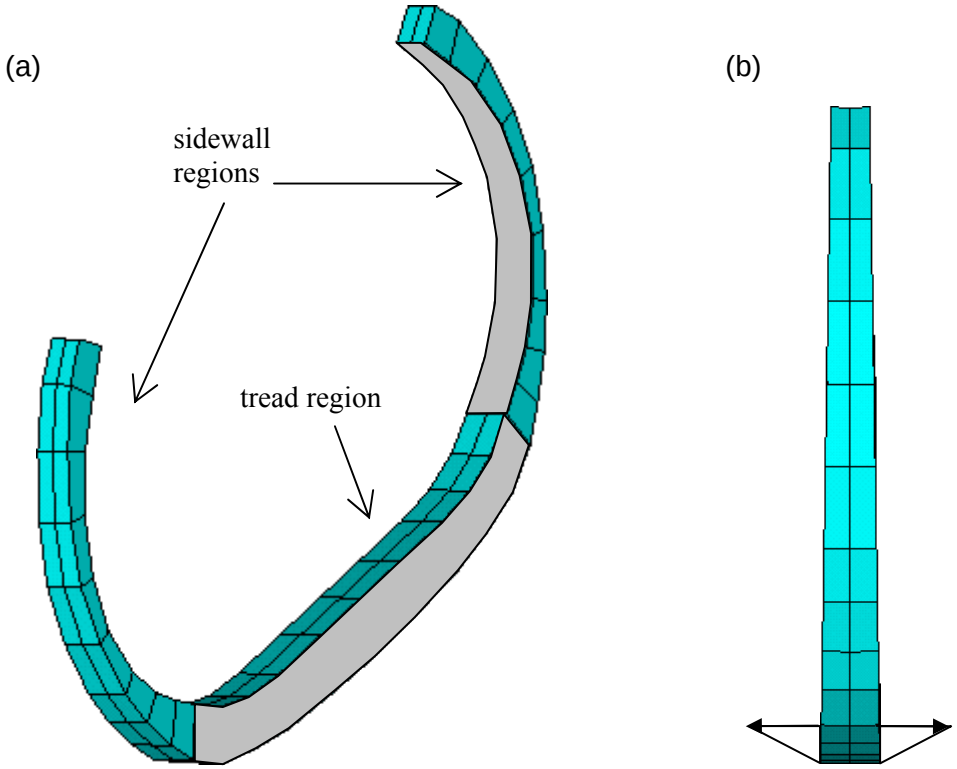

Figure A3.3: Modelling of internal pressure using surface loads: (a) regions where the loads applied (masked regions); (b) pressure distribution in the tread region.

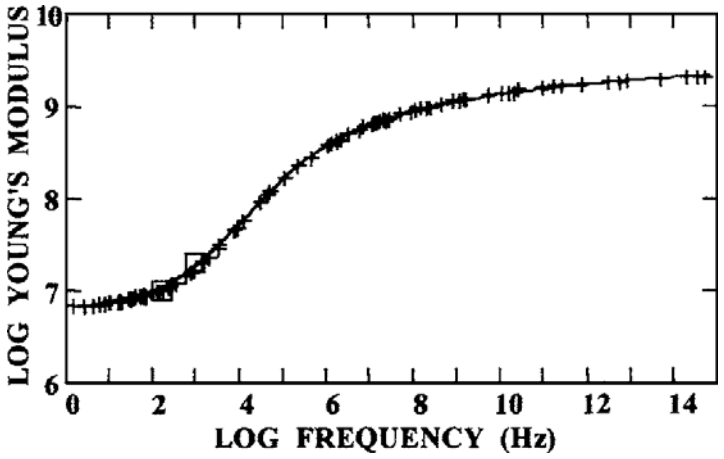

Figure A3.4: Relationship between the Young's modulus and the reduced frequency [140].

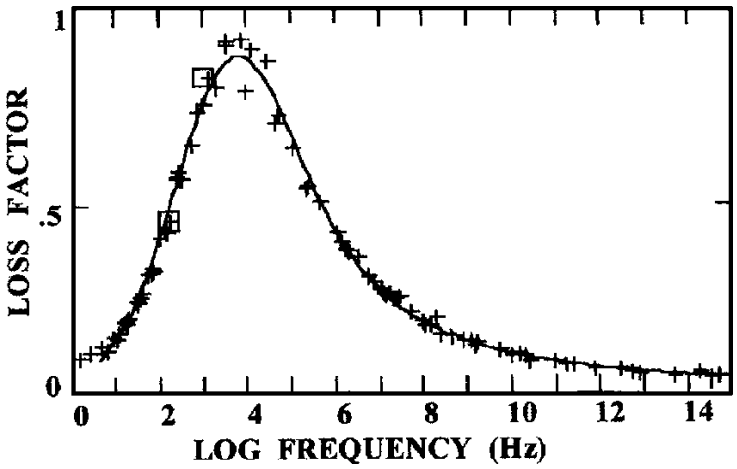

Figure A3.5: Relationship between the loss factor and the reduced frequency [140].

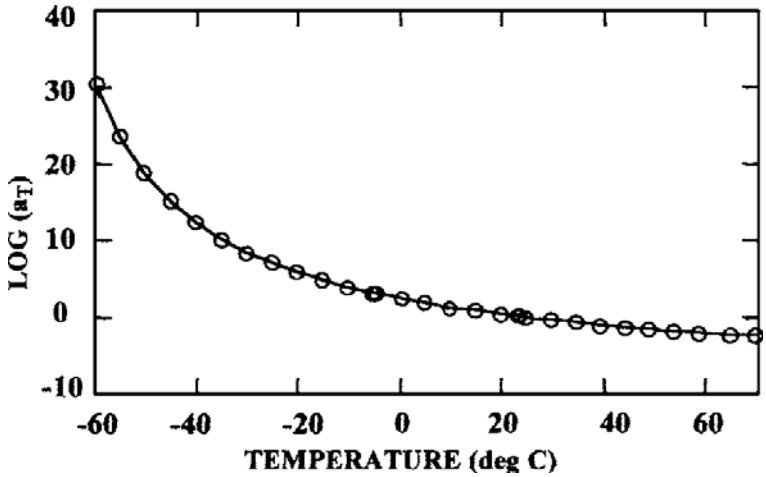

Figure A3.6: Relationship between temperature and the shift factor [140].

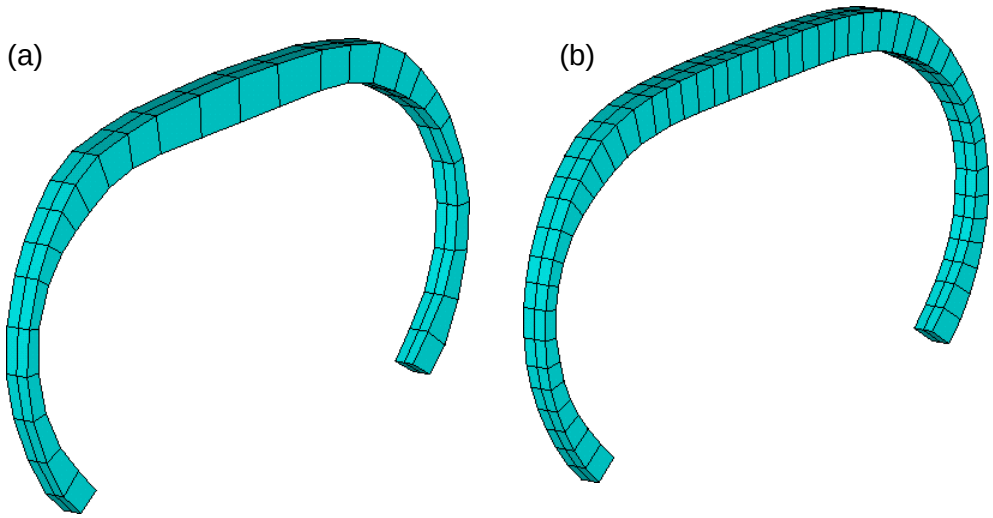

Figure A3.7: FE model of a tyre using (a) 28 FEs; (b) 50 FEs in the cross-section.

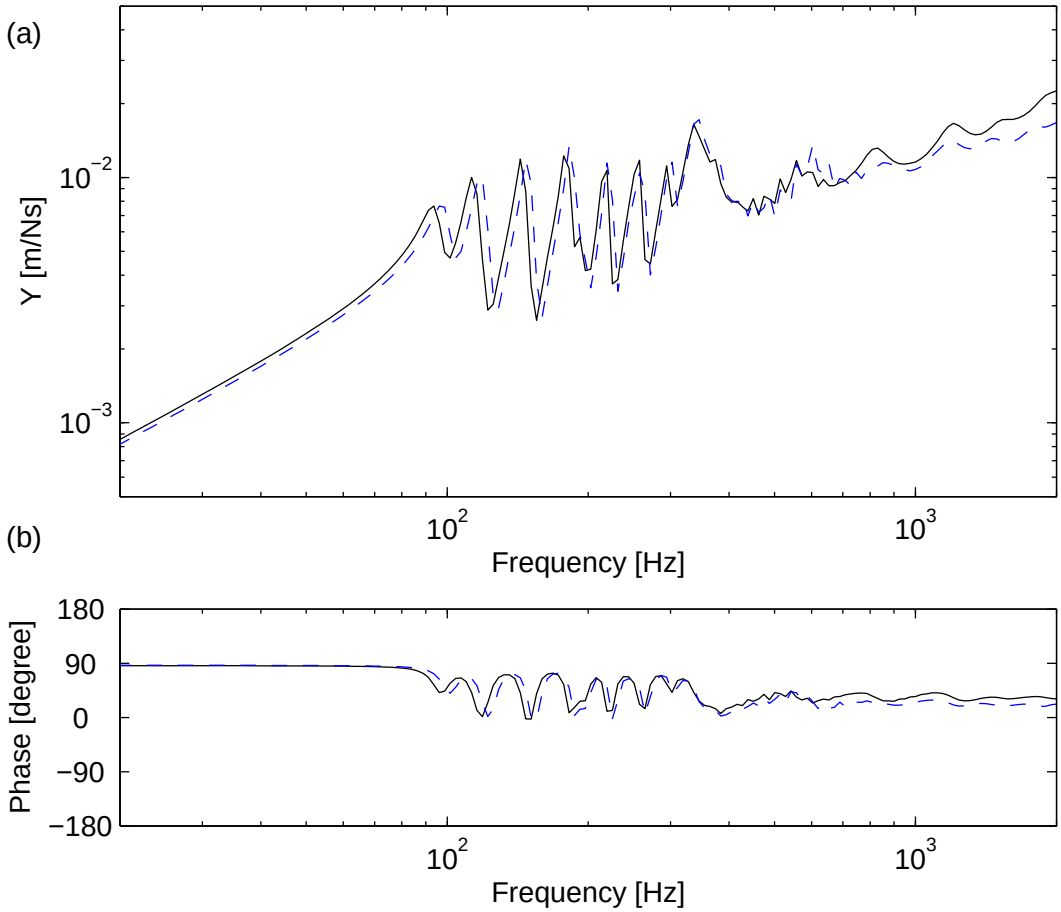

Figure A3.8: (a) Magnitude and (b) phase of the predicted input mobilities of the tyre using — 28 elements; – – 50 elements in the cross-section.

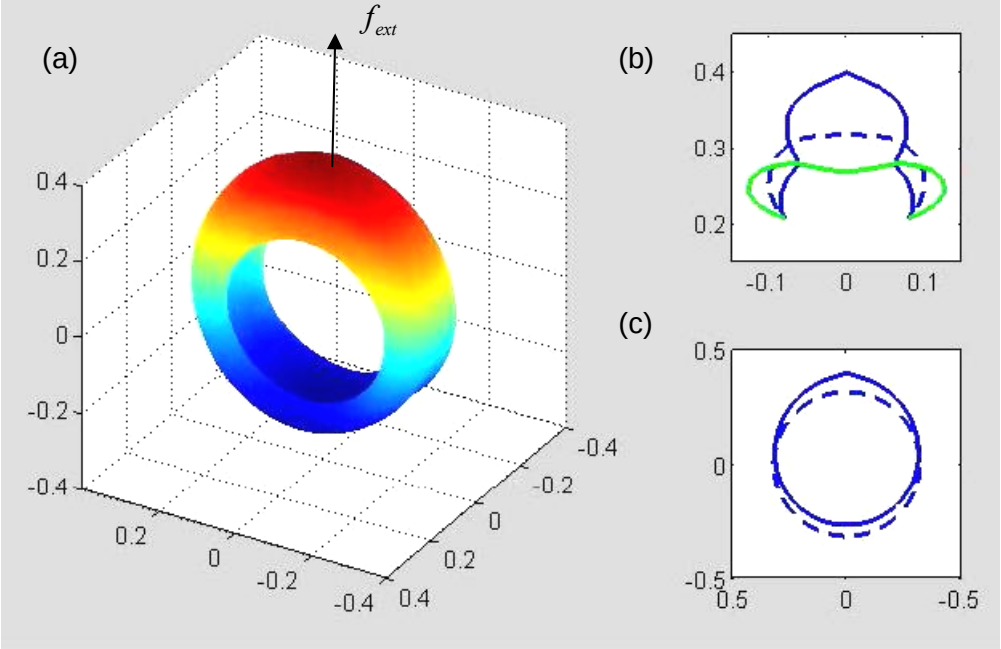

Figure A3.9: Operational deflection shape at 93 Hz. Deformations of (a) a whole tyre; (b) the cross-section at which the excitation is applied and that at the right opposite side; (c) a ring along the tyre centre.

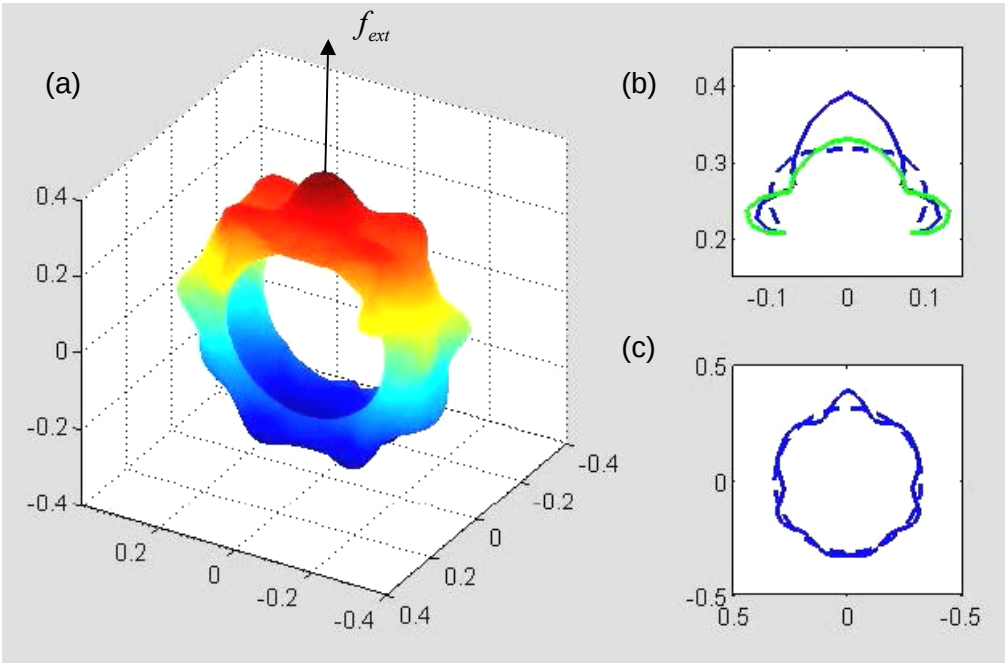

Figure A3.10: Operational deflection shape at 374 Hz. Notation is the same as Figure A3.9

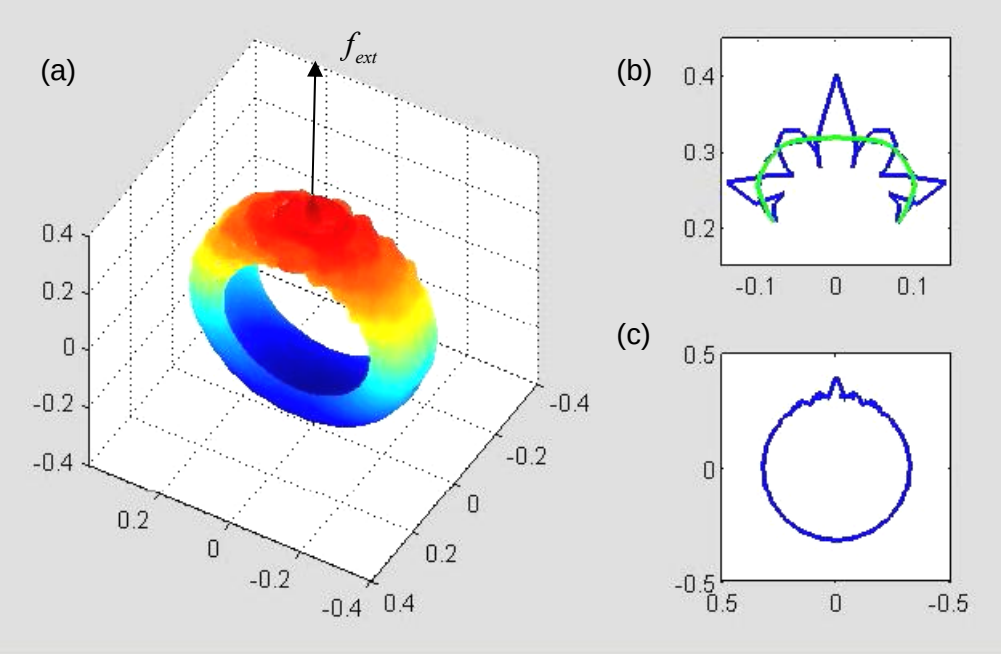

Figure A3.11: Operational deflection shape at 1209 Hz. Notation is the same as Figure A3.9

References

1. K. F. Graff 1975 *Wave Motion in Elastic Solids*. Dover.

2. L. Cremer, M. Heckl, B. A. T. Petersson 2005 *Structure-Borne Sound (Third edition)*. Springer-Verlag.

3. D. J. Mead 2000 *Passive Vibration Control*. John Wiley & Sons.

4. J. N. Reddy 1996 *Mechanics of Laminated Composite Plates: Theory and Analysis*. CRC Press.

5. G. B. Warburton 1976 *The Dynamical Behaviour of Structures, Second edition*. Pergamon Press.

6. E. C. Pestel, F. A. Leckie 1963 *Matrix Methods in Elastomechanics*. McGRAW-HILL.

7. C. M. Nilsson 2004 *Waveguide Finite Elements Applied on a Car Tyre.* Doctoral thesis, Department of Aeronautical and Vehicle Technology, Royal Institute of Technology, Sweden.

8. B. R. Mace, D. Duhamel, M. J. Brennan, L. Hinke 2005 *Journal of the Acoustical Society of America* 117 (5), 2835-2843. Finite element prediction of wave motion in structural waveguides.

9. D. Duhamel, B. R. Mace, M. J. Brennan 2006 *Journal of Sound and Vibration* 294, 205-220. Finite element analysis of the vibrations of waveguides and periodic structures.

10. M. N. Ichchou, S. Akrout, J. M. Mencik 2007 *Journal of Sound and Vibration* 305, 931-944. Guided Waves Group Velocity and Energy Velocities via Finite Elements.

11. J. F. Doyle 1997 *Wave Propagation in Structures, Second edition*. Springer-Verlag.

12. F. Fahy, P. Gardonio 2007 *Sound and Structural Vibration, Second edition*. Elsevier.

13. F. Fahy, J. W. (ed.) 2004 *Advanced Applications in Acoustics, Noise and Vibration*. Spon Press.

14. B. R. Mace 1984 *Journal of Sound and Vibration* 97, 237-246. Wave Reflection and Transmission in Beams.

15. D. W. Miller, A. H. Von Flotow 1989 *Journal of Sound and Vibration* 128 (1), 145-162. A Travelling Wave Approach to Power Flow in Structural Networks.

16. Y. I. Bobrovnitskii 1992 *Journal of Sound and Vibration* 152 (1), 175-176. On the Energy Flow in Evanescent Waves.

17. H. K. Milne 1986 *Journal of Sound and Vibration* 114 (1), 149-151. A Note on Beam Reflection Matrices and Reciprocity.

18. B. R. Mace 1992 *Journal of Sound and Vibration* 155 (2), 375-381. Reciprocity, Conservation of Energy and Some Properties of Reflection and Transmission Coefficients.

19. B. R. Mace 1992 *Journal of Sound and Vibration* 159 (2), 303-325. Power Flow between Two Coupled Beams.

20. E. C. N. Wester, B. R. Mace 2005 *Journal of Sound and Vibration* 285, 209-227. Wave Component Analysis of Energy Flow in Complex Structures - Part 1: A Deterministic Model.

21. S. K. Lee, B. R. Mace, M. J. Brennan 2007 *Journal of Sound and Vibration* 306, 636-656. Wave Propagation, Reflection and Transmission in Curved Beams.

22. Y. Yong, Y. K. Lin 1989 *Journal of Sound and Vibration* 129 (2), 99-118. Propagation of Decaying Waves in Periodic and Piecewise Periodic Structures of Finite Length.

23. N. R. Harland, B. R. Mace, P. W. Jones 2001 *Journal of Sound and Vibration* 241 (5), 735-754. Wave Propagation, Reflection and Transmission in Tunable Fluid-Filled Beams.

24. D. J. Mead 1996 *Journal of Sound and Vibration* 190 (3), 495-524. Wave Propagation in Continuous Periodic Structures: Research Contributions from Southampton 1964-1995.

25. A. Y. T. Leung, S. P. Zeng 1994 *Journal of Sound and Vibration* 177 (4), 555-564. Analytical Formulation of Dynamic Stiffness.

26. N. J. Fergusson, W. D. Pilkey 1993 *The Shock and Vibration Digest* 25, 3-10. Literature Review of Variants of the Dynamic Stiffness Method, Part 1: The Dynamic Element Method.

27. R. S. Langley 1990 *Journal of Sound and Vibration* 136 (3), 439-452. Analysis of Power Flow in Beams and Frameworks using the Direct-Dynamic Stiffness Matrix Method.

28. J. Lee, D. J. Thompson 2001 *Journal of Sound and Vibration* 239 (2), 297-320. Dynamic Stiffness Formulation, Free Vibration and Wave Motion of Helical Springs.

29. J. R. Banerjee 1997 *Computers & Structures* 63 (1), 101-103. Dynamic Stiffness Formulation for Structural Elements: A General Approach.

30. J. R. Banerjee 2003 *Computers & Structures* 81 (18-19), 1915-1922. Free Vibration of Sandwich Beams using the Dynamic Stiffness Method.

31. R. S. Langley 1989 *Journal of Sound and Vibration* 135 (2), 319-331. Application of the Dynamic Stiffness Method to the Free and Forced Vibrations of Aircraft Panels.

32. R. S. Langley 1992 *Journal of Sound and Vibration* 156 (3), 521-540. A Dynamic Stiffness Technique for the Vibration Analysis of Stiffened Shell Structures.

33. L. Meirovitch 1997 *Principles and Techniques of Vibrations*. Prentice-Hall.

34. Y. K. Lin, B. K. Donaldson 1969 *Journal of Sound and Vibration* 10 (1), 103-143. A Brief Survey of Transfer Matrix Techniques with Special Reference to the Analysis of Aircraft Panels.

35. Y. K. Lin, J. N. Yang 1974 *Trans. of ASME, Journal of Applied Mechanics* June, 383-391. Free Vibration of a Disordered Periodic Beam.

36. D. J. Mead 1971 *Journal of Engineering for Industry* August, 783-792. Vibration Response and Wave Propagation in Periodic Structures.

37. L. Brillouin 1953 *Wave Propagation in Periodic Structures (Second edition)*. Dover.

38. D. J. Mead 1973 *Journal of Sound and Vibration* 27 (2), 235-260. A General Theory of Harmonic Wave Propagation in Linear Periodic Systems with Multiple Coupling.

39. D. J. Mead 1975 *Journal of Sound and Vibration* 40 (1), 1-18. Wave Propagation and Natural Modes in Periodic Systems: 1. Mono-Coupled Systems.

40. D. J. Mead 1975 *Journal of Sound and Vibration* 40 (1), 19-39. Wave Propagation and Natural Modes in Periodic Systems: 2. Multi-Coupled Systems, With and Without Damping.

41. D. J. Mead, A. D. Bansal 1978 *Journal of Sound and Vibration* 61 (4), 481-496. Mono-Coupled Periodic Systems with a Single Disorder: Free Wave Propagation.

42. D. J. Mead, A. D. Bansal 1978 *Journal of Sound and Vibration* 61 (4), 497-515. Mono-Coupled Periodic Systems with a Single Disorder: Response to Convected Loadings.

43. D. J. Mead, S. Markus 1983 *Journal of Sound and Vibration* 90 (1), 1-24. Coupled Flexural-Longitudinal Wave Motion in a Periodic Beam.

44. R. M. Orris, M. Petyt 1974 *Journal of Sound and Vibration* 33 (2), 223-236. A Finite Element Study of Harmonic Wave Propagation in Periodic Structures.

45. R. M. Orris, M. Petyt 1975 *Journal of Sound and Vibration* 43 (1), 1-8. Random Response of Periodic Structures by a Finite Element Technique.

46. M. Petyt 1990 *Introduction to Finite Element Vibration Analysis*. Cambridge University Press.

47. K. J. Bathe 1996 *Finite Element Procedures*. Prentice-Hall Inc.

48. S. Finnveden 2004 *Journal of Sound and Vibration* 273, 51-75. Evaluation of modal density and group velocity by a finite element method.

49. L. Gavric 1994 *Journal of Sound and Vibration* 173 (1), 113-124. Finite Element Computation of Dispersion Properties of Thin-Walled Waveguides.

50. R. H. Lyon, R. G. Dejong 1995 *Theory and Application of Statistical Energy Analysis, Second edition*. Butterworth-Heinamann.

51. S. K. Datta, A. H. Shah, R. L. Bratton, T. Chakraborty 1988 *Journal of the Acoustical Society of America* 83 (6), 2020-2026. Wave Propagation in Laminated Composite Plates.

52. P. J. Shorter 2004 *Journal of Acoustical Society of America* 115 (5), 1917-1925. Wave Propagation and Damping in Linear Viscoelastic Laminates.

53. M. M. Ettouney, R. P. Daddazio, N. N. Abboud 1997 *Computers and Structures* 65 (3), 423-432. Some Practical Applications of the Use of Scale Independent Elements for Dynamic Analysis of Vibrating Systems.

54. A. Y. A. Abdel-Rahmen 1980 *Matrix Analysis of Wave Propagation in Periodic Systems.* Ph.D. thesis, ISVR, University of Southampton.

55. J. Signorelli, A. H. Von Flotow 1988 *Journal of Sound and Vibration* 126 (1), 127-144. Wave Propagation, Power Flow and Resonance in a Truss Beam.

56. M. L. Accorsi, M. S. Bennett 1991 *Journal of Sound and Vibration* 148 (2), 279-292. A Finite Element Based Method for the Analysis of Free Wave Propagation in Stiffened Cylinders.

57. M. S. Bennett, M. L. Accorsi 1994 *Journal of Sound and Vibration* 171 (1), 49-66. Free Wave Propagation in Periodically Ring Stiffened Shells.

58. D. J. Thompson 1993 *Journal of Sound and Vibration* 161 (3), 421-446. Wheel-Rail Noise Generation, Part 3: Rail Vibration.

59. L. Houillon, M. N. Ichchou, L. Jezequel 2005 *Journal of Sound and Vibration* 281, 483-507. Wave Motion in Thin-Walled Structures.

60. L. Gry 1996 *Journal of Sound and Vibration* 195 (3), 477-505. Dynamic Modelling of Railway Track Based on Wave Propagation.

61. J. M. Mencik, M. N. Ichchou 2007 *International Journal of Solids and Structures* 44, 2148-2167. Wave Finite Elements in Guided Elastodynamics with Internal Fluid.

62. J. M. Mencik, M. N. Ichchou 2005 *European Journal of Mechanics, A/Solids* 24 (5), 877-898. Multi-Mode Propagation and Diffusion in Structures through Finite Elements.

63. M. Maess, N. Wagner, L. Gaul 2006 *Journal of Sound and Vibration* 296, 264-276. Dispersion Curves of Fluid Filled Elastic Pipes by Standard FE Models and Eigenpath Analysis.

64. E. Manconi, B. R. Mace 2007 *ISVR Technical Memorandum No:966*. Modelling Wave Propagation in Two-dimensional Structures using a Wave/Finite Element Technique.

65. E. Manconi, B. R. Mace 2007 *19th International Congress on Acoustics*, Madrid, CD-ROM. Modelling Wave Propagation in Cylinders using a Wave/Finite Element Technique.

66. W. X. Zhong, F. W. Williams 1995 *Journal of Sound and Vibration* 181 (3), 485-501. On the Direct Solution of Wave Propagation for Repetitive Structures.

67. D. Duhamel, B. R. Mace, M. J. Brennan 2003 *ISVR Technical Memorandum No:922*. Finite Element Analysis of the Vibrations of Waveguides and Periodic Structures.

68. L. Hinke, B. R. Mace, M. J. Brennan 2004 *ISVR Technical Memorandum No:932*. Finite Element Analysis of Waveguides.

69. ANSYS Inc. Corporate 2003 *ANSYS 7.1 Manual Documentation*.

70. Y. Waki, B. R. Mace, M. J. Brennan 2006 *ISVR Technical Memorandum No:964*. On Numerical Issues for the Wave/Finite Element Method.

71. Y. Waki, B. R. Mace, M. J. Brennan 2006 *Proceedings of ISMA2006*, Leuven, 2435-2449. Waveguide finite element modelling: numerical issues and application to simple waveguides.

72. Y. Waki, B. R. Mace, M. J. Brennan 2007 *INTER-NOISE 2007*, Istanbul, CD-ROM. Flexural Wave Propagation in a Plate Strip with Free Boundaries using the Wave Finite Element Method.

73. Y. Waki, B. R. Mace, M. J. Brennan 2007 *19th International Congress on Acoustics*, Madrid, CD-ROM. Vibration Analysis of a Tyre Model using the Wave Finite Element Method.

74. Y. Waki, B. R. Mace, M. J. Brennan 2007 *INTER-NOISE 2007*, Istanbul, CD-ROM. Vibration Analysis of a Tyre using the Wave Finite Element Method.

75. M. I. Friswell, J. E. Mottershead 1995 *Finite Element Model Updating in Structural Dynamics*. Kluwer Academic Publishers.

76. J. R. Banerjee 2003 *Journal of Vibration and Acoustics, Trans. of ASME* 125, 351-358. Dynamic Stiffness Formulation and Its Application for a Combined Beam and a Two Degree-of-Freedom System.

77. O. C. Zienkiewicz, R. L. Taylor 1994 *The Finite Element Method, Volume 1 (Fourth edition)*. McGRAW-HILL.

78. L. N. Trefethen, D. BauIII 1997 *Numerical Linear Algebra*. Society for Industrial and Applied Mathematics.

79. G. H. Golub, C. F. V. Loan 1996 *Matrix Computations (Third edition)*. Johns Hopkins University Press.

80. J. H. Wilkinson 1965 *The Algebraic Eigenvalue Problem*. Oxford University Press.

81. W. X. Zhong, G. Cheng 1991 *Proceedings of the Asia-Pacific Conference on Computational Mechanics*, Blakema, Rotterdam, 373-378. Regularization of Singular Control and Stiffness Shifting.

82. W. X. Zhong, F. W. Williams 1992 *Proceedings of the Institution of Mechanical Engineers, Part C* 206, 371-379. Wave Problems for Repetitive Structures and Symplectic Mathematics.

83. V. C. Klema, A. J. Laub 1980 *IEEE Transactions on Automatic Control* AC-25 (2), 164-176. The Singular Value Decomposition: Its Computation and Some Applications.

84. C. R. Fuller, S. J. Elliott, P. A. Nelson 1996 *Active Control of Vibration*. Academic Press.

85. M. A. Biot 1957 *The Physical Review* 105 (4), 1129-1137. General Theorem on the Equivalence of Group Velocity and Energy Transport.

86. K. A. Stroud, D. J. Booth 2003 *Advanced Engineering Mathematics, Fourth edition*. Palgrave Macmillan.

87. L. A. Pipes 1963 *Matrix Methods for Engineering*. Prentice-Hall Inc.

88. A. Bernard, M. J. S. Lowe, M. Deschamps 2001 *Journal of the Acoustical Society of America* 110 (1), 186-196. Guided waves energy velocity in absorbing and non-absorbing plates.

89. F. Ahmad 2004 *Archives of Mechanics* 56 (2), 157-165. Shape of Dispersion Curves in the Rayleigh-Lamb Spectrum.

90. J. N. Goodier, N. J. Hoff 1960 *Structural Mechanics*. Pergamon Press.

91. C. F. Gerald 1980 *Applied Numerical Analysis (second edition)*. Addison-Wesley Publishing Company.

92. K. Knopp 1996 *Theory of functions: Parts 1 and 2*. Dover.

93. J. R. Kutter, V. G. Sigillito 1981 *Journal of Sound and Vibration* 75 (4), 585-588. On Curve Veering.

94. N. C. Perkins, C. D. Mote 1986 *Journal of Sound and Vibration* 106 (3), 451-463. Comments on Curve Veering in Eigenvalue Problems.

95. C. Pierre 1988 *Journal of Sound and Vibration* 126 (3), 485-502. Mode Localization and Eigenvalue Loci Veering Phenomena in Disordered Structures.

96. P. T. Chen, J. H. Ginsberg 1992 *Journal of the Acoustical Society of America* 92 (3), 1499-1508. Modal Properties and Eigenvalue Veering Phenomena in the Axisymmetric Vibration of Spheroidal Shells.

97. X. L. Liu 2002 *Journal of Sound and Vibration* 256 (3), 551-564. Behaviour of Derivative of Eigenvalues and Eigenvectors in Curve Veering and Mode Localization and Their Relation to Close Eigenvalues.

98. A. W. Leissa 1974 *Journal of Applied Mathematics and Physics* 25, 99-111. On a curve veering aberration.

99. G. B. Warburton 1954 *Proceedings of the Institution of Mechanical Engineering* 168, 371-384. The Vibration of Rectangular Plates.

100. W. Leissa 1969 *Vibration of Plates, NASA SP-160*. National Technical Information Service.

101. Y. K. Konenkov 1960 *Soviet Physics Acoustics* 6, 122-123. A Rayleigh-Type Flexural Wave.

102. B. K. Sinha 1974 *Journal of the Acoustical Society of America* 56 (1), 16-18. Some Remarks on Propagation Characteristics of Ridge Guides for Acoustic Surface Waves at Low Frequencies.

103. R. N. Thurston, J. McKenna 1974 *IEEE Transactions on Sonics and Ultrasonics* SU-21 (4), 296-297. Flexural Acoustic Waves Along the Edge of a Plate.

104. U. Orrenius, S. Finnveden 1996 *Journal of Sound and Vibration* 198 (2), 203-224. Calculation of Wave Propagation in Rib-Stiffened Structures.

105. A. N. Norris, V. V. Krylov, I. D. Abrahams 2000 *Journal of Acoustical Society of America* 107 (3), 1781-1784. Flexural Edge Waves and Comments on "A New Bending Wave Solution for the Classical Plate Equation".

106. A. N. Norris 2003 *Journal of Acoustical Society of America* 113 (5), 2647-2658. Flexural Waves on Narrow Plates.

107. S. J. Walsh, R. G. White 2000 *Journal of Sound and Vibration* 233 (3), 455-488. Vibrational Power Transmission in Curved Beams.

108. W. Leissa 1973 *Vibration of Shells, NASA SP-288*. National Technical Information Service.

109. S. K. Lee 2006 *Wave Reflection, Transmission and Propagation in Structural Waveguides.* Ph.D. thesis, ISVR, University of Southampton.

110. M. Abramowitz, I. A. S. (Ed.) 1972 *Handbook of Mathematical Functions*. Dover Publications.

111. H. Stolarski, T. Belytschko 1982 *Journal of Applied Mechanics, Transaction of ASME* 49, 172-176. Membrane Locking and Reduced Integration for Curved Elements.

112. S. P. Shone 2006 *A Flexural Wave Scattering Method for Damage Detection in Beams.* Ph.D. thesis, ISVR, University of Southampton.

113. C. R. Fuller 1981 *Journal of Sound and Vibration* 75 (2), 207-228. The Effects of Wall Discontinuities on the Propagation of Flexural Waves in Cylindrical Shells.

114. F. Fahy 1985 *Sound and Structural Vibration*. Academic Press.

115. W. Variyart, M. J. Brennan 2002 *Journal of Sound and Vibration* 256 (5), 955-967. Simplified Dispersion Relationships for In-Vacuo Pipes.

116. W. Flugge 1973 *Stresses in Shells, Second edition*. Springer-Verlag.

117. A. W. Leissa, A. S. Kadi 1971 *Journal of Sound and Vibration* 16 (2), 173-187. Curvature Effects on Shallow Vibrations.

118. R. S. Langley 1994 *Journal of Sound and Vibration* 169 (1), 29-42. Wave Motion and Energy Flow in Cylindrical Shells.

119. R. S. Langley 1996 *Journal of Sound and Vibration* 169 (1), 43-53. The Modal Density and Mode Count of Thin Cylinders and Curved Panels.

120. W. Soedel 1981 *Vibrations of shells and plates*. MARCEL DEKKER.

121. U. Sandberg, J. A. Ejsmont 2002 *Tyre/Road Noise Reference Book*. Informex.

122. U. Sandberg 2001 *Proceedings of INTER-NOISE 2001*, Hague, The Netherlands, 35-56. Tyre/road noise- Myths and realities.

123. T. L. Richards 1991 *Journal of Sound and Vibration* 149 (2), 235-243. Finite Element Analysis of Structural-Acoustic Coupling in Tyres.

124. Y. Nakajima, Y. Inoue, H. Ogawa 1993 *Tire Science & Technology*, 67-90. Application of the Boundary Element Method and Modal Analysis to Tire Acoustics Problems.

125. R. Gunda, S. Gau, C. Dohrmann 2000 *Tire Science & Technology*, 33-49. Analytical Model of Tire Cavity Resonance and Coupled Tire/Cavity Modal Model.

126. T. Saguchi, T. Tomida, S. Urata, K. Kato 2006 *Proceedings of INTER-NOISE 2006*, Honolulu, ID264. Tire Radiation-Noise Prediction Using FEM.

127. F. Böhm 1966 *Ingenieru Archiv* 35, 82-101. Mechanik des Gürtelreifens.

128. R. J. Pinnington 2006 *Journal of Sound and Vibration* 290, 101-132. A Wave Model of a Circular Tyre. Part 1: Belt Modelling.

129. W. Kropp 1989 *Applied Acoustics* 26, 181-192. Structure-Borne Sound on a Smooth Tyre.

130. K. Larsson, W. Kropp 2002 *Journal of Sound and Vibration* 253 (4), 889-908. A High-Frequency Three-Dimensional Tyre Model Based on Two Coupled Elastic Layers.

131. F. Wullens, W. Kropp 2004 *Acta Acustica United with Acustica* 90, 702-711. A Three-Dimensional Contact Model for Tyre/Road Interaction in Rolling Conditions.

132. W. Kropp, K. Larsson, F. Wullens, P. Andersson 2004 *Proceedings of the Institute of Acoustics* 26 (2), 1-12. Tyre/Road Noise Generation - Modelling and Understanding.

133. P. Andersson, K. Larsson, F. Wullens, W. Kropp 2004 *Acta Acustica United with Acustica* 90 (445-456). High Frequency Dynamic Behaviour of Smooth and Patterned Passenger Cars.

134. R. J. Pinnington 2006 *Journal of Sound and Vibration* 290, 133-168. A Wave Model of a Circular Tyre. Part 2: Side-wall and Force Transmission Modelling.

135. R. J. Pinnington, A. R. Briscoe 2002 *Journal of Sound and Vibration* 253 (5), 941-959. A Wave Model for a Pneumatic Tyre Belt.

136. J. M. Muggleton, B. R. Mace, M. J. Brennan 2003 *Journal of Sound and Vibration* 264, 929-950. Vibrational response prediction of a pneumatic tyre using an orthotropic two-plate wave model.

137. J. S. Bolton, H. J. Song, Y. K. Kim, Y. J. Kang 1998 *Proceedings of NOISE-CON 98*, 97-102. The Wave Number Decomposition Approach to the Analysis of Tire Vibration.

138. Y. J. Kim, J. S. Bolton 2001 *Proceedings of Inter-Noise 2001*, Hague, Netherlands, 2605-2610. Modeling of Tire Treadband Vibration.

139. A. D. Nashif, D. I. G. Jones, J. P. Henderson 1985 *Vibration Damping*. John Wiley & Sons.

140. W. M. Madigosky, G. F. Lee, J. M. Niemiec 2006 *Journal of the Acoustical Society of America* 119 (6), 3760-3765. A method for modeling polymer viscoelastic data and the temperature shift function.

141. D. J. Ewins 2000 *Modal Testing, Second edition*. Research Studies Press.

142. B. A. T. Petersson, M. Heckl 1996 *Journal of Sound and Vibration* 196 (3), 295-321. Concentrated Excitation of Structures.

143. P. Andersson, K. Larsson 2005 *Acta Acustica United with Acustica* 91, 121-131. Validation of a High Frequency Three-Dimensional Tyre Model.

144. H. Xu 2003 *Linear Algebra and its Applications* 368, 1-24. An SVD-Like Matrix Decomposition and Its Applications.

145. W. X. Zhong, F. W. Williams, A. Y. T. Leung 2003 *Journal of Sound and Vibration* 267, 227-244. Symplectic Analysis for Periodical Electro-magnetic Waveguides.

146. W. Zhong, F. W. Williams 1993 *Computers & Structures* 49 (4), 749-750. Physical Interpretation of the Symplectic Orthogonality of the Eigensolutions of a Hamilton or Symplectic Matrix.

147. H. Fassbender, D. Kressner 2006 *GAMM Mitteilungen, Themenheft Applied and Numerical Linear Algebra (Part 2)* 29 (2), 297-318. Structured Eigenvalue Problems.

148. J. A. Carrilho 2006 *The thirteenth International Congress on Sound and Vibration (ICSV 13)*, Vienna. A Reliable Root Finder for Systems of Coupled Equations: Application to Eigenvalues in Duct Acoustics.

149. A. Rinde 1970 *Journal of Applied Polymer Science* 14, 1913-1926. Poisson's ratio for rigid plastic foams.

150. T. Akasaka 1998 *Textile Structural Composite*. Elsevier Science.

151. S. Timochenko, S. Woinowsky-Kreiger 1959 *Theory of Plates and Shells, second edition*. McGraw-Hill.